How structural factors influence the performance of copper(I) bis(diimine) based DSCs

Inauguraldissertation

zur

Erlangung der Würde eines Doktors der Philosophie

vorgelegt der

Philosophisch-Naturwissenschaftlichen Fakultät

der Universität Basel

von

Sven Yves Brauchli

von Basel (BS)

Basel, 2014

Genehmigt von der Philosophisch-Naturwissenschaftlichen Fakultät der Universität Basel auf Antrag von

Prof. Dr. Edwin C. Constable und Prof. Dr. Oliver S. Wenger

Basel, den 24. Juni 2014

Prof. Dr. Jörg Schibler

Dekan

creative commons

Namensnennung-Keine kommerzielle Nutzung-Keine Bearbeitung 3.0 Schweiz
(CC BY-NC-ND 3.0 CH)

Sie dürfen: **Teilen** — den Inhalt kopieren, verbreiten und zugänglich machen

Unter den folgenden Bedingungen:

Namensnennung — Sie müssen den Namen des Autors/Rechteinhabers in der von ihm festgelegten Weise nennen.

Keine kommerzielle Nutzung — Sie dürfen diesen Inhalt nicht für kommerzielle Zwecke nutzen.

Keine Bearbeitung erlaubt — Sie dürfen diesen Inhalt nicht bearbeiten, abwandeln oder in anderer Weise verändern.

Wobei gilt:

- **Verzichtserklärung** — Jede der vorgenannten Bedingungen kann **aufgehoben** werden, sofern Sie die ausdrückliche Einwilligung des Rechteinhabers dazu erhalten.

- **Public Domain (gemeinfreie oder nicht-schützbare Inhalte)** — Soweit das Werk, der Inhalt oder irgendein Teil davon zur Public Domain der jeweiligen Rechtsordnung gehört, wird dieser Status von der Lizenz in keiner Weise berührt.

- **Sonstige Rechte** — Die Lizenz hat keinerlei Einfluss auf die folgenden Rechte:

  - Die Rechte, die jedermann wegen der Schranken des Urheberrechts oder aufgrund gesetzlicher Erlaubnisse zustehen (in einigen Ländern als grundsätzliche Doktrin des **fair use** bekannt);

  - Die **Persönlichkeitsrechte** des Urhebers;

  - Rechte anderer Personen, entweder am Lizenzgegenstand selber oder bezüglich seiner Verwendung, zum Beispiel für **Werbung** oder Privatsphärenschutz.

- **Hinweis** — Bei jeder Nutzung oder Verbreitung müssen Sie anderen alle Lizenzbedingungen mitteilen, die für diesen Inhalt gelten. Am einfachsten ist es, an entsprechender Stelle einen Link auf diese Seite einzubinden.

Table of contents

CHAPTER I: THE EFFECT OF THE ANCHORING LIGAND UPON DEVICE PERFORMANCE

CHAPTER II: THE INFLUENCE OF DIFFERENT SUBSTITUENTS IN THE 6,6'-POSITIONS OF THE ANCILLARY LIGAND ON DSC PERFORMANCE

CHAPTER III: OPTIMIZING THE ATOM ECONOMY

CHAPTER IV: THE INFLUENCE OF DYE CONCENTRATION

CHAPTER V: ENHANCING THE PHOTON ABSORBANCE

Chapter VI: Solvent effect on DSC performance

Chapter VII: Avoiding aggregation

Synthesis

Acknowledgements

First of all, I want to thank my supervisors Prof. Dr. Edwin C. Constable and Prof. Dr. Catherine E. Housecroft for giving me the opportunity to do my PhD project in their research group. During the last almost four years, they always had an open ear for any questions and were giving advice whenever I needed some.

Secondly I thank Prof. Dr. Oliver S. Wenger for being my co-examiner.

I would like to thank all the members of the technical staff of the Department of Chemistry who give their best that this old house does not fall apart. Especially I would like to thank Markus Hauri for keeping the system of the department running and supplying us with chemicals and other materials. Beatrice Erismann is thanked for her hard administrative work, for answering my questions and for her great sense of humour.

I thank the following people for carrying analytical methods on my samples: Nik Hostettler, Cathrin Ertl and Roché Walliser for measuring 500 MHz NMR spectra, Steffen Müller for measuring MALDI mass spectroscopy, Dr. Iain Wright for measuring some electro chemistry, Dr. Jennifer Zampese and Dr. Markus Neuburger for measuring X-ray diffraction and Sylvie Mittelheisser for supplying the whole Department with elemental analysis.

A very big thanks especially goes to Liselotte Siegfried, Ewald Schönhofer and Annika Büttner for the preparation of nanoporous TiO_2 particles and screenprinting photoanodes for the DSCs. Additionally Ewald Schönhofer is thanked for evaluating the exact area of the over 120 copper masks for the DSCs. Jonas Schönle has to be mentioned because without him the lab would be „reduced to ashes", thank you very much!

Over the last years I shared the laboratory with Ewald and Nik. Not only did I share the lab with them but also have we together run through our whole studies in Basel. I thank both of you for your good sense humour, your advice and your help not only concerning chemical issues. The working atmosphere in our lab, the Swiss lab, was just unique and I will keep it in good mind.

I would like to thank Prof. Dr. Catherine E. Housecroft, Dr. Colin J. Martin, Dr. Collin Morris and Dr. Niamh Murray for their help in reading and correcting this thesis.

I thank the whole Constable-Housecroft research group (only current members are listed by lab) for the familiar contact which made it easy to communicate with each other, inside and outside the laboratories: Andreas Bünzli, Cathrin Ertl, Jonas Schönle, Roché Walliser, Dr. Niamh Murray, Sarah Keller, Frederik Malzner, Max (Yannick M.) Klein, Dr. Collin Morris, Dr. Colin J. Martin, Steffen Müller, Sebastian O. Fürer, Annika Büttner, Ewald Schönhofer Nik Hostettler and Dr. Bilijana Bozic-Weber.

Abbreviations

2-Naph	2-Naphthyl
A	Ampere
bpy	2,2´-bipyridine
cm	Centimetre
DCM	Dichloromethane
dm	Decimetre
dmbpy	6,6´-dimethyl-2,2´-bipyridine
DMSO	Dimethylsulfoxide
dpp	2,9-diphenyl-phenanthroline
e.g.	„exempli gratia" (latin) – meaning "for example"
HOMO	Highest occupied molecular orbital
i.e.	„id est" (latin) – meaning „that is to say"
isoBu	isobutyl
LUMO	Lowest unoccupied molecular orbital
mA	Milliampere
Me	Methyl
MeCN	Acetonitrile
mV	Millivolt
mW	Milliwatt
n-Bu	*n*-butyl
n-Hex	*n*-hexyl
Ph	Phenyl
TBAPF$_6$	tert-butylammonium hexafluoridophosphate
TFA	Trifluoroacetic acid
TW	Terawatt
V	Volt
W	Watt

Photovoltaics

AM	Air mass
DSC	Dye sensitized solar cell
EQE	External quantum efficiency

ff	Fill factor
FTO	Fluorine doped SnO_2
G	Global
η	Global conversion efficiency
IPCE	Incident photon to current conversion efficiency
IQE	Internal quantum efficiency
Isc	Photocurrent measured at short-circuit
ITO	Indium doped SnO_2
Jsc	Short circuit current density
MPP	Maximum power point
TCO	Transparent conducting oxide
Voc	Open circuit voltage

Analysis and experimental

°C	Degree Celsius
Å	Angstrom
br	Broad
calc.	Calculated
CV	Cyclic voltammetry (cyclic voltammogram)
d	Chemical shift, ppm
d	Doublet
dd	Doublet of doublets
dt	Doublet of triplets
EI	Electron impact
eq.	Equivalent
ESI	Electrospray ionisation
FAB	Fast-atom bombardment
g	Gram
h	Hour
Hz	Hertz [$Hz = s^{-1}$]
J	Coupling constant in Hz
m	Medium
m	Multiplet
M	Parent ion

m/z	Mass to charge ratio
MALDI	Matrix assisted laser desorption ionisation
mg	Milligram
MHz	Megahertz
mL	Millilitre
MLCT	Metal-to-ligand charge transfer
mmol	Millimole
mmol	Micromole
Mp.	Melting point
ppm	Parts per million
q	Quartet
rt	Room temperature
s	Strong
s	Singlet
t	Triplet
TMS	Tetramethylsilane
UV-vis	Ultra-Violet Visible Spectroscopy
w	Weak
ε	Extinction coefficient in $dm^3 \ mol^{-1} \ cm^{-1}$
λ_{abs}	Wavelength of a certain absorption band in nm
λ_{max}	Wavelength at which maximum absorption occurs in nm
υ	Wavenumber in cm^{-1}

Analytical methods

^{1}H and ^{13}C NMR spectra were recorded using a Bruker Avance III-250, 400 or 500 NMR spectrometer with chemical shifts referenced to residual solvent peaks with respect to δ(TMS) = 0 ppm. Absorption spectra were recorded on a Cary-5000 spectrophotometer, FT-IR spectra were recorded on a PerkinElmer UATR Two spectrometer. Electrospray ionization (ESI) mass spectra were recorded on a Bruker Esquire 3000^{plus} instrument. Electron impact (EI) and MALDI-TOF mass spectra were recorded on Finnigan MAT 95Q instrument and Bruker Daltonics microflex respectively. Melting points were measured on a Bibby Melting Point Apparatus SMP3.

Electrochemical measurements were made on a CH Instruments 900B potentiostat using glassy carbon, platinum wire and silver wire as the working, counter, and reference electrodes, respectively. Samples were dissolved in HPLC grade CH_2Cl_2 (10^{-4} to 10^{-5} mol dm^{-3}) containing 0.1 mol dm^{-3} [^{n}Bu$_4$N][PF$_6$] as the supporting electrolyte; all solutions were degassed with argon. Cp$_2$Fe was used as the internal reference.

Data for the crystal structure determination were collected on a Bruker APEX-II diffractometer with data reduction, solution and refinement using the programs APEX [1] and SHELXL97 or SHELX-13 [2]. ORTEP-type diagrams and structure analysis were generated using Mercury v. 3.0 [3][4].

The current density-voltage (*IV*) measurements were recorded using the solar simulator Soalronix SolarSim 150. The external quantum efficiency (EQE) measurements were made using a Spe-Quest quantum efficiency instrument from Rera Systems (Netherlands) equipped with a 100 W halogen lamp (QTH) and a lambda 300 grating monochromator (Lot Oriel). The monochromatic light was modulated to 3Hz using a chopper wheel (ThorLabs). The cell response was amplified with a large dynamic range IV converter (CVI Melles Griot) and then measured with a SR830 DSP Lock-In amplifier (Stanford Research).

Secondary electron SEM micrograph images were recorded under vacuum (~1 $\times$ 10^{-6} mbar) using an FEI Nova Nano SEM 230 at an accelerating voltage of 5 keV and magnification of ~9000X. The sample was prepared by scoring and fracturing the glass electrode in order to image the cross section of the different layers.

Abstract

This PhD thesis is based on the synthesis of new *homoleptic* copper(I) complexes and their applications in dye-sensitized-solar-cells (DSCs).

Chapter I: Is an evaluation of the anchoring ligands effect upon device performance containing ancillary ligands of 1st and 2nd generation hole transport triphenylamino-dendrons.

Chapter II: Describes the influence of six different substituents in the 6,6'-positions of the ancillary ligands on the device performance.

Chapter III: Is a short study of a more atom economic device assembling method, where the copper(I) complex is formed in situ on the TiO$_2$ surface.

Chapter IV: Shows the influence of the dye conentration used during the dyeing process of the semi-conductor.

Chapter V: Is a study of how the enhanced photon absorption, achieved by extending the aromatic system of the ancillary ligand, affects the cell performance.

Chapter VI: Describes the use of different solvents during the dyeing process of the photoanode and their influence on DSC performance.

Chapter VII: Addresses issues concerning the TiO$_2$ surface such as the aggregation of dye molecules and how the addition of co-adsorbants during the dyeing cycle may prohibit the formation of such aggregates.

Parts of this work have been published:

- B. Bozic-Weber, S. Y. Brauchli, E. C. Constable, S. O. Fürer, C. E. Housecroft and I. A. Wright, *Phys. Chem. Chem. Phys.*, **2013**, *13*, 4500-4504.

- B. Bozic-Weber, S. Y. Brauchli, E. C. Constable, S. O. Fürer, C. E. Housecroft, F. J. Malzner, I. A.Wright and J. A. Zampese, *Dalton Trans.*, **2013**, *34*, 12293-12308.

- S. Y. Brauchli, B. Bozic-Weber, E. C. Constable, N. Hostettler, C. E. Housecroft and J. A. Zampese, *RSC Advances*, **2014**, *4*, 34801-34815.

- S. Y. Brauchli, F. J. Malzner, E. C. Constable and C. E. Housecroft, *RSC Advances*, **2014**, *4*, 62728-62736.

- S. Y. Brauchli, E. C. Constable, C. E. Housecroft, *Dyes and Pigments*, **2015**, *113*, 447-450.

INTRODUCTION

Motivation

In 1950, about 2.5 billion people were living on planet Earth and since then, the world's population has grown rapidly. By the end of 2010, the population had already reached 6.9 billion people (Figure 1) [5]. Consulting the 2012 "Revision of the official United Nations population estimates and projections", the world population had exceeded 7.2 billion in July 2013 and is projected to grow by almost an additional billion in the next decade to reach 8.1 billion in 2025 and further increasing up to 10.9 billion by the end of this century [6].
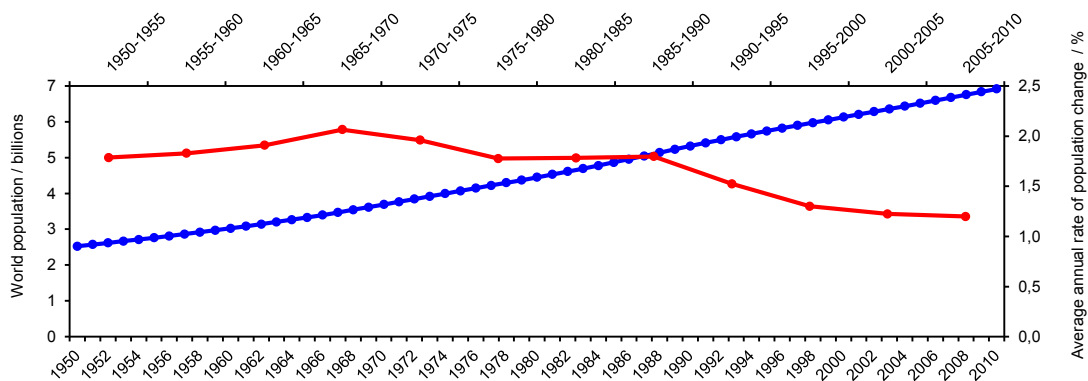
Figure 1: Evolution of total world population from 1950-2010 (blue curve) and the average annual rate of population growth from 1950-2010 (red curve).

Concurrent with the growing world population is the increasing demand of energy. Not only is the rising population number responsible for the enhanced energy consumption, it also depends on the technical progress and mechanisation. Industrial countries are responsible for a large boost in energy demand and, additionally, developing countries and emerging nations contribute more than ever to the worldwide power consumption (Figure 2) [7].
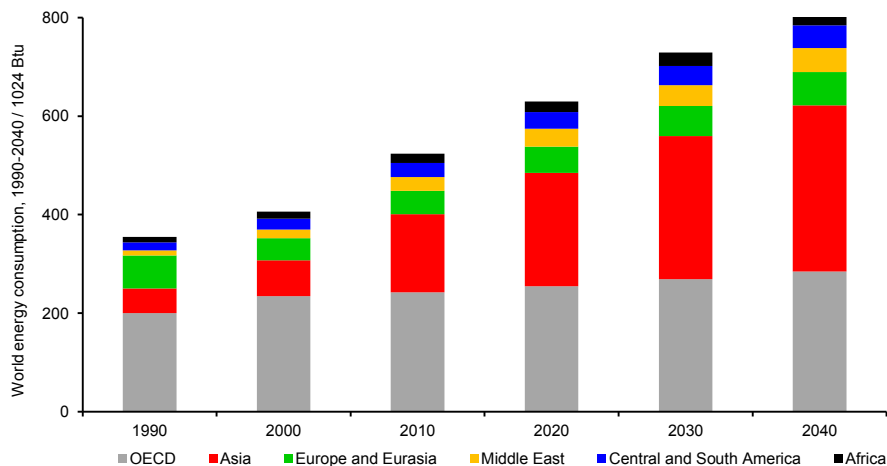
Figure 2: World total energy consumption: history (1990-2010) and projections (2020-2040).

The world energy consumption reached 524 quadrillion Btu in 2010 (Btu = British thermal unit, $\approx$ 1055.06 J) and is projected to exceed 800 quadrillion Btu ($8.65 \cdot 10^{29}$ J) by 2040 [7]. As seen in Figure 2, this increase in energy demand occurs mainly among the developing nations outside the Organization for Economic Cooperation and Development (non-OECD). This progress is driven by economic development and growing populations.

Nowadays, more and more electronics are available in our everyday life and every year new electronic gadgets (such as smart phones, smart watches, tablets, laptops, computers, game consoles, etc.) are released. Although most of these new electronics have been improved in terms of their electric power consumption it is the overall mass/amount of devices on the market and in circulation that causes the continuous increase in power consumption.

From the discovery of nuclear fission by Otto Hahn in 1938 [8][9][10][11][12] and the theoretical explanation by Lise Meitner in 1939,[13][14] the final boost came from the scientific exploration of nuclear power during World War II in the "*Manhattan project*" (1942-1946). This resulted in the construction of the first atomic bomb. Some years later, in 1951, was the first time in history that a nuclear reactor produced electricity [15]. Three years later in Russia at Obninsk the first commercial nuclear power plant with an output of 5 MW was connected to the grid[16][17] and in 1956 the first commercial nuclear power plant outside the USSR with an electrical output of 50 MW was also connected to the national grid[18]. From then on, the triumphal procession of nuclear power was unstoppable. On 23 May 2014, 435 commercial nuclear power reactors were in operation and 72 reactors were under construction [19]. Over the years, the composition by source of energy of the world's electricity generation has changed drastically [20].
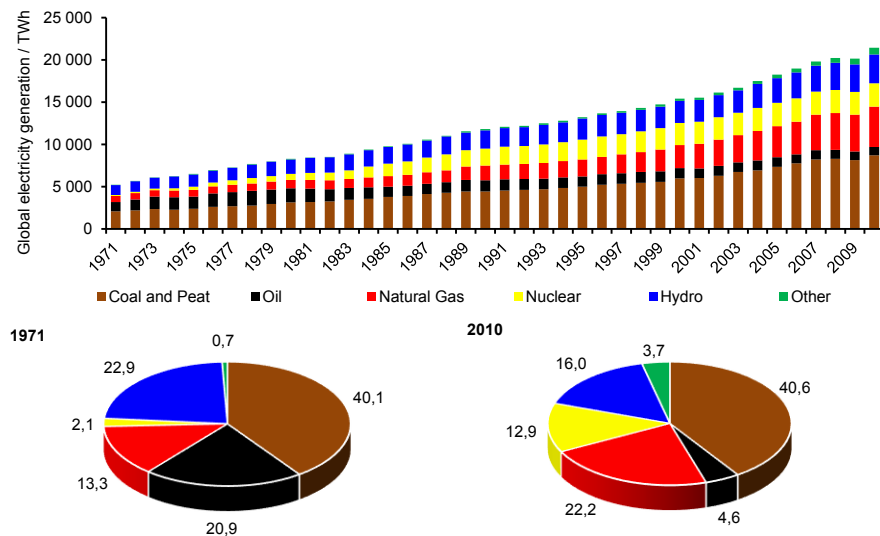
Figure 3: World electricity generation by source of energy from 1971 to 2010 (top) and as a percentage by source of energy for the years 1971 and 2010 (bottom).

Within forty years (1970-2010) the annual produced electricity increased by more than a factor of four. With the rising global electricity production over the years (Figure 3), coal and peat remained the major source for electricity. While the relative contribution of oil was reduced, the electricity produced from natural gases and nuclear power plants drastically increased. Unfortunately, all these energy sources have their disadvantages. Fossil fuels and other hydrocarbon energy sources are based on combustion to produce energy and a downside is the emission of CO_2 [21] and other greenhouse gases. Nuclear power is non emissive in terms of greenhouse gases but the problem of long term storage of radioactive waste has not yet been solved.
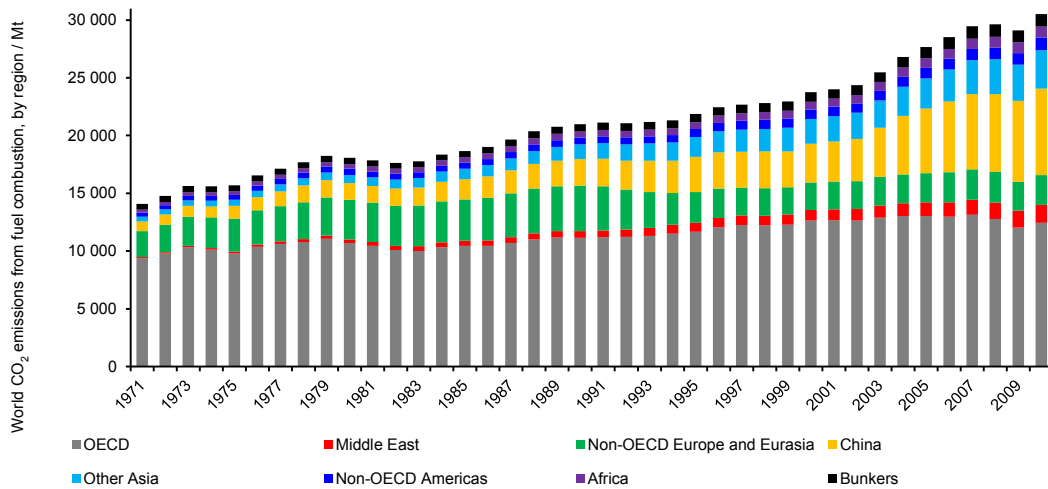
Figure 4: World CO₂ emissions from fuel combustion, by region from 1971 to 2010 [21].

The most common way to treat high-level nuclear waste is to dig tunnels into mountains and bury it[22]. Although this may not appear an ideal disposal technique, experts call this an engineered barrier system that is surrounded by the natural host rock [23]. Ideally, this so called engineered barrier system prevents the release of nuclear waste. Unfortunately there are still factors that cannot be controlled, such as earthquakes causing cracks in this barrier and water intrusion. Under this scenario, the waste can be transferred relatively quickly to the surrounding rocks and, in the worst case, washed out into the ground water [24][25].
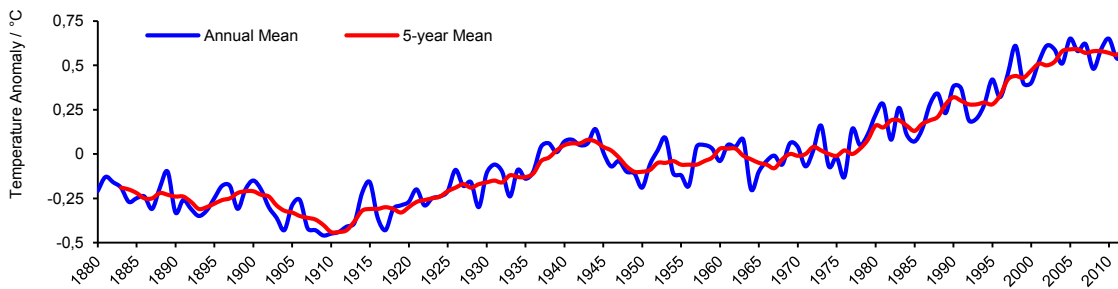
Figure 5: Line plot of global mean land-ocean temperature index, 1880 to present, with the base period 1951-1980.[26]

The emission of CO_2 and other gases from combustion processes (greenhouse gases) has led to global warming. The global temperature rose $\approx 0.2°C$ per decade over the last 30 years [26] (Figure 5). Snow and glaciers are melting, the melting of permafrost has destabilized rocks, polar caps build less ice during winter time and with the meltdown, the mean sea-level is rising. Global warming concerns not only land but also the oceans. In 1998, the phenomenon of *El Niño* was heating the Pacific and Indian Oceans and brought the ecological system close to a collapse. Climatological phenomena such as floodings, storms and meagreness are only the initial signs of global warming. Consequences that mankind has to deal with are water shortage, crop failures, hunger crises and extermination of species. These dreary perspectives should be motivation enough for everyone to, on the one hand, save energy, and on the other hand, use renewable energy sources to reduce CO_2 emissions.

Nowadays there is a wide range of possible green/renewable energy sources. Some of them still rest on the combustion of hydrocarbon sources such as bio-gas, bio-mass and bio-ethanol. Of course this is a step in the right direction to replace oil, coal, and nuclear-energy with these new energy sources but the emission of CO_2 is still not avoided. Other renewable energy sources without greenhouse gas emission, besides emissions for their construction sites, are wind (on and off shore), hydropower (wave and tidal power plants, river etc.), geothermal energy and solar energy (photovoltaic and solar power plants).
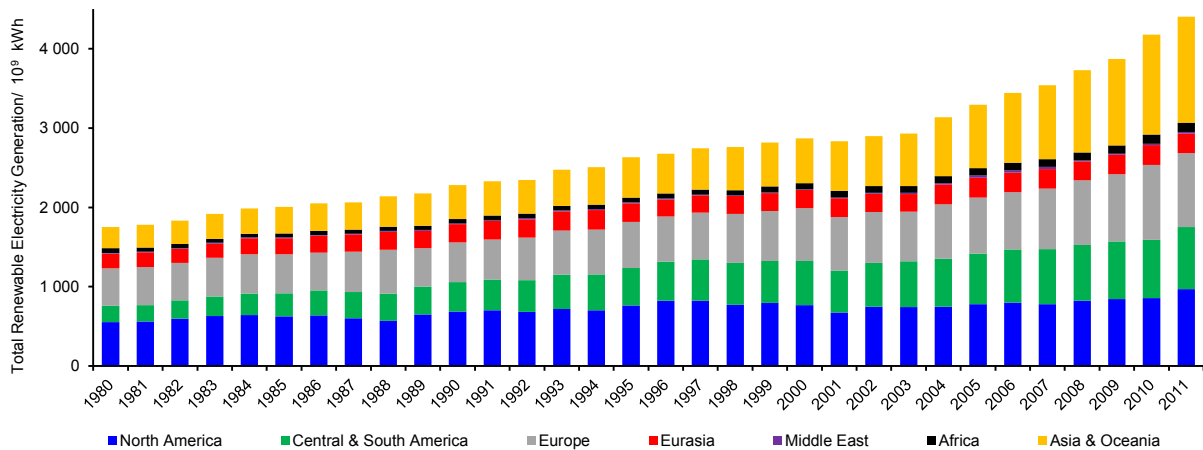
Figure 6: Total renewable electricity generation in billion kWh from 1980 to 2011. [27]

The global renewable produced energy increased from in $1753 \cdot 10^9$ kWh in 1980 to $4400 \cdot 10^9$ kWh in 2011 (Figure 6), making a relatively small contribution to the total global energy consumption in the last decades. Within these years, the composition of the produced electricity from renewable sources has changed. While in 1980 98% of the generated renewable electricity came from hydroelectric power plants, its relative contribution decreased in 2011 to 79% (Figure 7). Besides hydroelectric power, electricity produced from biomass and waste as well

as wind energy has begun to contribute in non- negligible amounts. Solar energy, geothermal heat and tidal and wave power generation still only play a minor role.
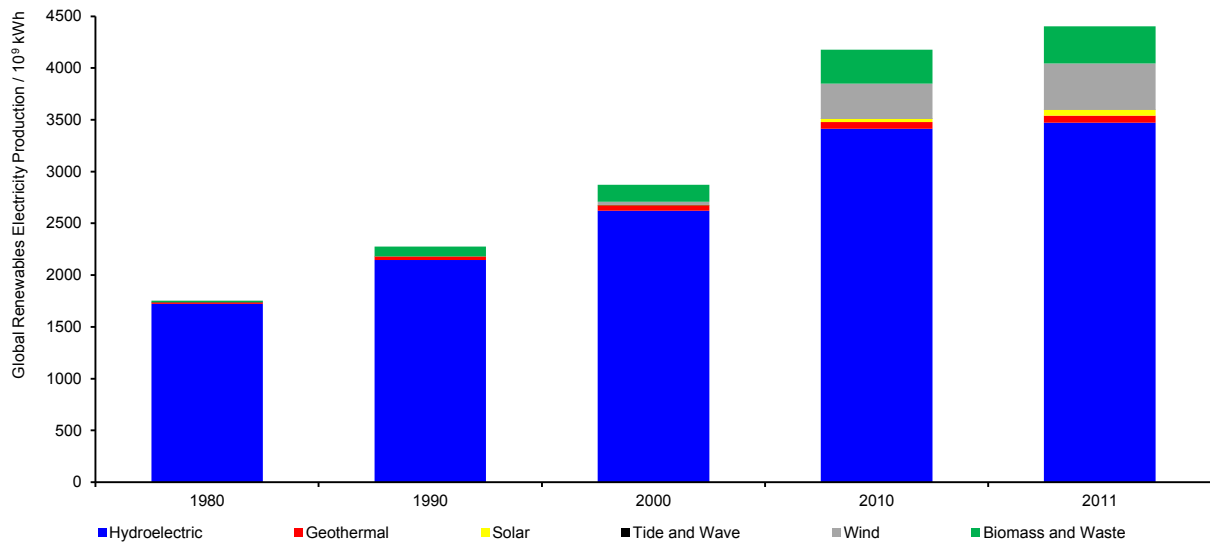
Figure 7: Total global renewable electricity production by energy source. [28]

Another point that has to be considered when comparing renewable energy sources is their impact on the environment during their construction. While for hydroelectric power a barrier lake or something similar is needed, huge turbines at geographically exclusive spots have to be built for wind and tidal electricity production. Biomass still emits CO_2, and only solar energy fulfils the requirements of a non-emissive (gas or noise) and practically unlimited application concerning the installation site.

To gain solar energy, a wide range of technologies such as solar heating, solar photovoltaic, solar thermal electricity and artificial photosynthesis, etc. can be applied [29][30]. The sun irradiates $173 \cdot 10^{15}$ watts (173 petawatts) into the Earth's atmosphere [31]. About 30% of this energy is reflected by the atmosphere back into space whereas the remaining energy is absorbed by the atmosphere, clouds, and sea and land surfaces. The sunlight that reaches the surface within a year corresponds to an energy of approximately 3850000 EJ ($\approx$ 107000 PWh). It is estimated that the terrestrial global solar potential lies at about 600 TW. The sun is considered to be the largest potential energy source to satisfy the demand for future renewable energy [32]. In 2000, the mean global energy consumption totaled 13 TW [33]. Assuming a continuous growth of population and power consumption, a projected total world energy demand of 28 TW in 2050 is predicted [34][35]. The sun emits radiation with a range from UV and visible to infrared. Its spectrum is similar to that of a blackbody at 5760 K. The atmosphere filters some wavelengths. Ozone absorbs UV light and water and CO_2 absorbs mainly radiation in the infrared part of the spectrum. These absorptions cause dips in the collected spectrum of the sun light at the Earth's surface (Figure 8).
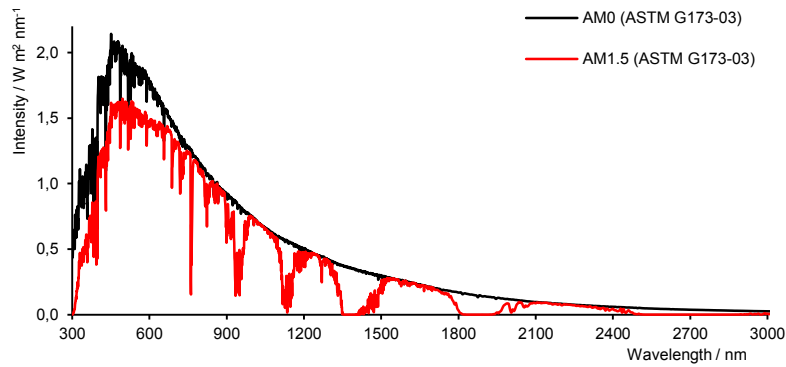
Figure 8: Solar spectrum, extra-terrestrial (black) and after atmospheric absorptions (red) [36].

Water dips in the solar flux can be seen at 900, 1100, 1400, and 1900 nm, whereas CO_2 absorptions occur at 1800 and 2600 nm.

The Sun provides the Earth in one hour with as much energy as all mankind uses in a whole year [37][38]. Comparing other energy sources, whether they are renewable or non-renewable, with solar energy, all appear to be tiny resources (Figure 9).
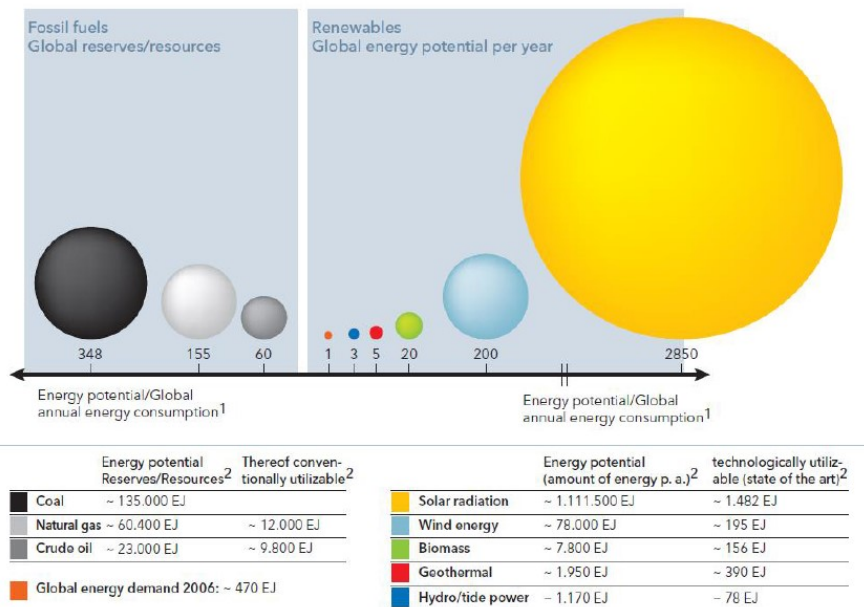
Figure 9: Global potential of available renewables and fossil fuels [39]. *Data refer to global energy consumption of 390 EJ in 1997* [40].

Energy production based on capturing and harnessing the delivered energy from the sun is regarded as a powerful, game-changing tool on the way to supply future mankind with clean energy. As part of these renewable solar based power production techniques, dye sensitized solar cells are considered to be one of the future key players concerning power generation.

1   Dye sensitized solar cells

Scientis have been fascinated by the idea of harnessing the sun for a long time[41][42]. In 1839, Alexandre-Edmond Becquerel observed current passing between two Pt-electrodes immersed in an electrolyte media in the presence of sunlight [43]. In 1877, Moser observed a "photosensitization" effect on silver halide grains (photography)[44]. One of the first chemists who investigated photochemical reactions was Giacomo Ciamician. At a meeting of the International Congress of Applied Chemistry in 1912, he suggested replacing fossil energy with solar irradiation [45]. Almost 80 years later, in 1991, O'Regan and Grätzel [46] started the boom within the field of DSC research. With their ongoing improvement, dye sensitized solar cells are nowadays challenging conventional solid state photovoltaic modules. The current record in conversion efficiency was also achieved by Grätzel et al. [47] with a solid state DSC incorporating a pervoskite sensitizer yielding 13% conversion efficiency. One of the main advantages of DSCs compared to conventional PV modules are the lower fabrication costs. Other advantages are new design applications such as transparent modules (windows), multi colours, flexibility, lightweight and abundant resources available to reach terawatt scale. Additionally, DSCs perform better under diffuse light and at higher temperatures than Si-PV units. Moreover, DSCs are bifacial, which means that the cells can capture light from both sides and essentially all angles. They can also be applied indoor. Furthermore, the devices have a low payback time concerning the energy (less than one year). All over the world research groups are investigating and improving DSCs and the interest in this field is fast growing (Figure 10).
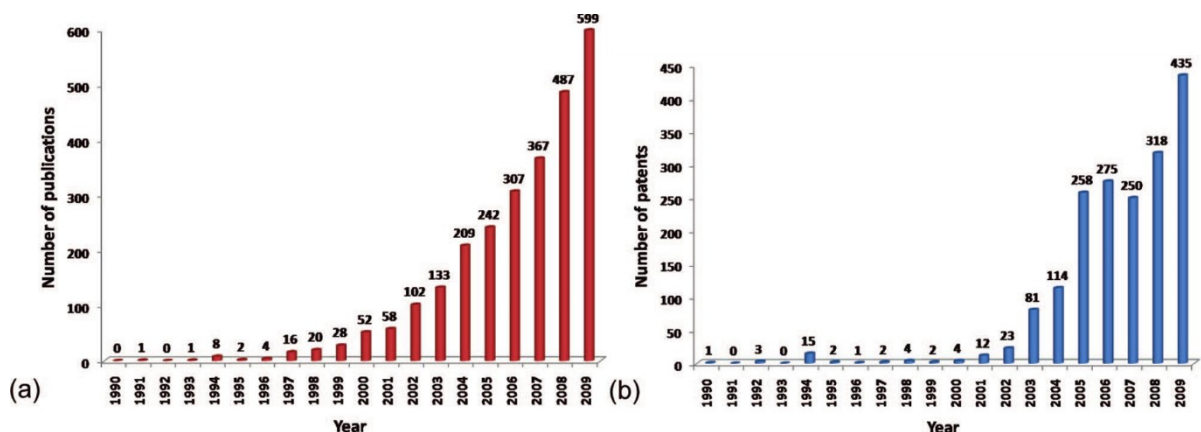
Figure 10: Number of publications (a) and patents (b) per year. Picture adapted from. [33]

1.1   General design and working principle

In general, a DSC is based on the following design (Figure 11): The two outer sides are formed by two pieces of glass covered with a transparent conducting oxide (TCO). The photoanode is covered with a few micron thick layer of mesoporous TiO_2. The TiO_2 (semiconductor) is coated

with dye (photosensitizer). The counter electrode consists of glass treated with a TCO and a layer of platinum. The inter-layer space between the two electrodes is filled with organic electrolyte (redox mediator), usually containing iodine, LiI, ionic liquids and other additives.
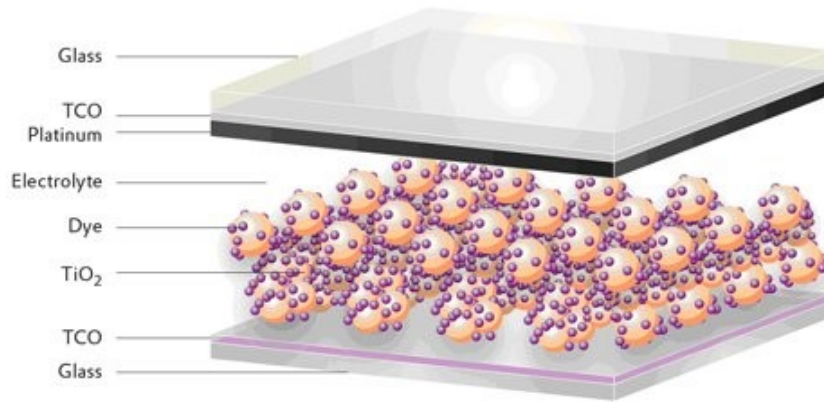
Figure 11: Schematic setup of a dye-sensitized solar cell (DSC).[48]

The Fermi level of the semiconductor is influenced at the point of physical contact of the semiconductor and the electrolyte solution. At the photoanode, the bending of the Fermi levels leads electrons from the conduction band to the interior of the semiconductor and the generated holes are mediated to the electrolyte (Figure 12). When injected electrons reach the counter electrode they reduce the previously oxidized electrolyte.
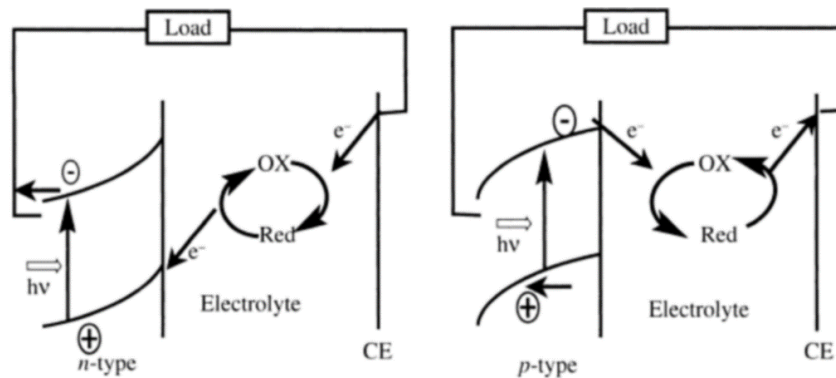
Figure 12: General operating principle of liquid junction solar cells (n-and p-type semiconductor electrodes).[49]

When the cell is irradiated with light, a negative potential is obtained at the photoanode. This forces the Fermi level at the anode to shift to negative potential. The overall outcome under illumination for a photoelectrochemical cell is the conversion of sunlight (energy) to electrical energy. Photosensitization can occur by the transfer of excitation energy or by electrons. In the presence of semiconductors, the dye gets oxidized by transferring an electron from its excited state to the conduction band of the semiconductor.
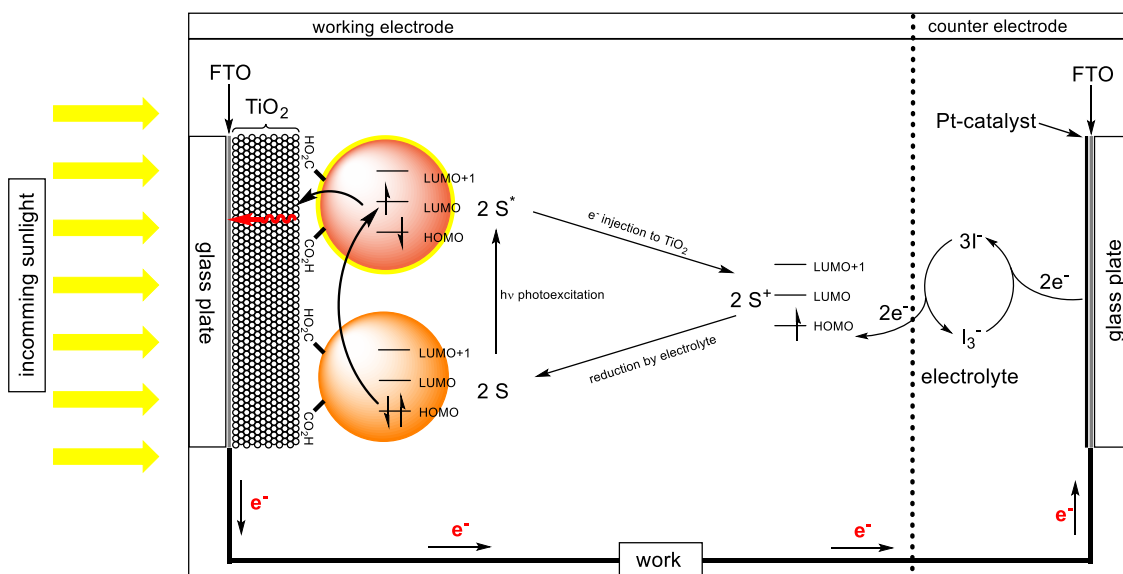
Figure 13: Schematic drawing of a DSC with main operation processes.

When sunlight hits the dyed semiconductor of a DSC, a sequence of reactions occurs (Figure 13). The reaction cycle starts at the anode where the absorption of photons by the sensitizer (S, dye) form an electronically excited state S^*.

$$S + h\nu \rightarrow S^* \text{ (photoexcitation)}$$
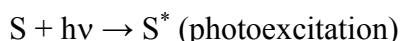
This photoexcited dye (S^*) can undergo several reaction paths to return to its ground state. It either decays back to the ground state or undergoes oxidative quenching. The favoured reaction to occur is the injection of an electron into the conduction band of TiO_2.

$$S^* \rightarrow S + h\nu' \text{ (emission)}$$
$$S^* \rightarrow S^+ + e_{cb} \text{ (electron injection)}$$
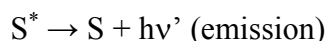
While the injected electrons diffuse through the semiconductor, enter the external circuit at the back-collector electrode and perform work, the oxidized dye (S^+) is reduced by the electrolyte (I^-/I_3^-).

$$2S^+ + 3I^- \rightarrow 2S + I_3^- \text{ (dye regeneration)}$$
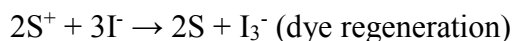
If the redox mediator cannot reach the oxidized dye fast enough, the oxidized dye (S^+) undergoes charge recombination with already injected electrons in the TiO_2.

$$S^+ + e^-(TiO_2) \rightarrow S \text{ (recombination)}$$
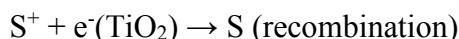
The electrons that reach the counter electrode through the external circuit regenerate (reduce) the oxidized electrolyte (I_3^-) back to I^-. At this point, the cycle is closed.

$$I_3^- + 2e^- \rightarrow 3I^- \text{ (regeneration of } I^-)$$
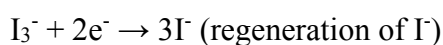
The desired processes in the working DSC are always in competition with other charge processes that lower the efficiency of a device (Figure 14).
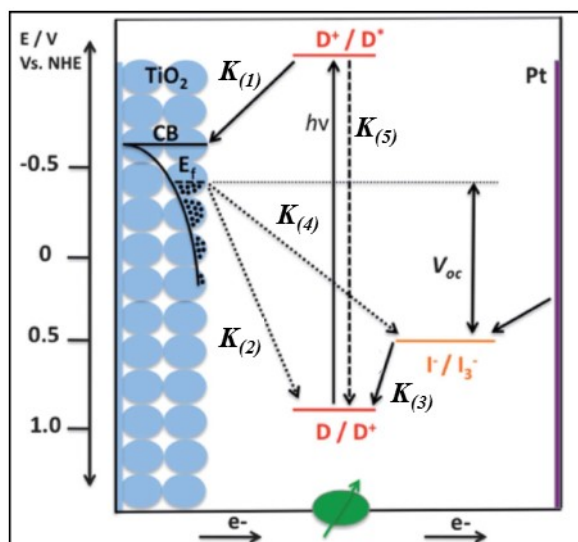
Figure 14: Main processes in a DSC with competing processes. [50]

In an efficient DSC the rate of electron injection, $K_{(1)}$, must be higher than the decay rate of the excited state (D^+/D^*) to the ground state (D/D^+), $K_{(5)}$. Additionally, the rate of recombination of the dye cation with electrons injected to into TiO_2, $K_{(2)}$, must be lower than the rate of reduction of dye cations by iodide, $K_{(3)}$. Another undesired process is the recombination of injected electrons and oxidized electrolyte, $K_{(4)}$.
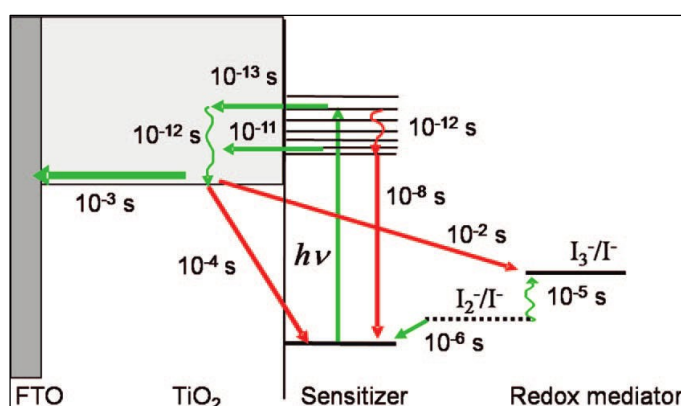
Figure 15: Overview of processes and typical time constants under working conditions in a Ru(II)-dye-sensitized solar cell with iodide/triiodide electrolyte. Recombination processes are indicated by red arrows.[33]

The charge injection for Ru(II) dyes into the TiO_2 conduction band was found to be ultrafast (Figure 15). The reason for this quick injection is attributed to the direct attachment of the sensitizer to the oxide surface [51][52][53][54]. For the DSC performance it is important that the electron injection process is faster than the decay of the excited state of the dye to the ground state. If the injection is too slow there could be a kinetic competition between charge injection and excited state decay, which would lower the overall performance of the device [55]. Due to the high amount of dye molecules, the oxidized dye must have a lifetime of >100s if the regeneration takes about 1μs [56]. Little is still understood about the mechanism of charge transport/diffusion through the nanoporous TiO_2. It is clear that because of the high porosity

and shape of the TiO$_2$ nanoparticles the conductivity must be low and the particles do not support a built in electrical field. Moreover the particles and the pores have a huge surface where a possible interaction between chare and oxidized electrolyte could happen.

The current output of a DSC depends strongly on the absorption properties of the dye. The stronger and broader the absorption, the more photons can be harvested from the sunlight. The characterisation of a device depends on several experimental parameters: photocurrent (*Isc*), photocurrent density (*Jsc*), open-circuit-voltage (*Voc*) and fill factor (*ff*). The internal quantum efficiency (*IQE*) is a term for the quantum yield. It gives information on how many incident photons at a certain wavelength are converted to electrons. It can also be described as the ratio of electrons generated by the solar cell to the number of photons that are absorbed at a given wavelength. Another type of quantum yield key factor is the external quantum efficiency or incident photon-to-electrical-conversion efficiency (*EQE* and *IPCE*). It is the ratio of the number of charge carriers (electrons) generated by the solar cell to the number of photons at a certain energy shining on the cell. The *IPCE* or *EQE* can be described as the number of electrons generated by light in the external circuit divided by the number of incident photons as a function of excitation wavelength. Both *IQE* and *EQE* are measured using a monochromatic light source.

$$EQE \; or \; IPCE = \frac{\# \; electrons}{\# \; photons}$$

$$IQE = \frac{EQE}{1 - tranmission - reflection}$$

The photocurrent *Isc* is defined as the integrated sum of *IPCE* measured over the whole spectrum.

$$Isc = \int_0^\infty IPCE\,(\lambda) \times I_{sun}(\lambda)d\lambda$$

The overall sunlight to electric power conversion efficiency of a DSC is defined as followed:

$$\eta = \frac{Isc \times Voc \times ff}{Pin}$$

The fill factor (*ff*) is defined as the ratio of ($I_{MPP} \times V_{MPP}/Isc \times Voc$). The four values *Isc*, *Voc*, *ff* and η are the key parameters of a DSC. The global efficiency of a device (η_{global}) can also be calculated as a product of the integrated photo current density (I_{ph}), the open-circuit-voltage (*Voc*) and the fill factor (*ff*) divided by the intensity of the incident light ($Is = 1000$ W/m^2)

$$\eta_{global} = (I_{ph} \times Voc \times ff)/Is$$

1.2 Device components

The DSC is an example of an electro-chemical system, where the function/output of the whole device is better than estimated from the properties of the components [57]. Since a DSC is built of many components, the device itself has numerous optimization sites. There are a number of complex interactions between the individual components of the device, especially at the oxide/dye/electrolyte interface. At first, all components have to be optimized individually and then again as part of the working device. The following factors have to be tuned in order to obtain the optimal output for a certain device: the transparent carrier material (glass or plastics) with the transparent conducting oxide layer, the semiconductor layer (mesoporous TiO_2), blocking and scattering layers, the dye, the electrolyte (already itself a multi component factor with solvent for the electrolyte, ionic liquids, etc.), and the counter electrode.

Transparent conducting oxide (TCO)

Since the active dye is bound to the semiconductor between two carrier substrate sheets (glass), the TCO is the connection between the semiconductor and the external circuit. The sunlight first has to shine through the carrier substrate and the TCO, therefore the first requirement the TCO has to fulfil is that it is transparent. Additionally, it has to be resistant to high temperature because of the high temperatures used during the sintering process of the TiO_2 (up to 500°C). In addition to the transparency and the thermal stability, a low resistance is also required. The most popular TCOs are indium-doped tin oxide ($In:SnO_2$, ITO) and fluorine-doped tin oxide ($F:SnO_2$, FTO). While there are benefits of using glass for the carrier substrate (e.g. good protection against water and oxygen penetration) its disadvantage is the heavy weight. For mobile applications, carrier substrates should be shock resistant, flexible and light.

Semiconductor on the photoanode

Up to now, several oxide semiconductors have been applied in DSCs (TiO_2, ZnO, SnO_2 …) (Figure 16). The increase in surface area by using mesoporous TiO_2 is about a factor of 1000. Besides simple oxides, ternary oxides such as Zn_2SnO_4 and $SrTiO_3$ have also been explored. Core-shell structures of ZnO-coated SnO_2 particles were applied as well [58][59][60][61].
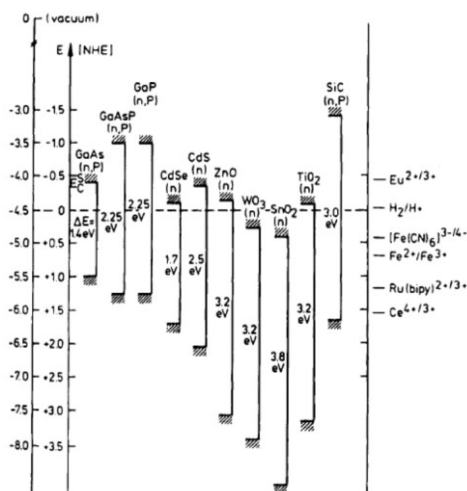
Figure 16: Band edge position of several semiconductors in contact with aqueous electrolyte at pH = 1.[62]

Of the simple oxides, the highest efficiencies were achieved with TiO_2. It has several advantages: it is non-toxic, chemically stable and also used in wider applications in our everyday life's (toothpaste, polishing agents, white paint, sun cream and also used as food additive E171). The industrial scale production and its various applications make TiO_2 a cheap semiconductor. TiO_2 adopts several crystalline forms such as anatase, brookite and rutile [63] (Figure 17).
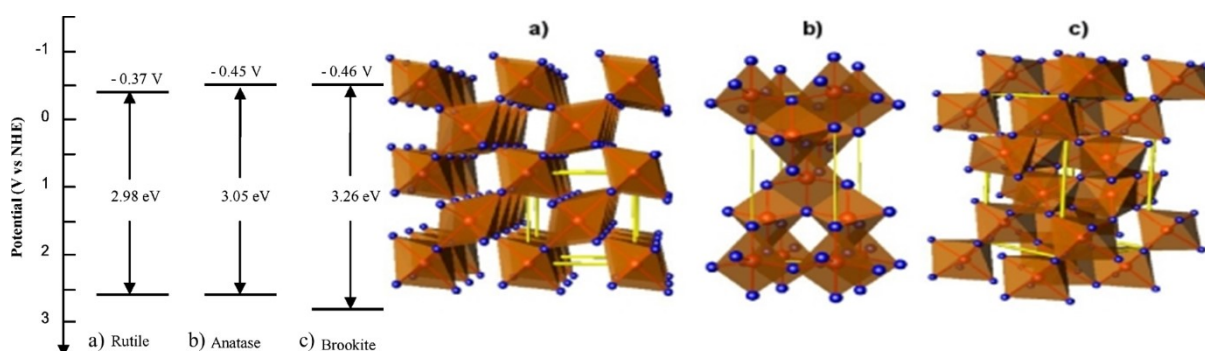
Figure 17: Electrochemical potentials (versus NHE) of the band edges of anatase, brookite, and rutile at pH = 7.[64]

Rutile is the most thermodynamically stable form. Anatase is, however, preferred because it has a larger band gap (Figure 17) and a higher conduction band edge energy, which leads to a higher *Voc*. In DSCs the usual TiO_2 thickness is 2-15μm and consists of several nanosized layers of TiO_2 particles with a diameter of 10-30 nm. The most common ways to apply the layers on the carrier substrate are by doctor blading, screen printing, spin coating [65], compressing [66][67][68] and spaying.
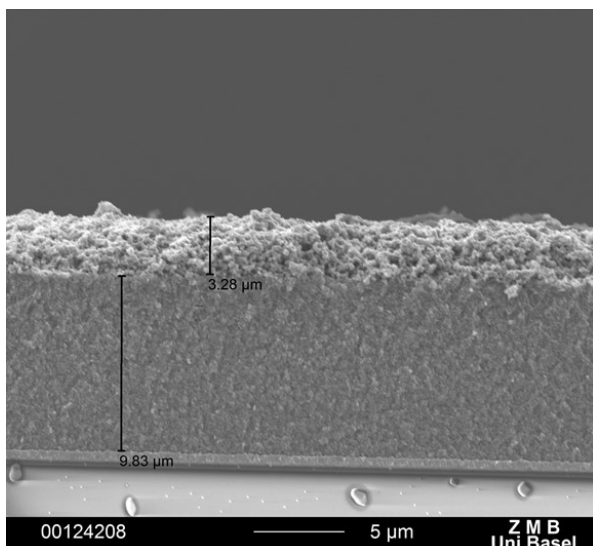
Figure 18: Cross-section SEM micrograph of a commercial Solaronix photoanode. Picture taken by Dr. Collin Morris, University of Basel.

Figure 18 shows a cross-section of a DSC, using FTO coated glass as carrier substrate. The bottom layer (9 μM) shows the uniformly densely packed mesoporous nano-sized TiO_2. On top of it, a scattering layer (3 μm, with bigger particles) is applied, reflecting un absorbed light back to the TiO_2.

In the beginning of DSC research, the conversion efficiencies with single crystal semiconductors were very low ($\leq$ 1%). The main drawbacks of these first attempts was that the excited electron injection was only efficient in a monolayer of adsorbed dye on the semiconductor. Since they used a single crystal semiconductor, basically only one monolayer of dye molecules was absorbing sunlight. One of the main breakthroughs that led to much higher sunlight to power conversion efficiencies was the substitution of single crystal TiO_2 with nanoscale mesoporous oxide films. With this change in design, an increase in surface area for dye loading was achieved (Figure 19). Higher porosity can be obtained by adding more polymer to the TiO_2 paste and is ideally about 50-60%. Higher porosity leads to less interconnections between the particles thereby decreasing the charge collection efficiency [69].
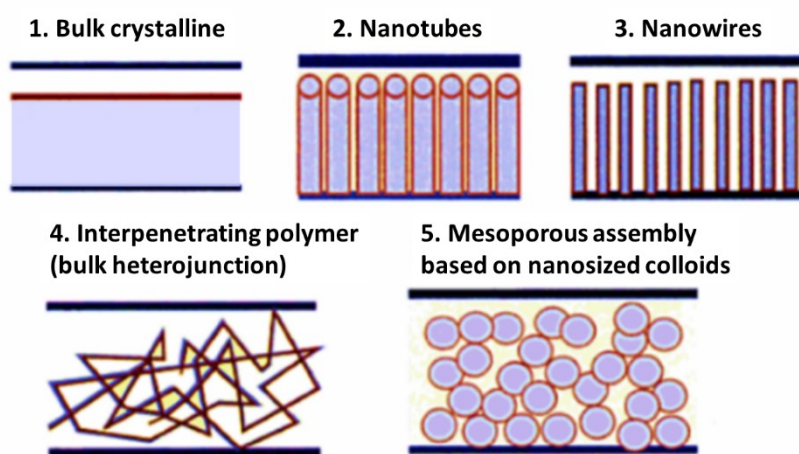
Figure 19: Different morphologies of TiO_2 for increasing the surface area.[49]

With the use of mesoporous TiO_2 as the semiconductor, a reevaluation took place. Earlier trials to obtain efficient DSCs were based on the belief that only smooth semiconductors could be used [70][71]. The main problem with this assumption was that the light harvesting efficiency of a monolayer on a smooth bulk semiconductor is very low [72]. One of the first who successfully

increased the semiconductor's surface and, with it, the dye loading was Augustynski and Grätzel [73]. Ordered TiO_2 nanotube structures can be obtained by potentiostatic anodization of Ti metal [74].

Dye molecules

The main key component, which is also investigated in this work, is the dye. The sensitizer absorbs the solar photon flux and injects electrons into the conduction band of the TiO_2. The diversity in molecular sensitizer is growing with almost every new publication in the field of DSCs and they can be divided into two main families: the organic dyes and sensitizers that are based on coordination complexes of transition metals. There are certain properties a sensitizer has to fulfil in order to obtain a good sunlight to power conversion efficiency. At first, the most obvious feature is a strong light absorption over an as broad as possible range in the solar spectrum in order to obtain good light harvesting. Concerning the dyeing process of the semiconductor, the dye should show good solubility properties in organic solvents. For the adsorption of the dye on the conducting oxide surface, the sensitizer must be decorated with suitable anchoring ligands/groups ($-CO_2H$, $-PO_3H_2$, $-SO_3H$, …), which interact strongly with the semiconductor surface (Figure 20).
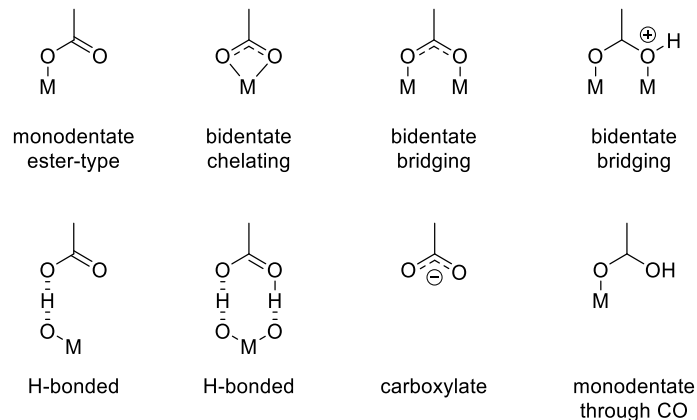
Figure 20: Binding modes for carboxylate unit on TiO_2 surface. [75]

Péchy and co-workers[76] found that phosphonic acids bind more strongly to the semiconductor than carboxylic acids and do not desorb from TiO_2 in the precense of water, in contrast to -CO_2H anchoring groups. Although $-PO_3H_2$ anchors have the stronger bonding, the $-CO_2H$ anchoring groups have a higher electron injection rate [77].The adsorption modes of the dye molecules are very important for the device efficiency [78][75]. Generally, the $-CO_2H$ anchors bind over three different modes: monodentate, chelating and bridging mode [79][80]. The bidentate binding mode is superior to the monodentate mode concerning the stability of the

anchored dye molecule and an increased electron injection could be observed because of the direct contact of both binding sites [80][81].

The excited state level of the sensitizer should be higher in energy than the conduction band edge of n-type semiconductors. This allows for efficient electron transfer from the excited dye to the conduction band. For the dye regeneration, the oxidized state level of the dye must be lower in energy (more positive) than the redox potential of the electrolyte.

Additionally, the HOMO and LUMO distribution over the molecule should be suitable to allow for effective charge injection from the excited state. Ideally, the HOMO of the non-excited dye molecule is localized further away from the TiO_2 surface whereas the LUMO of the non-excited sensitizer is located near the anchoring units (close to the TiO_2).

Since the dye (sensitizer) can be exposed to high temperatures in outdoor applications (roof top), the molecule has to show good thermal stability properties as well as good chemical stability (reversible oxidation and reduction processes during energy production). The following examples of dyes have yielded good DSC performances (conversion efficiencies): Ru(II) coordination complexes[82][83] ($\approx$10%), Osmium(II) complexes[84] ($\approx$8%), Zn-porphyrins[85][86][87] ($\approx$13%), squarines[88], perylenes[89], cyanines[90][91], coumarines[92] (5.6%) and pentacene[93].

DSCs based on Ru(II) complexes are well investigated. Their main benefits are broad absorption spectra and favourable photophysical properties [94]. They consist of a central metal ion and ancillary ligands (bipyridines or terpyridines) decorated with anchoring groups. The sunlight absorption in the visible region is due to the metal to ligand charge transfer (MLCT) based process. Since Ru(II) dyes reach high efficiencies, they are very popular among the metal complexes for DSC applications[95][54][96].
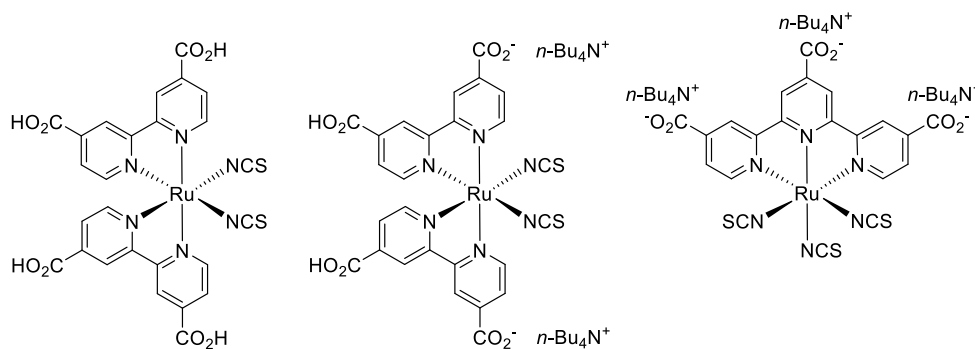
Figure 21: A selection of successful Ru(II) complexes.

In 1993, Grätzel et al. presented a paper of Ru(II) dyes in which two bipyridine ligands and two additional electron donating molecules were coordinated to the metal ion[97]. The dye with

thiocyanate molecules, called **N3** (Figure 21), was found to give the highest efficiency within this publication. Upon extending the spectral response of the dye into the near IR-region, Grätzel et al. synthesized the dye **N749** (black dye), containing a Ru(II) centre, three thiocyanate ligands and a triply carboxylated terpyridine[98]. By investigating the effect of the protonation state of the ancillary ligands, Grätzel and Nazeeruddin [99] achieved an increase in conversion efficiency with the doubly deprotonated form of **N3**, which they called **N719**. The dyes **N3** and **N719** are widely used as internal reference dyes for the screening of new sensitizers (in our lab **N719** is used).

Since Cu(I) complexes have similar photophysical properties to Ru(I) complexes, Sauvage and co-workers introduced Copper(I) bis-phenanthroline complexes into DSCs[100]. With suitable positioning of the anchoring groups, an increase in efficiency of Cu(I)-based DSCs was achieved because the electron injection was enhanced[101].

Electrolyte

Another important factor that can influence the device performance of a DSC is the electrolyte. It is responsible for the charge transport (electrons) between the photoanode and the cathode (working and counter electrode). Ideally, the electrolyte shows a low viscosity, high boiling point, almost no vapour pressure and high dielectric moments. One of the most popular electrolytes is based on the redox couple I^-/I_3^- (iodide/triiodide) dissolved in a mixture of acetonitlie and valeronitrile (MeCN and VCN) or pure N-methoxypriopionitrile (MPN). Unfortunately, this redox couple also absorbs visible light from the incoming sunlight, therefore its concentration has to be kept as low as possible. By using MeCN as solvent, the iodide concentration can be kept low. While electrolytes based on low viscosity solvents such as MeCN achieve the best device performance, their major drawbacks are their high vapour pressures at higher temperatures. Especially in a sealed DSC, the pressure can rise quickly and, when the temperature surpasses the boiling point of the solvent, it is very likely that components of any non-chemically inert parts (sealing foil) can be dissolved.

Alternative electrolytes have been found in $Co^{(II)}/Co^{(III)}$ [102] and Fc/Fc^+ [103] redox copuples. A possibility to overcome the issue of high vapour pressures from neat MeCN in the electrolyte is to mix an ionic liquid (dialkyl imidazolium) with MeCN. With this method, not only can the vapour pressure be drastically reduced but the problem of the high viscosity of the ionic liquid can also be overcome.

Counter electrode

The counter electrode is the site where the oxidized form of the electrolyte is reduced by electrons entering from the external circuit.

$$I_3^- + 2e^- \rightarrow 3I^-$$
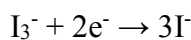
(net reaction for the regeneration of I^-)

In principle, the regeneration can occur by two routes. The first step is the electron uptake by I_3^-.

$$I_3^- + e^- \rightarrow I_2^- + I^-$$
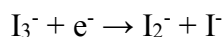
For the complete regeneration there are two possible steps:

$$I_2^- + e^- \rightarrow 2I^-$$

or

$$2I_2^- \rightarrow I_3^- + I^-$$
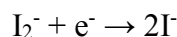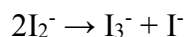
Without platinum, the TCO (transparent conducting oxide) covered glass would have a very high resistance [104]. To date platinum is the most successful material. Only a small amount of Pt deposited on the carrier substrate is necessary. There are several ways to apply Pt as fine particles on the substrate. It can be applied by thermal decomposition of a Pt-precursor to form nano-sized Pt metal clusters[105]. Instead of using heat to apply Pt on the carrier substrate, the electrodes can be prepared by using pulse- and direct-current electrodeposition, forming uniform Pt nanoclusters[106][107]. Another, and less expensive material, that was successfully applied is carbon, which was explored by Kay and Grätzel[108]. Carbon is used in different forms on the counter electrode including graphite and carbon nanotubes[109][110][111]. The best performance and long term stability has been obtained with nanoscale Pt clusters prepared by thermal decomposition of platinum precursors (Pt-Cl compounds)[105]. Platinum films that were prepared by techniques other than thermal decomposition of a precursor, such as electrodeposition or vapour deposition, were not stable under the influence of I^-/I_3^- electrolyte.[112]

1.3 A short insight into photophysical properties

In the 1970s McMillin[113] and co-workers explored the photophysical properties of Cu(I)-bisphenanthrolines ($[Cu(NN)_2]^+$) and revealed that these types of coordination complexes are promising candidates for replacing Ru(II)-polypyridines in photophysical applications such as solar energy conversion[114].

The key difference between Cu(I) and Ru(II) coordination compounds is their coordination numbers. While Ru(II) shows an octahedral coordination sphere (coordination number, CN = 6), Cu(I) exhibits an almost tetrahedral coordination environment (CN = 4). The less demanding coordination geometry of Cu(I) complexes allows more structural distortions than Ru(II)-polypyridines complexes. This diversity in geometry allows a fine tuning of the photophysical and electrochemical properties by varying the substitution pattern of the coordinating ligands. Copper is a first row transition metal in group 11 with Ag and Au. The eleven valence electrons of Copper(I) completely fill the 3d shell/orbitals and leave the 4s orbital half filled. ($Ar4s^13d^{10}$).
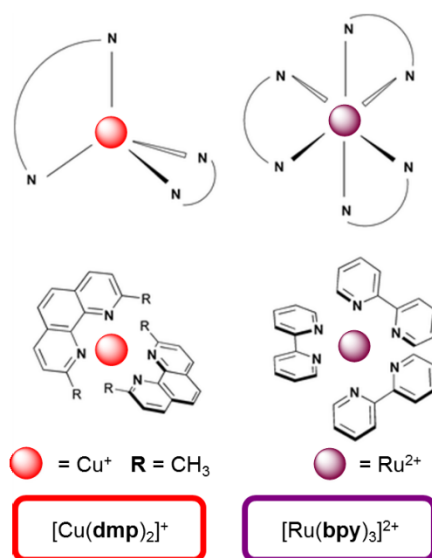
Figure 22: Coordination geometry of $[Cu(dmp)_2]^+$ and $[Ru(bpy)_3]^{2+}$.

The photophysical properties of $[Cu(NN)_2]^+$ complexes strongly depend on the size and the position of the substituents on the phenanthroline ligands. Not only can they influence the coordination sphere of the ground state but also the properties of the excited state. In fact, the ground state geometry of $[Cu(NN)_2]^+$ complexes can range from nearly tetrahedral to a severely flattened tetrahedral coordination environment.
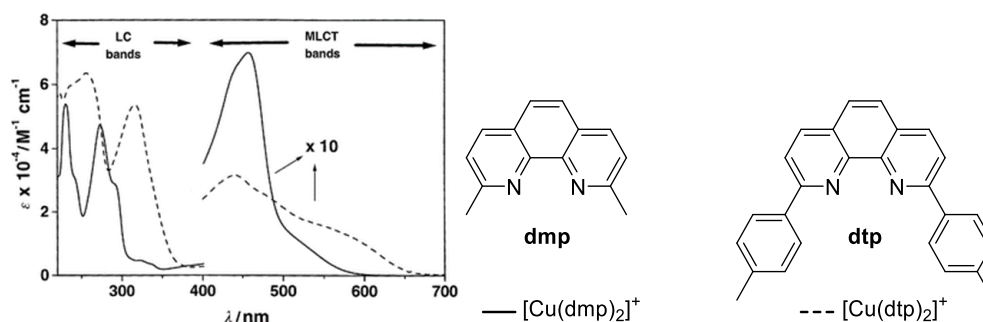
Figure 23: Solution absorption spectra of [Cu(dmp)₂]⁺ and [Cu(dtp)₂]⁺ in CH₂Cl₂ at room temperature.[115]

Normally the UV region of the absorption spectra of $[Cu(NN)_2]^+$ complexes is dominated by intense characteristic ligand centered (LC) bands of $\pi^* \leftarrow \pi$ transitions (Figure 23: Solution absorption spectra of $[Cu(dmp)_2]^+$ and $[Cu(dtp)_2]^+$ in CH2Cl2 at room temperature.[115][116]. The absorption bands in the visible region are typically weaker than those in the UV part of the spectrum and are assigned to MLCT transitions [113]. The shape and intensity of the MLCT band is depends on the structural distortion of the complex from the ideal tetrahedral geometry [117][118][119]. The main trends are the following: the introduction of aryl substituents at the 2,9-positions of the phenanthroline ligands leads to a decrease in intensity of the MLCT band, whereas the introduction of such substituents in the 4,7-positions leads to an increased absorption intensity for the MLCT band[119].

The spectra of $[Cu(dtp)_2]^+$ is shown as an exampke in Figure 23. The weaker absorption in the visible region of the spectrum and the presence of the shoulder at ≈550 nm is assigned to a typical absorption for complexes with a 2,9-aryl substitution pattern on the phenanthroline ligands. It has been found that this shoulder arises from an interaction (π-stacking) of the aryl groups of one ligand and the phenanthroline moiety of the other ligand[120]. This interaction leads to a strongly distorted, flattened tetrahedral structure.
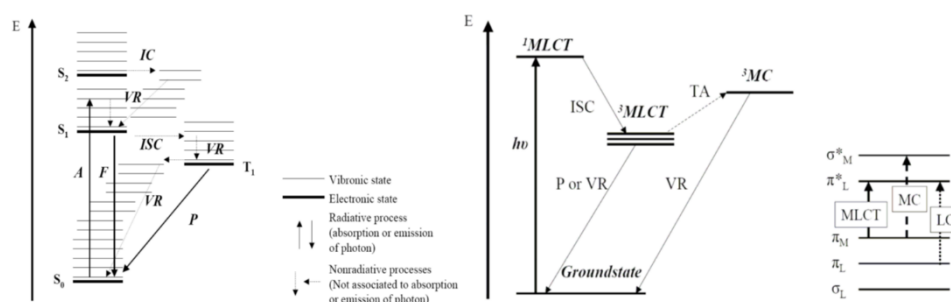
Figure 24: Jablonski diagram with photopysical processes (left) and simplified diagram for the most common transitions in Ru(II) polypyridine compleces.[121]

The different photochemical processes that occour upon irradiation are represented in Figure 24. Upon light absorption (A), the ground state S_0 is excited to an electronic state of higher energy (S_1 or higher, with the same multiplicity). The radiationless transition/decay between two electronic states with the same multiplicity is known as internal conversion (IC). If a

transition between two states with different multiplicity occurs, it is called inter system crossing (ISC). The relaxation process between two states with the same multiplicity is called fluoresence (F), whereas the relaxation between to states with different multiplicities is called phosphorescence (P). The right part of Figure 24 shows the main tranistions for an octahedral $[Ru(bpy)_3]^{2+}$ complex. The orbitals involved in these transitions are at the very right side, representing the relative energies of the transitions. For Cu(I) complexes, the metal centered (MC) charge transfer does not occur because of the d^{10} configuration of the metal ion centre.
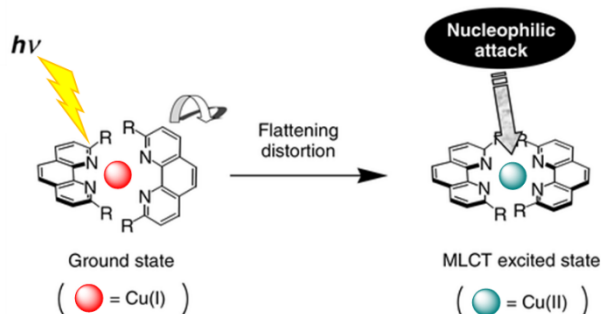
Figure 25: Flattening distortion caused by light absorption, followed by a nucleophilic attack of donating solvent or counterion.

By exciting a $[Cu(NN)_2]^+$ complex, the metal centre formally changes its oxidation state from Cu(I) to Cu(II). Since the preferred coordination geometry of Cu(II) is square planar, the excited molecule tends to adopt a more flattened coordination environment (Figure 25)[120]. In this flattened structure, the newly formed copper d^9 offers a fifth coordination site. This position can be attacked by coordinating solvent, or other donating molecules, forming a penta coordinated excited complex (exciplex). To avoid the formation of such a penta coordinated complex, no coordinating solvents should be used. Another possibility to diminish its formation is the introduction of bulky substituents in the 2, 9-positions of the phenanthroline ligands. The hindering groups physically prevent flattening and the associated undesired nucleophilic attack [122].
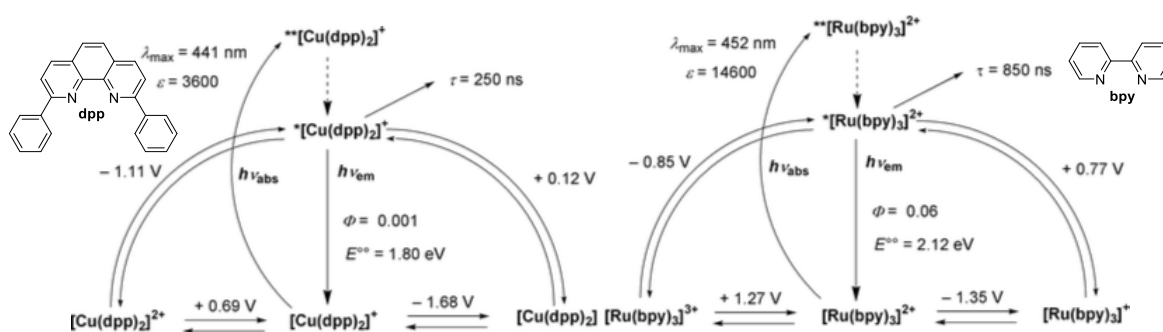
Figure 26: A comparison of the electrochemical and photopysical properties of [Cu(dpp)₂]⁺ (left) and [Ru(bpy)₃]²⁺.

By comparing the ground *vs* the excited states of $[Cu(dpp)_2]^+$ and $[Ru(bpy)_3]^{2+}$, one can see that both complexes are better oxidizing and reducing agents in their excited states than in their

ground states. The excited state complex $^*[Cu(dpp)_2]^+$ is a better reducing agent than $^*[Ru(bpy)_3]^{2+}$. Additionally $^*[Cu(dpp)_2]^+$ is the stronger reducing agent than $^*[Ru(bpy)_3]^{2+}$. Other parameters such as extinction coefficient, excited state lifetime and emission quantum yield somehow disfavour $[Cu(dpp)_2]^+$ against $[Ru(bpy)_3]^{2+}$. An improvement in photopysical performance can be achieved by suitable tuning the structural motif of the phenanthroline ligand [115].
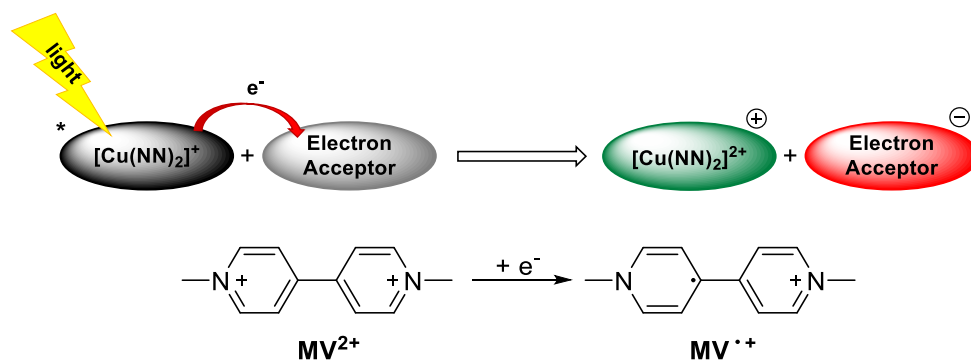
Figure 27: Schematic presentation of a bimolecular photo induced electron transfer.

As can be seen from the data in Figure 26, $^*[Cu(dpp)_2]^+$ is a rather effective reducing agent. For exploring the oxidative quenching, viologens (V) are one of the most widely used indicators. In transient absorption spectroscopy, they were used to detect the reduced form of the viologen[123][124]. In these studies, the use of methyl viologen with $[Cu(dpp)_2]^+$ yielded an electron transfer that was significantly higher than for $[Ru(bpy)_3]^{2+}$. This oxidative quenching behaviour of $^*[Cu(dpp)_2]^+$ is closely related to the sensitization of a large bandgap semiconductor (such as TiO_2) for the application in photovoltaic devices. In 1980, Kirsch de Measmaeker et al. coated the surface of SnO with $[Cu(dmp)_2]NO_3$ and observed a photocurrent upon irradiation[125][126]. The radiation of visible light caused an electron injection from the Cu(I) complex to the semiconductor material.

1.4   Why copper?

As mentioned above, Cu(I) complexes have the advantage of easy structural modifications.The copper ion centre offers a wider structural coordination geometry, arising by distortion, which could be used as an advantage in order to tune the photophysical properties. It also has been shown that $[Cu(NN)_2]^+$ complexes are a true altenative for Ru(II) polypyrdine complexes concerning photophysical applications.
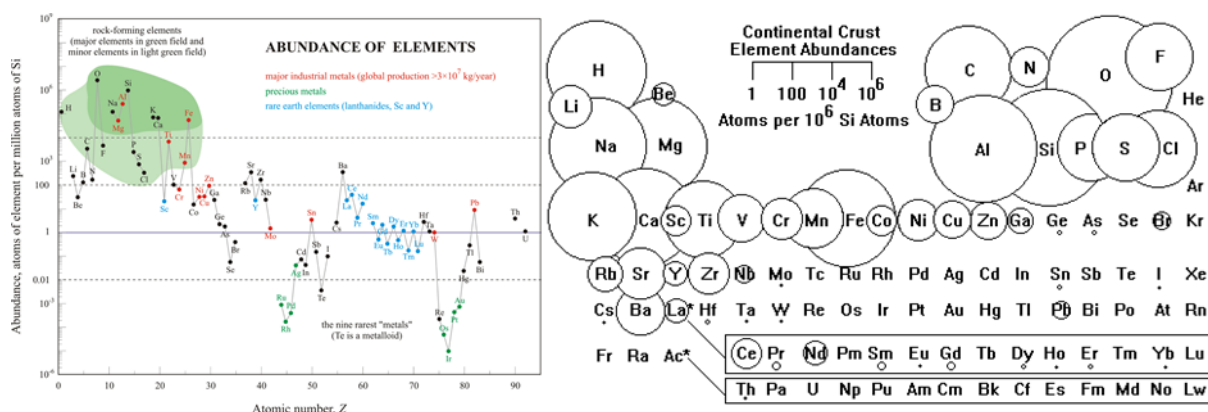
Figure 28: Abundance (atom fraction) of the chemical elements in Earth's upper continental crust as a function of atomic number. Si is normalized to 10^6. [127][128][129]

Another factor one has to bear in mind is the natural abundance of the element. As seen in Figure 28, the natural abundance of ruthenium in the Earth's crust is about four orders of magnitude smaller than that for copper. A further advantage of copper is that it can be recycled from disposed electronics and other discarded metal.
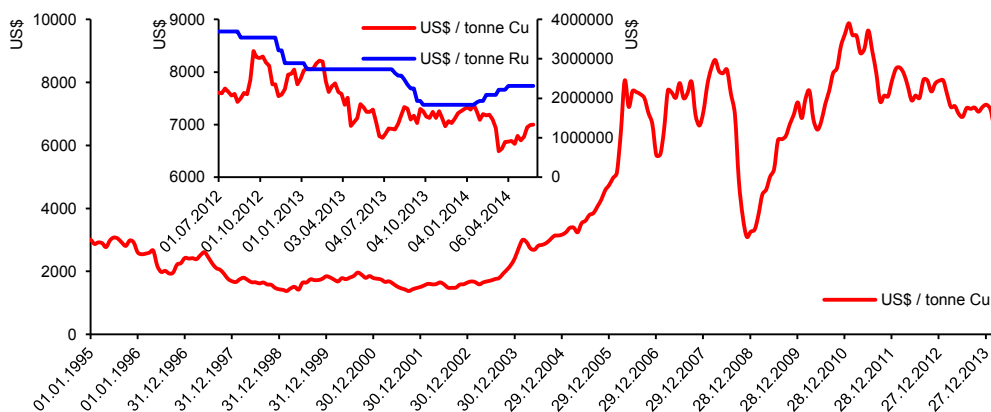
Figure 29: The development of copper price over the last 19 years. Price in US$/tonne (red) in CHF/tonne (blue). [130]

Due to its abundance, copper is much cheaper than ruthenium. On the stock market on 1st June 2014, one tonne of copper cost 6995.25 US$, whereas one tonne of ruthenium cost about 2314854 US$[131]. The Cu price in Figure 29 shows an immense increase between 2003 and 2005. This falls in the same time period where the number of publications and patents concerning DSCs was rising. On the other hand, the drop around 2008 is possible due to the financial crisis.

2 Dyeing process of the photoanode

Since the bandgap of TiO$_2$ is too large to promote electrons into the conduction band by visible light absorption, the semiconductor has to be sensitized. The surface of the semiconductor has to be treated with a photosensitizer possessing appropriate HOMO and LUMO energies, which allow electron injection into the semiconductor's conduction band[94][132].

Copper(I) bis(diimine) based complexes are labile in solution. This we used to our advantage because it allowed us to prepare *in situ heteroleptic* copper(I) complexes containing [Cu(bpy)$_2$]$^+$ cores by ligand exchange[133][134] (Scheme 1).
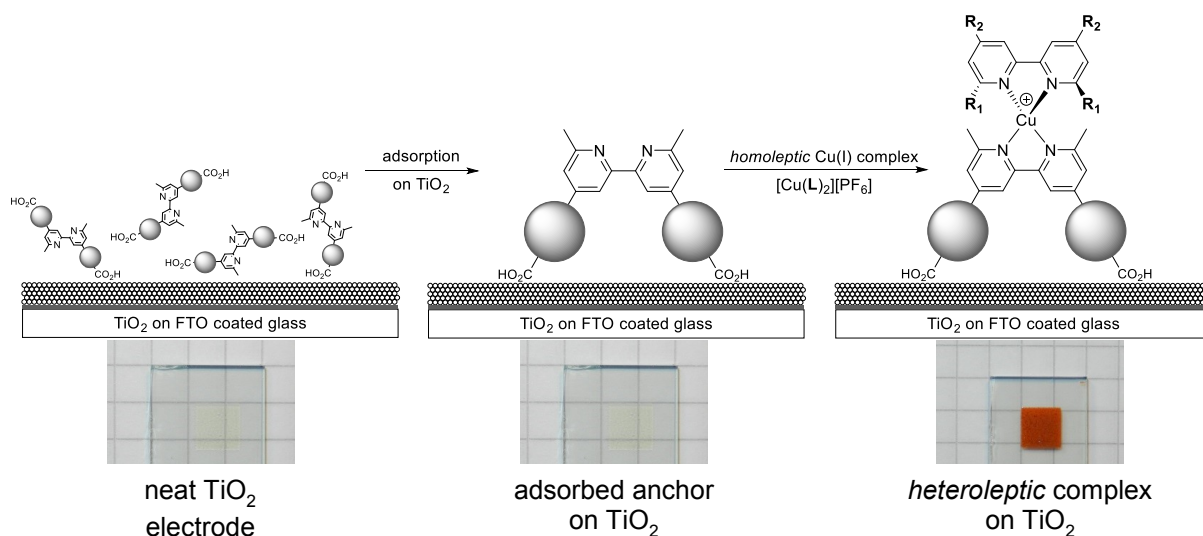
Scheme 1: The in situ preparation of a heteroleptic Cu(I) complex adsorbed on a photoanode covered with mesoporous TiO$_2$.

The first step consists of a neat TiO$_2$ anode, which is immersed in a solution of anchoring ligand. Since the anchoring ligand is decorated with acid functionalities, it binds to the TiO$_2$ surface. After removing, washing, and drying, the anode was immersed in a solution of *homoleptic* copper(I) complex. During this step, the TiO$_2$ becomes a red-orange colour. The origin of the colour change is due to the ligand exchange reaction on the semicounductor surface. To terminate the dyeing process, the electrode is removed from the dye solution. After washing the anode with an appropriate solvent (normally the same as for the dye sloution), the electrode is dried under N$_2$ or at slightly increased temeratures (50°C) with a heatgun.

This method allows one to screen a large number of dyes without having to isolate the *heteroleptic* compound. On the other hand, it is also a disadvantage not having the *heteroleptic* dye in your own hands. Without isolating the *heteroleptic* complex, it is not possible to give absolute information about the dye loading on the surface because the extinction coefficient (ε) is not known. Another drawback is that it is not possible to measure any redox potentials of the compound, which would give information about HOMO-LUMO gaps.

3 Device measurement
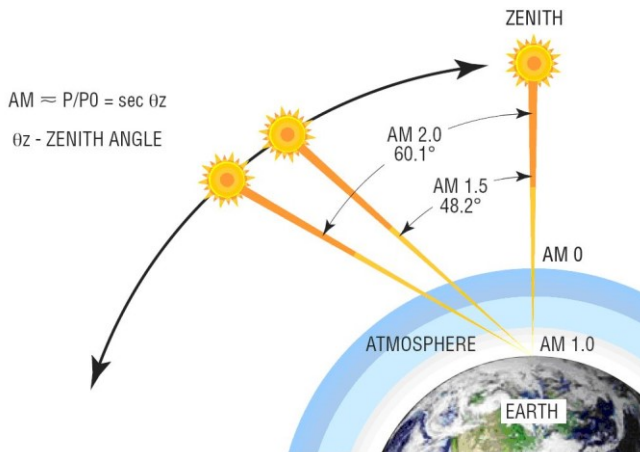
Figure 30: Schematic presentation of the influence of the zenith angle on the irradiation intensity.

The maximum irradiation from the sun is obtained when the sun reaches its zenith, having the shortest path length through the atmosphere. The path length of the sunlight through the atmosphere is called air mass (AM). AM can be approximated by $AM = 1/\cos\theta$ or $1/\sin(90-\theta)$. The international standard solar spectrum which, is used for efficiency measurements of DSCs, is AM1.5 G (G = global). This normalized spectrum is defined as 1000 W m^{-2} irradiance energy. Not only direct light contributes to the device performance but also diffuse light. The diffuse light arises from scattering in the atmosphere and on other objects. Diffuse light contributes about 15% to the total irradiation [135].

3.1 Setup

At first the reference cell is calibrated/certified by a standard cell under standard conditions to determine its performance in a research centre. Then the reference cell can be sold on the market to calibrate solar simulators in laboratories.
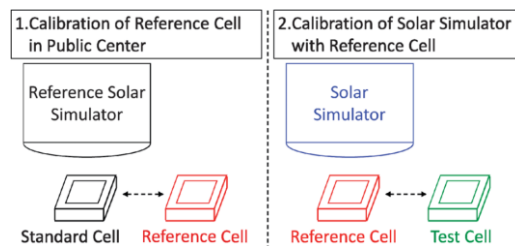
Figure 31: Schematic procedure of calibration of the sun simulator by reference cell.[136]

The sun simulator is adjusted until the reference cell shows the same performance (current) as recorded during its calibration. The reference cell has to be stable over time for frequent calibrations. Crystalline silicon solar cells are currently the only cells with such stabilitiy properties. [136]
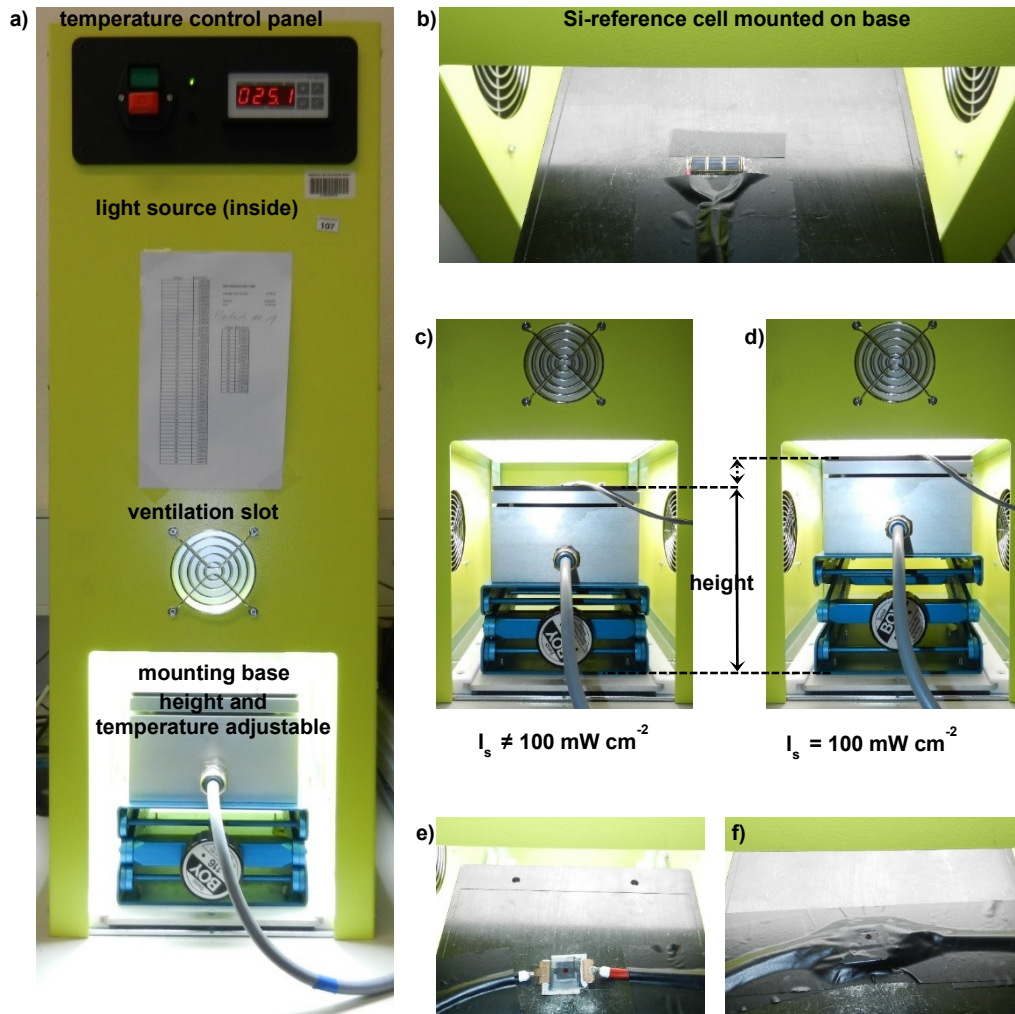
Figure 32: a) Solar simulator Solaronix SolarSim 150. b) Si-reference cell mounted on temperature controlled basis. c) and d) height adjustable basis. e) Copper(I) based DSC connected to external potentiostat. f) fully masked DSC.

In our lab, all dye sensitized solar cells were measured with a *Solaronix SunSim 150* (Figure 32, a), which consists of an internal light source in the top part and a temperature and height adjustable mounting base.

After switching on the light source, the silicon reference cell was placed on the base and irradiated for 30 minutes. By measuring the Si-reference cell and changing the height of the base, the intensity of the incident light (I_s), was adjusted to $I_s = 100$ mW cm^{-2} (Figure 32, c and d). In the next step, the reference cell was replaced by the copper(I) based DSC, connected to the external potentiostat (*Keithley 2400* series source meter), and completely masked to prevent scattered and diffuse light from reaching the dyed semiconductor surface. In the final step the device is measured under irradiation. The parameters such as *Jsc*, *Voc*, *JV*-curve *ff* and efficiency are calculated by the *ReRa Tracer2* software.

3.2 Measurement output

From the initial output file a graph of current vs. potential is obtained. By dividing the current (Y-axis) by the illuminated area of TiO_2 in cm^{-2}, a current density vs. potential (JV) curve is obtained. In Figure 33, such a JV-curve is represented by the black solid line.
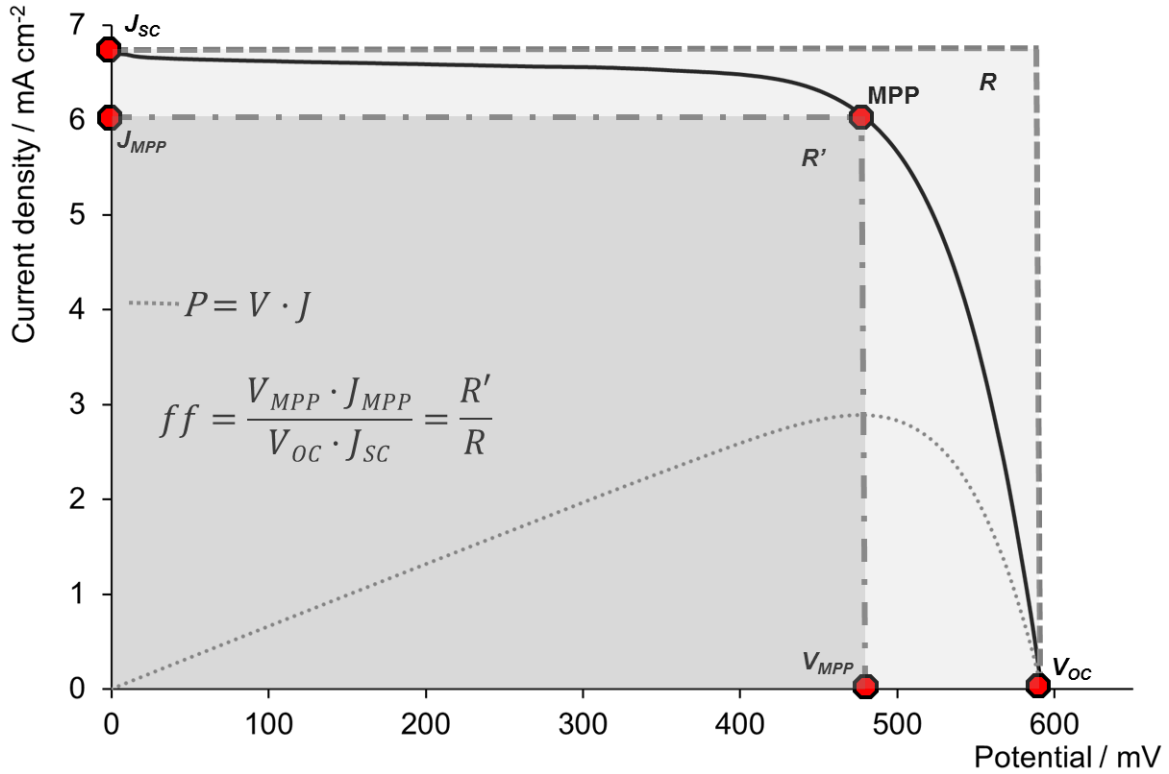
Figure 33: Obtained JV-curve from the experiment (black solid curve) with key parameters. Jsc: short-circuit-current density, J_{MPP}: Maximum-power-point current, Voc: Open-circuit-voltage, V_{MPP}: Maximum-power-point voltage, MPP: Maximum-power-point, ff: Fill factor.

The advantage of converting the measured photocurrent (*Isc*) to photocurrent density (*Jsc*) (*i.e.,* dividing the current by the active irradiated area) is that cells are directly comparable with each other.

$$Isc = 0.5 \text{ mA and area} = 0.06 \text{ cm}^{-2}$$
$$Jsc = 0.5\text{mA}/0.06\text{cm}^{-2} = 8.3 \text{ mA/cm}^{-2}$$

The fill factor (*ff*) is the ratio of rectangles R' to R. Normally the *ff* is given in % and adopts values from 0 to 100. The outer rectangle (R) is defined by the product of the short-circuit-current density (*Jsc*) and the open-circuit voltage (*Voc*). The inner rectangle is defined by the maximum-power-point (MPP). The MPP is obtained by the product of potential and current-density. V_{MPP} and J_{MPP} are obtained where the first derivative of the function $dP/dV = 0$.

$$ff\,[\%] = (\text{R'}/\text{R})\times100$$

Basically, the more rectangular the JV curve is, the higher the *ff*.

SYNTHETIC STRATEGY & CHARACTERIZATION

4 Synthetic route

4.1 Target molecules

4.1.1 Ligands

At the beginning of this work six bipyridine derivatives (**L1.1**-**L1.6**) were synthesized. They only differ in their substituents in the 6,6'-positions on the pyridine rings. In the next stage, the basic structure was extended by the introduction of bis(methoxyphenyl)amine (**L2.1**-**L2.6**). The aim was to enhance the light absorption over the photon flux. In the third phase, the aryl system was further extended (**L3.1**-**L3.6**) with the aim again being to improve the absorption range over the spectrum.
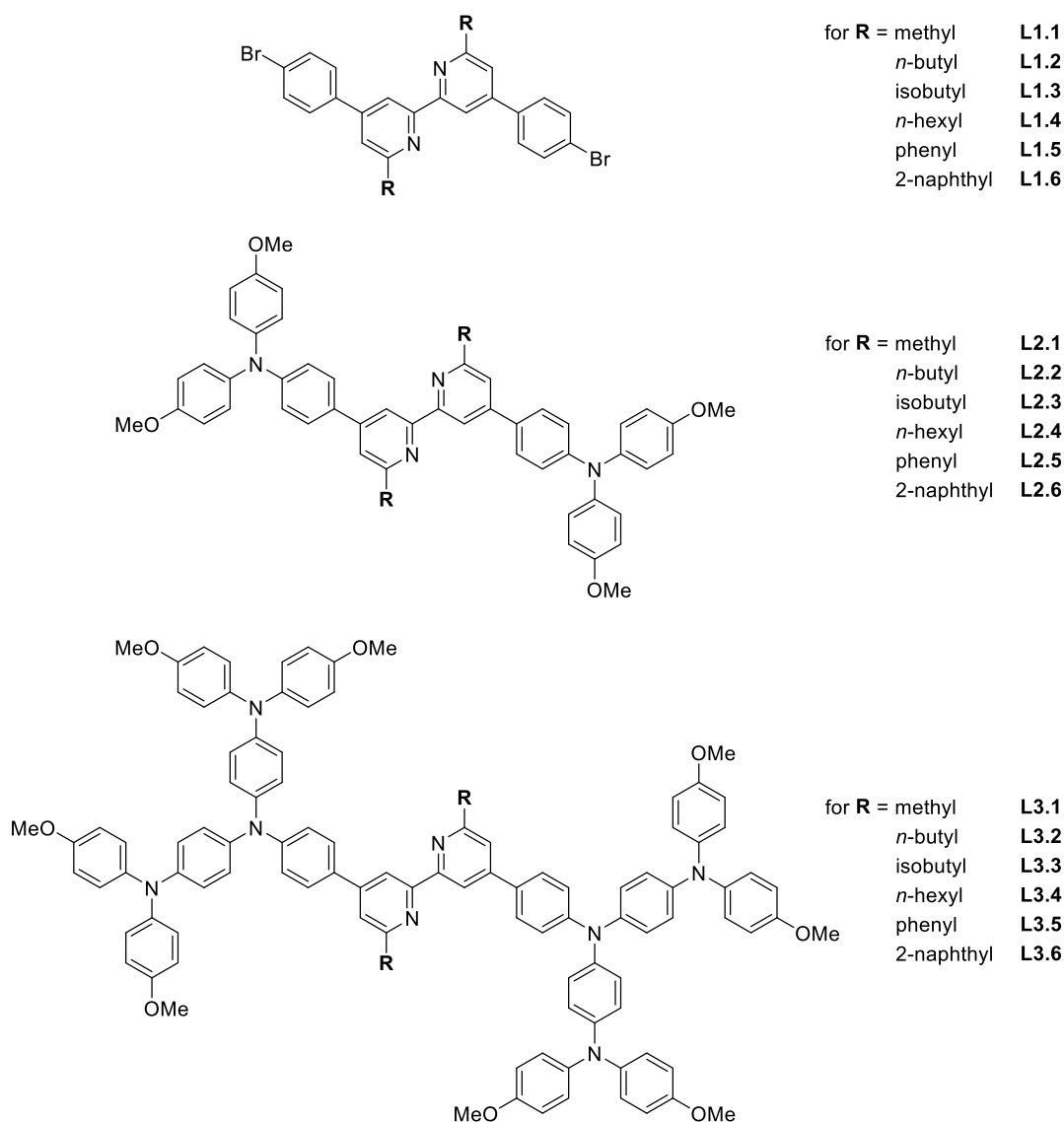
Scheme 2: Overview of relevant ligands and abbreviations.

4.1.2 Copper(I) complexes

The ligand synthesis was followed by the preparation of *homoleptic* copper(I) complexes. Since the initial idea was to implement the prepared ligands in copper(I) based dye sensitized solar cells, two equivalents of ligand were reacted with *tetrakis*(acetonitrile)copper(I)[PF$_6$], forming the tetrahedral *homoleptic* complexes.

for **R** = methyl	**L1.1**	
n-butyl	**L1.2**	
isobutyl	**L1.3**	
n-hexyl	**L1.4**	
phenyl	**L1.5**	
2-naphthyl	**L1.6**	

$[Cu(MeCN)_4][PF_6]$ → $[Cu(\text{L1.1-1.6})_2][PF_6]$ ≡ **C1.1-C1.6**

for **R** = methyl	**L2.1**	
n-butyl	**L2.2**	
isobutyl	**L2.3**	
n-hexyl	**L2.4**	
phenyl	**L2.5**	
2-naphthyl	**L2.6**	

$[Cu(MeCN)_4][PF_6]$ → $[Cu(\text{L2.1-2.6})_2][PF_6]$ ≡ **C2.1-C2.6**

for **R** = methyl	**L3.1**	
n-butyl	**L3.2**	
isobutyl	**L3.3**	
n-hexyl	**L3.4**	
phenyl	**L3.5**	
2-naphthyl	**L3.6**	

$[Cu(MeCN)_4][PF_6]$ → $[Cu(\text{L3.1-3.6})_2][PF_6]$ ≡ **C3.1-C3.6**
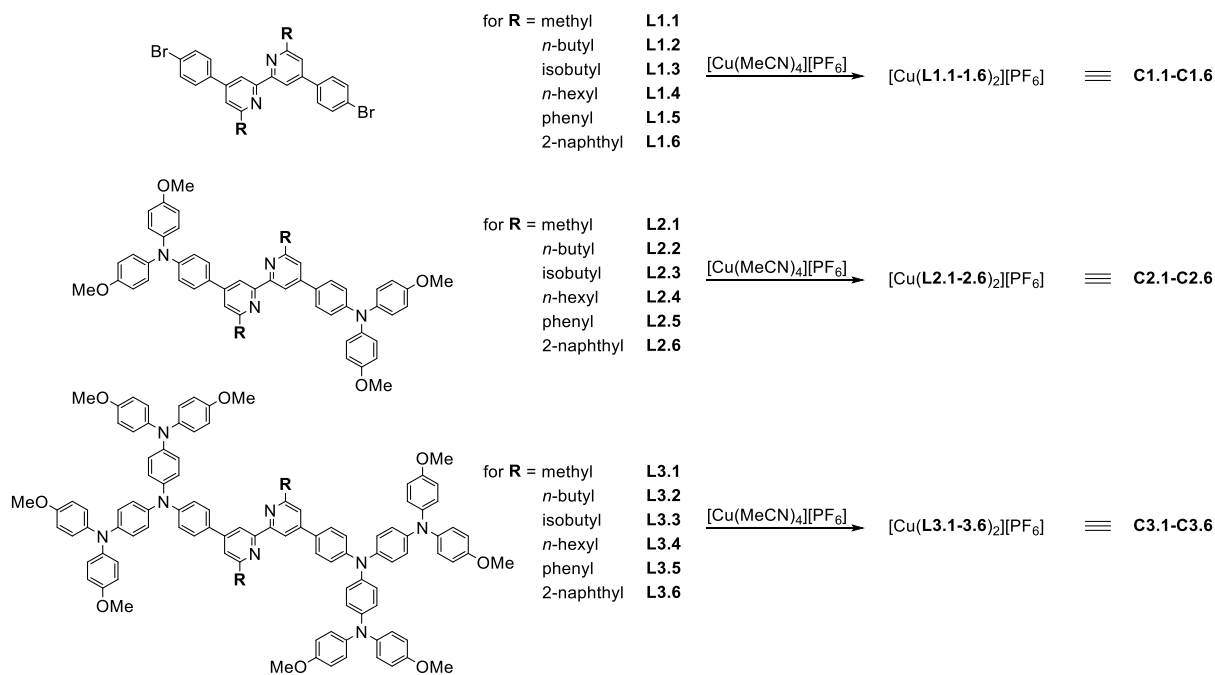
Scheme 3: Overview of the prepared and characterized homoleptic copper(I) complexes.

The synthesized *homoleptic* copper(I) complexes (**C1.1-3.6**) were in a later step used to perform a ligand exchange reaction on TiO$_2$ covered with adsorbed anchoring ligand, implementing the copper(I) centre and one ancillary ligand in a DSC.

4.2 Pyridinium salts

The synthetic method to obtain pyridinium salts **S1-S6** was that reported by Kröhnke[137][138] and King[139][140][141].
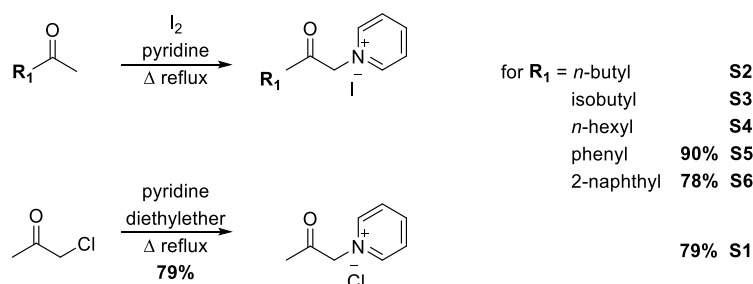
Scheme 4: Preparation of pyridimium halide salts (S1-S6).

For the preparation of **S1**, chloroacetone was used, whereas salts **S2-S6** were prepared from a mixture of ketone and iodine. **S1** was isolated as a chloride salt, whereas **S2-S6** were isolated as iodide salts. For salts **S2**, **S3** and **S4**, the product was not isolated and the reaction mixture was used without any further purification. Hence, no yields were determined.

4.3 2,2'-Bipyridine core

For the synthesis of the bipyrdine core, one of the cheapest, easiest and most versatile synthetic approaches was applied, the *Kröhnke* synthesis (Scheme 4 and Scheme 5). From the early 1960's, Fritz Kröhnke and Wilfried Zecher[142][143] investigated the synthesis of substituted pyridines. With ongoing research in this field, the synthesis was optimized, which resulted in several reviews[137][138].

The *Kröhnke* method is a one-pot type reaction, where a pyridinium salt (activated ketone) reacts with an α,β-unsaturated diketone via a *Michael* addition[144][145] to a 1,5-diketone. In the reaction, ammonium acetate acts as a source of ammonia. In the presence of NH_3 the *Michael* product undergoes a condensation followed by a ring closure.

With this type of reaction, a diverse catalogue of substituted pyridines, from mono- and bi-pyridines up to septi-pyridines can be synthesized. One of the big advantages is that this diversity can be obtained from simple building blocks, such as pyridinium salts, unsaturated ketones or *Mannich* bases[146].

This method also has other advantages related to the reaction mechanism. The pyridinium salt of the ketone has a higher oxidation state than the unsubstituted ketone. Therefore the dehydrogenation reaction which is required in the *Hantzsch* synthesis[147], is no longer needed. Compared to the *Tschitschibabin* reaction[148], in which half of the unsaturated ketone is used to oxidize the pyridine, the yield will never exceed 50%[149]. In contrast, a yield of up to 92%

can be obtained with the *Kröhnke* methodology. Additionally in a Tschitschibabin reaction, the product is always symmetrical, whereas the *Kröhnke* product can be substituted by three different groups [148].
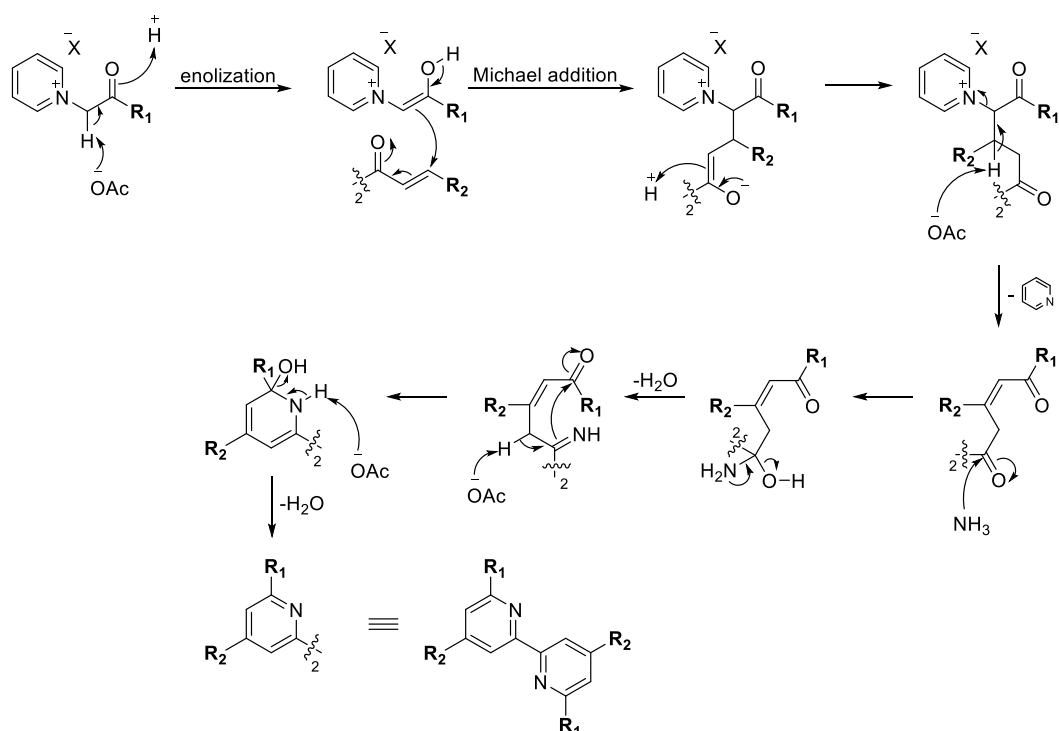
Scheme 5: General reaction mechanism for the bipyrdine core structure applying the Kröhnke synthesis [150].

4.4 Ligands I: L1.1-L1.6

As mentioned above, the *Kröhnke* methodology was applied to obtain the bipyridine core. In three steps, six different 2,2'-bipyridine derivatives were synthesized. 4-Bromobenzaldehyde was reacted with 2,3-butanedione and a catalytic amount of piperidine. The α,β-unsaturated ketone precipitated out of the reaction mixture and was isolated as an orange solid. It was found to be poorly soluble in organic solvents.

The α,β-unsaturated ketone was further reacted with the pyridinium salts prepared earlier. The yields for the ligands varied from 25% to 66%. Upon cooling the reaction mixture to ambient temperature, the ligands precipitated out of solution and were isolated as colourless to off-white solids. Ligands **L1.1** to **L1.5** showed good solubility properties, whereas **L1.6** was only soluble in TFA. The isolated pure ligands **L1.2**, **L1.3** and **L1.4** had an intense bloomy scent. All ligands were fully characterized.
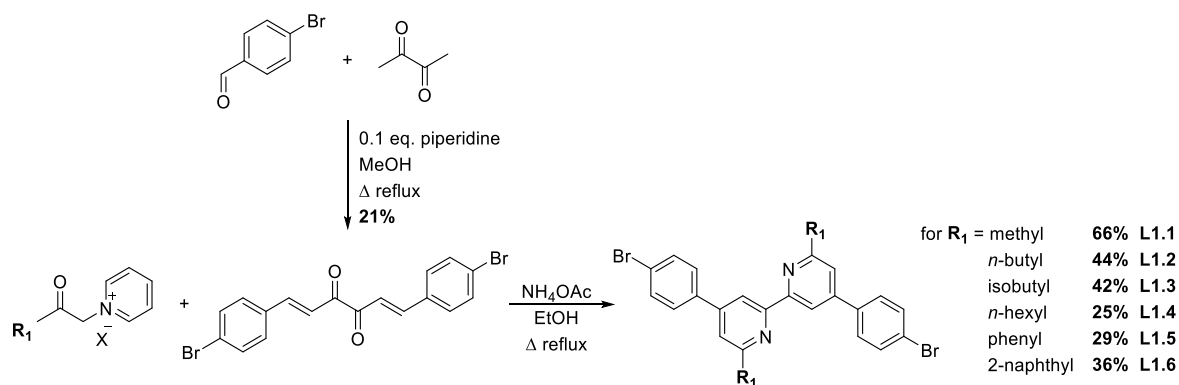
*Scheme 6: Reaction scheme for ligands **L1.1** to **L1.6**.*

One can see that the yield for the α,β-unsaturated ketone is relatively low (21%). It is essential to say that in order to maintain this yield, the temperature of the reaction mixture must not exceed the boiling point of methanol. If the reaction is carried out in solvents with higher boiling points (*e.g.* ethanol) the yield dropped drastically. A prolonged reaction time failed to lead to an increase in yield, nor did it work at ambient temperature. Also, the subsequent separation of precipitated product could not force the reaction to reach higher yields.

The same observations were made for the preparation of ligands **L1.1** to **L1.6**. The yield could not be improved by a longer reaction time, nor by refluxing in solvents with higher boiling points. Furthermore, the successive isolation of precipitated ligand did not lead to a higher yield.

4.5 Ligands II: 1st Generation dendrimers L2.1-L2.6

In 1994, John F. Hartwig[151] and Stephen L. Buchwald[152] developed in parallel the palladium catalyzed cross coupling of amines and aryl halides. Upon developing and improving the *Buchwald-Hartwig* coupling, numerous catalyst generations for this system were found[153][154]. With each new catalyst a greater scope of coupling partners was revealed and milder conditions were established. Since in pharmaceutical and natural products C-N bonds are omnipresent, the reaction gained interest and is nowadays widely used not only in organic chemistry, but has numerous applications in academia and in industrial preparations[155].

The steps of the reaction mechanism are similar to those known from palladium catalyzed C-C coupling reactions. The first step is the oxidative addition of the aryl halide to the Pd(0) species, followed by ligand exchange of the base. The coordinating base deprotonates the aryl amine and undergoes another ligand exchange with the deprotonated amine. In the last step the reductive elimination takes place, closing the catalytic cycle [156][157][158][159].
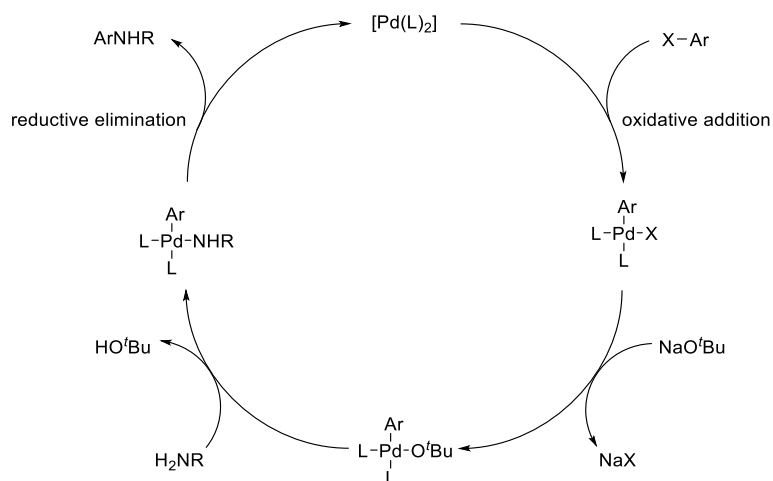
Scheme 7: Proposed catalytic cycle of the Buchwald-Hartwig coupling.

To obtain **L2.1-2.6**, compounds **L1.1-1.6** were each reacted with 2.0 equivalents of bis(4-methoxyphenyl)amine in the presence of base and 5 mol% catalyst under inert conditions. Upon cooling the reaction mixture, the formed product normally precipitated out of solution. After separation of the crude product via filtration, the solid was boiled in methanol and filtered off again. All ligands **L2.1-2.6** were isolated as yellow to green powders.

For the preparation of **L2.6**, the starting material **L1.6** was weakly soluble in hot toluene. Therefore the reaction suspension was allowed to react overnight. On the following day, all starting material had dissolved and a dark solution had formed. The purification and isolation were analogous to those for **L2.1-2.5**.

All the ligands were obtained in moderate (for **L2.6**) to very good yields and were fully characterized. Ligands **L2.1-2.6** are readily soluble in chlorinated solvents, such as chloroform and dichloromethane

for **R₁** = methyl	75%	**L2.1**
n-butyl	88%	**L2.2**
isobutyl	86%	**L2.3**
n-hexyl	86%	**L2.4**
phenyl	86%	**L2.5**
2-naphthyl	60%	**L2.6**
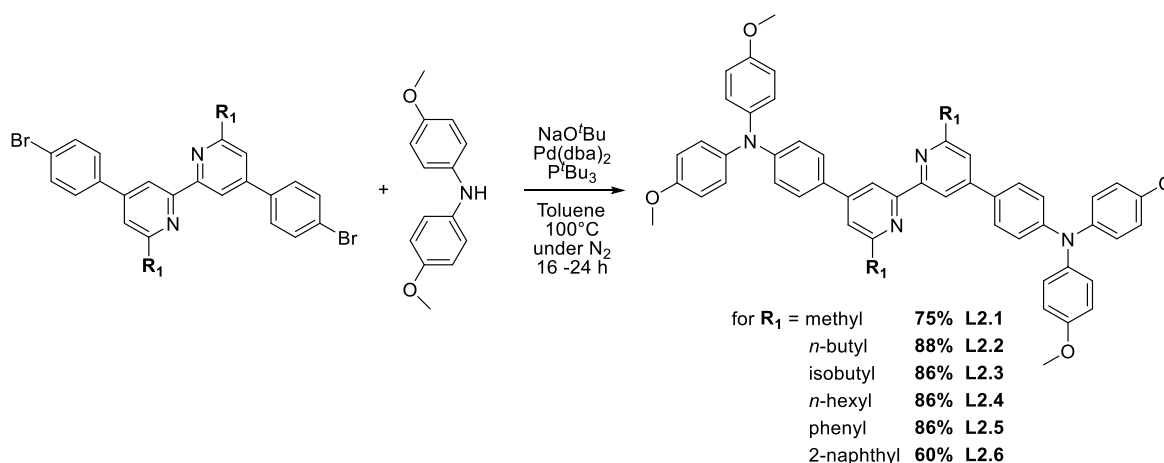
*Scheme 8: Synthesis of ligands **L2.1-2.6**.*

4.6 Ligands III: 2nd Generation dendrimers L3.1-3.6

Ligands **L3.1-3.6** were synthesized in order to broaden and increase the photon harvesting properties (*i.e.* stronger absorption on going from **L2.1** to **L3.1**).

Since use of bis(4-bromophenyl)amine would lead to polymer formation when reacted under *Hartwig-Buchwald* conditions, the amine had to be protected. This was achieved by reacting bis(4-bromophenyl)amine with 4-DMAP and (Boc)₂O, leading to the Boc-protected arylamine in very good yield.
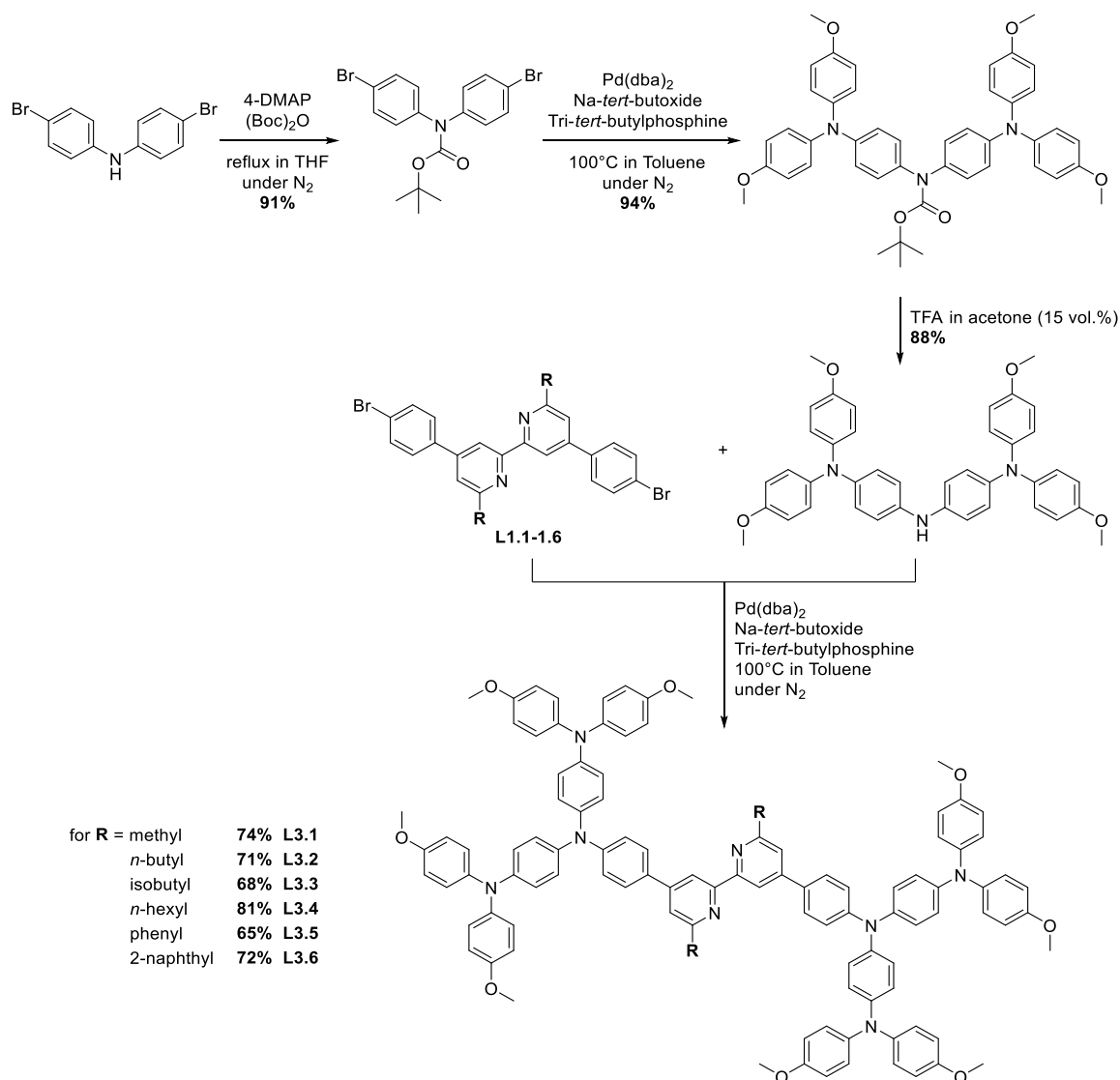
*Scheme 9: Overview of the synthetic route for ligands **L3.1-3.6**.*

In a subsequent step the protected amine was reacted with bis(4-methoxyphenyl)amine in a *Buchwald-Hartwig* coupling. After purification the carbamate was isolated as a colourless solid in very good yield (94%). The deprotection was performed in an acetone/TFA mixture (20/5 mL) at room temperature. This reaction proceeded smoothly in good yields leading to the deprotected *sec*-amine. The last step on the way to the 2nd generation dendrimer ligands (**L3.1-**

3.6) again involved a *Buchwald-Hartwig* style coupling, where one equivalent of the previously synthesized ligand (**L1.1-1.6**) was coupled with two equivalents of the deprotected *sec*-amine. All ligands were obtained in reasonable to good yields and isolated as yellow-green solids. For the preparation of **L3.6**, the starting material **L1.6** was weakly soluble in hot toluene. Therefore the reaction suspension was allowed to react overnight. On the following day all starting material had dissolved and a dark solution had formed. The purification and isolation were done in an analogous matter to that of **L3.1-3.5**.

4.7 Complexes

for R_1 = methyl   80%   C1.1
   n-butyl   39%   C1.2
   isobutyl   86%   C1.3
   n-hexyl   37%   C1.4
   phenyl   59%   C1.5
   2-naphthyl   84%   C1.6

for R_1 = methyl   83%   C2.1
   n-butyl   78%   C2.2
   isobutyl   42%   C2.3
   n-hexyl   86%   C2.4
   phenyl   90%   C2.5
   2-naphthyl   92%   C2.6

for R_1 = methyl   96%   C3.1
   n-butyl   77%   C3.2
   isobutyl   83%   C3.3
   n-hexyl   84%   C3.4
   phenyl   86%   C3.5
   2-naphthyl   89%   C3.6
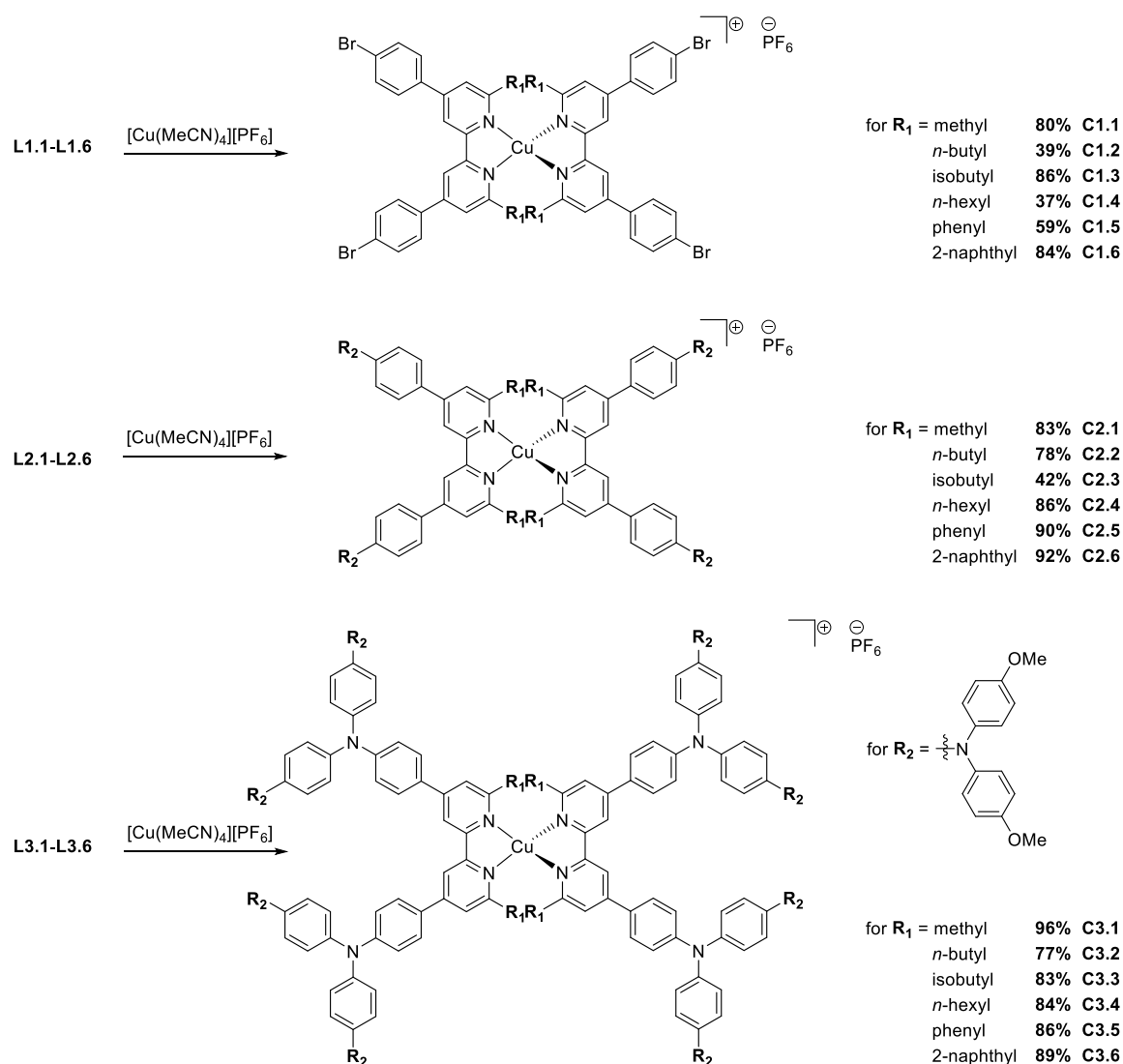
Scheme 10: General preparation of homoleptic Cu(I) complexes.

For the preparation of the *homoleptic* complexes (**C1.1-3.6**) two equivalents of ligands were reacted with *tetrakis*(acetonitrile)copper(I), forming the tetrahedral *homoleptic* complexes. For ligands bearing aryl substituents in the 6,6'-positions, non-coordinating solvents have to be used to dissolve the ligands, otherwise the desired complex would dissociate.

$$[CuL_2]^+ + 4MeCN \rightleftharpoons [CuL(MeCN)_2]^+ + L + 2MeCN \rightleftharpoons [Cu(MeCN)_4]^+ + 2L$$
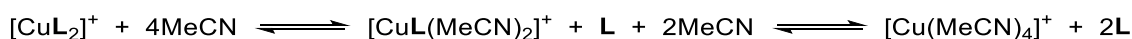
Equation 1: A possible dissociation of homoleptic Cu(I) complexes bearing aryl substituents in the 6,6'-positions of the ligands.
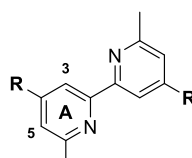
Complexes with alkyl groups in the 6,6'-positions were obtained as red powders, whereas complexes with aryl groups were obtained as green-black solids. All complexes were isolated as PF_6^- salts.

5   Characterisation

5.1   Spectroscopic NMR studies

For the assignment of all ligands and complexes, a Bruker Avance III-500 NMR spectrometer was used to record ^{1}H and ^{13}C NMR spectra. The chemical shifts were referenced to residual solvent peaks to δ (TMS) = 0 ppm. Since ligand **L1.6** was not soluble in any common organic solvent it had to be dissolved in d-TFA. Therefore, the double protonated species of **L1.6** was observed and its spectrum assigned. While complexes [Cu(**L1.1-1.4**)$_2$][PF$_6$] were measured in CD$_3$CN, complexes [Cu(**L1.5/1.6**)$_2$][PF$_6$] were not stable in acetonitrile, which caused a dissociation of the complexes to [Cu(MeCN)$_4$][PF$_6$] and **L1.5/1.6**. Therefore they had to be measured in chlorinated solvents. For ligands **L2.1-2.6** and complexes **C2.1-2.6**, a common solvent was used (CDCl$_3$) which had the advantage that the spectra were directly comparable. Although the complexes containing the 2nd generation ligands (**L3.1-3.6**) were soluble in CDCl$_3$, signals in the ^{1}H NMR spectrum were broadened, which was not reversible by the addition of base (K$_2$CO$_3$). This made a solvent change necessary. Therefore CD$_2$Cl$_2$ in the presence of basic aluminia was used and lead to well resolved spectra.

5.1.1   Signal shifts for protons H^{A3} and H^{A5} upon coordination

Ligand L	Solvent for L	H^{A3} in L	H^{A5} in L	Solvent for [CuL$_2$][PF$_6$]	H^{A3} in [CuL$_2$][PF$_6$]	H^{A5} in [CuL$_2$][PF$_6$]
		δ / ppm			δ / ppm	
L1.1	CDCl$_3$	8.44	7.36	CD$_3$CN	8.66	7.82
L1.2	CDCl$_3$	8.48	7.34	CD$_3$CN	8.67	7.84
L1.3	CDCl$_3$	8.48	7.30	CD$_3$CN	8.68	7.78
L1.4	CDCl$_3$	8.48	7.33	CD$_3$CN	8.70	7.85
L1.5	CD$_2$Cl$_2$	8.91	8.04	CDCl$_3$	8.23	7.64
L1.6	d-TFA	8.68	8.66	CD$_2$Cl$_2$	7.55	7.66
L2.1	CDCl$_3$	8.39	7.33	CDCl$_3$	8.25	7.59
L2.2	CDCl$_3$	8.44	7.31	CDCl$_3$	8.27	7.57
L2.3	CDCl$_3$	8.46	7.28	CDCl$_3$	8.27	7.52
L2.4	CDCl$_3$	8.44	7.31	CDCl$_3$	8.26	7.56
L2.5	CDCl$_3$	8.82	7.95	CDCl$_3$	7.95	7.61
L2.6	CDCl$_3$	8.89	8.11	CDCl$_3$	7.32	7.57
L3.1	CDCl$_3$	8.40	7.33	CDCl$_3$	8.26	7.57
L3.2	CDCl$_3$	8.46	7.32	CD$_2$Cl$_2$	8.34	7.60
L3.3	CDCl$_3$	8.46	7.28	CD$_2$Cl$_2$	8.35	7.56
L3.4	CDCl$_3$	8.46	7.32	CD$_2$Cl$_2$	8.34	7.61
L3.5	CDCl$_3$	8.83	7.96	CD$_2$Cl$_2$	8.02	7.66
L3.6	CDCl$_3$	8.93	8.12	CD$_2$Cl$_2$	7.43	7.60

*Table 1: A comparison of the chemical shifts of the bpy protons H^{A3} and H^{A5} in the free ligand (**L1.1-3.6**) and in the homoleptic copper(I) complex [Cu(**L1.1-3.6**)$_2$][PF$_6$].*

The shift for the proton signals H^{A3} and H^{A5} is consistent with the range affected by the conformation change (from *trans* in the free ligand to *cis* in the complex) of the bpy unit upon coordination. The proton signals for the Br-C$_6$H$_4$-spacer (**L1.1-1.6/C1.1-1.6**) and those for the peripheral dendrons (**L2.1-3.6/C2.1-3.6**) stay approximately unaffected.
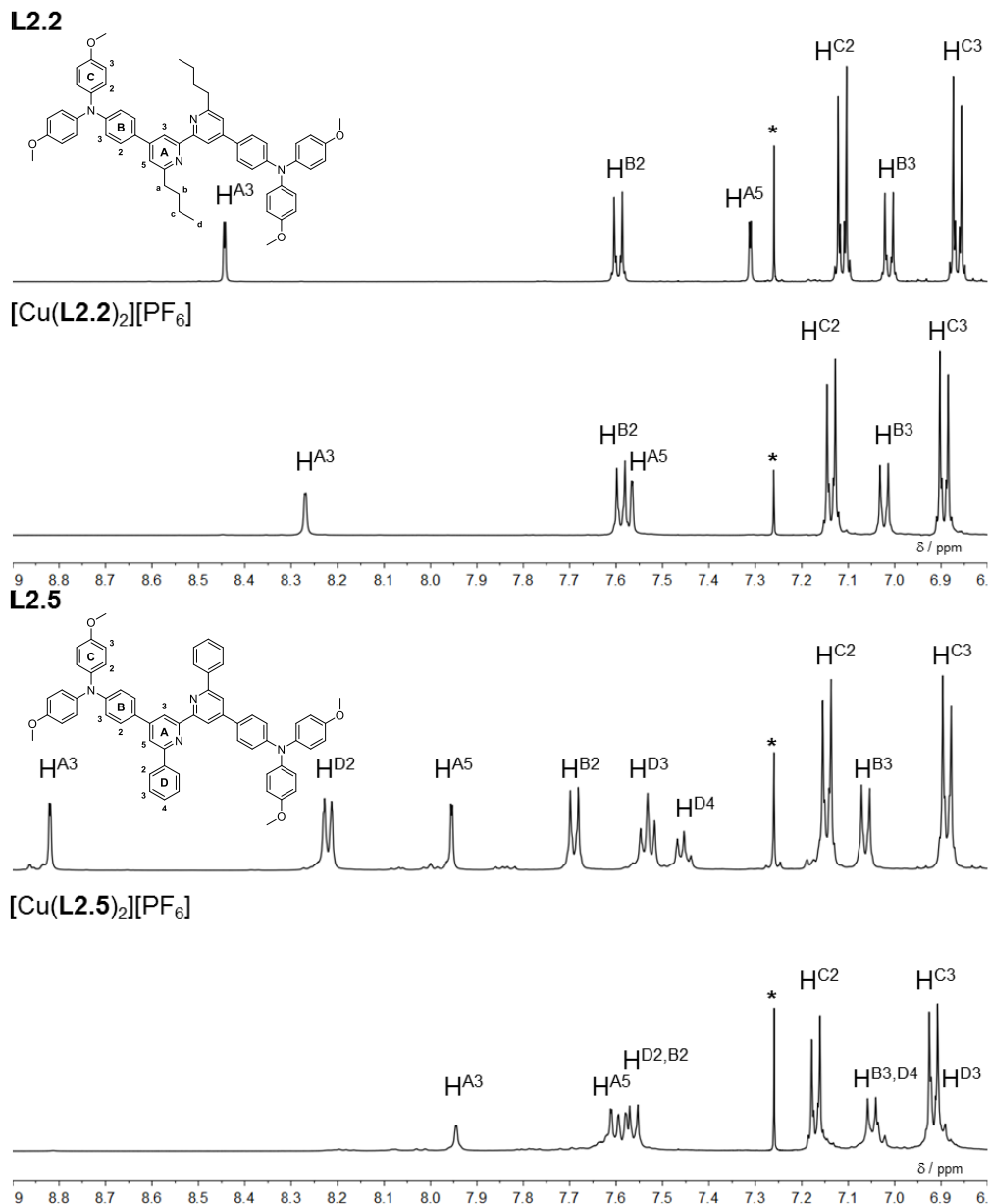
*Figure 34: : Aromatic region of the 500 MHz ^{1}H NMR spectra of L2.2 and L2.5 and their homoleptic copper(I) complexes [Cu(L2.2/L2.5)$_2$][PF$_6$]. * = residual CHCl$_3$.*

These shifts for protons H^{A3} and H^{A5} are observed for all ligand complex pairs in which the ligand is decorated with alkyl substituents in the 6,6'-positions (Table 1).

The shift for H^{A3} to lower frequency on going from ligand to complex is more pronounced for ligands bearing aryl groups in the 6,6'-positions (**L1.5**, **1.6**, **L2.5**, **2.6** and **L3.5**, **3.6**), than for alkylated ligands/complexes (see Figure 34).

5.1.2 Assigning protons H^{A3} and H^{A5} by protonation of ligand L2.1

Pure ligand **L2.1** (6.4 mg, 8.09·10^{-6} mol) was dissolved in 0.5 mL CDCl$_3$ and the 400 MHz ^{1}H NMR spectrum was recorded. For the preparation of the acidic solution, 10 eq. of TFA (9.27·10^{-3} g, 6.25·10^{-3} mL) were dissolved in 2.0 mL CDCl$_3$. The sample was subsequently acidified and after each acidification step a ^{1}H NMR spectrum was recorded. After the addition of 10 equivalents of acid the sample was treated with an excess of K$_2$CO$_3$ and a final ^{1}H NMR spectrum was measured (Figure 35).
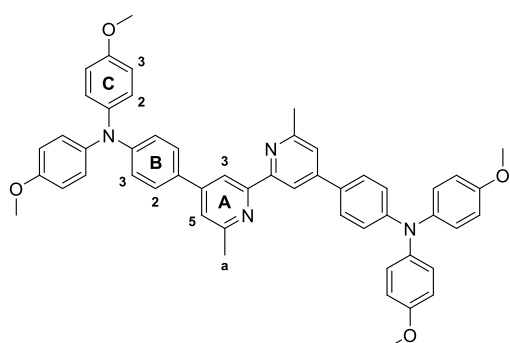
*Scheme 11: Structure and ring numbering of **L2.1**.*

In the stacked ^{1}H NMR spectra of **L2.1** the developing broad peak at δ ≈ 5.2 ppm is assigned to the TFA protons (Figure 35). With the addition of up to 1.4 eq. of TFA, the protons H^{A3} and H^{A5} are low field shifted (from δ 8.4 to 8.5 and δ 7.3 to 7.45 ppm respectively). This correlates with a change in conformation. While **L2.1** in CDCl$_3$ exists in the *trans* conformation without acid present, the addition of acid causes the bpy to change its conformation to *cis* due to the protonation of both pendant nitrogen lone pairs with one proton (scheme next to Figure 35). Upon further addition of TFA, the concentration of protons increases, which causes another change in conformation (back to *trans*). This is emphasized by the high field shift of H^{A3} and the continued low field shifting of H^{A5}.
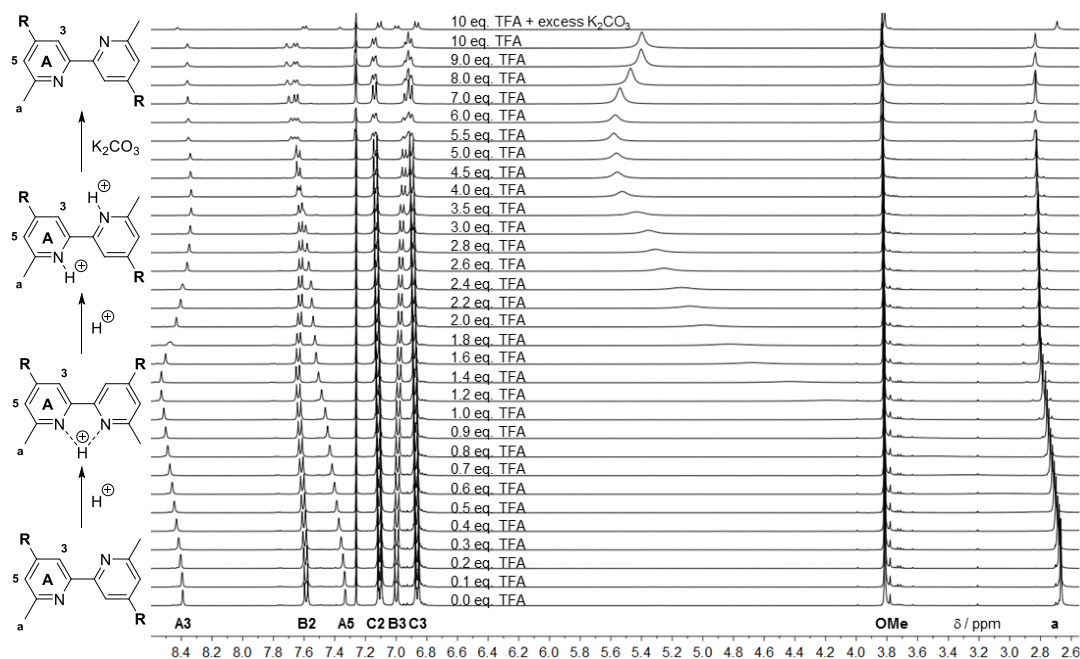
*Figure 35: 400 MHz ^{1}H NMR titration of **L2.1**. Series of ^{1}H NMR spectra containing 0.0 to 10 eq. of TFA.*

In addition to the shift of protons $H^{A3,A5}$, the addition of acid also affects the chemical shift of the protons of the phenylene spacers H^{B3} and the methyl groups H^a. Since the signals for protons H^{B3} are shifted to higher field one can assume that the arylamines are also protonated. For the protons on the methyl groups H^a, a shift is only observed up to the addition of 1.6 equivalents of acid. On adding more TFA (> 1.6 eq.) the chemical shift of H^a is no longer affected. On adding more than 5.0 eq. of TFA, the high amount of acid/protons starts to affect the chemical shifts of protons H^{C2} and H^{C3}.

In the final step of the addition of K_2CO_3, several processes happen. In general, upon addition of base the whole spectrum could be regenerated to the initial chemical shifts (protonation is reversible). At first, the broad signal at $\delta \approx 5.2$ ppm disappears, which confirms the assumption that this signal arose from TFA. The signals for the methyl groups (H^a) are high field shifted to their initial chemical shift. Also the MeO signal undergoes a slight shift to higher field. Signals for protons H^{C2} and H^{C3}, which were broadened or overlapping with other signals, are again well separated and resolved. Signals for the phenylene spacer (H^{B2} and H^{B3}) are shifted to their initial chemical shifts. While H^{B2} undergoes a shift to higher field its neighbouring proton H^{B3} undergoes a shift to lower field. For the protons H^{A3} and H^{A5}, the initial chemical shift is restored by the addition of base. For H^{A3}, a minor low field shift is observed (on going from 10 eq. TFA to the addition of K_2CO_3). In contrast, the signal for proton H^{A5} shows a drastic shift to higher field ($\delta \approx 7.65$ to $\delta \approx 7.30$ ppm).

5.2 UV-vis spectroscopy

5.2.1 Ligands L1.1-1.6

The photophysical properties of the six ligands **L1.1-1.6** were measured in CH_2Cl_2 solutions. The electronic absorption spectra for the ligands with alkyl substituents in the 6,6'-positions on the pyridine rings (**L1.1-1.4**) are comparable (see Figure 36). The spectra show intense bands at 255 nm with a weaker band close to 305 nm. The introduction of the phenyl substituents (**L1.5**) causes a red shift for both of these absorption bands (to 265 and 320 nm). The insertion of the 2-naphthyl groups in the 6,6'-positions on the pyridine rings, also causes a red shift for those bands. While the first absorption band is red shifted by the same amount (to 263 nm, as for **L1.5**), the second band is broadened (shoulder at 330 nm). The increase in absorption intensity at lower wavelength is consistent with the band arising from $\pi* \leftarrow \pi$ transitions. The lower energy band shows no change in intensity within the series of these six ligands, and is assigned to $\pi* \leftarrow n$ transitions.
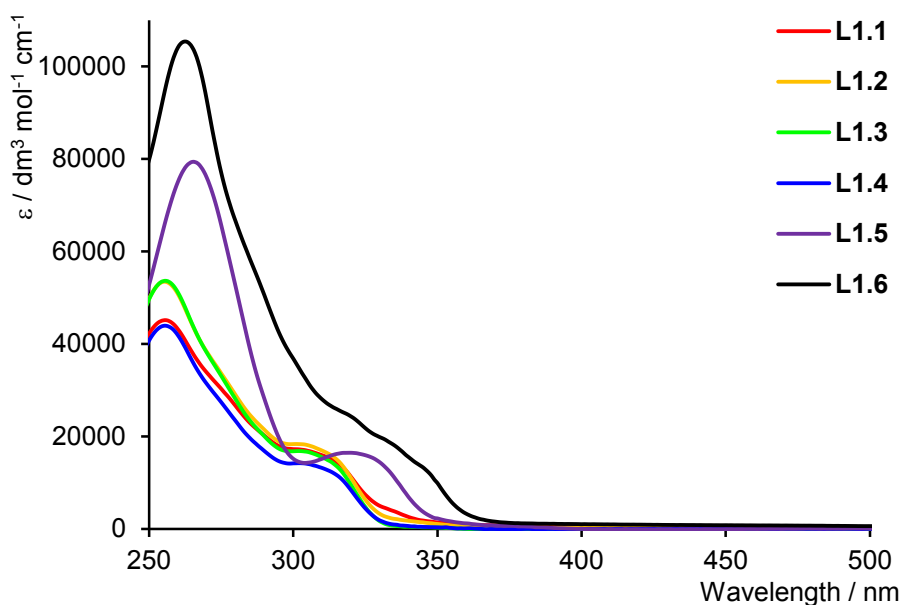
*Figure 36: Absorption spectra of ligands **L1.1-1.6** in CH_2Cl_2 (c = 1.0×10^{-5} M).*

5.2.2   Ligands L2.1-2.6

The solution absorption spectra of the six ligands **L2.1-2.6** (Figure 37) were measured in CH_2Cl_2 solutions. The electronic absorption spectra for ligands containing alkyl substituents in the 6,6'-positions (**L2.1-2.4**) are comparable. They exhibit absorption bands close to 300 and at $\approx$ 360 nm that tail into the visible region. The observed absorptions arise from spin allowed $\pi* \leftarrow \pi$ and $\pi* \leftarrow n$ transitions.

For ligands with aryl substituents in the 6,6'-positions (**L2.5** and **L2.6**), the intensity of the high energy absorption bands in the spectra are substantially enhanced compared to the alkyl-substituted ligands. The lowest energy absorption band is slightly red-shifted (to 370 nm) but is similar in intensity compared to the alkyl-substituted ligands. The bands at lower wavelength are assigned to $\pi* \leftarrow \pi$ transitions, whereas the lowest energy band is assigned to spin allowed $\pi* \leftarrow n$ transitions.
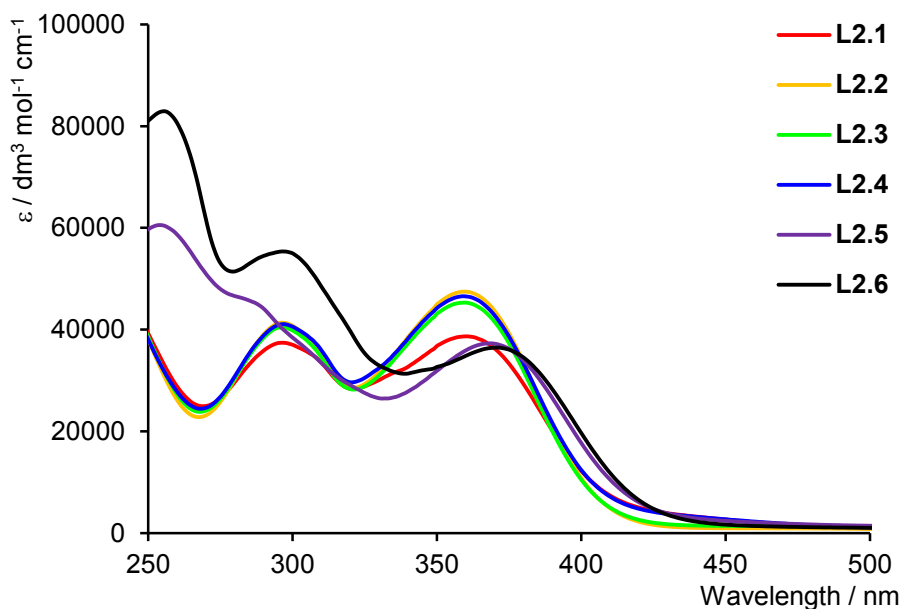
*Figure 37: Absorption spectra of ligands **L2.1-2.6** in CH_2Cl_2 (c = 1.0$\times$10^{-5} M).*

5.2.3   Ligands L3.1-3.6

The solution absorption spectra of ligands **L3.1-3.6** (Figure 38) were measured in CH_2Cl_2 solutions. The electronic absorption spectra for ligands containing alkyl substituents in the 6,6'-positions (**L3.1-3.4**) are almost superimposable. They exhibit absorption bands at ≈ 307 and at ≈ 344 nm that tail into the visible region of the spectrum. The observed absorptions arise from spin allowed $\pi* \leftarrow \pi$ and $\pi* \leftarrow n$ transitions.

For ligands with aryl substituents in the 6,6'-positions (**L3.5** and **L3.6**), the intensity of the high energy absorption bands in the spectra are substantially enhanced compared to the alkyl-substituted ligands. The lowest energy absorption band is slightly red-shifted (shoulder at ≈ 400 nm) compared to the alkyl-substituted ligands. The bands at lower wavelength are assigned to $\pi* \leftarrow \pi$ transitions, whereas the lowest energy band is assigned to spin allowed $\pi* \leftarrow n$ transitions.
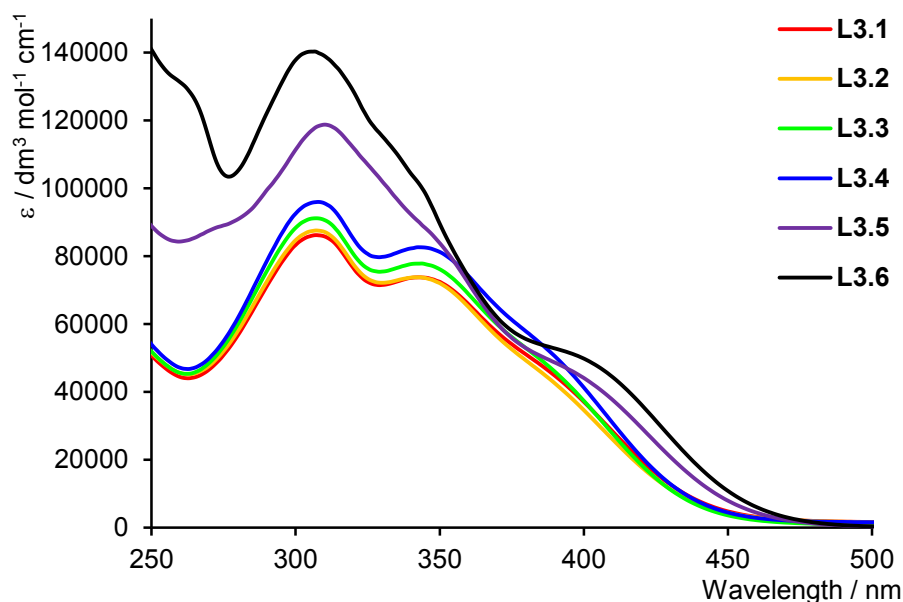
*Figure 38: Solution absorption spectra of ligands **L3.1-3.6** in CH₂Cl₂ (c = 1.0×10⁻⁵ M).*

5.2.4 Ligands L1.1-3.6

To emphasize the changes in the absorption spectra on going from the first set of ligands (**L1.1-1.6**) by the insertion of an arylamine (**L2.1-2.6**) and how the absorption properties were affected by the extension of the aryl system (**L3.1-3.6**), the electronic absorption spectra of all ligands are shown in Figure 39.
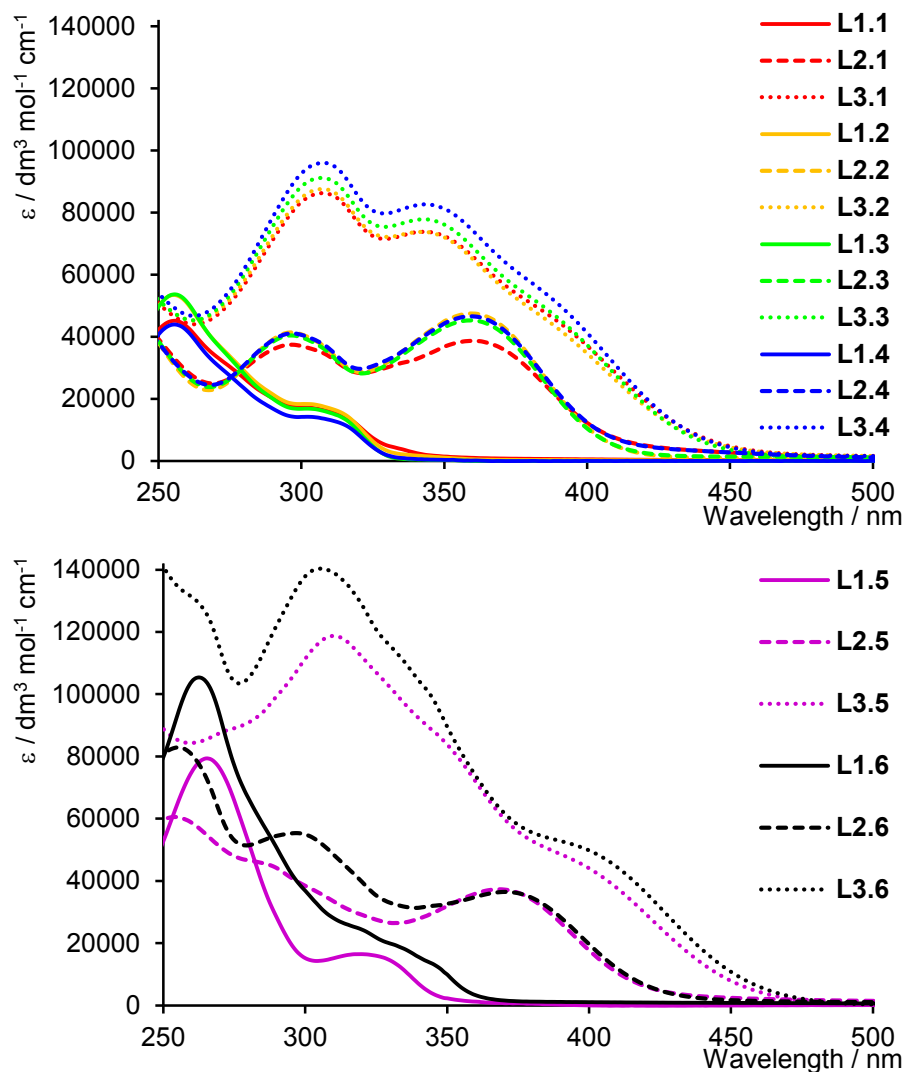
Figure 39: A comparison of solution absorption spectra of all ligands in CH₂Cl₂ (c = 1.0×10⁻⁵ M).

Ligands **L1.1-1.6** show the weakest absorption intensities, which is as expected as their structure has the smallest aromatic system. By introducing an arylamine (**L2.1-2.6**) the absorption intensity has not increased, but the ligands absorb across a wider range of wavelengths.

The extension of the aromatic domains (**L3.1-3.6**) leads to the anticipated increase in extinction coefficients. Additionally, the onset of the lowest energy absorption band underwent a red-shift of about 40 nm.

5.2.5 Complexes C1.1-1.6

The photophysical properties of complexes **C1.1-1.6** were measured in CH_2Cl_2 solutions. Their electronic absorption spectra are shown in Figure 40. Complexes with aliphatic substituents in the 6,6'-positions of the bipyridine (**L1.1-1.4**) exhibit the same spectrum with nearly the same intensity. They show high energy absorption bands assigned to ligand based $\pi* \leftarrow \pi$ transitions and an MLCT band in the visible region ($\lambda_{max} \approx 480$ nm). For complexes **C1.5** and **C1.6** a dual band in the visible region of the spectrum is observed ($\lambda_{max} \approx 430$ and 580 nm). These two bands and their relative red and blue shift compared to **C1.1-1.4** (480 nm) are consistent with the observed spectrum of $[Cu(dpp)_2]^+$ (dpp = 2,9-diphenyl-1,10-phenanthroline), which are explained with a flattened structure of the complex[160][120]. Concerning the high energy bands for **C1.5** and **C1.6**, the enhanced spectral response observed for ligands **L1.5** and **L1.6** is retained.
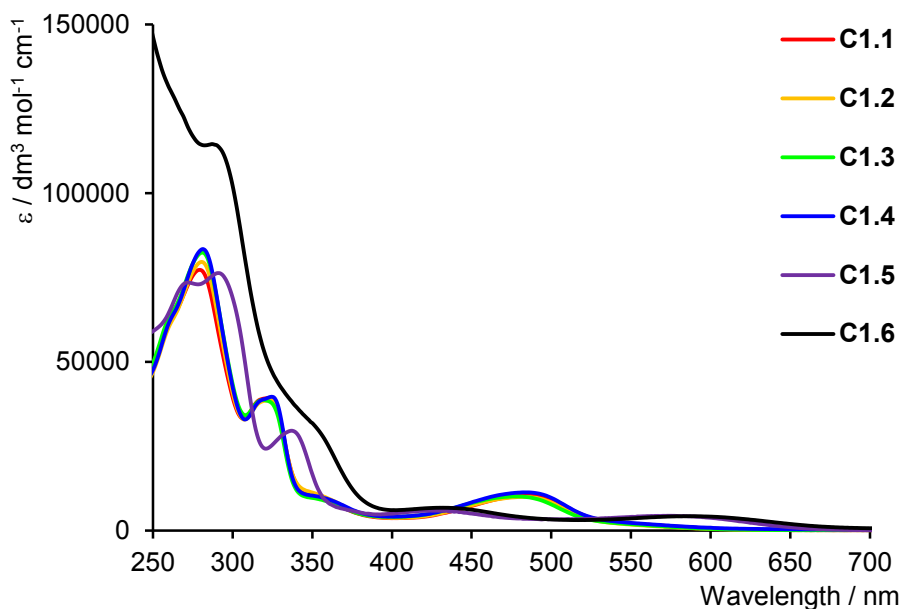
*Figure 40: Absorption spectra of complexes **C1.1-1.6** in CH_2Cl_2 (c = 1.0×10^{-5} M).*

5.2.6 Complexes C2.1-2.6

The solution absorption spectra of complexes **C2.1-2.6** were measured in CH_2Cl_2. Their electronic absorption spectra are shown in Figure 41. Complexes containing alkyl substituents (**C2.1-2.4**) show very similar absorption spectra. They exhibit sharp absorption bands at ≈ 305 nm, a broad absorption at ≈ 390 nm and a shoulder at ≈ 480 nm. The low energy band is assigned to the MLCT transition. This absorption band is consistent with the energy that has been confirmed from TD-DFT calculations for the MLCT of $[Cu(6,6'-Me_2bpy)_2]^{+[160]}$ and also agrees with the experimental data[161]. For complexes **C2.5** and **C2.6**, the increase in absorption intensity at high energy (>300 nm) is consistent with the introduction of aromatic substituents in the 6,6'-positions. The absorption band at ≈ 408 nm underwent a red-shift of about 10-20 nm compared to the alkyl substituted complexes. The low intensity bands at 560 and 576 nm for **C2.5** and **C2.6**, respectively, are assumed to arise from MLCT transitions. This is consistent with complexes **C1.5** and **C1.6** and was also reported in the literature for $[Cu(dtp)_2]^+$ (dtp = 2.9-di-*p*-tolyl-1,10-phenanthroline)[115].
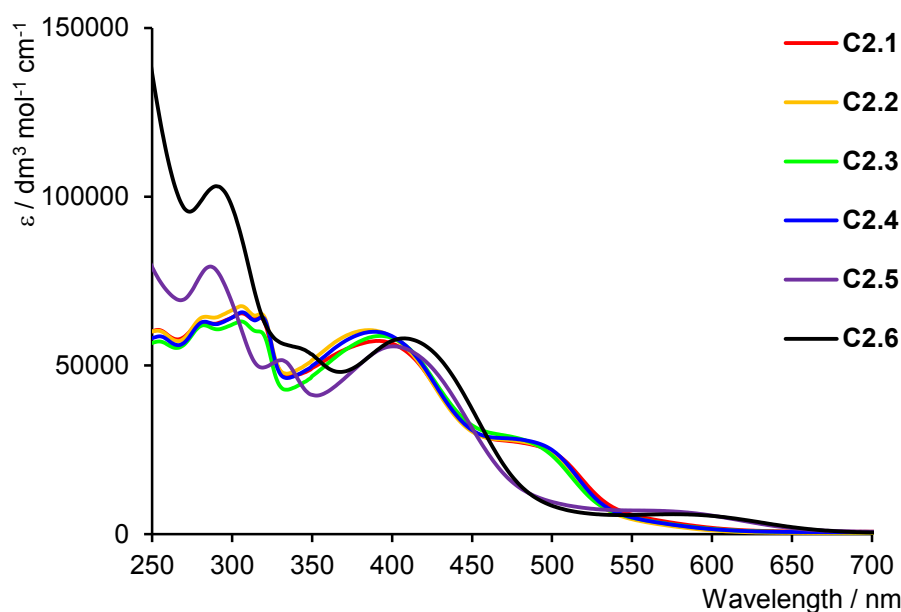
Figure 41: Absorption spectra of complexes C2.1-2.6 in CH₂Cl₂ (c = 1.0×10⁻⁵ M).

An approximate doubling of the extinction coefficient when one compares the spectra of the ligands with those of the complexes is consistent with the *homoleptic* complexes [Cu(**L2.1-2.6**)$_2$][PF$_6$]. At higher energy (>450 nm) the absorption spectra of [Cu(**L2.1-2.6**)$_2$][PF$_6$] has similar absorption bands to those of ligands **L2.1-2.6**; however the ligand centred band at ≈ 360 nm undergoes a red-shift of 10-30 nm on going from ligand to complex.

5.2.7 Complexes C3.1-3.6

The solution absorption spectra of complexes **C3.1-3.6** were measured in CH_2Cl_2. Their electronic absorption spectra are shown in Figure 42. All complexes exhibit broad absorption bands. They are dominated by high energy bands at $\approx$ 310 and $\approx$ 340 nm, originating from ligand based $\pi* \leftarrow \pi$ and $\pi* \leftarrow n$ transitions. The broad shoulder in the solution spectra of alkyl substituted complexes (**C3.1-3.4**) centred around 480 nm is assigned to the MLCT transition. The low energy absorption band at $\approx$ 580 nm for complexes **C3.5** and **C3.6** is assigned to the MLCT transition. This shift to lower energy is consistent with the analogous complexes **C1.5**, **C1.6**, **C2.5** and **C2.6**.
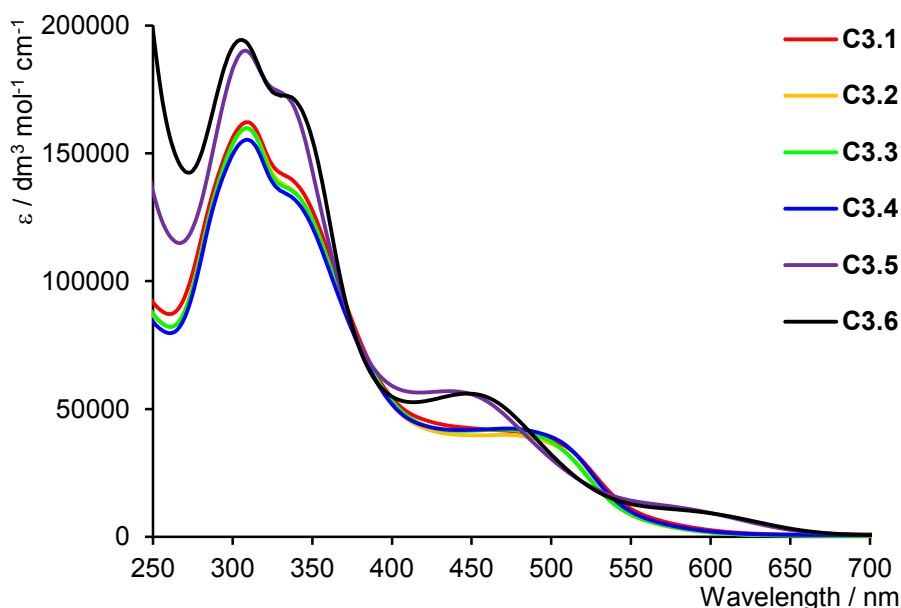
Figure 42: Solution absorption spectra of complexes C3.1-3.6 in CH₂Cl₂ (c = 1.0×10⁻⁵ M).

An approximate doubling of the extinction coefficient when one compares the spectra of the ligands with those of the complexes is consistent with the *homoleptic* complexes [Cu(L**3.1-3.6**)$_2$][PF$_6$]. At higher energy (>400 nm) the absorption spectra of [Cu(L**3.1-3.6**)$_2$][PF$_6$] have similar band shapes compared to those of ligands **L3.1-3.6**.

5.2.8 Complexes C1.1-3.6

To visualize the enhancement in the absorbance on going from the first set of complexes (**C1.1-1.6**) by the insertion of an arylamine (**C2.1-2.6**) and how the absorption properties were affected by the extension of the aryl system (**C3.1-3.6**), the electronic absorption spectra of all ligands are shown in Figure 43.
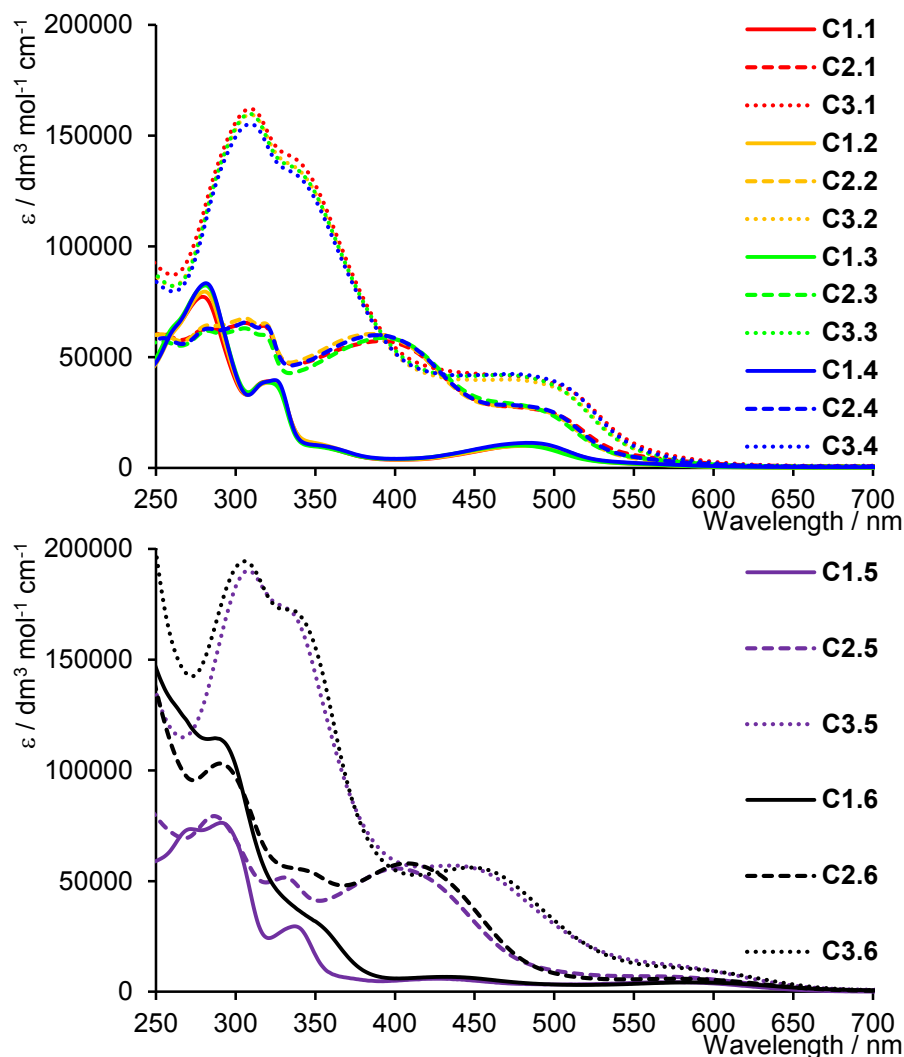
Figure 43: A comparison of solution absorption spectra of all complexes in CH₂Cl₂ (c = 1.0×10⁻⁵ M).

The *homoleptic* copper(I) complexes **C1.1-1.6** exhibit the weakest absorption intensity. With the insertion of the arylamine (**C2.1-2.6**) a broadening in absorption was achieved. A final increase in extinction coefficient was obtained through a further extension of the aryl moiety (C**3.1-3.6**). All complexes with alkyl substituents in the 6,6'-positions on the bipyridine show approximately the same energy for the MLCT transition in solution. Complexes with aryl group substituents in the 6,6'-positions on the bipyridine also exhibit the same energy band in the absorption spectra for the MLCT transitions.

5.3 Electrochemistry

5.3.1 Complexes C1.1-1.6

All the complexes were electrochemically analysed by cyclic voltammetry and the data are given in Table 2. All cyclic voltammograms were recorded in CH_2Cl_2 to avoid any interaction of coordinating solvents such as MeCN.

Complex	$E^{1/2}_{ox}$ [V] (E_{pc}-E_{pa} [mV])	$E^{1/2}_{ox}$ [V]	$E^{1/2}_{red}$ [V]
[Cu(**L1.1**)$_2$][PF$_6$]	+0.42 (94)	+1.49[ir]	-2.16[ir]
[Cu(**L1.2**)$_2$][PF$_6$]	+0.52 (87)	+1.47[ir]	-2.16[ir]
[Cu(**L1.3**)$_2$][PF$_6$]	+0.54 (96)	+1.47[ir]	-2.20[ir]
[Cu(**L1.4**)$_2$][PF$_6$]	+0.54 (84)	+1.49[ir]	-2.14[ir]
[Cu(**L1.5**)$_2$][PF$_6$]	+0.36 (86)	—	—
[Cu(**L1.6**)$_2$][PF$_6$]	+0.37 (76)	—	—

*Table 2: Cyclic voltammetric data for [Cu(**L1.1-1.6**)$_2$][PF$_6$] with respect to Fc/Fc$^+$; degassed CH$_2$Cl$_2$ solutions with [^{n}Bu$_4$N][PF$_6$] as electrolyte and a scan rate of 0.1 V s^{-1}. Processes are reversible unless otherwise stated (ir = irreversible).*

It is known that in copper(I) diimine complexes the *ortho* substituents to the N,N-donors (6,6'-positions in 2,2'-bpy) are responsible for the stabilization of the copper(I) centre, with respect to oxidation. Due to the steric hindrance of the substituents, the d^{10} metal centre (Cu$^+$) is protected from a possible oxidation (with O$_2$), which would cause a change in electronic configuration to d^9 (Cu^{2+}) which would result in a with a flattening of the coordination environment[162][163] (square planar for Cu^{2+}).

The oxidation potential assigned to the metal-centred oxidation (Table 2) in the complexes **C1.1-1.4** follows the following trend: the less sterically demanding the substituents in the 6,6'-positions, the easier it is to oxidize the copper(I) centre.

Oxidation potential: **C1.1 < C1.2 ≈ C1.3 ≈ C1.4**

All complexes containing alkyl substituents exhibit an irreversible oxidation process at higher potential. This irreversible signal is probably the oxidation of a 4-bromophenyl substituent to the corresponding radical cation[164].

The oxidation potential of **C1.1** (+0.42 V) compares to +0.5 V for [Cu(dmp)$_2$][PF$_6$] (dmp = 2,9-dimethyl-1,10-phenanthroline)[163]. The oxidation processes for **C1.5** and **C1.6** assigned to the metal oxidation are observed at lower potential. The measured values of +0.36 and +0.37 V for **C1.5** and **C1.6**, respectively, are similar to [CuL$_2$]$^+$, where L = 4,4',6,6'-tetraphenyl-2,2'-bpy (+0.39 V *vs.* Fc/Fc$^+$ in CH$_2$Cl$_2$)[165]. Upon oxidation of the copper centre the structure undergoes a flattening. This structural reorganisation is less pronounced for **C1.5** and **C1.6** than for **C1.1**.

This is based on the flattened structure of **C1.5**, which was found in the crystal structure (section 5.4.7).
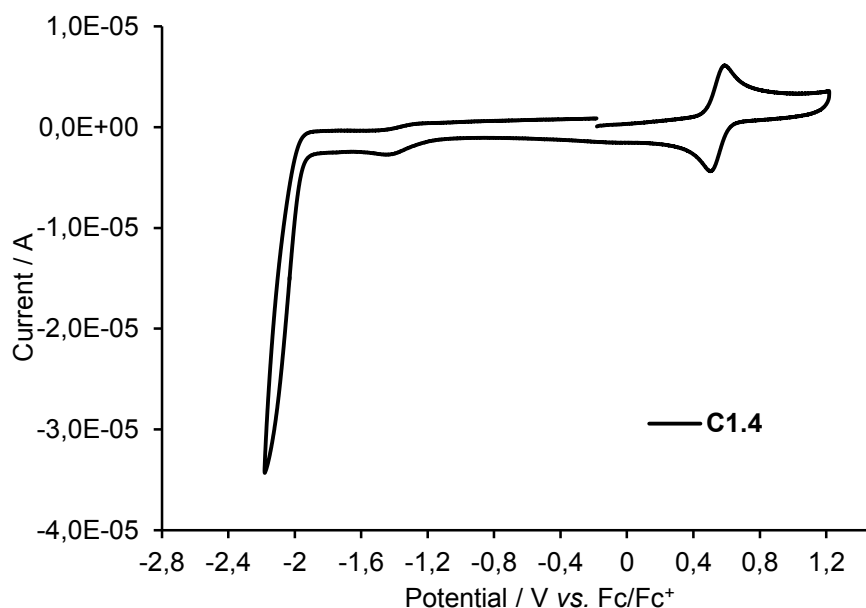
Figure 44: Cyclic voltammogram for [Cu($L1.4$)$_2$][PF$_6$] with respect to Fc/Fc$^+$; degassed CH$_2$Cl$_2$ solution with [^{n}Bu$_4$N][PF$_6$] as electrolyte and a scan rate of 0.1 V s^{-1}.

5.3.2   Complexes C2.1-2.6

All the *homoleptic* complexes were electrochemically analyzed by cyclic voltammetry and the data are given in Table 3. All cyclic voltammograms were recorded in CH$_2$Cl$_2$ to avoid association of the metal ion with coordinating solvents such as MeCN [163]. The voltammograms are always referenced internally to ferrocene.

Complex	$E^{1/2}_{ox}$ [V] (E_{pc}-E_{pa} [mV])	$E^{1/2}_{ox}$ [V]	$E^{1/2}_{ox}$ [V]	$E^{1/2}_{red}$ [V]
[Cu(**L2.1**)$_2$][PF$_6$]	+0.29 (96)	+0.44 (87)	+1.00^{ir}	-2.04^{ir}
[Cu(**L2.2**)$_2$][PF$_6$]	+0.29 (79)	+0.57 (65)	+0.98 (94)^{qr}	-2.09^{r}
[Cu(**L2.3**)$_2$][PF$_6$]	+0.29 (86)	+0.58 (66)	+0.99 (102)^{qr}	-2.07^{ir}
[Cu(**L2.4**)$_2$][PF$_6$]	+0.29 (89)	+0.57 (74)	+0.96 (106)^{qr}	-2.08^{ir}
[Cu(**L2.5**)$_2$][PF$_6$]	+0.32 ^{a}	+0.40 ^{a}	+0.99 (83)^{qr}	-2.25^{ir}
[Cu(**L2.6**)$_2$][PF$_6$]	+0.31 ^{a}	+0.40 ^{a}	+0.97 (96)^{qr}	-2.07^{ir}

*Table 3: Cyclic voltammetric data for [Cu(**L2.1-2.6**)$_2$][PF$_6$] with respect to Fc/Fc$^+$; degassed CH$_2$Cl$_2$ solutions with [^{n}Bu$_4$N][PF$_6$] as electrolyte and a scan rate of 0.1 V s^{-1}. Processes are reversible unless otherwise stated (qr = quasi-reversible; ir = irreversible). ^{a} 1st and 2nd oxidation processes overlap.*

For complexes **C2.1-2.6** three oxidation processes are observed. A representative CV for **C2.4** is shown in Figure 45. By comparing CVs from free ligands, the oxidation processes from +0.40 to +0.58 V are assigned to the Cu$^+$/Cu^{2+} process and signals at ≈ +0.30 and ≈ +1.00 V respectively, could be assigned to ligand based oxidations[166]. As already mentioned the substituent in the 6,6'-positions on the bipyridine core stabilize the tetrahedral Cu(I)

conformation with respect to the square-planar Cu(II). With their steric hindrance it is harder to flatten the coordination sphere. The oxidation potentials for the Cu^+/Cu^{2+} process for **C2.1-2.6** follow the same trend as for **C1.1-C1.6**. For nBu, isoBu and nHex substituents, the metal oxidation occurs at a similar potential +0.54 ± 0.04V, which is at higher potential than for methyl, phenyl and 2-naphthyl containing complexes. The complexes **C2.5** and **C2.6** exhibit the lowest metal oxidation potentials. For the alkylated complexes, the trend follows the steric hindrance of the substituents, with the least sterically demanding groups being the easiest to oxidize. As already mentioned, the metal centre of **C1.5** possesses a flattened structure in the solid state. A phenyl substituent in the 6 or 6'-position of one ligand and the bipyridine domain of the other ligand are interacting via π-stacking. This leads to a so called entatic[167] state, where less energy is needed to oxidize the copper(I) centre, since its geometry is already close to that favoured by copper(II). Entatic is derived from *entasis* (Greek), meaning tension[168].
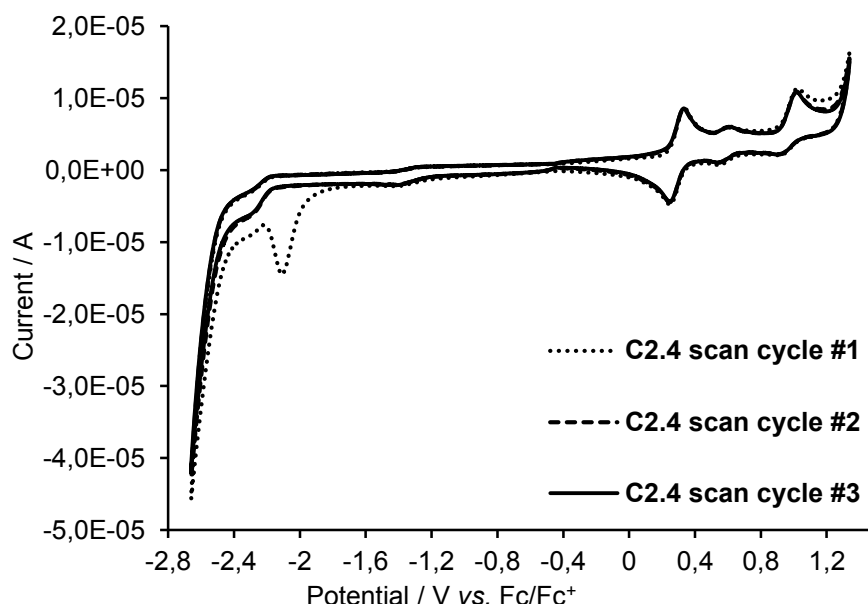
*Figure 45: Cyclic voltammogram curve for [Cu(**L2.4**)₂][PF₆] with respect to Fc/Fc⁺; degassed CH₂Cl₂ solution with [ⁿBu₄N][PF₆] as electrolyte and a scan rate of 0.1 V s⁻¹.*

A representative CV for the 2nd generation complexes (Figure 45, **C2.4**) shows an irreversible reduction at -2.08 V displayed with the dotted line. This reduction was only detectable within the first scan cycle and was observed for all complexes **C2.1-2.6**.

From square wave experiments, the relative intensities of the oxidation peaks were 2 : 1 : 2. Therefore the first and third oxidation signals were assigned to two electron processes involving the oxidation of the aryl amine. The formed radical is probably stabilized and delocalized over the aniline groups due to the π-conjugation[169].

5.3.3   Complexes C3.1-3.6

All the *homoleptic* complexes were electrochemically analysed by cyclic voltammetry and the data are given in Table 4. All cyclic voltammograms were recorded in CH_2Cl_2 to avoid association of the metal ion with coordinating solvents such as MeCN[163]. The voltammograms are referenced internally to ferrocene.

Complex	$E^{1/2}_{ox}$ [V] $(E_{pc}-E_{pa}$ [mV])	$E^{1/2}_{ox}$ [V] $(E_{pc}-E_{pa}$ [mV])	$E^{1/2}_{ox}$ [V] $(E_{pc}-E_{pa}$ [mV])	$E^{1/2}_{ox}$ [V] $(E_{pc}-E_{pa}$ [mV])	$E^{1/2}_{ox}$ [V] $(E_{pc}-E_{pa}$ [mV])	$E^{1/2}_{red}$ [V]
[Cu(**L3.1**)$_2$][PF$_6$]	-0.07 (78)	+0.20 (75)	+0.47 (129)	+0.69 (168)	+1.03[ir]	-2.03[ir]
[Cu(**L3.2**)$_2$][PF$_6$]	-0.07 (83)	+0.19 (83)	+0.54 (99)	+0.69 (155)	+1.01 (111)[qr]	-2.07[r]
[Cu(**L3.3**)$_2$][PF$_6$]	-0.08 (65)	+0.18 (88)	+0.55 (90)	+0.68 (157)	+1.02 (85)[qr]	-2.06[ir]
[Cu(**L3.4**)$_2$][PF$_6$]	-0.07 (79)	+0.18 (89)	+0.55 (84)	+0.69 (150)	+1.03 (86)[qr]	-2.06[ir]
[Cu(**L3.5**)$_2$][PF$_6$]	-0.07 (81)	+0.19 (103)	+0.39 (81)	+0.69 (170)	+1.03 (69)[qr]	-2.19[ir]
[Cu(**L3.6**)$_2$][PF$_6$]	-0.08 (63)	+0.19 (85)	+0.39 (67)	+0.68 (168)	+1.02[ir]	-2.08[ir]

*Table 4: Cyclic voltammetric data for [Cu(**L3.1-3.6**)$_2$][PF$_6$] with respect to Fc/Fc⁺; degassed CH_2Cl_2 solutions with [ⁿBu$_4$N][PF$_6$] as electrolyte and a scan rate of 0.1 V s⁻¹. Processes are reversible unless otherwise stated (qr = quasi-reversible; ir = irreversible). ᵃ 1ˢᵗ and 2ⁿᵈ oxidation processes overlap.*

For the complexes **C3.1-3.6** similar trends are observed as for **C1.1-1.6** and **C2.1-2.6**. The complexes **C3.1-3.6** show five oxidation processes. A representative CV for **C3.4** is shown in Figure 46. Due to the absence of the oxidation signal at +0.47 V in the CV of the free ligand **L3.1**[166], the processes in the range of +0.39 to +0.55 V are assigned to the Cu^+/Cu^{2+} process. The remaining four oxidation signals could be assigned to ligand based processes.

As mentioned above, the substituents in the 6,6'-positions on the bipyridine core stabilize the tetrahedral Cu(I) with respect to the square-planar Cu(II). The oxidation potentials for the Cu^+/Cu^{2+} process for **C3.1-3.6** follow the same trend as for **C1.1-C1.6** and **C2.1-2.6**. For alkylated complexes (**C3.2**, **C3.3** and **C3.4**), the metal oxidation occurs at a similar potential (+0.54 ± 0.01V), which is at higher potential than for methyl, phenyl and 2-naphthyl containing complexes. The complexes **C2.5** and **C2.6** exhibit the lowest metal oxidation potentials. For the alkylated complexes the trend follows the steric hindrance of the substituents, with the least sterically demanding groups being the easiest to oxidize.
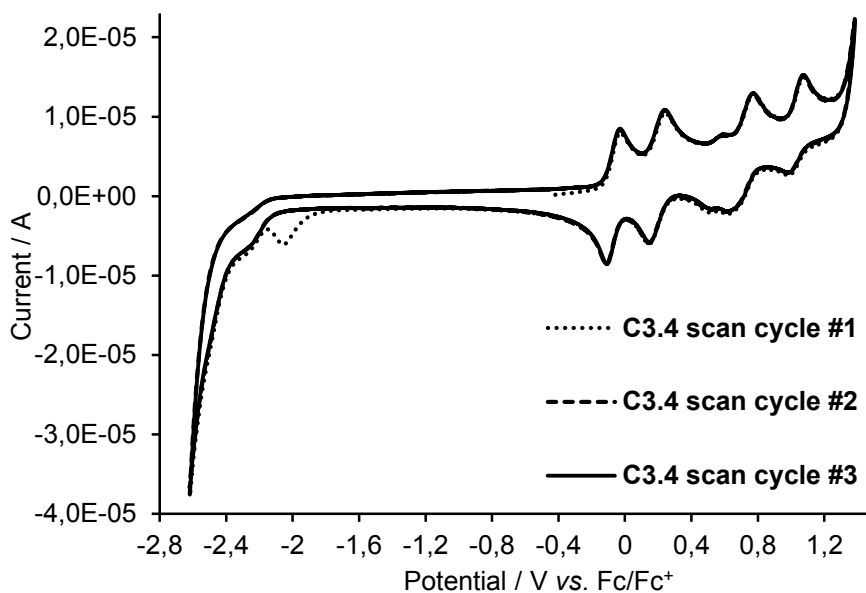
*Figure 46: Cyclic voltammogram curve for [Cu(**L3.4**)$_2$][PF$_6$] with respect to Fc/Fc$^+$; degassed CH$_2$Cl$_2$ solution with [^{n}Bu$_4$N][PF$_6$] as electrolyte and a scan rate of 0.1 V s^{-1}.*

A representative CV for the 3rd generation complexes (Figure 46, **C3.4**) shows an irreversible reduction at -2.06 V displayed with the dotted line. This reduction was only detectable within the first scan cycle and was observed for all complexes **C3.1-3.6**. This is consistent with complexes **C2.1-2.6**, where this reduction was also only visible on the first scan cycle. The ligand based reductions in the complexes lie close to the edge of the solvent accessible window and are poorly resolved.

In the square wave experiments, the relative intensities of the oxidation peaks were 2 : 2 : 1 : 2 : 2. The least intense signal was assigned to the Cu$^{+/2+}$ process. Therefore the remaining oxidation processes were assigned to two electron processes involving the oxidation of the peripheral aryl amines. The formed radicals are probably stabilized and delocalized over the aniline and aryl amine groups due to the extension of π-conjugation[169].

5.4 Crystal structures

5.4.1 Ligand L1.1

Crystallographic data:

$C_{24}H_{18}Br_2N_2$, $M = 494.20$, white blocks, triclinic, space group $P\text{–}1$, $a = 9.326(3)$, $b = 10.153(3)$, $c = 11.952(3)$ Å, $\alpha = 99.64(2)$, $\beta = 106.87(2)$, $\gamma = 108.02(2)°$, $U = 988.0(5)$ Å^3, $Z = 2$, $D_c = 1.661$ Mg m^{-3}, μ(Mo-Kα) = 4.115 mm^{-1}, $T = 123$ K. Total 23798 reflections, 4074 unique, R_{int} = 0.1572. Refinement of 3534 reflections (255 parameters) with >2σ (I) converged at final R_1 = 0.0613 (R_1 all data = 0.0686), $wR_2 = 0.1575$ (wR_2 all data = 0.1645), gof = 1.055.

Selected bond distances:

N1–C2 = 1.339(6), N1–C6 = 1.337(4), C1–C2 = 1.497(5), C6–C7 = 1.486(6), N2–C7 = 1.335(4), N2–C11 = 1.343(6), C11–C12 = 1.487(5), C16–Br1 = 1.897(4), C22–Br2 = 1.887(4) Å.

Selected angles:

C2–N1–C6 = 117.5(3), C7–N2–C11 = 117.7(3), N1–C2–C1 = 116.4(4), N2–C11–C12 = 116.3(4), Br1–C16–C17 = 120.0(3), Br2–C22–C23 = 120.0(3)°.
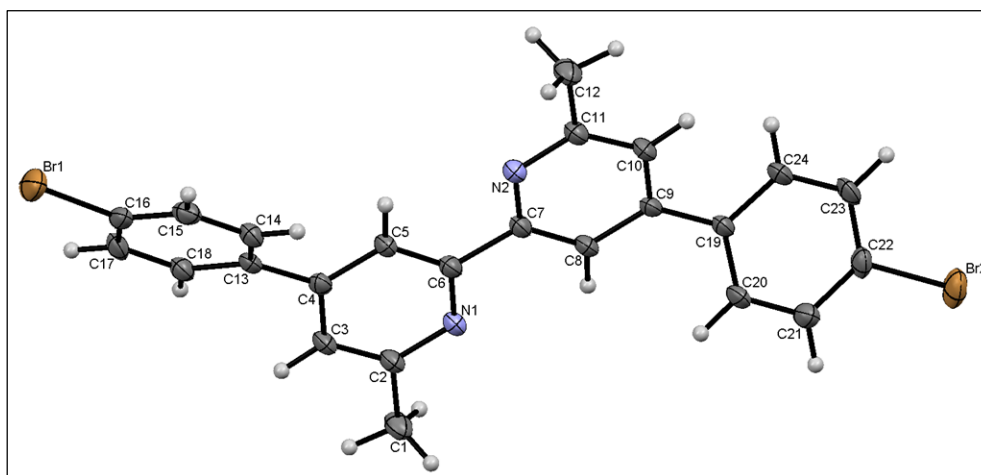
*Figure 47: Structure of ligand **L1.1** with ellipsoids plotted at 50% probability.*

The compound crystallizes in the space group $P\text{–}1$ and the bpy unit adopts a *trans*-conformation and is almost planar with the planes containing the two pyridine rings having an angle of 1.56°. The phenylene units are twisted 25.33° and 34.55° with respect to the pyridine ring to which they are bonded, thereby minimizing inter-ring H...H interactions.

5.4.2   Ligand L2.3

X-Ray single crystals of **L2.3** were grown by Et_2O diffusion into an acetone/chloroform solution of the compound. The structure of **L2.3** is shown in Figure 48.

Crystallographic data:

$C_{58}H_{58}N_4O_4$, $M = 875.08$, yellow plate, triclinic, space group $P–1$, $a = 9.9980(4)$, $b = 11.2625(4)$, $c = 11.6848(5)$ Å, $\alpha = 64.9850(10)$, $\beta = 80.227(2)$, $\gamma = 89.948(2)^o$, $U = 1171.31(8)$ Å^3, $Z = 1$, $D_c = 1.241$ Mg m^{-3}, μ(Cu-Kα) = 0.611 mm^{-1}, $T = 123$ K. Total 23653 reflections, 4153 unique, $R_{int} = 0.0258$. Refinement of 3800 reflections (302 parameters) with $I > 2\sigma (I)$ converged at final $R_1 = 0.0343$ (R_1 all data = 0.0376), $wR_2 = 0.0910$ (wR_2 all data = 0.0942), gof = 1.040. CCDC 987649.

Selected bond distances:

N1–C5 = 1.3451(14), N1–C9 = 1.3453(14), N2–C13 = 1.4006(14), N2–C22 = 1.4262(14), N2–C16 = 1.4302(14), C19–O1 = 1.3649(14), C25–O2 = 1.3697(14), O1–C28 = 1.4225(16), O2–C29 = 1.4274(15) Å.

Selected angles:

C13–N2–C22 = 121.22(9), C13–N2–C16 = 120.38(9), C22–N2–C16 = 118.16(9), C19–O1–C28 = 117.40(10), C25–O2–C29 = 116.05(9)^o.
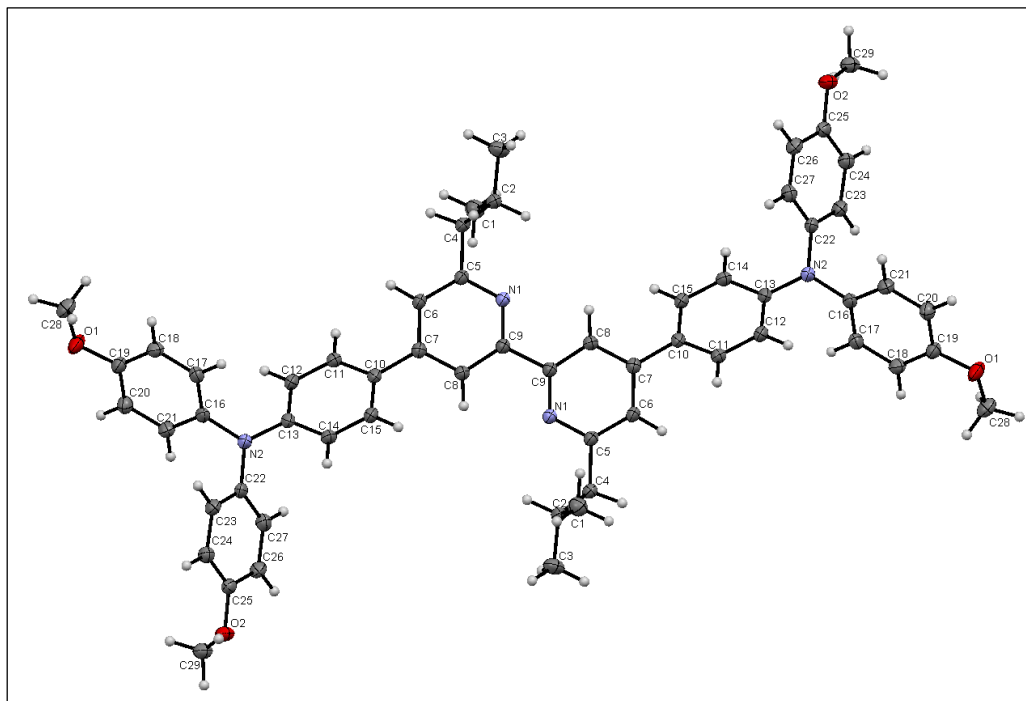
*Figure 48: Structure of ligand **L2.3** with ellipsoids plotted at 50% probability.*

The compound crystallizes in the space group $P–1$ with half of the molecule in the asymmetric unit; the second half is generated through an inversion centre and the bpy unit adopts a *trans*-conformation and is planar.

The phenylene unit (grey rings in Figure 49) is twisted 36.69º with respect to the pyridine ring to which it is bonded, thereby minimizing inter-ring H...H interactions. Atom N2 is in a planar environment, consistent with delocalization of the lone pair into the arene π-systems. The twisted arrangement of the three arene rings bonded to N2 is expected when considering sterics. The arene rings are twisted compared to each other from 69.94 to 79.05° (grey to yellow ring, 69.94°, grey to yellow 71.59° and light blue to yellow 79.05°).
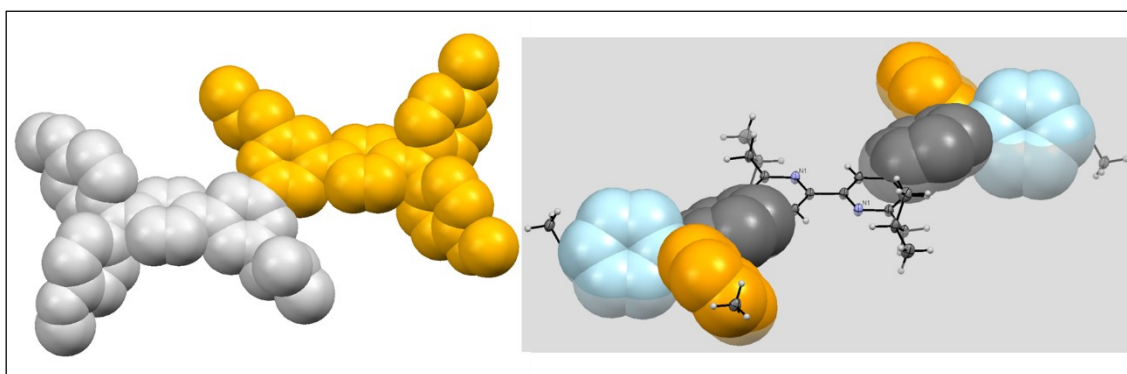
*Figure 49: Presentation symmetry in ligand **L2.3** (left) and the twisted arene rings (right).*

The presence of the isobutyl groups prevents face-to-face interactions between bpy domains of neighbouring molecules. Dominant packing interactions involve methoxy CH...$\pi_{pyridine}$ contacts (CH...centroid = 2.39 Å) which lead to a centrosymmetric embrace between adjacent molecules. These interactions lead to the assembly of hydrogen-bonded chains which slice indirectly through the unit cell.
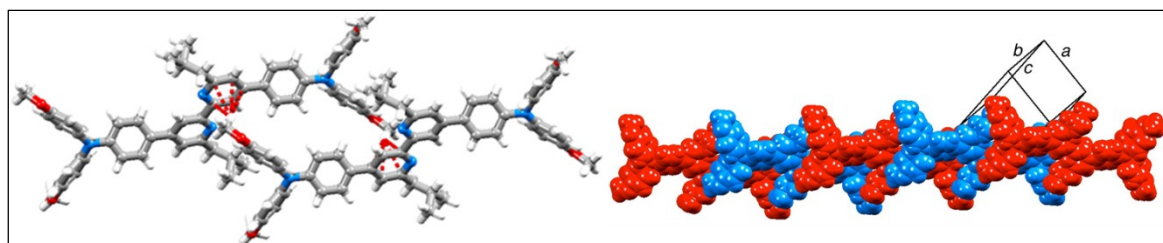
Figure 50: A pair of ligands with an inversion centre with embrace through CH$_{OMe}$...$\pi_{pyridine}$ contacts. (left) and the packing which is a consequence of the hydrogen bonds.

5.4.3   C1.1 ≡ [Cu(L1.1)$_2$][PF$_6$]

X-Ray quality crystals of 2{[Cu(**L1.1**)$_2$][PF$_6$]}·3Me$_2$CO were grown by Et$_2$O diffusion into an acetone solution of the complex at room temperature. The structure of the complex cation [Cu(**L1.1**)$_2$]$^+$ is shown in Figure 51.

Crystallographic data:

C$_{105}$H$_{90}$Br$_8$Cu$_2$F$_{12}$N$_8$O$_3$P$_2$, M = 2568.09, yellow plate, triclinic, space group P–1, a = 11.7229(6), b = 14.2639(8), c = 15.9549(8) Å, α = 93.364(3), β = 100.301(3), γ = 91.589(3)$^{\circ}$, U = 2618.4(2) Å^3, Z = 1, D_c = 1.629 Mg m^{-3}, μ(Cu-Kα) = 4.998 mm^{-1}, T = 123 K. Total 36736 reflections, 9192 unique, R_{int} = 0.0380. Refinement of 7490 reflections (657 parameters) with I >2σ (I) converged at final R_1 = 0.0575 (R_1 all data = 0.0703), wR_2 = 0.1655 (wR_2 all data = 0.1785), gof = 1.038. CCDC 942070.

Selected bond distances:

Cu1–N4 = 2.010(4), Cu1–N1 = 2.027(4), Cu1–N3 = 2.034(4), Cu1–N2 = 2.038(4), C6–C7 = 1.482(8), C30–C10 = 1.483(7) Å.

Selected angles:

N1–Cu1–N4 = 130.7(2), N3–Cu1–N4 = 80.7(2), N1–Cu1–N3 = 124.0(2), N2–Cu1–N4 = 129.0(2), N1–Cu1–N2 = 81.5(2), N2–Cu1–N3 = 116.1(1), N1–C2–C1 = 116.6(5), N2–C11–C12 = 116.7(5). N3–C26–C25 = 117.1(5), N4–C35–C36 = 116.3(5)°.
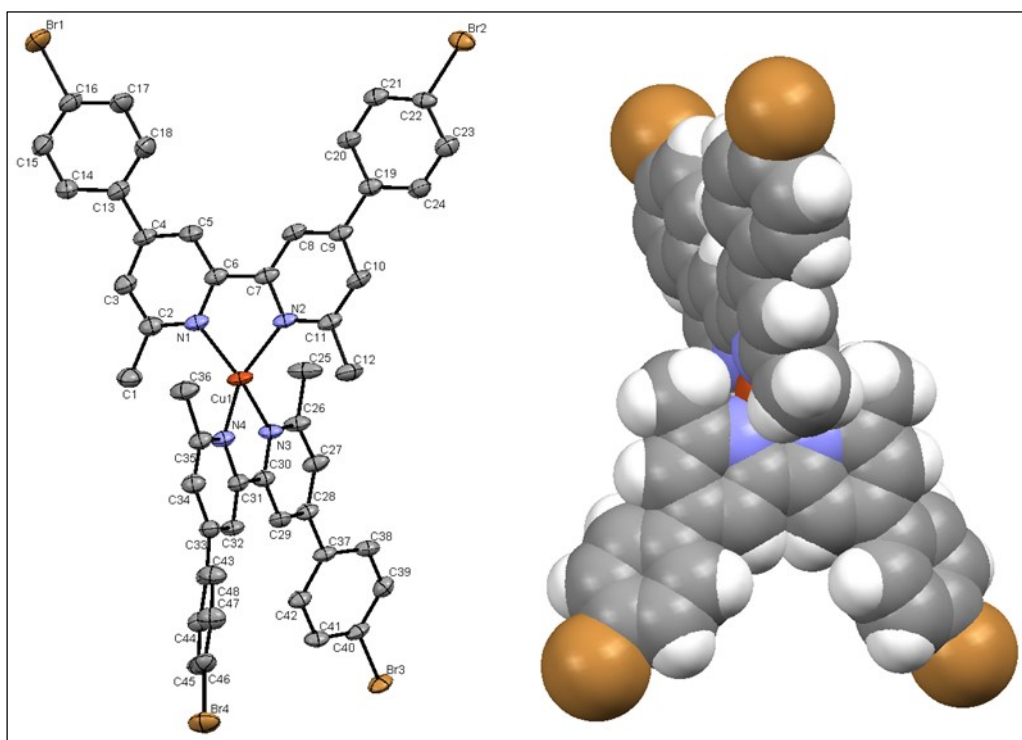
*Figure 51: ORTEP diagram of the [Cu(**L1.1**)$_2$]$^+$ cation. H atoms are omitted and ellipsoids plotted at 50% probability level (left). Space filling representation of the [Cu(**L1.1**)$_2$]$^+$ cation (right).*

The distorted tetrahedral coordination geometry of the copper atom is less flattened than in [Cu(dmbpy)$_2$]$^+$ (dmbpy = 6,6'-dimethyl-2,2'-bipyridine); in [Cu(**L1.1**)$_2$]$^+$, the angle between the least squares planes containing Cu1 and each bpy unit is 85.6°, compared to angles of 74.3° in [Cu(dmbpy)$_2$][PF$_6$] [160], 80.9° in [Cu(dmbpy)$_2$][BF$_4$] [170] and 80.9° in [Cu(dmbpy)$_2$][ClO$_4$][171]. The two bpy units are almost planar (angles between the planes of the rings containing N1/N2 and N3/N4 = 5.5 and 7.9°, respectively), and the angles between the planes of the pairs of bonded phenyl and pyridine rings range from 10.1 to 34.9°.

5.4.4   C1.2 ≡ [Cu(L1.2)$_2$][PF$_6$]

Single crystals of [Cu(**L1.2**)$_2$][PF$_6$] were grown by Et$_2$O diffusion into an acetone solution of the complex. The structure of the complex cation [Cu(**L1.2**)$_2$]$^+$ is shown in Figure 52.

Crystallographic data:

C$_{60}$H$_{60}$Br$_4$CuF$_6$N$_4$P, M = 1365.24, orange block, monoclinic, space group $P2_1/n$, a = 17.7430(13), b = 16.0855(12), c = 20.9134(16) Å, α = 90°, β = 105.193(3)° γ = 90°, U = 5760.2(8) Å^3, Z = 4, D_c = 1.574 Mg m^{-3}, μ(Cu-Kα) = 4.560 mm^{-1}, T = 123 K. Total 63279 reflections, 10359 unique, R_{int} = 0.0513. Refinement of 9481 reflections (747 parameters) with I >2σ (I) converged at final R_1 = 0.0372 (R_1 all data = 0.0406), wR_2 = 0.0958 (wR_2 all data = 0.0985), gof = 1.037. CCDC 942069.

Bond distances:

Cu1–N1 = 2.037(2), Cu1–N2 = 2.039(2), Cu1–N3 = 2.028(2), Cu1–N4 = 2.048(1), C9–C10 = 1.495(2), C39–C401 = 1.487(2) Å.

Selected angles:

N1–Cu1–N3 = 130.38(6), N2–Cu1–N4 125.08(5), N1–Cu1–N2 = 81.35(6), N3–Cu1–N4 = 81.16(6), N2–Cu1–N3 = 126.86(6), N1–Cu1–N4 = 117.95(6), N1–C5–C6 = 122.2(2), N2–C14–C13 = 122.2(2), N3–C35–C34 = 116.8(2), N4–C44–C43 = 121.6(2)°.
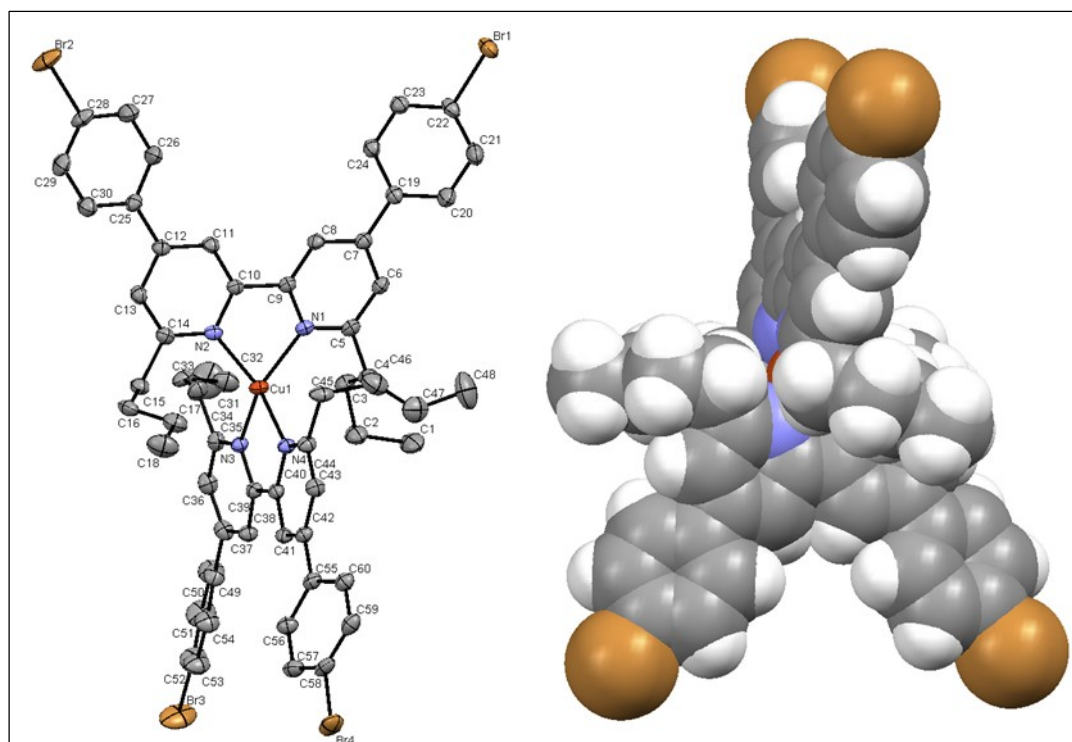
*Figure 52: ORTEP diagram of the [Cu(**L1.2**)$_2$]$^+$ cation. H atoms are omitted and ellipsoids plotted at 50% probability level (left). Space filling representation of the [Cu(**L1.2**)$_2$]$^+$ cation (right).*

The distorted tetrahedral environment of Cu1 is basically the same as that in [Cu(**L1.1**)$_2$]$^+$. The angles of least squares planes containing Cu1 and each bpy unit is 86.4°. Each bpy unit is slightly twisted (angles between the planes of the rings containing N1/N2 and N3/N4 = 7.1 and 12.3°, respectively), and the angles between the planes of the pairs of bonded phenyl and pyridine rings lie in the range 11.1 to 29.8°. The butyl substituents of the ligand containing N3 and N4 are disordered; each of the three terminal C and attached H atoms have been modelled over two sites (C31, C32 and C33 with fractional occupancies 0.54 and 0.46, and C46, C47 and C48 with fractional occupancies 0.51 and 0.49).

5.4.5   C1.3 ≡ [Cu(L1.3)₂][PF₆]

Single crystals of 2{[Cu(**L1.3**)₂][PF₆]}·Et₂O were obtained by Et₂O diffusion into an acetone/chloroform solution of the complex. The structure of the complex cation [Cu(**L1.3**)₂]⁺ is shown in Figure 53.

Crystallographic data:

$C_{124}H_{130}Br_8Cu_2F_{12}N_8OP_2$, M = 2804.61, yellow plate, monoclinic, space group $P2_1/c$, a = 15.5265(7), b = 23.9138(9), c = 17.7749(7) Å, β = 114.893(2)°, U = 5986.6(4) Å³, Z = 2, D_c = 1.556 Mg m⁻³, μ(Cu-Kα) = 4.410 mm⁻¹, T = 123 K. Total 46225 reflections, 10612 unique, R_{int} = 0.0480. Refinement of 8760 reflections (761 parameters) with $I > 2\sigma$ (I) converged at final R_1 = 0.0467 (R_1 all data = 0.0581), wR_2 = 0.1168 (wR_2 all data = 0.1244), gof = 1.037. CCDC 942071.

Bond distances:

Cu1–N1 = 2.049(3), Cu1–N2 = 2.029(3), Cu1–N3 = 2.063(3), Cu1–N4 = 2.039(3)Å.

Selected angles:

N1–Cu1–N2 = 81.3(1), N1–Cu1–N3 = 127.6(1), N1–Cu1–N4 = 126.0(1), N2–Cu1–N3 = 122.7(1), N2–Cu1–N4 = 124.3(1), N3–Cu1–N4 = 81.2(1)°.
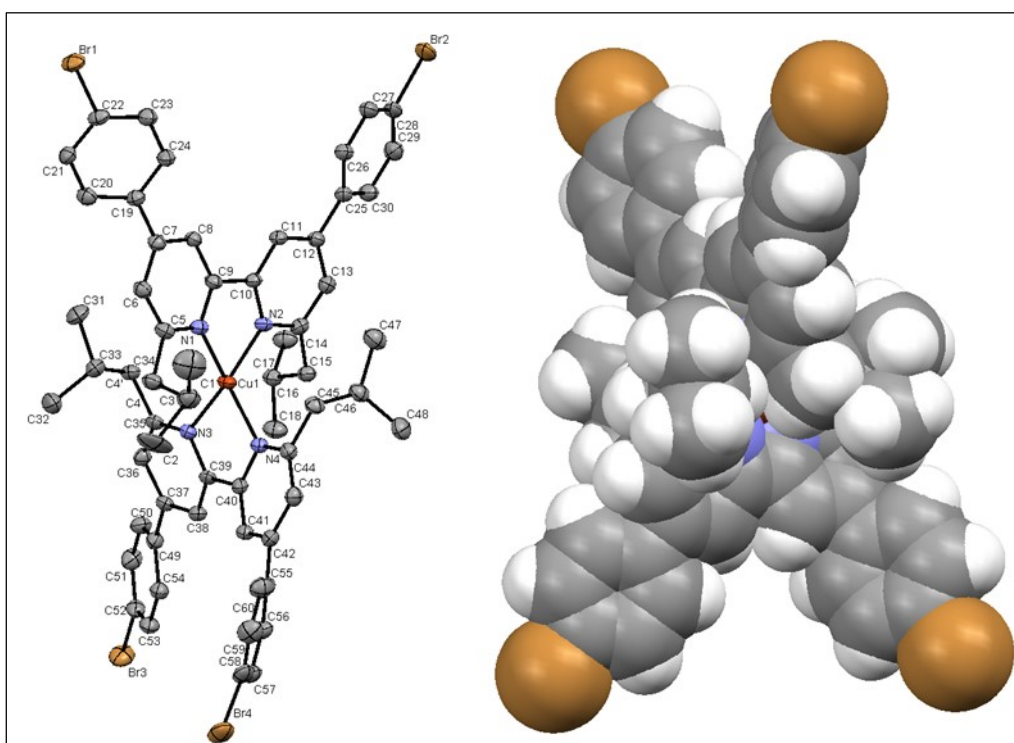
*Figure 53: ORTEP diagram of the [Cu(**L1.3**)₂]⁺ cation. H atoms are omitted and ellipsoids plotted at 50% probability level (left). Space filling representation of the [Cu(**L1.3**)₂]⁺ cation (right).*

The distorted tetrahedral coordination environment is similar to those in 2{[Cu(**L1.1**)₂][PF₆]}·3Me₂CO and [Cu(**L1.2**)₂][PF₆]; the angle between the least squares planes containing Cu1 and each bpy unit is 82.9°. However, one bpy unit in [Cu(**L1.3**)₂]⁺ is

significantly more twisted than in the complexes containing **L1.1** and **L1.2**. The angles between the planes of the pyridyl rings with N1/N2 and N3/N4 are 12.3 and 29.0° respectively. This is probably a consequence of steric hindrance arising from the isobutyl groups. The isobutyl group containing C1 and C2 is disordered and has been modelled over two positions with site occupancies of 0.59 and 0.41; the carbon atom of the CH_2 group is common to both positions. The distortion of the ligand containing N3 and N4 extends to the bromophenyl unit with Br4 and the phenylpyridine unit is significantly bowed.

5.4.6   C1.4 ≡ [Cu(L1.4)₂][PF₆]

Crystals of $[Cu(\textbf{L1.4})_2][PF_6]$ were obtained by Et_2O diffusion into an acetone/chloroform solution of the complex. The structure of the complex cation $[Cu(\textbf{L1.4})_2]^+$ is shown in Figure 54. For **C1.4**, only preliminary data were obtained.

Crystallographic data:

$C_{68}H_{76}Br_4CuF_6N_4P$, $M = 1477.45$, $a = 17.2042(17)$, $b = 17.4508(17)$, $c = 21.958(2)$ Å, $\alpha = 90.00$, $\beta = 114.893(2)$, $\gamma = 90.00°$, $U = 6581.2(11)$ Å^3, $Z = 4$, $D_c = 1.491$ Mg m^{-3}, μ(Cu-Kα) = 4.035 mm^{-1}, $T = 123$ K. Total 11598 reflections, 11598 unique, $R_{int} = 0.0884$. Refinement of 9139 reflections (762 parameters) with 2σ (I) converged at final $R_1 = 0.1664$ (R_1 all data = 0.1879), $wR_2 = 0.4559$ (wR_2 all data = 0.4733), gof = 1.070.

Bond distances:

Cu1–N1 = 2.04(1), Cu1–N2 = 2.014(9), Cu1–N3 = 2.04(1), Cu1–N4 = 2.01(1) Å.

Selected angles:

N1–Cu1–N2 = 82.9(4), N1–Cu1–N3 = 123.1(4), N1–Cu1–N4 = 124.7(4), N2–Cu1–N3 = 126.6(4), N2–Cu1–N4 = 124.5(4), N3–Cu1–N4 = 81.2(4) °.
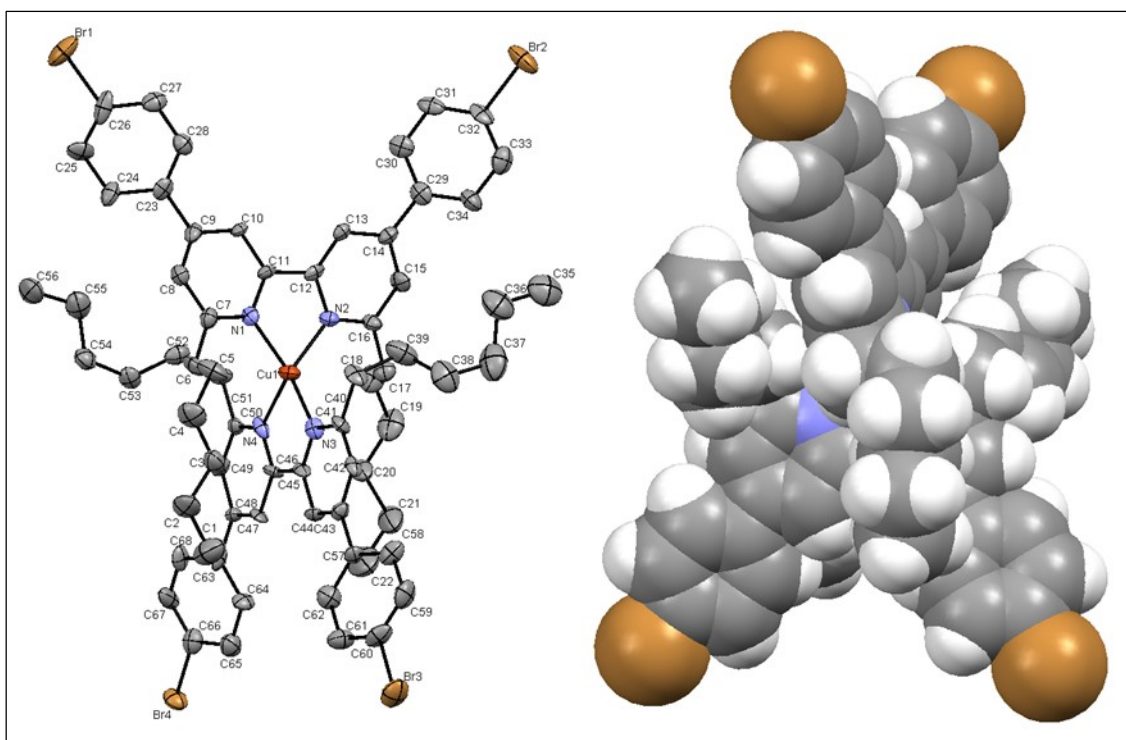
*Figure 54: ORTEP diagram of the [Cu(**L1.4**)$_2$]$^+$ cation. H atoms are omitted and ellipsoids plotted at 50% probability level (left). Space filling representation of the [Cu(**L1.4**)$_2$]$^+$ cation (right).*

The distorted tetrahedral coordination environment in [Cu(**L1.4**)$_2$]$^+$ between the least squares planes containing Cu1 and each bpy unit is 89.73°. The angles between the planes of the pyridyl rings with N1/N2 and N3/N4 are 20.3 and 4.53°, respectively.

5.4.7   C1.5 ≡ [Cu(L1.5)$_2$][PF$_6$]

Crystals of 2{[Cu(**L1.5**)$_2$][PF$_6$]}·CH$_2$Cl$_2$ were obtained by Et$_2$O diffusion into a CH$_2$Cl$_2$ solution of the complex. The structure of the complex cation [Cu(**L1.5**)$_2$]$^+$ is shown in Figure 55.

Crystallographic data:

C$_{69}$H$_{46}$Br$_4$Cl$_2$CuF$_6$N$_4$P, M = 1530.12, yellow plate, orthorhombic, space group *Pbcn*, a = 7.5560(15), b = 28.392(7), c = 27.854(6) Å, U = 5976(2) Å^3, Z = 4, D_c = 1.701 Mg m^{-3}, μ(Cu-Kα) = 5.284 mm^{-1}, T = 123 K. Total 37392 reflections, 5233 unique, R_{int} = 0.318. Refinement of 1637 reflections (395 parameters) with $I > 2\sigma$ (I) converged at final R_1 = 0.0825 (R_1 all data = 0.2739), wR_2 = 0.1280 (wR_2 all data = 0.1881), gof = 0.933. CCDC 942071.

Bond distances:

Cu1–N1 = 2.013(6), Cu1–N2 = 2.018(6), Br1–C15 = 1.893(9), Br2–C32 = 1.892(9) Å.

Selected angles:

N1–Cu1–N1^i = 83.6(2), N2^i–Cu1–N2 = 81.9(2), N1–Cu1–N2^i = 138.5(2), N1–Cu1–N2 = 112.1(2)°.
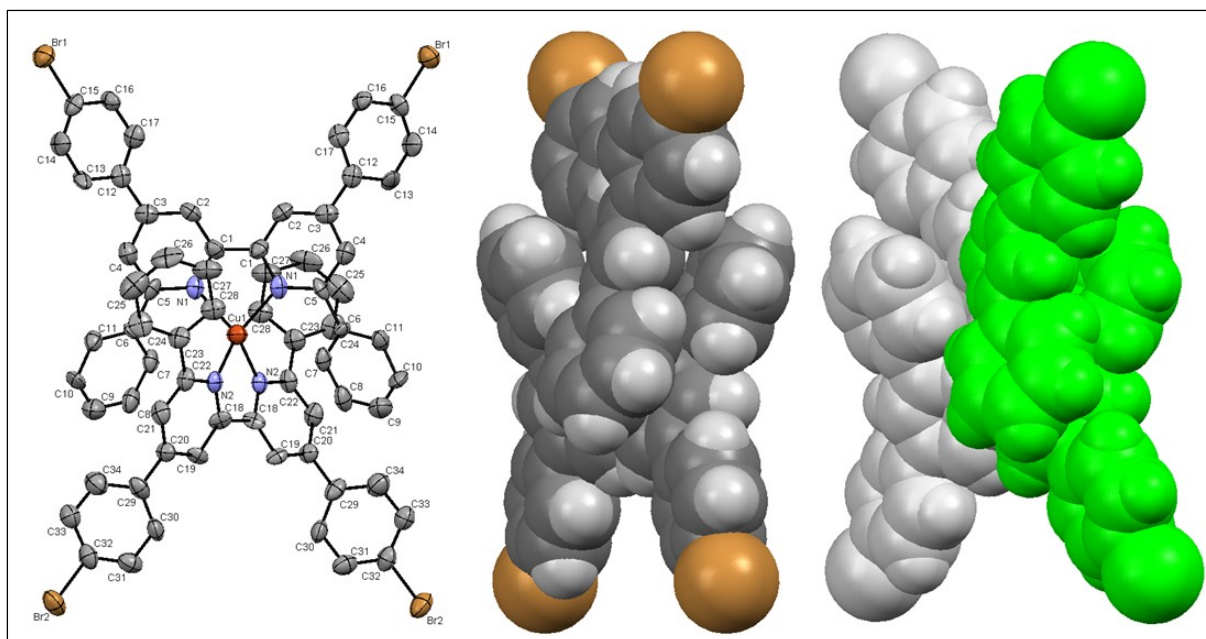
*Figure 55: ORTEP diagram of the [Cu(**L1.5**)$_2$]$^+$ cation. H atoms are omitted and ellipsoids plotted at 50% probability level (left). Space filling representation of the [Cu(**L1.5**)$_2$]$^+$ cation (middle)and symmetry in the crystal (right).*

The complex crystallizes in the orthorhombic space group *Pbcn* with the central atom Cu1 lying on a two-fold axis. In contrast to the other complexes, the [Cu(**L1.5**)$_2$]$^+$ cation has a flattened structure with an angle between the least squares planes containing Cu1 and each bpy unit of only 44.1°. This flattened structure arises from the π-stacking interaction between the phenyl-substituents and a pyridine ring of the nearby ligand. These interactions are obtained by twisting

the bipyridine core domains out of planarity (19.6 and 30.3º, respectively) and each phenyl ring screws (31.2 and 62.4º) with respect to the pyridine ring to which it is bonded.

The properties of the crystal $[Cu(\mathbf{L1.5})_2]^+$ are consistent with the observed flattened structures for $[Cu(6,6'\text{-}Ph_2bpy)_2]^+$, $[Cu(2,9\text{-}Ph_2phen)_2]^+$ and other similar complexes[120][172][173][174][175][165][176][177][178][179][180][181][182][183][184].

Chapter I: the effect of the anchoring ligand upon device performance

I   Evaluating the optimal anchoring ligand

In this chapter anchoring ligands (**ALC**, **ALC1**, **ALP** and **ALP1**) and ancillary ligands (**L2.1** and **L3.1**) were incorporated into DSCs. The main interest was to see whether there was a difference in device performance which could be related to the introduction of these four different anchoring ligands.
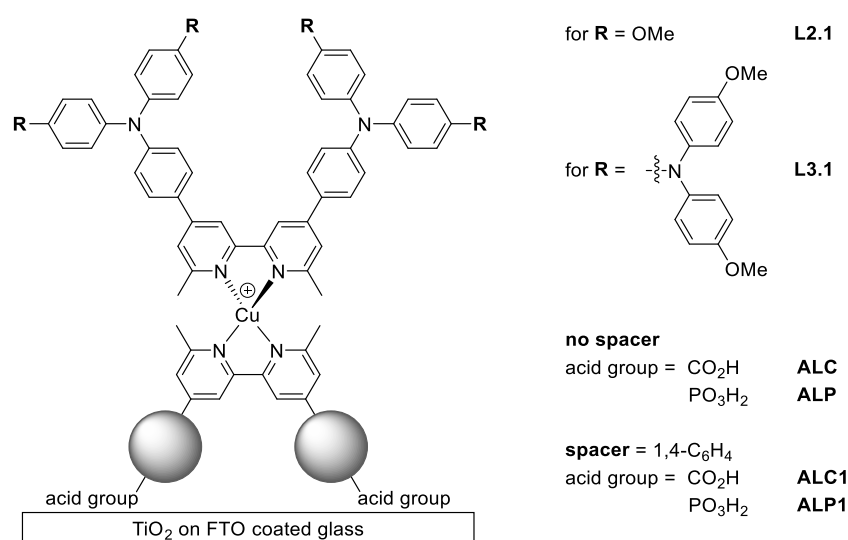
*Scheme 12: Schematic representation of dyes. Anchoring ligands (**ALC, ALC1, ALP** and **ALP1**) and ancillary ligands **L2.1** and **L3.1** studied in this chapter.*

Along with the influence of different anchoring ligands upon device performance, the effect of extending the light harvesting backbone of the ancillary ligand (*e.g.* on going from **L2.1** to **L3.1**) was studied. **L2.1** and **L3.1** were introduced via their *homoleptic* copper(I) complexes ([Cu(**L2.1/L3.1**)$_2$][PF$_6$]) and served as representative examples of capping ligands. In a later stage of these studies, a set of their derivatives was analysed further (see chapter V).

I.1   Anchoring Ligands

In the beginning of this research project, the question arose which anchoring ligands see (Scheme 13), would yield the highest global efficiency. This is based upon earlier work of Hernandez Redondo[185], who synthesised and characterised the anchoring ligands (**ALC**, **ALC1** and **ALP**) shown in Scheme 13 during her Ph.D. studies in the Constable-Housecroft-research group. Additionally, one new anchoring ligand was synthesised by Fürer and Wright [166][186] during the time of this project in the Constable-Housecroft-research group.
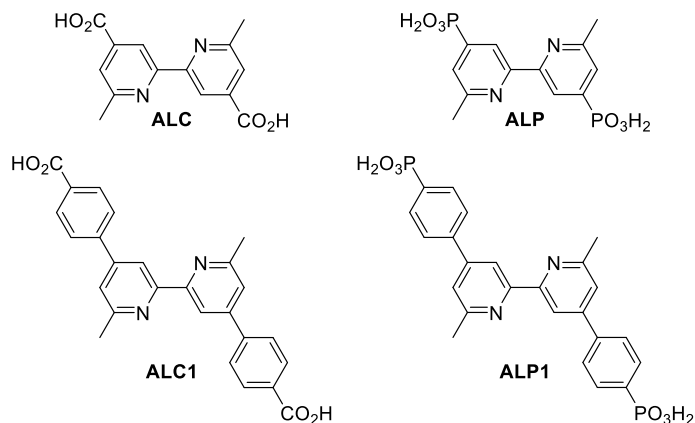
*Scheme 13: Anchoring ligands. **ALC, ALC1 and ALP** were synthesized as earlier reported* [185][187][188]. ***ALP1** was prepared as described by Fürer and Wright*[166][186].

There are two main differences between these four anchoring ligands (Scheme 13).

1. Functional groups: **ALC** and **ALP** differ in the functional groups at the 4,4'-positions of the pyridine rings. Whereas **ALC** bears carboxylic acids, **ALP** is substituted with phosphonic acids. **ALC1** and **ALP1** differ in their acid functionalities. While **ALC1** is substituted with a carboxylic acid in the 4-position at the phenylene ring, in **APL1** the carboxylic acid is replaced by a phosphonic acid.

2. Structural differences: The main structural difference between **ALC** and **ALC1**, and between **ALP** and **ALP1** is the additional phenyl-spacer in **ALC1** and **ALP1** in the 4,4'-positions of the bipyridine unit.

These structural and functional variances lead to the abbreviations of these four anchoring ligands (Scheme 13) used in this work.

- **ALC**: anchoring ligand with carboxylic acids.
- **ALP**: anchoring ligand with phosphonic acids.
- **ALC1**: anchoring ligand with carboxylic acids and a phenylene spacer.
- **ALP1**: anchoring ligand with phosphonic acids and a phenylene spacer.

I.2 DSC performances: finding the optimal anchoring ligand

Table 5 summarizes the performance characteristics resulting from incorporating *homoleptic* copper(I) complexes ([Cu(**L2.1**)$_2$][PF$_6$] and [Cu(**L3.1**)$_2$][PF$_6$]) in dye sensitized solar cells. The light to power conversion efficiency of each cell was measured under illumination of 100 mW/cm^2 (1 sun) 1, 3 and 6 days after assembling the DSCs. All cells were measured under the same conditions with respect to **N719**, which is set to η = 100% to allow an assessment of relative efficiencies.

dye	day	J_{sc} [mA/cm^2]	V_{oc} [mV]	ff [%]	η [%]	rel. η [%]	dye	J_{sc} [mA/cm^2]	V_{oc} [mV]	ff [%]	η [%]	rel. η [%]
[Cu(**L2.1**)(**ALC**)]$^+$	1	0.77	419	67.21	0.22	2.1	[Cu(**L3.1**)(**ALC**)]$^+$	0.89	416	65.53	0.24	2.4
[Cu(**L2.1**)(**ALC1**)]$^+$	1	2.74	499	71.76	0.98	9.7	[Cu(**L3.1**)(**ALC1**)]$^+$	4.19	534	69.61	1.56	15.4
[Cu(**L2.1**)(**ALP**)]$^+$	1	4.56	555	70.29	1.78	17.5	[Cu(**L3.1**)(**ALP**)]$^+$	5.25	578	66.00	2.02	19.9
[Cu(**L2.1**)(**ALP1**)]$^+$	1	6.13	568	56.40	1.97	19.4	[Cu(**L3.1**)(**ALP1**)]$^+$	4.89	558	61.91	1.69	16.7
N719	1	23.69	721	59.34	10.14	100.0	**N719**	23.69	721	59.34	10.14	100.0
[Cu(**L2.1**)(**ALC**)]$^+$	3	0.93	416	68.86	0.27	2.4	[Cu(**L3.1**)(**ALC**)]$^+$	1.15	428	68.49	0.34	3.1
[Cu(**L2.1**)(**ALC1**)]$^+$	3	2.90	496	71.51	1.03	9.5	[Cu(**L3.1**)(**ALC1**)]$^+$	4.56	530	69.73	1.69	15.5
[Cu(**L2.1**)(**ALP**)]$^+$	3	5.59	546	70.40	2.15	19.7	[Cu(**L3.1**)(**ALP**)]$^+$	6.62	580	65.00	2.51	23.1
[Cu(**L2.1**)(**ALP1**)]$^+$	2	6.28	560	67.62	2.38	21.8	[Cu(**L3.1**)(**ALP1**)]$^+$	7.27	568	65.40	2.70	24.8
N719	3	22.91	776	61.23	10.89	100.0	**N719**	22.91	776	61.23	10.89	100.0
[Cu(**L2.1**)(**ALC**)]$^+$	6	0.93	422	69.00	0.27	2.5	[Cu(**L3.1**)(**ALC**)]$^+$	1.19	435	69.00	0.36	3.3
[Cu(**L2.1**)(**ALC1**)]$^+$	6	2.74	500	72.00	0.99	9.1	[Cu(**L3.1**)(**ALC1**)]$^+$	4.45	535	70.00	1.67	15.3
[Cu(**L2.1**)(**ALP**)]$^+$	6	5.49	551	71.00	2.14	19.6	[Cu(**L3.1**)(**ALP**)]+	6.74	585	66.00	2.61	23.9
[Cu(**L2.1**)(**ALP1**)]$^+$	6	6.63	563	68.90	2.57	23.5	[Cu(**L3.1**)(**ALP1**)]$^+$	7.72	583	66.20	2.98	27.3
N719	6	22.69	785	61.00	10.93	100.0	**N719**	22.69	785	61.00	10.93	100.0

*Table 5: DSC performance parameters for [Cu(**L2.1**)(**AL**)]$^+$, [Cu(**L3.1**)(**AL**)]$^+$, where **AL** = **ALC, ALC1, ALP & ALP1**.*

From the results shown in Table 5, trends concerning the anchoring ligands, ancillary ligands and age of the device arise.

I.2.1 DSC performances comparing anchoring ligands
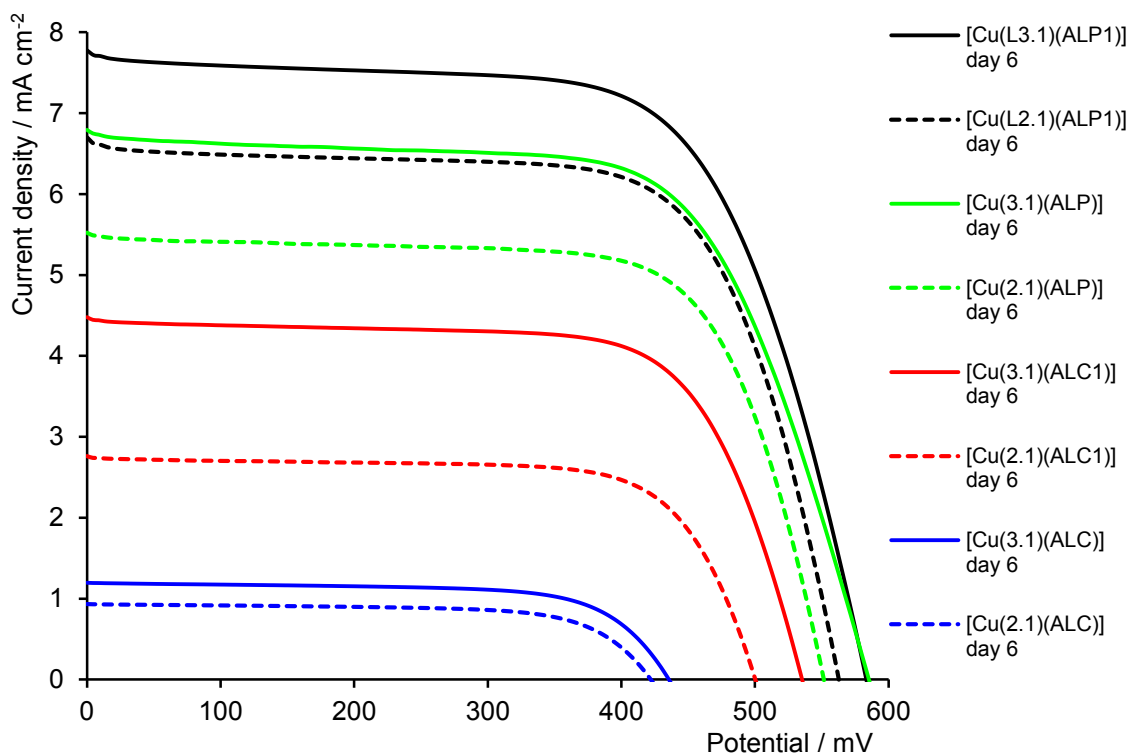
*Figure 56: Current density-voltage curves for DSCs in which the sensitizer is assembled from [Cu(**L2.1**)$_2$][PF$_6$] and [Cu(**L3.1**)$_2$][PF$_6$] using four different anchoring ligands (**ALC**, **ALC1**, **ALP** and **ALP1**). Six days after sealing.*

Dyes where **ALC** is present as the anchoring unit exhibit in all cases the lowest efficiency due to their *Voc* and *Jsc* being much lower than the other dyes (Figure 56). The addition of a phenylene spacer to the anchoring group in the 4,4'-positions (*i.e.* replacing **ALC** by **ALC1**) leads to a very significant increase in global efficiency from 0.27% to 0.99% on day 6 for [Cu(**L2.1**)(**ALC**)]$^+$ and [Cu(**L2.1**)(**ALC1**)]$^+$ and 0.36% to 1.67% for [Cu(**L3.1**)(**ALC**)]$^+$ and [Cu(**L3.1**)(**ALC1**)]$^+$, respectively. By replacing the carboxylic acids with phosphonic acids (*i.e.* substitution of **ALC** and **ALC1** with **ALP**) leads to even more distinct rise in *Voc* and *Jsc* and yields an even higher efficiency. This is consistent with the literature [134][189][76], indicating phosphonate anchors perform better than carboxylate ones. By supplying **ALP** with a phenylene spacer, *i.e.* going from **ALP** to **ALP1**, a final additional increase in *Voc* and *Jsc* can be achieved. The dyes having **ALP1** incorporated as anchor yielded the highest efficiencies compared to the other three anchoring ligands.

I.2.2 Effect of the ancillary ligands on DSC performance
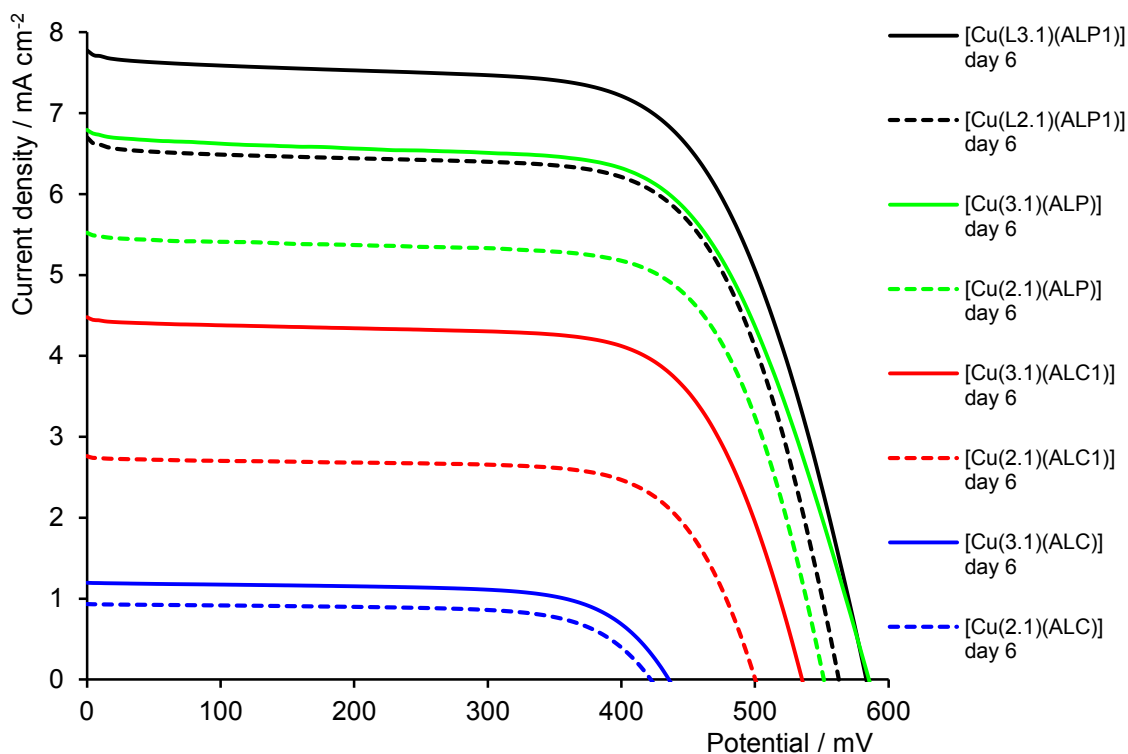
Figure 57: Current density-voltage curves for DSCs. Comparing [Cu(L2.1)$_2$][PF$_6$] and [Cu(L3.1)$_2$][PF$_6$] using four different anchoring ligands (ALC, ALC1, ALP and ALP1). Six days after sealing.

Concentrating on the ancillary ligands **L2.1** (Figure 57, dashed lines) and **L3.1** (Figure 57, solid lines) and comparing their corresponding active dyes in devices, assuming a similar dye loading on the surface, another important trend can be found. Independent of the anchoring ligand present in the dye, on going from [Cu(**L2.1**)(**AL**)]$^+$ to [Cu(**L3.1**)(**AL**)]$^+$ an increase in *Jsc* is observed as well as an increase in *Voc*. The global light to power conversion efficiency rises significantly with the incorporation of the more conjugated aryl-amine domain in the dye, due to their enhanced absorptivity.
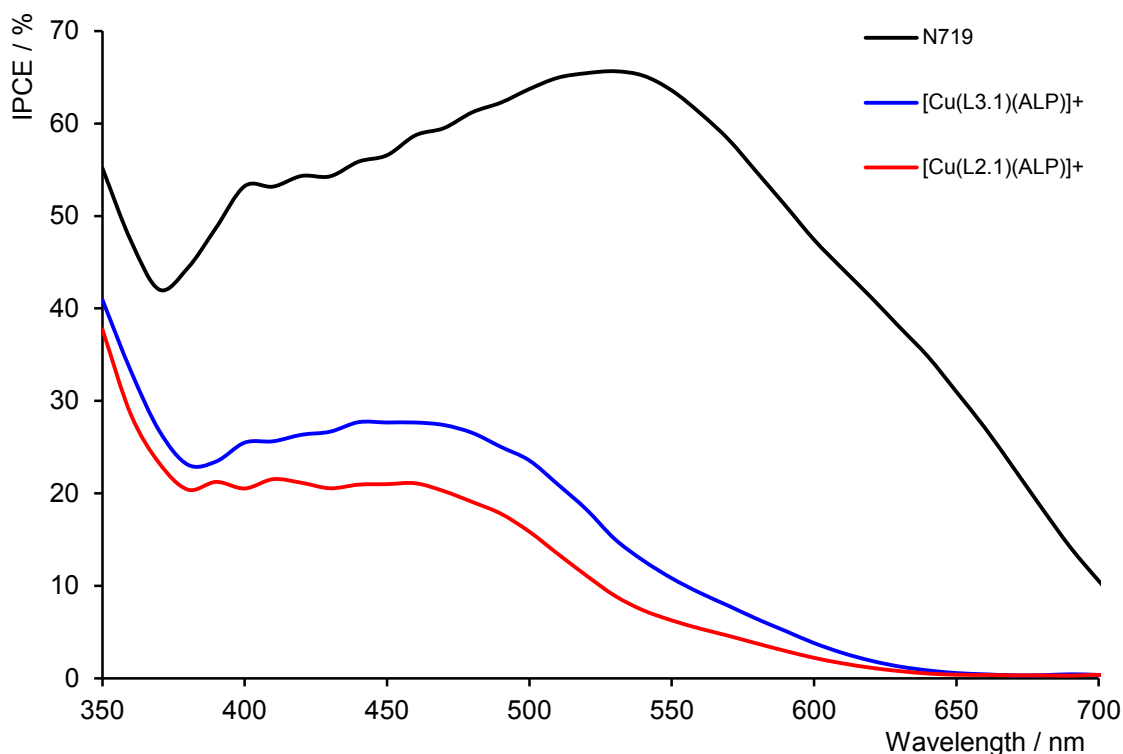
*Figure 58: IPCE measurements. A comparison of [Cu(**L2.1**)(**ALP**)]⁺ and [Cu(**L3.1**)(**ALP**)]⁺.*

Comparing the IPCE measurements of [Cu(**L2.1**)(**ALP**)]⁺ and [Cu(**L3.1**)(**ALP**)]⁺ (Figure 58) we see the curves exhibit the same shape and have their λ_{max} at about 460 nm. However, while [Cu(**L2.1**)(**ALP**)]⁺ shows an injection efficiency of about 21% (at 460 nm), [Cu(**L3.1**)(**ALP**)]⁺ shows an increased injection efficiency over the whole spectrum. This indicates that more photons are absorbed and converted to electrical power by using [Cu(**L3.1**)(**ALP**)]⁺ and the device therefore exhibits a higher *Jsc* and efficiency.

The observed *Jsc* values for [Cu(**L2.1**)(**ALP**)]⁺ and [Cu(**L3.1**)(**ALP**)]⁺ on day 6 (Table 5) of 5.49 and 6.75 mA cm⁻², respectively, are consistent with the measured IPCE curves.

I.2.3   Ripening effect: rising efficiency over time
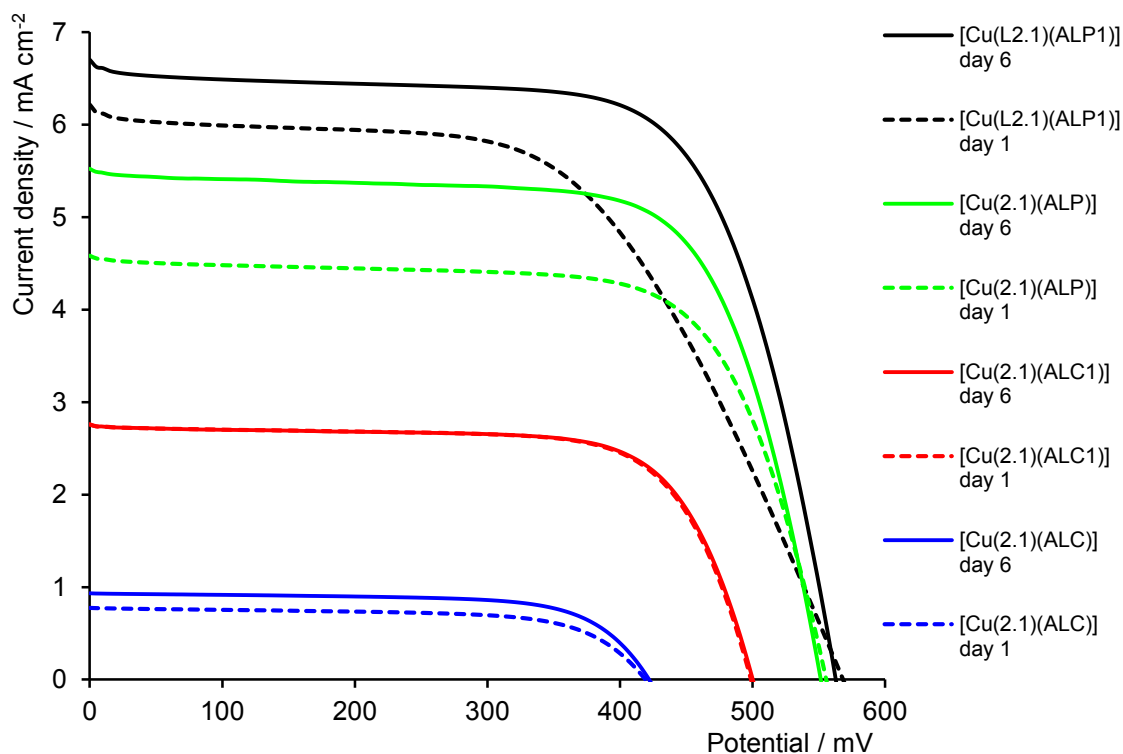
*Figure 59: Current density-voltage curves for DSCs in which the sensitizer is assembled from [Cu(**L2.1**)₂][PF₆] using four different anchoring ligands (**ALC, ALC1, ALP** and **ALP1**).*

In this series, an improvement of each dye over time is observed. Table 5 shows that η increases with time. This is consistent with previous observations from our research group for copper(I) DSCs[160][190]. The preliminary increase is possibly related to reorganization and/or de-aggregation of dye molecules on the semiconductor surface [191][192][193]. In all cases except one ([Cu(**L2.1**)(**ALC1**)]⁺), a clear rise in *Jsc* is observed going from day 1 to day 6. Additionally *Voc* does not seem to be affected and stays more or less constant over this period of time. Furthermore, a clear difference in ripening over time can be seen by comparing **ALC** and **ALC1** with **ALP** and **ALP1** (Figure 59). While devices containing **ALC** and **ALC1** only slightly gain in *Jsc*, cells with **ALP** and **ALP1** show a much higher improvement in *Jsc* over time and an even higher efficiency on day 6 compared to day 1.

I.3   Avoiding absorbance of scattered and diffuse light in DSCs

In 2006 Grätzel[194] and in 2012 Snaith[195] highlighted the importance of masking dye sensitized solar cells during the measurements in order to obtain trustworthy results. Due to the structural properties of DSCs, such as a glass-glass interface, the light source will never be perfectly linear and this leads to more light absorbed on TiO_2 than expected. One of the points one has to assume is that light which collides with the glass edges is scattered between the two electrodes and finally absorbed by the dye in TiO_2.
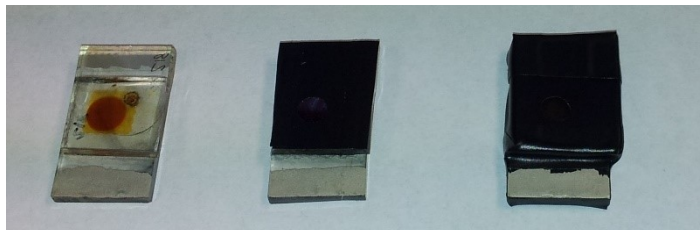
Figure 60: DSCs with different masking configurations.
From left to right: Not masked, top-masked and completely masked

Other reflecting surfaces and edges besides those of the device alone scatter light back into the device, resulting in additional absorption by the dye-sensitized semiconductor. If these reflecting parts are near or even underneath the device, their influence contributes strongly to the perceived performance of the device.
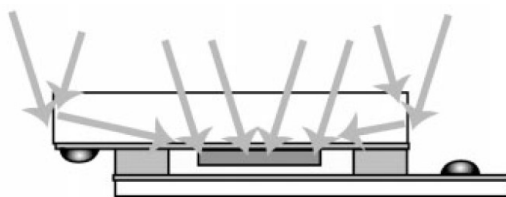
Figure 61:Light collection in a DSC without masking.[194]

Therefore, measuring cells without applying a shading mask leads to a false assessment of performance due to too high measured efficiencies.

The very high short circuit current densities measured for **N719** (Table 5) are a clear indication that the use of unmasked cells show the effect of the coabsorbance of scattered light. By not masking the cells, the final efficiencies are overestimated. Therefore the same cells were measured again using masked DSCs. The performances of cells which were top-masked and fully masked were measured and the performance parameters are shown in Table 6 and Table 7 along with data of the same, unmasked cells. A representative current density-voltage plot is shown in Figure 62 presenting the influence of applying different masks to DSCs.

I.3.1   DSC devices with applied masks

dye	day	J_{sc} [mA/cm²]	V_{oc} [mV]	ff [%]	η [%]	rel. η [%]	dye	J_{sc} [mA/cm²]	V_{oc} [mV]	ff [%]	η [%]	rel. η [%]
not masked							**not masked**					
[Cu(**L2.1**)(**ALC**)]⁺	47	0.72	442	71.00	0.23	2.3	[Cu(**L3.1**)(**ALC**)]⁺	0.97	475	71.00	0.33	3.3
[Cu(**L2.1**)(**ALC1**)]⁺	47	1.69	551	75.00	0.70	7.1	[Cu(**L3.1**)(**ALC1**)]⁺	3.16	548	74.00	1.27	12.8
[Cu(**L2.1**)(**ALP**)]⁺	47	3.91	592	74.00	1.72	17.4	[Cu(**L3.1**)(**ALP**)]⁺	5.51	610	71.00	2.37	23.9
N719	47	18.33	806	67.01	9.90	100.0	**N719**	18.33	806	67.01	9.90	100.0
masked on top							**masked on top**					
[Cu(**L2.1**)(**ALC**)]⁺	47	0.66	408	69.00	0.19	1.9	[Cu(**L3.1**)(**ALC**)]⁺	0.95	445	71.00	0.30	3.0
[Cu(**L2.1**)(**ALC1**)]⁺	47	1.51	513	76.00	0.59	5.9	[Cu(**L3.1**)(**ALC1**)]⁺	2.79	514	75.00	1.07	10.7
[Cu(**L2.1**)(**ALP**)]⁺	47	3.53	558	75.00	1.48	14.9	[Cu(**L3.1**)(**ALP**)]⁺	5.32	573	73.00	2.22	22.3
N719	47	17.54	770	74.00	9.96	100.0	**N719**	17.54	770	74.00	9.96	100.0
completely masked							**completely masked**					
[Cu(**L2.1**)(**ALC**)]⁺	47	0.50	401	69.00	0.14	1.8	[Cu(**L3.1**)(**ALC**)]⁺	0.72	435	69.00	0.22	2.9
[Cu(**L2.1**)(**ALC1**)]⁺	47	1.16	508	76.00	0.45	5.9	[Cu(**L3.1**)(**ALC1**)]⁺	2.17	502	75.00	0.82	10.8
[Cu(**L2.1**)(**ALP**)]⁺	47	2.70	550	75.00	1.12	14.8	[Cu(**L3.1**)(**ALP**)]+	3.83	557	74.00	1.57	20.7
N719	47	13.72	747	74.00	7.57	100.0	**N719**	13.72	747	74.00	7.57	100.0

*Table 6: A comparison of not masked, top-masked and completely masked cells. DSC performance parameters for [Cu(**L2.1**)(**AL**)]⁺, [Cu(**L3.1**)(**AL**)]⁺, where **AL** = **ALC, ALC1, ALP**.*

Applying only a top mask to the devices, the current density decreases slightly on going from the unmasked to top-masked device. The open circuit voltage also decreases. The current density drops drastically on going from top-masked to completely masked devices. Here the open-circuit voltage also drops. More drastic than the slight decrease in open circuit voltage is the drop in short circuit current density, which is responsible for the reduced efficiencies. All cells show a high fill factor. Similar trends apply for **N719**. It is also important to note that the relative efficiencies of each cell, no matter if masked or not masked, stay approximately the same compared to **N719** (final column in Table 6).

dye	day	J_{sc} [mA/cm^2]	V_{oc} [mV]	ff [%]	η [%]	rel. η [%]	dye	J_{sc} [mA/cm^2]	V_{oc} [mV]	ff [%]	η [%]	rel. η [%]
not masked							**not masked**					
[Cu(**L2.1**)(**ALP1**)]$^+$	**2**	6.28	560	67.62	2.38	27.0	[Cu(**L3.1**)(**ALP1**)]$^+$	7.27	568	65.40	2.70	30.7
N719	**2**	20.49	732	58.72	8.80	100.0	**N719**	20.49	732	58.72	8.80	100.0
masked on top							**masked on top**					
[Cu(**L2.1**)(**ALP1**)]$^+$	**2**	4.79	541	67.78	1.75	23.4	[Cu(**L3.1**)(**ALP1**)]$^+$	5.19	547	67.36	1.91	25.6
N719	**2**	16.65	722	62.17	7.47	100.0	**N719**	16.65	722	62.17	7.47	100.0
completely masked							**completely masked**					
[Cu(**L2.1**)(**ALP1**)]$^+$	**2**	4.36	537	69.35	1.63	25.6	[Cu(**L3.1**)(**ALP1**)]$^+$	4.65	547	67.62	1.72	27.0
N719	**2**	14.18	712	62.97	6.36	100.0	**N719**	14.18	712	62.97	6.36	100.0

*Table 7: A comparison of not masked, top-masked and completely masked cells. DSC performance parameters for [Cu(**L2.1**)(**ALP1**)]$^+$ and [Cu(**L3.1**)(**ALP1**)]$^+$.*

For cells containing **ALP1** (Table 7), basically the same trends as for cells containing **ALC**, **ALC1** or **ALP** (Table 6) are observed. On going from unmasked to fully masked cells the factors defining the final global efficiency all decrease. While the open-circuit voltage is slightly lower in masked devices, the short circuit current density undergoes a much stronger decrease and is lowered by about 30% compared to its initial value. Also, the efficiencies lose about 30% of their initial values, which shows that current is the limiting factor. Their efficiencies relative to **N719** stay more or less constant.

Since data from Table 6 are on day 47 and data from Table 7 are on day 2, the ripening effect is not considered in the following comparison of devices bearing anchoring ligands **ALP** and **ALP1**. Comparing results from Table 6 with those from Table 7, the highest efficiencies are achieved using **ALP1** as anchoring ligand followed by **ALP**. The least efficient anchor seems to be **ALC** followed by **ALC1**. Another important observation is that on going from ancillary ligand **L2.1** to **L3.1**, there is an increase in *Jsc* and *Voc*. The rise in *Voc* is less significant than the improvement in *Jsc*. The fill factor stays more or less the same on going from **L2.1** to **L3.1** or drops slightly. The light to power conversion efficiency increases considerably using the larger and more conjugated domain in the dye.
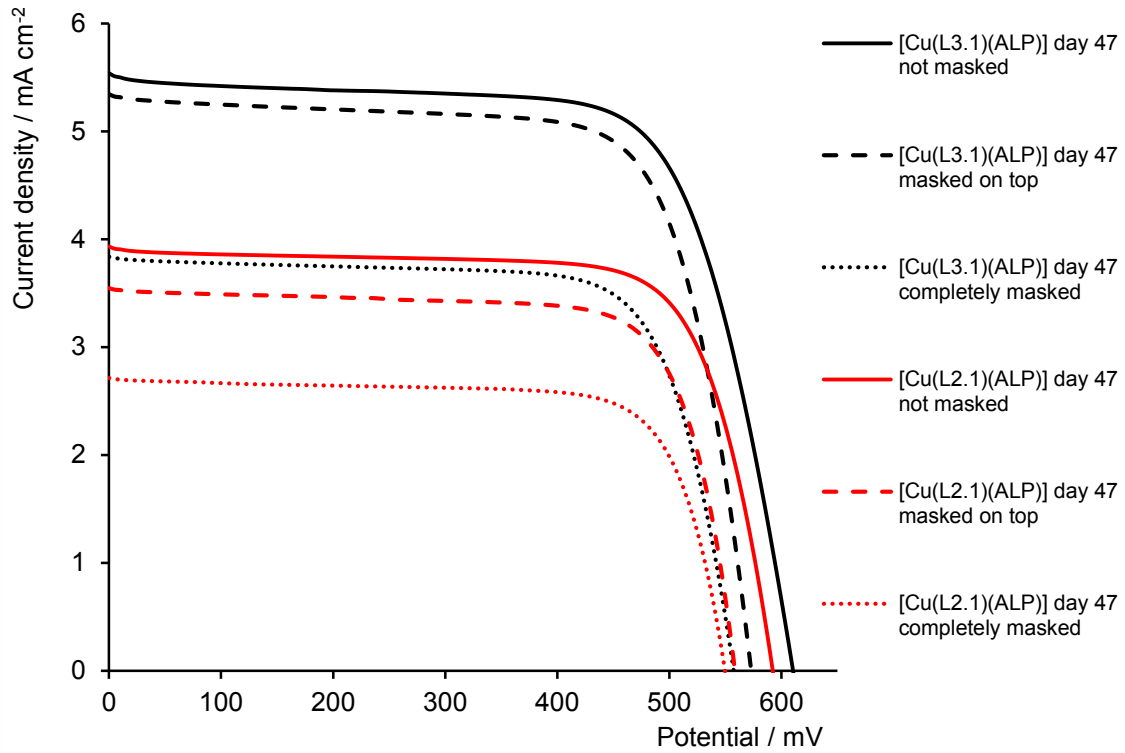
Figure 62: A representative picture of JV curves for unmasked, top-masked and fully masked DSCs.

In Figure 62, some representative parameters are shown that correspond to data in Table 6. In this graphical representation of [Cu(**L3.1**)(**ALP**)]$^+$ vs. [Cu(**L2.1**)(**ALP**)]$^+$ comparing different mask applications, the trends become even more obvious. [Cu(**L3.1**)(**ALP**)]$^+$ surpasses [Cu(**L2.1**)(**ALP**)]$^+$ in all cases. On going from an unmasked device to a top-masked device, *Jsc* drops only slightly. However on using a completely masked cell, *Jsc* drops drastically compared to its corresponding top-masked device. Additionally, the *Voc* is lowered, but not in such a severe manner.
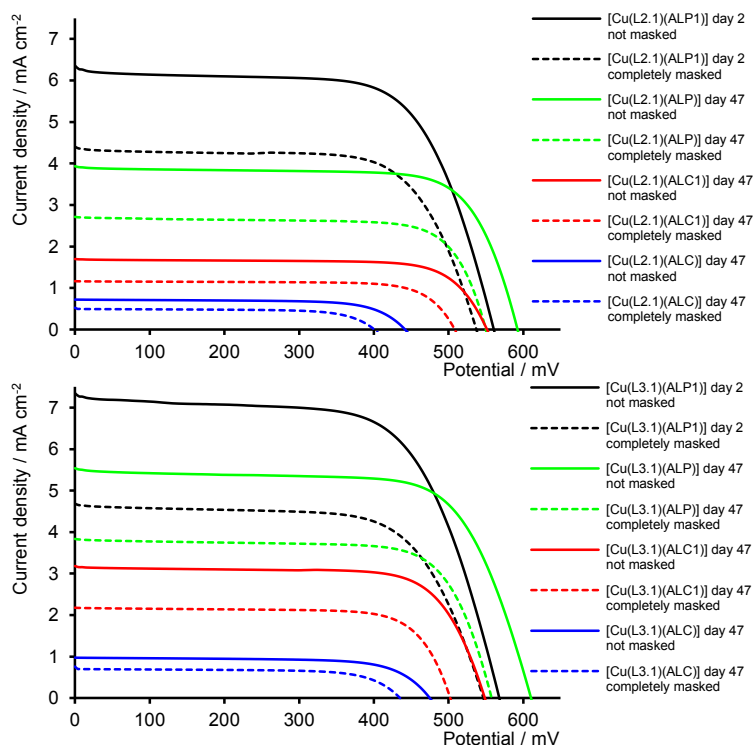
*Figure 63: Comparison of [Cu(**L2.1**)(AL)]⁺ with [Cu(**L3.1**)(AL)]⁺ applying no mask and fully masked conditions. **AL** = **ALC, ALC, ALP** and **ALP1**.*

Figure 63 compares the results from Table 6 and Table 7. Over all measurements, it is consistent that devices which had **ALC** implemented as anchoring ligand show the lowest *Jsc* and the poorest efficiency. Devices with **ALC1** show the second poorest *Jsc* and efficiency but clearly higher than dyes with **ALC** as anchoring unit. A huge improvement is made by replacing **ALC1** by **ALP** ending up with higher *Voc*, higher *Jsc* and higher efficiency. As **ALP** is substituted by **ALP1** in the cell architecture, a final increase is achieved in *Jsc* but not in *Voc*. Nevertheless dyes with **ALP1** show the highest efficiency than any other dyes with different anchoring ligands:

<div align="center">

ALP1 > ALP > ALC1 > ALC

</div>

Upon covering the DSCs with different masks, a stepwise reduction of *Jsc* and *Voc* was obtained. The loss in *Voc* was not as significant as the loss in *Jsc* for the global efficiency of the devices:

<div align="center">

unmasked > top masked > completely masked

</div>

Dyes which possess **L3.1** as ancillary ligand show a higher *Jsc* and higher efficiency than their corresponding dyes with **L2.1** and this is consistent over the whole series.

[Cu(**L3.1**)(AL)]⁺ > [Cu(**L2.1**)(AL)]⁺ where **AL** = **ALC, ALC1, ALP** or **ALP**.

I.4 Discussion

I.4.1 Anchoring ligands

The poorest efficiencies are obtained with anchoring ligand **ALC** (Table 5). Through comparing performances where the only difference is the anchoring ligand **ALC** vs. **ALP**, it can be observed that the low efficiencies of cells containing **ALC** do not arise from a steric hindrance resulting from the extended aromatic systems from ancillary ligands **L2.1** and **L3.1**. The enhanced performance on going from **ALC** to **ALC1** suggests that the introduction of a phenylene spacer in the 4,4'-positions of the bpy unit may give rise to improved electron injection and therefore result in a higher global efficiency. The observation of enhanced device performance on going from **ALC** to **ALC1** is consistent with the trend on going from **ALP** to **ALP1**. The findings that the introduction of a phenylene spacer in **ALP** improved the efficiency on going from **ALP** to **ALP1** confirms the suggestion that the phenylene spacer has a positive effect on the electron injection.

In this study, higher efficiencies are obtained with anchoring ligands which incorporate phosphonic acids as anchoring groups. These results are consistent with previous results [134][189] of our research group where phosphonic acid anchors show improved adsorption properties on TiO$_2$ compared to their carboxylic analogues. Furthermore, these results are supported by Grätzel et al.[76], who show phosphonic acids have enhanced adsorption on TiO$_2$ compared to carboxylic acids and thereby provide the excited dye with an improved light induced charge separation.

I.4.2 Ancillary ligands

On comparing devices where the only variable is the ancillary ligand (going from [Cu(**ALP**)(**L2.1**)]$^+$ to [Cu(**ALP**)(**L3.1**)]$^+$), the power conversion efficiency increases significantly due to more photons being absorbed per molecule with the incorporation of the more conjugated light harvesting domain. This is also confirmed by the IPCE measurements (Figure 58) where [Cu(**ALP**)(**L3.1**)]$^+$ shows a higher incident photon-to-current conversion efficiency over the whole spectrum compared to [Cu(**ALP**)(**L2.1**)]$^+$.

I.4.3 Ripening effect

The results from Table 5 clearly show that the device performance increases over time and gives the highest efficiencies after roughly one week. This observation is confirmed by earlier results for copper(I) DSCs of our research group[160][190]. Grätzel and co-workers described similar observations for Ru(II) based DSCs[192]. In the case of the lower efficiencies at the beginning

of the measurements (*e.g.* one day after sealing the cells), a reductive self-quenching of aggregated dye molecules on the TiO_2 surface is the most likely explanation. Over time, a de-aggregation or reorganisation of dye molecules on the semiconductor surface may take place, which leads to enhanced electron injection and improved efficiency. Grätzel also showed that the use of a more dilute dye solution leads to less aggregation of dye molecules on the surface and a higher initial efficiency. However, this also gives a lower surface coverage[192]. The dye concentration is addressed at a later stage of this work.

I.4.4 Cell measurements with masked cells

As can be seen from Table 6 and Table 7, the effect of applying an appropriate mask to devices while measuring drastically reduces their measured absolute efficiencies. This leads to the conclusion that the silicon reference cell is not able to profit from scattered or diffuse light in the same way that the copper(I)-DSCs do. In other words, by using a silicon reference cell the sun simulator is not calibrated correctly while measuring unmasked cells.

$$\eta_{global} = (I_{ph} \cdot V_{oc} \cdot ff) / I_s$$

Equation 2: Definition of the overall efficiency (η_{global}).

I_{ph} (the integral photocurrent density)

V_{oc} (open-circuit voltage)

ff (fill factor)

I_s (intensity of the incident light $I_s = 1000$ W m^{-2})

Consulting Equation 2, it becomes clear why it is important to measure cells with a mask, which prevents scattered light from reaching the sensitizer. Once the instrument is calibrated so that $I_s = 1000$ Wm^{-2} with the use of a Si-reference cell, the device's efficiencies are being calculated without the contribution of diffuse/scattered light to I_s. However, as soon as unmasked DSCs are measured, scattered light contributes to I_s and the real I_s is now >1000 W m^{-2}.

I.5   Conclusion

A comparison of anchoring **ALC**, **ALC1**, **ALP** and **ALP1** ligands showed that devices which incorporate phosphonic acids as anchoring units perform much better than corresponding DSCs with carboxylic acid anchoring domains. In this set of four anchoring ligands, devices with **ALP1** yielded the highest efficiencies. Therefore it is concluded that the of use **ALP1** as anchoring unit for further investigations is the best choice out of this series of anchors for screening of ancillary ligands/active dyes in DSCs.

Furthermore it has been shown that extending the aryl-system in the ancillary ligand (*e.g.* on going from [Cu(**ALP**)(**L2.1**)]$^+$ to [Cu(**ALP**)(**L3.1**)]$^+$) leads to enhanced device performance due to better photon absorption.

Additionally the absolute importance of the appropriate masking of DSCs in order to obtain non overestimated efficiencies has been demonstrated. Future measurements of new dyes in DSCs must be done under masked conditions to obtain reliable results.

I.6   Solar cell fabrication and characterisation I

DSCs were prepared adapting the method of Grätzel and coworkers[196][197]. The TiO$_2$ paste was prepared following the published method with adaptations: a porcelain (in place of alumina) mortar, sonicator bath (in place of an ultrasonic horn), and terpineol (CAS: 8000-41-7, in place of α-terpineol). Each working electrode was prepared from an FTO glass plate (Solaronix TCO22-7, 2.2 mm thickness, sheet resistance ≈7 Ω square^{-1}), which was cleaned by sonicating in Hellmanex® surfactant (2% in milliQ water), and rinsed with milliQ water and EtOH. After a surface activation in a UV-O$_3$ system (Model 256-220, Jelight Company Inc) for 20 min, the FTO plates were immersed in aqueous TiCl$_4$ solution (40 mmol dm^{-3}) at 70 ºC for 30 min, and then washed with milliQ water and EtOH. The FTO plate was dried and a layer of TiO$_2$ paste was screen printed (90T, Serilith AG, Switzerland). The printed plate was kept in an EtOH chamber for 3 min to reduce surface irregularities of the printed layer and dried for 6 min at 125 ºC on a heating plate. The screen printing process was repeated 6 times and then the electrodes were gradually heated at 75 °C for 30 min, at 135 °C for 15 min, at 325 °C for 5 min, at 375 °C for 5 min, at 450 °C for 15 min and at 500 °C for 15 min. After the final sintering, the thickness of the TiO$_2$ layer was 12 μm (measured with Tencor Alpha-Step 500 profilometer). The annealed TiO$_2$ film was post-treated with 40 mM aqueous TiCl$_4$ solution (see above), rinsed with milliQ water and EtOH and sintered at 500 ºC for 30 min. The electrodes were cooled to ca. 80 ºC and immersed in a 1 mM DMSO solution of the anchoring ligand **ALC**, **ALC1**, **ALP** or **ALP1** for 20 h. The colourless electrode was removed from the solution, washed with DMSO and EtOH and dried under a stream of N$_2$. The electrode with adsorbed anchoring ligand was immersed in a 1 mM CH$_2$Cl$_2$ solution of [Cu(**L2.1**)$_2$][PF$_6$] or [Cu(**L3.1**)$_2$][PF$_6$] for 20 h, and during this time, the electrodes turned red-orange. The electrodes were removed from the solution and were washed with CH$_2$Cl$_2$ and dried under a stream of N$_2$. Each counter electrode was prepared from an FTO glass plate (Solaronix TCO22-7, 2.2 mm thickness, sheet resistance ≈7 Ω square^{-1}) with a previously drilled hole. Residual organic impurities were removed by heating for 15 min at 500 ºC on a heating plate and the perforated plate was washed with water, then 0.1 M HCl solution in EtOH and finally ultrasonicated in an acetone bath for 10 min. It was dried on the heating plate at 500 °C for 15 min. The Pt catalyst was deposited on the FTO glass plate by coating with Platisol T (2 × 10.0 μL), obtained from Solaronix SA, and dried on a heating plate at 500 °C for 15 min.

The dye-covered TiO$_2$ electrode and Pt counter-electrode were assembled using thermoplast hot-melt sealing foil (Solaronix, Meltonix 1170-25 Series, 25 microns thick) by heating while pressing them together. The electrolyte was comprised of LiI (0.1 mol dm^{-3}), I$_2$ (0.05 mol dm^{-3}), 1- methylbenzimidazole (0.5 mol dm^{-3}) and 1-butyl-3-methylimidazolinium iodide (0.6 mol dm^{-3}) in 3-methoxypropionitrile, and was introduced into the cell by vacuum backfilling. The hole on the counter electrode was finally sealed using the hot-melt sealing foil and a cover glass. The solar cell measurements and testing protocol were performed using unmasked, top-masked and fully masked cells. Opaque black tape was used for masking with a single aperture of area 0.126 cm^2 placed over the screen printed dye-sensitized TiO$_2$ circle (see Figure 64). The holes were punched manually using a 4 mm diameter punch tool (MEKANO). The area of the aperture in the mask was smaller than the active area of the dye-sensitized TiO$_2$ dot (0.288 cm^2).
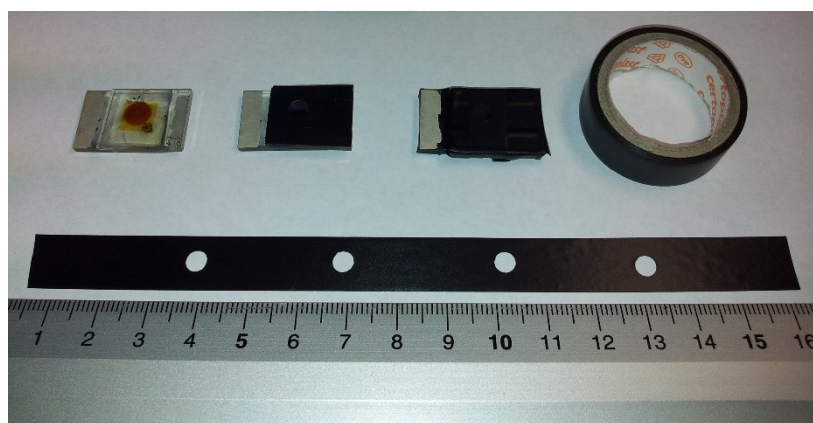
Figure 64: Unmasked, top-masked and completely masked DSC.

For complete masking, tape was also applied over the edges and rear of cell.

Current density-voltage (*JV*) measurements were made by irradiating from behind using a light source SolarSim 150 (100 mW cm^{-2} = 1 sun). The power of the simulated light was calibrated by using a reference Si photodiode. The standard dye N719 was purchased from Solaronix.

The quantum efficiency measurements were performed on a Spe-Quest quantum efficiency setup from Rera Systems (Netherlands) equipped with a 100 W halogen lamp (QTH) and a lambda 300 grating monochromator from Lot Oriel. The monochromatic light was modulated to 3 Hz using a chopper wheel from ThorLabs. The cell response was amplified with a large dynamic range IV converter from CVI Melles Griot and then measured with a SR830 DSP Lock-In amplifier from Stanford Research.

CHAPTER II: THE INFLUENCE OF DIFFERENT SUBSTITUENTS IN THE 6,6'-POSITIONS OF THE ANCILLARY LIGAND ON DSC PERFORMANCE

II   Substituents in the 6,6'-positions

This study was carried out in collaboration with F. J. Malzner as part of his "Wahl-Praktikum" (internship). In this chapter, six new ligands (**L1.1-L1.6**) and Cu(I)-complexes (**C1.1-C1.6**, see Scheme 14) were incorporated into DSCs. The main interest was to see whether there was a difference in device performance which could be related to the modification of the 2,2'-bipyridine core unit of the dyes by introducing various alkyl or aryl groups in the 6,6'-positions.

for **R** = methyl	**L1.1**		for **R** = methyl	**C1.1**
n-butyl	**L1.2**		*n*-butyl	**C1.2**
isobutyl	**L1.3**		isobutyl	**C1.3**
n-hexyl	**L1.4**		*n*-hexyl	**C1.4**
phenyl	**L1.5**		phenyl	**C1.5**
2-naphthyl	**L1.6**		2-naphthyl	**C1.6**
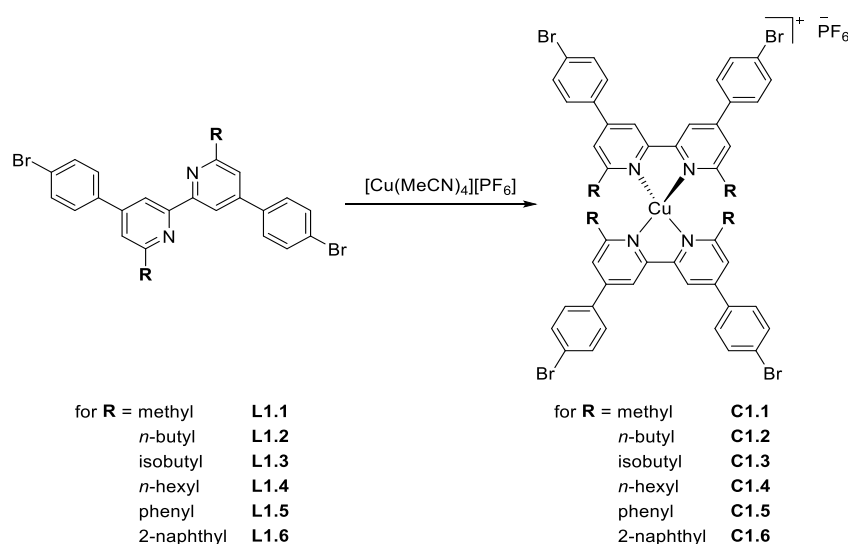
*Scheme 14: Ligands (**L1.1-L1.6**) and homoleptic Cu(I)-complexes (**C1.1-C1.6**) which were used to assemble the dyes in DSCs.*

Since the results of Chapter I showed that **ALP** and **ALP1** are better anchoring ligands than **ALC** and **ALC1**, only **ALP** and **ALP1** were used as anchoring ligands in the study described in this chapter.

for **R** = methyl	**L1.1**
n-butyl	**L1.2**
isobutyl	**L1.3**
n-hexyl	**L1.4**
phenyl	**L1.5**
2-naphthyl	**L1.6**

| **ALP** | no spacer |
| **ALP1** | spacer = 1,4-C₆H₄ |
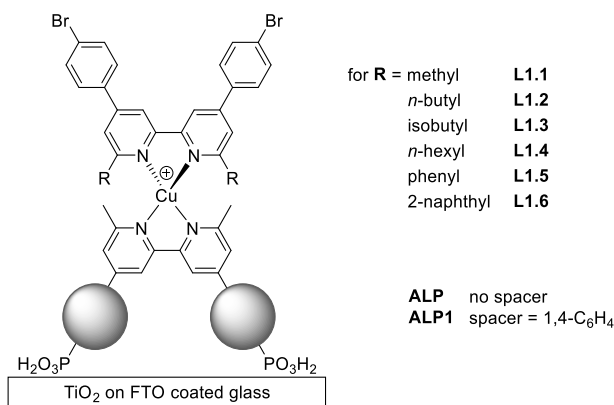
Scheme 15: Schematic representation of the dyes studied in this chapter.

II.1   DSC performances with different anchoring ligands

In a first part of this Chapter, dyes with Me, ^{n}Bu, ^{iso}Bu, n-hexyl and phenyl substituents in the ancillary ligands, will be discussed. In a later stage, dyes with ancillary ligands containing 2-naphthyl groups will be discussed separately.

dye	day	J_{sc} [mA/cm^2]	V_{oc} [mV]	ff [%]	η [%]	rel. η [%]	dye	J_{sc} [mA/cm^2]	V_{oc} [mV]	ff [%]	η [%]	rel. η [%]
[Cu(**L1.1**)(**ALP**)]$^+$	1	3.21	477	72	1.10	16.6	[Cu(**L1.1**)(**ALP1**)]$^+$	5.09	497	72	1.82	27.5
[Cu(**L1.2**)(**ALP**)]$^+$	1	3.64	478	71	1.24	18.8	[Cu(**L1.2**)(**ALP1**)]$^+$	5.50	497	71	1.95	29.5
[Cu(**L1.3**)(**ALP**)]$^+$	1	4.32	515	69	1.54	23.2	[Cu(**L1.3**)(**ALP1**)]$^+$	6.73	541	70	2.55	38.5
[Cu(**L1.4**)(**ALP**)]$^+$	1	3.57	475	71	1.21	18.3	[Cu(**L1.4**)(**ALP1**)]$^+$	5.07	507	71	1.83	27.7
[Cu(**L1.5**)(**ALP**)]$^+$	1	0.35	473	56	0.09	1.4	[Cu(**L1.5**)(**ALP1**)]$^+$	2.74	605	66	1.10	16.6
N719	1	15.06	634	69	6.62	100.0	**N719**	15.06	634	69	6.62	100.0
[Cu(**L1.1**)(**ALP**)]$^+$	4	4.44	500	72	1.60	26.3	[Cu(**L1.1**)(**ALP1**)]$^+$	5.85	519	72	2.19	36.0
[Cu(**L1.2**)(**ALP**)]$^+$	4	3.51	506	67	1.19	19.5	[Cu(**L1.2**)(**ALP1**)]$^+$	5.17	524	67	1.82	29.9
[Cu(**L1.3**)(**ALP**)]$^+$	4	4.35	543	65	1.54	25.3	[Cu(**L1.3**)(**ALP1**)]$^+$	7.02	566	63	2.49	40.8
[Cu(**L1.4**)(**ALP**)]$^+$	4	3.97	505	70	1.40	23.0	[Cu(**L1.4**)(**ALP1**)]$^+$	5.54	496	68	1.87	30.6
[Cu(**L1.5**)(**ALP**)]$^+$	4	2.22	534	68	0.81	13.2	[Cu(**L1.5**)(**ALP1**)]$^+$	6.41	600	73	2.80	45.9
N719	4	14.80	673	61	6.09	100.0	**N719**	14.80	673	61	6.09	100.0
[Cu(**L1.1**)(**ALP**)]$^+$	5	4.53	507	72	1.65	27.7	[Cu(**L1.1**)(**ALP1**)]$^+$	6.01	527	73	2.3	38.6
[Cu(**L1.2**)(**ALP**)]$^+$	5	3.56	502	66	1.18	19.8	[Cu(**L1.2**)(**ALP1**)]$^+$	5.3	525	65	1.8	30.2
[Cu(**L1.3**)(**ALP**)]$^+$	5	4.44	549	66	1.61	27.0	[Cu(**L1.3**)(**ALP1**)]$^+$	7.06	571	60	2.43	40.8
[Cu(**L1.4**)(**ALP**)]$^+$	5	4.21	514	69	1.5	25.2	[Cu(**L1.4**)(**ALP1**)]$^+$	6.07	520	60	1.9	31.9
[Cu(**L1.5**)(**ALP**)]$^+$	5	3.53	536	68	1.29	21.6	[Cu(**L1.5**)(**ALP1**)]$^+$	6.7	592	73	2.89	48.5
N719	5	14.66	679	60	5.96	100.0	**N719**	14.66	679	60	5.96	100.0

*Table 8: Summary of DSC parameters over four measuring days. [Cu(**L1.1-1.5**)(**AL**)]$^+$ where **AL** = **ALP** or **ALP1**.*

Table 8 summarizes the DSC parameters over a measuring period of four days with respect to N719, which is set to 100%. From Table 8 several trends are observable.

For dyes where the only variable is the anchoring ligand (*e.g.* on going from [Cu(**L1.1**)(**ALP**)]$^+$ to [Cu(**L1.1**)(**ALP1**)]$^+$), all dyes with a phenylene spacer exhibit a much higher efficiency than the corresponding dye with **ALP** as anchor. This result supports our previous findings from section I.2.1 where we concluded **ALP1** gave the best cell performance compared to the other anchoring ligands.

Another observation that is found and was already seen in section I.2.3 is the so called ripening effect of copper(I)-DSCs. All cells show a rising efficiency on going from day 1 to day 4, which is mainly due to the gain in *Jsc*. On day 1 the best performing dye was [Cu(**L1.3**)(**ALP1**)]$^+$ with η = 2.55%, whereas on day 5 the best efficiency was exhibited by device [Cu(**L1.5**)(**ALP1**)]$^+$

with η = 2.89%. The dye showing the highest increase in efficiency was [Cu(**L1.5**)(**ALP1**)]$^+$. While performing poorly on day 1 (η = 1.10%), its global efficiency increased up to η = 2.89% on day 5. All dyes showed a higher efficiency on day four except dyes which incorporated **L1.2** as ancillary ligand.

The effect of the substituent in the 6,6'-positions seems to depend on the anchoring ligand in the device. Where the anchoring ligand is **ALP** (*i.e.* no phenylene spacer) the best performance was achieved at day 5 with capping ligand **L1.1** (η = 1.65%) closely followed by **L1.3** (η = 1.61%) and **L1.4** (η = 1.50%). The two remaining dyes with ancillary ligands **L1.5** (η = 1.29%) and **L1.2** (η = 1.18%) demonstrate a distinct reduction in performance. For DSCs where **ALP1** serves as the anchoring ligand, a different order is observed. The highest energy-conversion efficiency is obtained with capping ligand **L1.5** at day 5 (η = 2.89%). A noticeably lower efficiency is shown by devices with **L1.3** (η = 2.43%) and **L1.1** (η = 2.3%). The devices with linear alkyl substituents in the 6,6'-positions (**L1.2** and **L1.4**) show the poorest performances (η = 1.80% and 1.90%, respectively).
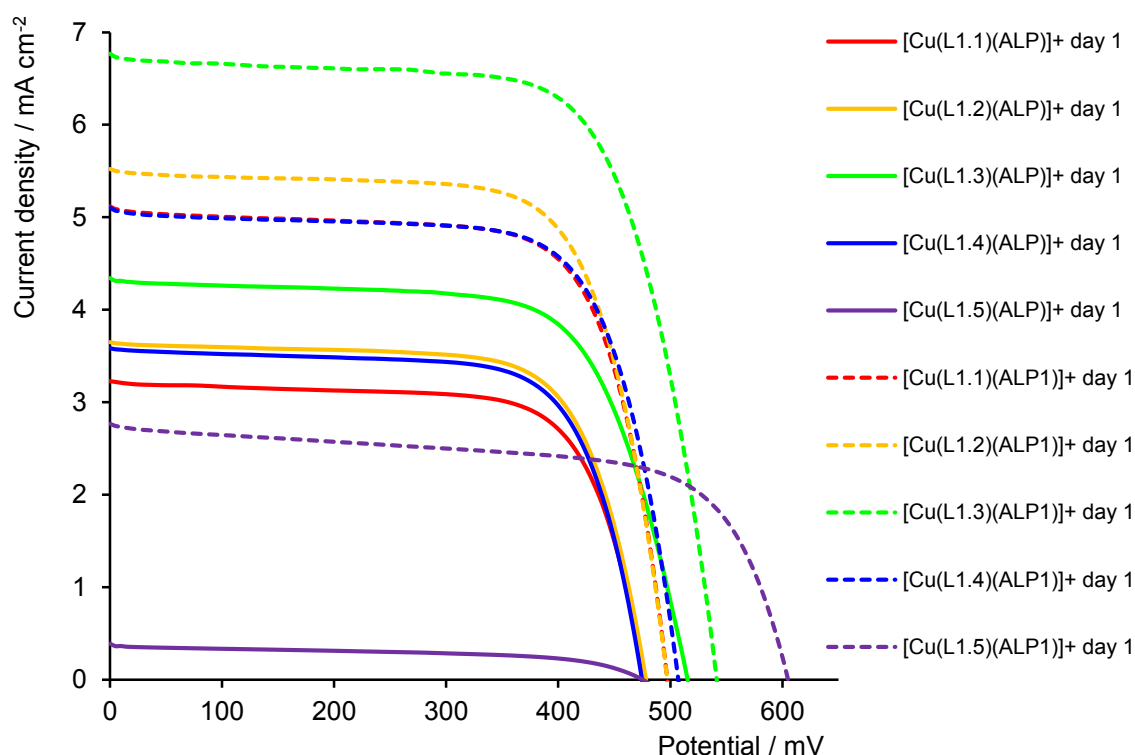
*Figure 65: JV plot. A graphical presentation of [Cu(**L1.1-L1.5**) (**AL**)]$^+$ parameters measured on day 1.*

Comparing devices where the only difference in the active dye lies in the anchoring ligand (*e.g.* on going from **ALP** to **ALP1**) (Figure 65), it is clear that all cells with **ALP1** perform with a higher efficiency than their corresponding dye with **ALP**. Furthermore, the order in short-circuit-current-density remains unchanged upon substitution of **ALP** with **ALP1**. Devices with

L1.3 as ancillary ligand show the best efficiency compared to the other four ancillary ligands, and cells with **L1.5** show the poorest performance at day 1.
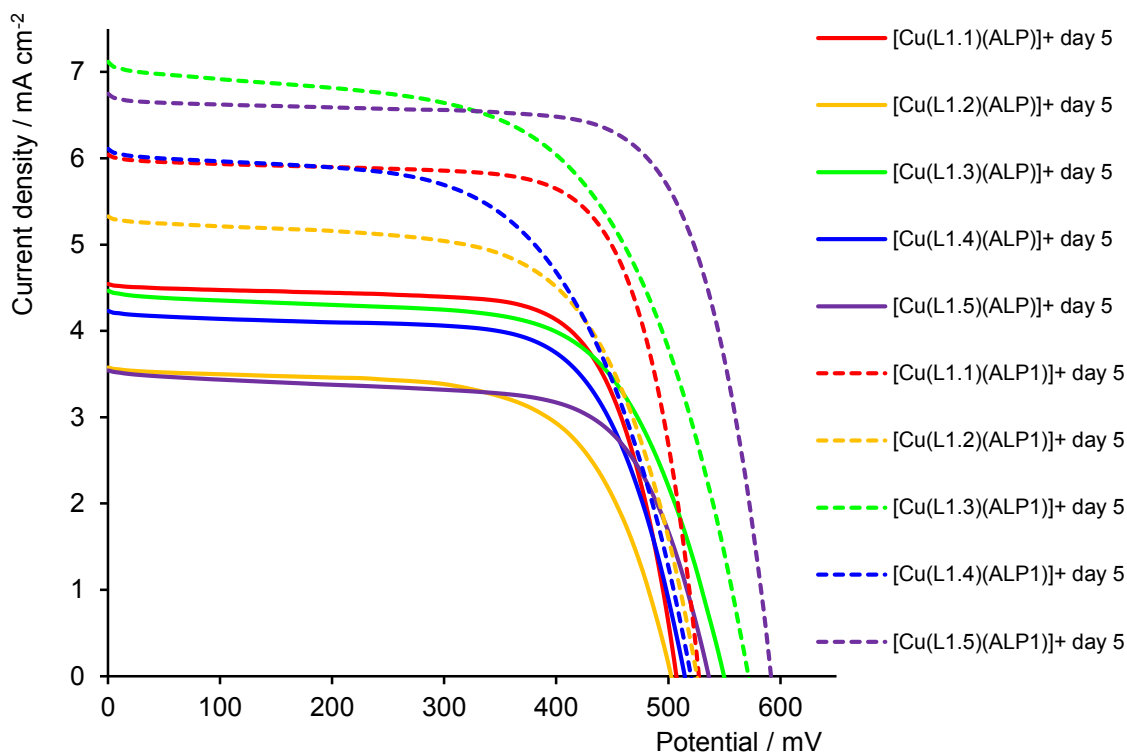
*Figure 66: JV-plot. A graphical presentation of [Cu(**L1.1-L1.5**)(**AL**)]⁺ parameters measured on day 5.*

Figure 66 shows a graphical representation where the only variance in the active dye is the anchoring ligand used (*e.g.* on going from **ALP** to **ALP1**). In both cases where **ALP** or **ALP1** is used, the cells containing ancillary ligand **L1.2** give the lowest efficiency. The main difference can be found comparing cells with capping ligand **L1.3** and **L1.5**. In DSCs in which **ALP** is the connection to the semiconductor, the cell with **L1.5** suffers from low current-density while the cell with **L1.3** is comparable with **L1.1** and **L1.4**. On the other hand with **ALP1**, the DSC with **L1.5** shows the second highest *Jsc* and the highest potential *Voc*.

II.1.1 Ripening effect
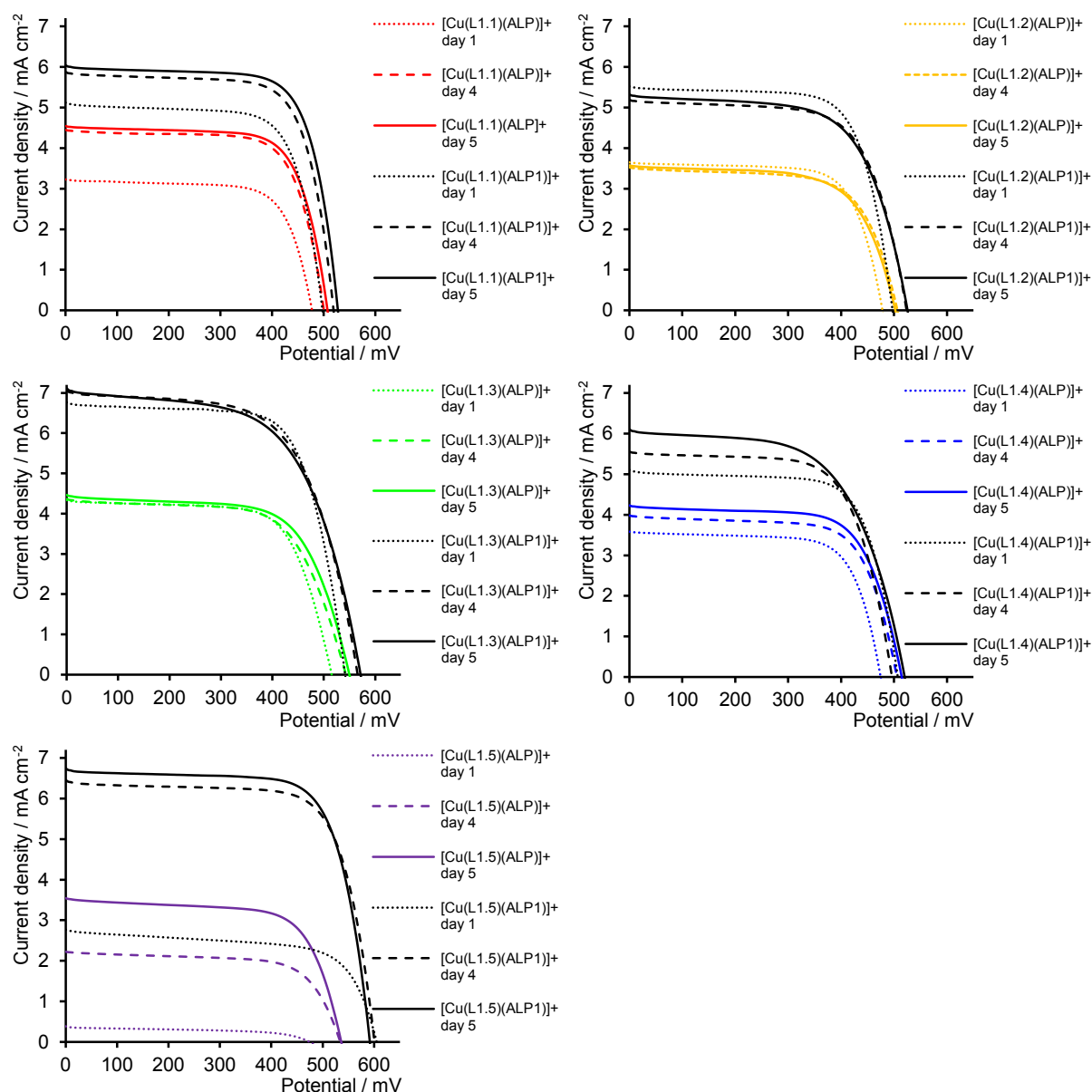
*Figure 67: JV-plots. [Cu(**L1.1-L1.5**)(**AL**)]⁺ where **AL** = **ALP** or **ALP1**. Curves for day 1, day 4 and day 5.*

For devices where the only difference is the anchoring ligand (*e.g.* on going from [Cu(**L1.1**)(**ALP**)]⁺ to [Cu(**L1.1**)(**ALP1**)]⁺) the ageing effect looks the same. While devices with **L1.1** gain in *Jsc* on going from day 1 to day 4, the current density stays approximately constant from day 4 to day 5. The open-circuit-voltage rises slightly from day 1 to day 5. Overall the DSCs containing dyes [Cu(**L1.1**)(**ALP/ALP1**)]⁺ improve in efficiency over time. For cells with capping ligands **L1.2** and **L1.3**, the current density remains unchanged over time and *Voc* increased only a little. Since there are only minor changes over time for DSCs containing **L1.2** and **L1.3**, the efficiency is more or less constant over the measuring period of 5 days. For DSCs with **L1.4**, there is a constant increase in *Jsc* and *Voc* over time and therefore the performance also improves constantly over time. The most striking improvement over time occurs when

L1.5 is implemented in devices, no matter if **ALP** or **ALP1** is used as the anchoring ligand. On day 1, the efficiency is worse than any of the other comparable cells. A remarkable gain in *Jsc* over the measuring period leads to a significant rise in conversion efficiency. After 4 days, [Cu(**L1.5**)(**ALP1**)]$^+$ ends up being the best performing cell of this set.

II.1.2   Anchoring ligand effect for ancillary ligands L1.1-L1.5

The introduction of a phenylene spacer was beneficial in all cases. Consulting Figure 65 and Figure 66 the observations from section I.2.1 confirm that devices with **ALP1** serving as an anchoring ligand yield higher conversion efficiencies than DSCs with **ALP** due to an improved current-density.

II.2   The effect of 6,6'-substituents on parameters
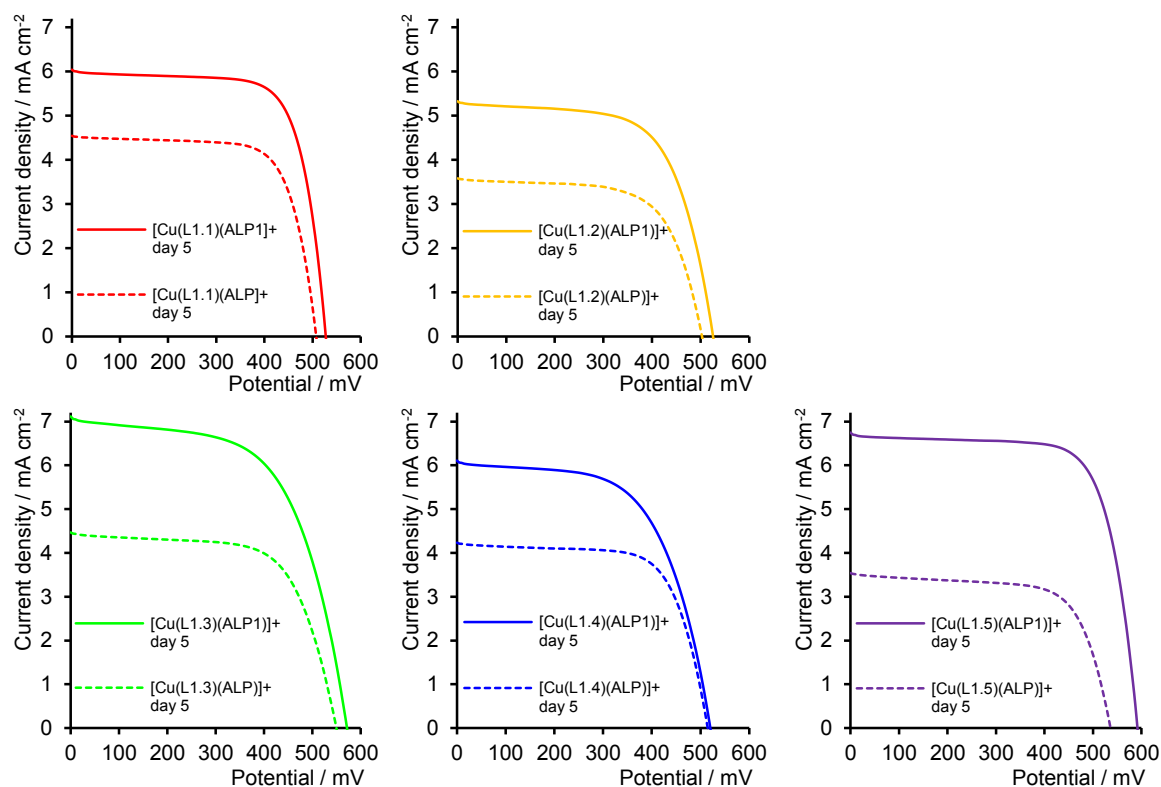
*Figure 68: JV-curves of [Cu(**L1.1-L1.5**)(AL)]$^+$ where **AL** = **ALP** or **ALP1**, for day 5.*

II.2.1   Fill Factor

Focusing our attention on the fill factor (*ff*, the shape of curve, Figure 68) one observes that cells with ancillary ligands **L1.1** exhibit the best *ff* independent of the anchoring ligand. Devices with **L1.5** as capping ligand, also show a good *ff* whereas the *ff* with **ALP** is slightly lower than with **ALP1**. For **L1.2** there is no change on going from **ALP** to **ALP1**. As substituents become sterically more demanding (**L1.3** and **L1.4**), the *ff* drops slightly on going from **ALP** to **ALP1**.

II.2.2   Short-circuit-current-density (Jsc)

As previously mentioned, all devices with **ALP1** exhibit a higher *Jsc* than their corresponding dyes with **ALP** (e.g. on going from [Cu(**L1.1**)(**ALP**)]$^+$ to [Cu(**L1.1**)(**ALP1**)]$^+$). While DSCs with **ALP** incorporated as anchoring ligand and using ligands **L1.1**, **L1.3** and **L1.4** show similar *Jsc* values, cells with **L1.2** and **L1.5** exhibit a reduced *Jsc*.

However for devices in which **ALP1** serves as the linker to the semiconductor, the cell with **L1.3** ends up yielding the highest *Jsc* closely followed by **L1.5**. DSCs with **L1.1** and **L1.4** display similar values of *Jsc* of about 6 mA cm^{-2}. The lowest *Jsc* is observed with **L1.2** as anchoring ligand.

II.2.3   Open circuit voltage (Voc)

As already mentioned, all devices with **ALP1** exhibit a higher *Voc* as their corresponding dyes with **ALP**. For dyes with **ALP** and ancillary ligands which possess linear alkyl substituents in the 6,6'-positions (**L1.1**, **L1.2** and **L1.4**), an approximately equal *Voc* is observed. A higher *Voc* value is seen for the device with **L1.5** and the best *Voc* is yielded by the active dye with **L1.3**. Concentrating on devices with **ALP1** as anchoring ligand again shows that cells with ligands that possess linear alkyl substituents in the 6,6'-positions (**L1.1**, **L1.2** and **L1.4**) show an equal *Voc*. Nevertheless in the case of **ALP1**, the second highest *Voc* is produced with ancillary ligand **L1.3** (isobutyl) and by far the best *Voc* is reached with **L1.5** (phenyl).

II.2.4   Efficiency

For devices with **ALP**, the following order in conversion efficiency on day 5 is observed:

    L1.1 > L1.3 > L1.4 > L1.5 > L1.2

For devices with **ALP1**, the following order in conversion efficiency on day 5 is observed:

    L1.5 > L1.3 > L1.1 > L1.4 > L1.2

II.3   Reproducibility

To check the reproducibility of our results a new set of masked cells was prepared using **ALP1** as anchoring ligand and the cells were measured over a period of one week (see Table 9).

dye	day	J_{sc} [mA/cm^2]	V_{oc} [mV]	ff [%]	η [%]	rel. η [%]
[Cu(**L1.1**)(**ALP1**)]$^+$	**1**	4.77	503	73	1.76	24.9
[Cu(**L1.2**)(**ALP1**)]$^+$	**1**	4.22	482	74	1.49	21.0
[Cu(**L1.3**)(**ALP1**)]$^+$	**1**	6.42	555	73	2.6	36.7
[Cu(**L1.4**)(**ALP1**)]$^+$	**1**	4.8	502	72	1.74	24.6
[Cu(**L1.5**)(**ALP1**)]$^+$	**1**	3.97	605	69	1.67	23.6
N719	**1**	15.37	648	71	7.08	100.0
[Cu(**L1.1**)(**ALP1**)]$^+$	**2**	6.09	520	74	2.33	28.3
[Cu(**L1.2**)(**ALP1**)]$^+$	**2**	5.61	499	74	2.06	25.1
[Cu(**L1.3**)(**ALP1**)]$^+$	**2**	6.74	571	73	2.81	34.2
[Cu(**L1.4**)(**ALP1**)]$^+$	**2**	5.92	510	73	2.19	26.6
[Cu(**L1.5**)(**ALP1**)]$^+$	**2**	6.81	611	72	3.01	36.6
N719	**2**	17.1	677	71	8.22	100.0
[Cu(**L1.1**)(**ALP1**)]$^+$	**3**	5.93	525	74	2.31	27.8
[Cu(**L1.2**)(**ALP1**)]$^+$	**3**	5.42	501	73	1.99	24.0
[Cu(**L1.3**)(**ALP1**)]$^+$	**3**	6.91	576	72	2.87	34.6
[Cu(**L1.4**)(**ALP1**)]$^+$	**3**	5.51	521	73	2.09	25.2
[Cu(**L1.5**)(**ALP1**)]$^+$	**3**	6.96	606	74	3.1	37.3
N719	**3**	17.2	684	71	8.3	100.0
[Cu(**L1.1**)(**ALP1**)]$^+$	**8**	5.73	530	74	2.26	26.7
[Cu(**L1.2**)(**ALP1**)]$^+$	**8**	5.51	513	74	2.09	24.7
[Cu(**L1.3**)(**ALP1**)]$^+$	**8**	6.69	584	73	2.85	33.7
[Cu(**L1.4**)(**ALP1**)]$^+$	**8**	5.44	531	71	2.05	24.3
[Cu(**L1.5**)(**ALP1**)]$^+$	**8**	7.03	590	73	3.01	35.6
N719	**8**	17.23	696	71	8.45	100.0

*Table 9: DSC performance data of a second independent set of masked cells using anchoring ligand **ALP1**.*

A comparison of data from Table 8 and Table 9 leads to similar trends. In particular, the order of efficiencies comparing these two sets reveals the same trend (**L1.5 > L1.3 > L1.1 > L1.4 > L1.2**).
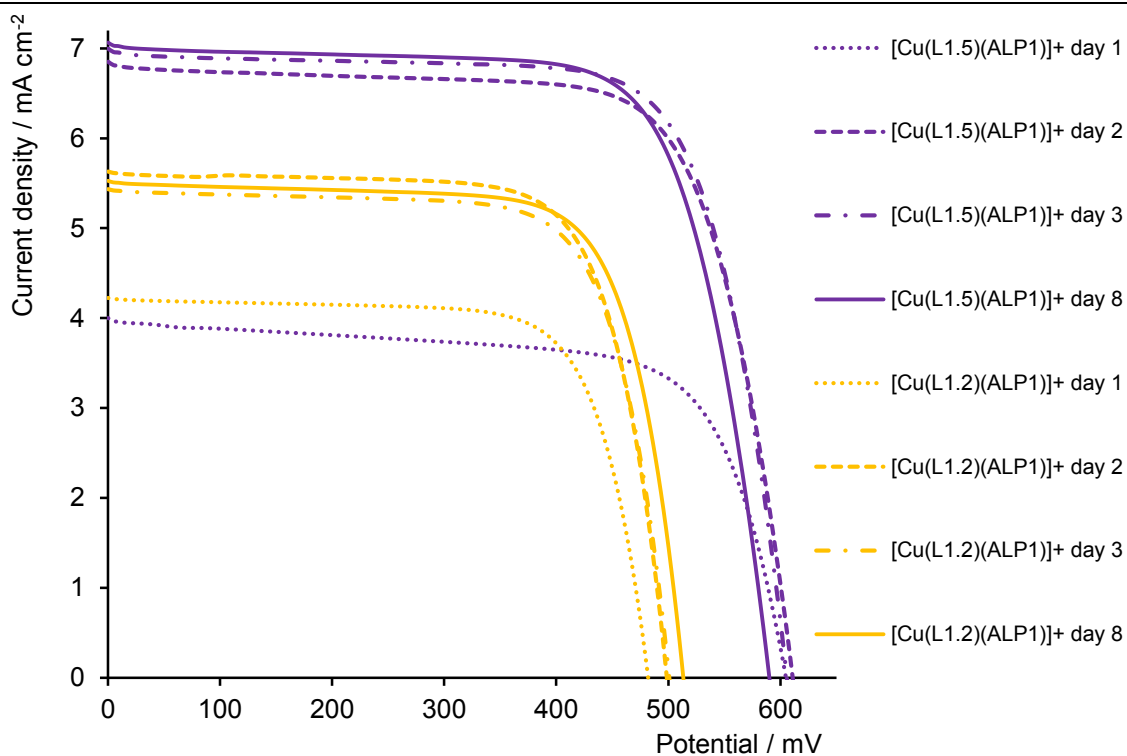
*Figure 69: JV-curves for [Cu(**L1.2**)(**ALP1**)]⁺ and [Cu(**L1.5**)(**ALP1**)]⁺ over one week.*

Figure 69 shows *JV*-plots of [Cu(**L1.2**)(**ALP1**)]⁺ and [Cu(**L1.5**)(**ALP1**)]⁺ illustrating the initial aging effect of the cells, which is then followed by a plateau of efficiency for a week. Also the ripening effect for [Cu(**L1.5**)(**ALP1**)]⁺ was reproducible from the previous set (Table 8).
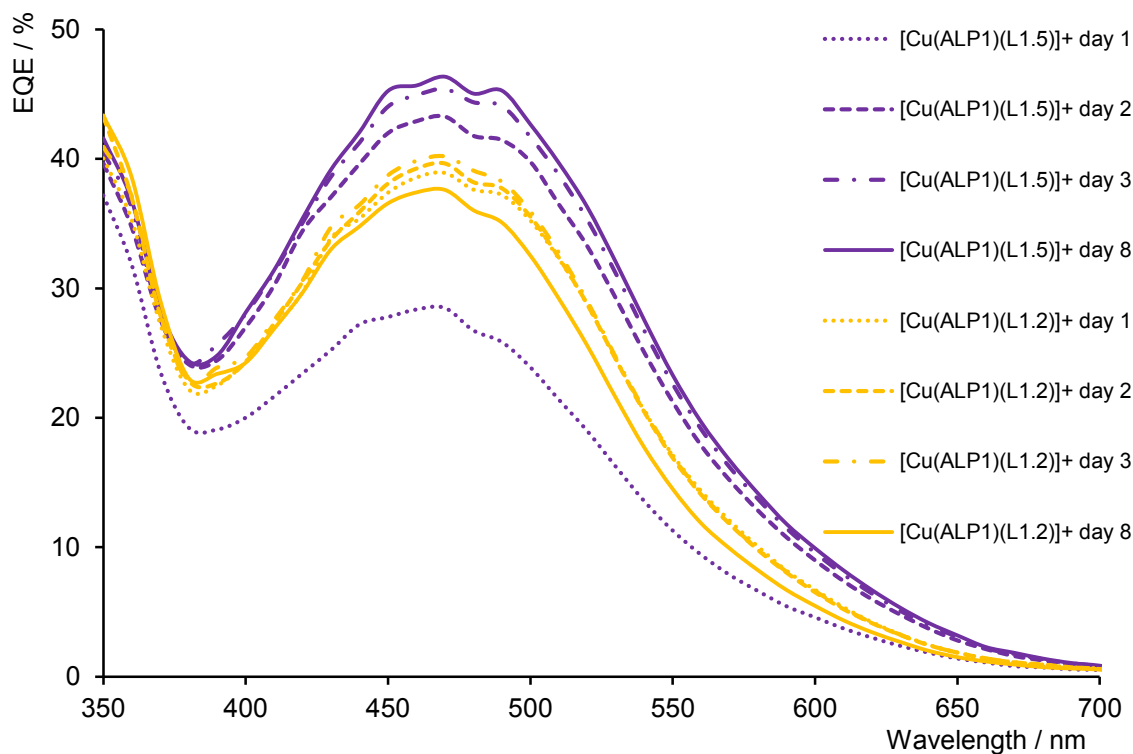
*Figure 70: External quantum efficiency of [Cu(**L1.2**)(**ALP1**)]⁺ and [Cu(**L1.5**)(**ALP1**)]⁺ over one week.*

External quantum efficiency measurements (Figure 70) explain the nature of the extreme ripening effect/improvement over time for [Cu(**L1.5**)(**ALP1**)]$^+$. On going from day 1 to day 2 for ancillary ligand **L1.5**, the *EQE* improves from 28% to 43% at λ_{max} of 470 nm. From day 2 to day 8, the *EQE* is continually rising from 43% to 46% at 470 nm. For [Cu(**L1.2**)(**ALP1**)]$^+$ the ripening effect is also detectable, although not as pronounced as for the dye with capping ligand **L1.5**.
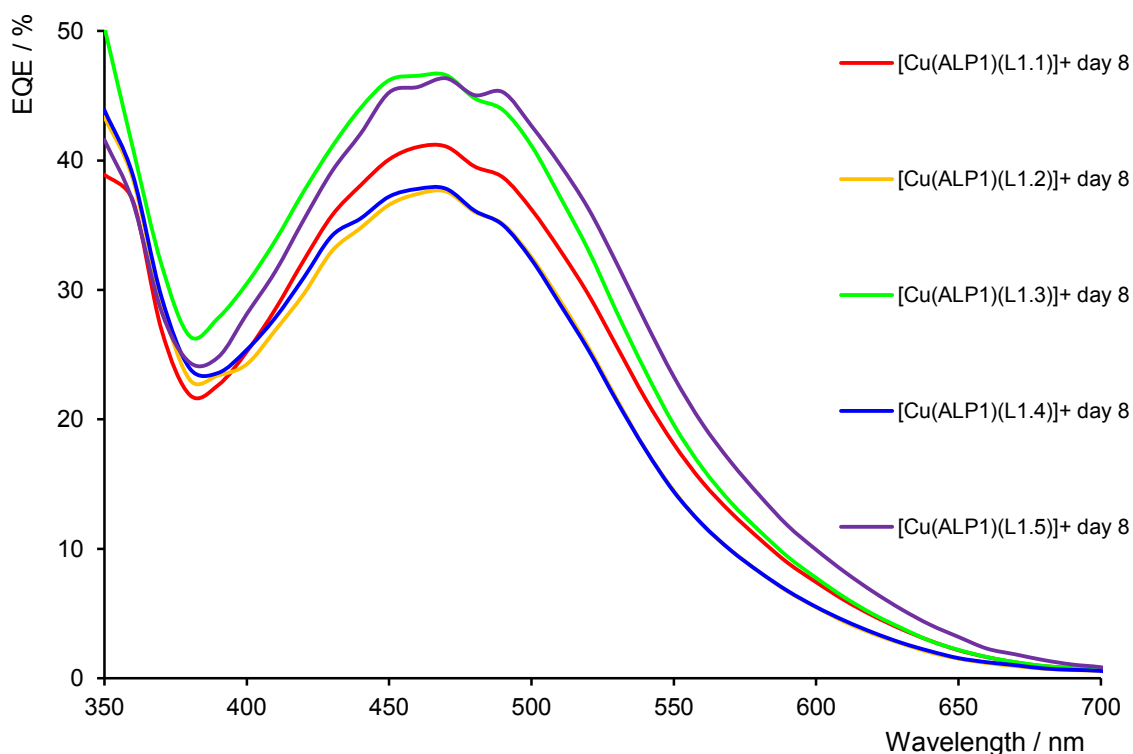
*Figure 71: EQE curves for [Cu(**ALP1**)(**L1.1-L1.5**)]$^+$ on day 8.*

For all dyes, the peak maxima in the *EQE* curves lie at $\approx$ 470nm, which correlates with the observed maxima in the solution UV-vis spectrum of the *homoleptic*-copper(I) complexes containing **L1.1** and **L1.4**. During the measuring period, *EQE* peak maxima of between 39 and 42% are recorded for [Cu(**L1.1**)(**ALP1**)]$^+$, 38-40% for [Cu(**L1.2**)(**ALP1**)]$^+$, 47-50% for [Cu(**L1.3**)(**ALP1**)]$^+$ and 38-39% for [Cu(**L1.4**)(**ALP1**)]$^+$, which corresponds to the trends in efficiencies listed in Table 9.

Although [Cu(**L1.5**)(**ALP1**)]$^+$ exhibits a λ_{max} at $\approx$ 470nm in the *EQE*, it is not consistent with the solution electronic absorption spectrum of the *homoleptic*-copper(I) complex. In contrast there is only a minor difference between the *EQE* curves of [Cu(**L1.5**)(**ALP1**)]$^+$ and the other four complexes but a distinct difference in solution absorption spectra between the homoleptic complexes containing alky and phenyl substituents.

Therefore the solid state absorption spectra of the semiconductor-anchored *heteroleptic* dyes of [Cu(**L1.3**)(**ALP1**)]$^+$ and [Cu(**L1.5**)(**ALP1**)]$^+$ were recorded (Figure 72). The anodes were prepared as previously described (see solar cell fabrication).
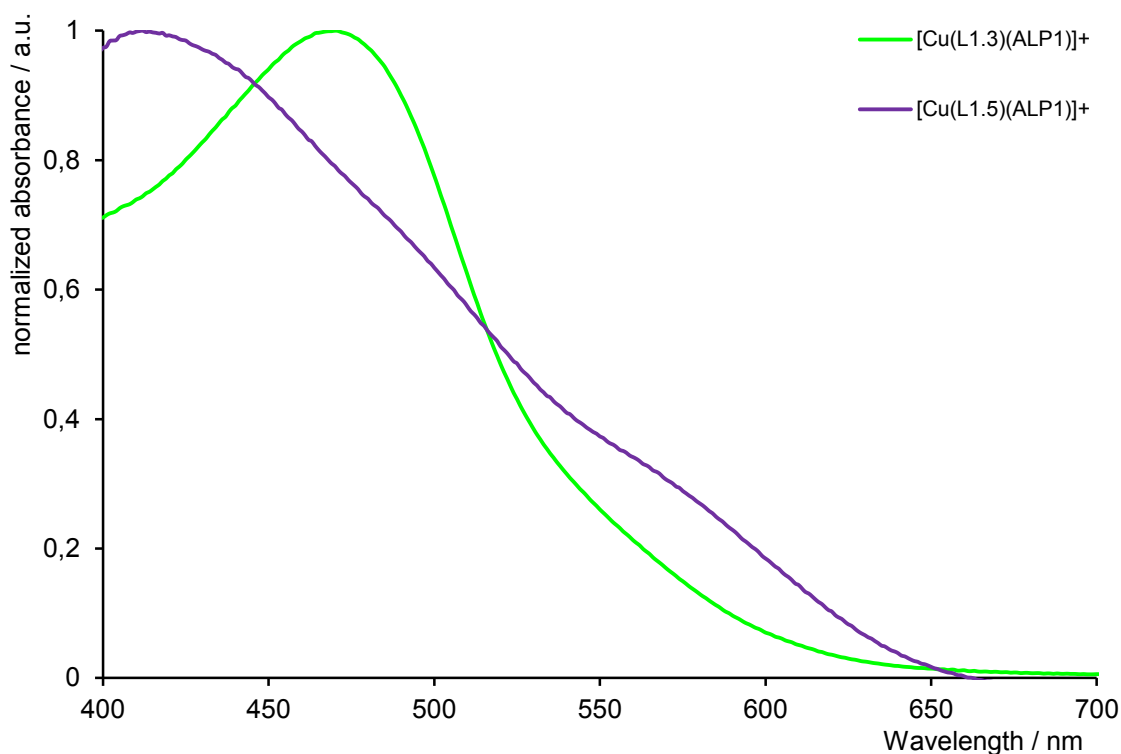
*Figure 72: Solid state absorption spectra of dyes containing ancillary ligands **L1.3** and **L1.5**.*

The absorption spectra of the anodes with adsorbed [Cu(**L1.3**)(**ALP1**)]$^+$ and [Cu(**L1.5**)(**ALP1**)]$^+$ are shown in Figure 72. The photoanode with the dye with ancillary ligand **L1.5** exhibits an enhanced absorption at >530 nm, which is also seen in the *homoleptic* complex [Cu(**L1.5**)$_2$][PF$_6$] in solution.

The *EQE* spectra (Figure 71) indicates an improved response in the red region of the spectrum, which is consistent with the red-shift of the UV-vis-absorption spectra of dyes containing ancillary ligand **L1.5**.

II.4 An additional substituent in the 6,6'-positions

Following the promising results obtained with ancillary ligand **L1.5** in DSCs, it was decided to introduce another more sterically demanding aromatic substituent in the 6,6'-positions. The chosen group was 2-naphthyl. The only anchoring ligand used in this set of experiments was **ALP1**.
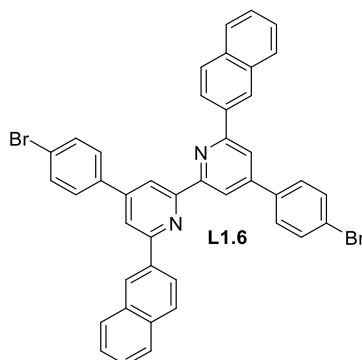
*Scheme 16: Ligand **L1.6**, which was introduced into the active dye via the homoleptic copper(I)-complex into DSCs.*

Cells were measured completely masked over a period of 18 days. Additionally, *EQE* spectra were recorded over this period.

II.4.1 DSC performance of [Cu(ALP1)(L1.6)]$^+$

dye	day	J_{sc} [mA/cm^2]	V_{oc} [mV]	*ff* [%]	η [%]	rel. η [%]
[Cu (ALP1)(L1.6)]$^+$	0	3.69	485	70.8	1.27	16.6
N719	0	17.17	643	69.1	7.63	100.0
[Cu (ALP1)(L1.6)]$^+$	1	4.01	516	70.4	1.46	18.1
N719	1	16.84	677	70.4	8.03	100.0
[Cu (ALP1)(L1.6)]$^+$	3	3.89	532	70.1	1.45	18.2
N719	3	16.56	688	70.0	7.98	100.0
[Cu (ALP1)(L1.6)]$^+$	10	4.27	529	63.8	1.44	18.2
N719	10	16.36	698	69.5	7.94	100.0
[Cu (ALP1)(L1.6)]$^+$	18	4.58	526	61.2	1.48	18.6
N719	18	16.28	685	71.3	7.95	100.0

*Table 10: DSC parameter of device [Cu(**ALP1**)(**L1.6**)]$^+$ with respect to N719.*

The *Jsc* values of cells with capping ligand **L1.6** undergo an improvement over time, from 3.69 mA cm^{-2} on day 0 to 4.58 mA cm^{-2} on day 18. The *Voc* rises over the measuring period of 18 days from an initial value of 485 mV on day 0 to a maximum of 532 mV on day 3 and then stays constant up to day 18 (526 mV is within the expt. error). Overall, the *Voc* improves with

time. The ff is more or less constant ($\approx$70%) from day 0 to day 3 and decreases on going from day 3 to day 18 to 61%.

Consistent with the increasing Jsc and Voc over time is the gain in conversion efficiency over the measuring period of 18 days. Devices with ancillary ligand **L1.6** exhibit an efficiency of 1.27% on day 0 and improve over time, reaching an efficiency of 1.48% on day 18. The cell with capping ligand **L1.6** shows a relative η of 18% compared to **N719** (set to 100%). Comparing this relative efficiency of 18% with that of a device with ancillary ligand **L1.5**, which exhibited a relative efficiency of 48.5% at day 5, one can say that no efficiency enhancement was achieved by replacing the phenyl rings with 2-naphthyl groups in the 6,6'-positions.
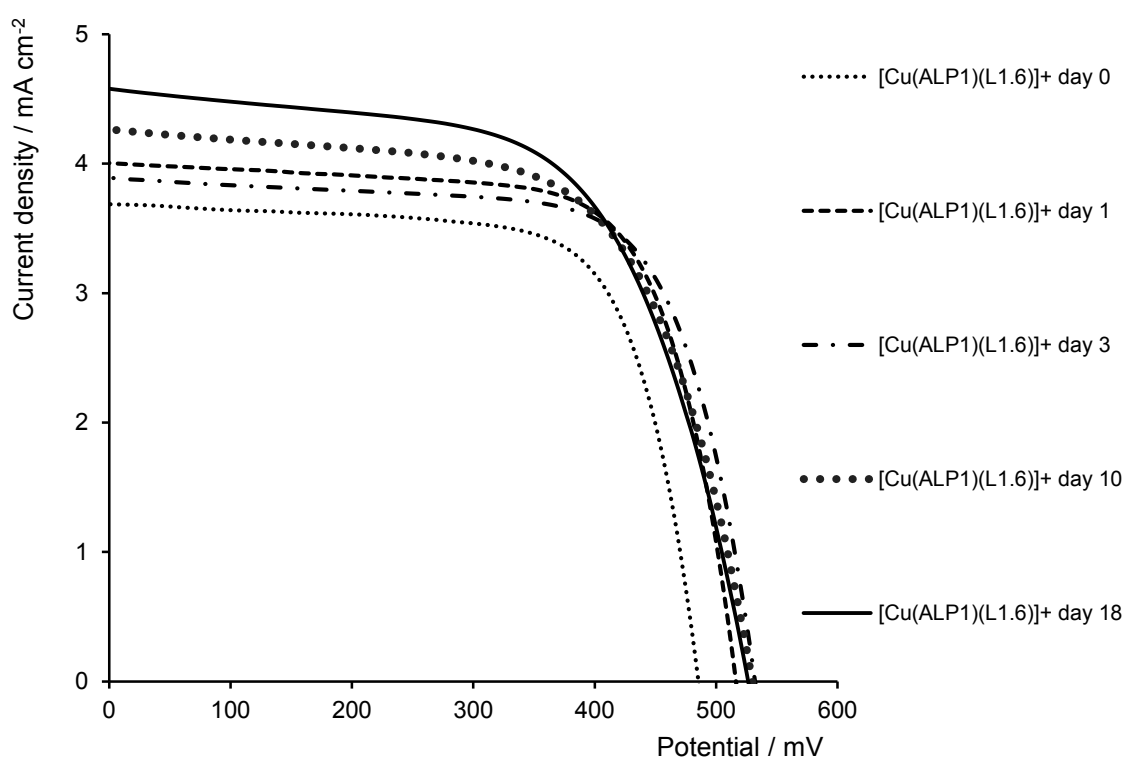
*Figure 73: JV curve of [Cu(**ALP1**)(**L1.6**)]$^+$ over 18 days.*

Figure 73 nicely displays the gain in Jsc on going from day 0 to day 18 for the dye [Cu(**ALP1**)(**L1.6**)]$^+$. It also reflects the increase in Voc, which levels off after 3 days. The curve shapes give direct information about the loss in ff of the cell over these 18 days.
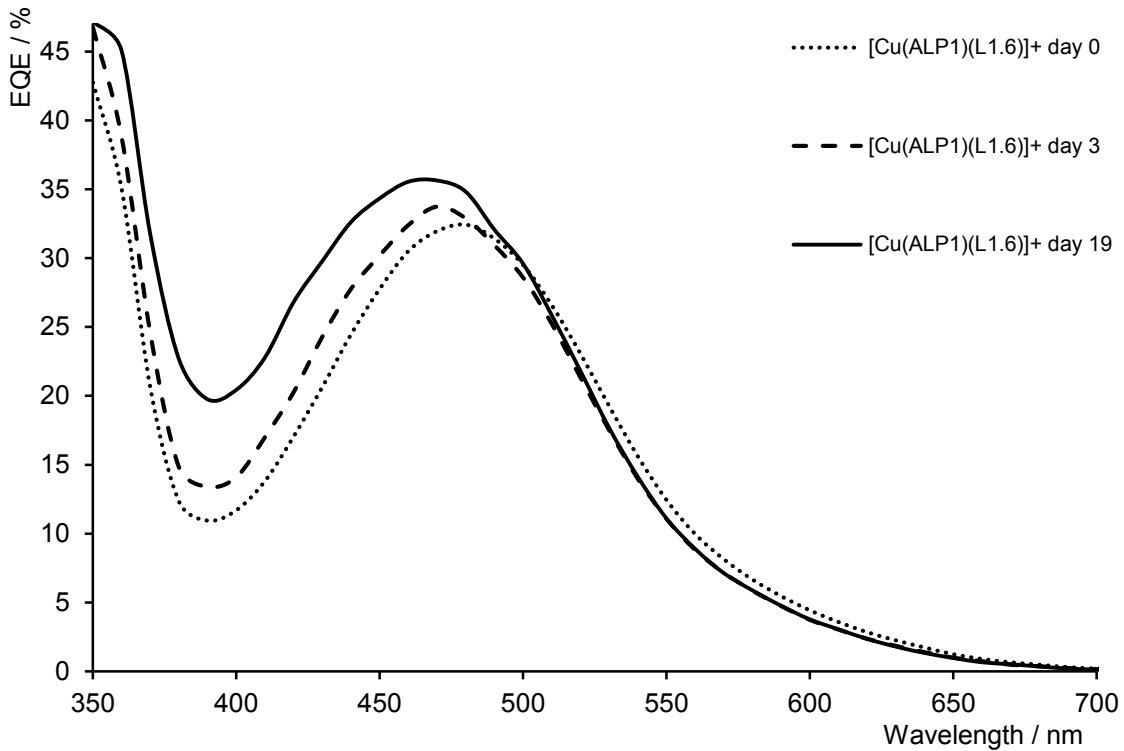
*Figure 74: EQE curves of [Cu(**ALP1**)(**L1.6**)]$^+$ on day 0, day 3 and day 19.*

In Figure 74 the gain in *Jsc*, *Voc* and η is represented by an enhanced external quantum efficiency on going from day 0 to day 19. In particular, the *EQE* increases from 380 to 500 nm but stays unchanged at wavelengths >500 nm. [Cu(**ALP1**)(**L1.6**)]$^+$ exhibits a much lower *EQE* than [Cu(**ALP1**)(**L1.5**)]$^+$ (see Figure 75).
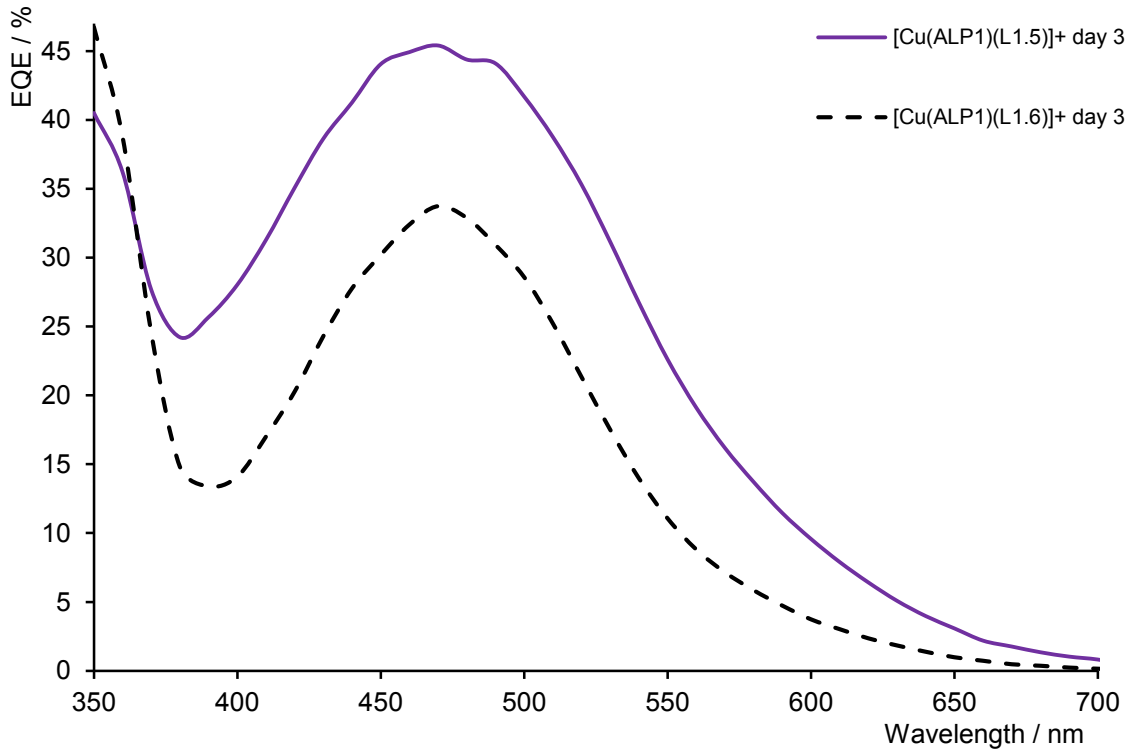
*Figure 75: An EQE comparison of [Cu(**ALP1**)(**L1.5**)]$^+$ and [Cu(**ALP1**)(**L1.6**)]$^+$.*

II.5   Solar cell fabrication and characterisation II

The fabrication of DSCs was based on the method of Grätzel and coworkers[196]. The TiO_2 paste was prepared adapting the published method using a three-roll mill (50 EC, EXAKT, Germany), sonicator bath and terpineol (CAS: 8000-41-7). Each working electrode was made from an FTO glass plate (Solaronix TCO22-7, 2.2 mm thickness, sheet resistance $\approx 7\ \Omega$ square^{-1}), which was cleaned by sonicating in Hellmanex® surfactant (2% in milliQ water), and rinsed with milliQ water and EtOH. After a surface activation in a UV-O_3 system (Model 256-220, Jelight Company Inc) for 20 min, the FTO plates were immersed in aqueous $TiCl_4$ (40 mmol dm^{-3}) at 70 ºC for 30 min, and then washed with milliQ water and EtOH. The FTO plate was dried and a layer of TiO_2 paste was screen printed (90T, Serilith AG, Switzerland). The printed plate was kept in an EtOH chamber for 3 min to reduce surface irregularities of the printed layer and dried for 6 min at 125 ºC on a heating plate. The screen printing process was repeated 8 times and then the electrodes were gradually heated at 75 °C for 30 min, at 135 °C for 15 min, at 325 °C for 5 min, at 375 °C for 5 min, at 450 °C for 15 min and at 500 °C for 15 min. After the final sintering, the thickness of the TiO_2 layer was 14-16 μm (measured with Tencor Alpha-Step 500 profilometer). The annealed TiO_2 film was post-treated with 40 mM aqueous $TiCl_4$ solution (see above), rinsed with milliQ water and EtOH and sintered at 500 ºC for 30 min.

The electrodes were cooled to ca. 80°C and immersed in a 1 mM DMSO solution of the anchoring ligand **ALP** or **ALP1** for 20 h. The colourless electrode was removed from the solution, washed with DMSO and EtOH and dried under a stream of N_2. The electrode with adsorbed anchoring ligand was immersed in a 1 mM MeCN solution of [Cu(**L**)$_2$][PF$_6$] for L = **1.1-1.4** and in a 1 mM CH_2Cl_2 solution of [Cu(**L**)$_2$][PF$_6$] for L = **1.5** and **1.6** for 4 days to produce red-orange coloured electrodes. The electrodes were removed from the solution and were washed with CH_2Cl_2 and dried under a stream of N_2.

Each counter electrode was prepared from an FTO glass plate (Solaronix TCO22-7, 2.2 mm thickness, sheet resistance $\approx 7\ \Omega$ square^{-1}) with previously drilled hole. Residual organic impurities were removed by heating for 15 min at 500 ºC on a heating plate and the perforated plate was washed with water, then 0.1 M HCl solution in EtOH and finally ultrasonicated in an acetone bath for 15 min. It was dried on the heating plate at 500 °C for 15 min. The Pt catalyst was deposited on the FTO glass plate by coating with Platisol T (2 × 25.0 μL), Solaronix, and dried on a heating plate at 500 °C for 15 min.

The dye-covered TiO_2 electrode and Pt counter-electrode were assembled using thermoplast hot-melt sealing foil (Solaronix, Meltonix 1170-25 Series, 25 microns thick) by heating while pressing them together. The electrolyte was comprised LiI (0.1 mol dm^{-3}), I_2 (0.05 mol dm^{-3}),

1-methylbenzimidazole (0.5 mol dm^{-3}) and 1-butyl-3-methylimidazolinium iodide (0.6 mol dm^{-3}) in 3-methoxypropionitrile, and was introduced into the cell by vacuum backfilling. The hole on the counter electrode was finally sealed using the hot-melt sealing foil and a cover glass. The solar cell measurements and testing protocol were performed using fully masked cells. A black coloured copper sheet was used for masking with a single aperture having an average area of 0.06012 cm^2 (with a standard deviation of 1%) placed over the screen printed dye-sensitized TiO$_2$ circle. The area of the aperture in the mask was smaller than the active area of the dye-sensitized TiO$_2$ dot (0.288 cm^2). For complete masking, tape was also applied over the edges and rear of cell. Current density-voltage (IV) measurements were made by irradiating from behind using a light source SolarSim 150 (100 mW cm^{-2} = 1 sun). The power of the simulated light was calibrated by using a reference Si photodiode. The standard dye N719 was purchased from Solaronix.

The quantum efficiency measurements were performed on a Spe-Quest quantum efficiency setup from Rera Systems (Netherlands) equipped with a 100 W halogen lamp (QTH) and a lambda 300 grating monochromator from Lot Oriel. The monochromatic light was modulated to 3Hz using a chopper wheel from ThorLabs. The cell response was amplified with a large dynamic range IV converter from CVI Melles Griot and then measured with a SR830 DSP Lock-In amplifier from Stanford Research.

II.6   Discussion

The results from Table 8 confirm the observation from Chapter I, with cells incorporating anchoring ligand **ALP1** surpassing their corresponding devices with **ALP** in all cases. For all these cells the introduction of phenylene spacers at the 4,4'-positions of the bpy domain was beneficial.
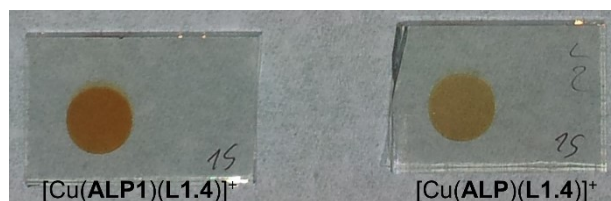
*Figure 76: A comparison of the photoanodes of heteroleptic dyes [Cu(**ALP1**)(**L1.4**)]$^+$ (left) and [Cu(**ALP**)(**L1.4**)]$^+$ (right) bound to the semi-conductor surface.*

A possible explanation might be seen in Figure 76 where the photoanode using **ALP1** as anchoring ligand exhibits a much stronger dyeing of the TiO$_2$ than the corresponding anode where **ALP** was used. This difference in colour leads to the assumption that upon using **ALP1** in a device, more dye can be loaded onto the surface than using **ALP**. A possible reason for the change in dye loading could be the introduction of the phenylene spacer. While using **ALP**, bulky substituents in the 6,6'-positions of the bipyridine unit might be the limiting factor for the amount of dye that can be bound to the surface due to intermolecular repulsion. When **ALP1** is used as anchoring ligand, the colouring of the TiO$_2$ increases indicating that bulky substituents in 6,6'-positions are not as limiting to the dye loading as they were for **ALP**.

II.6.1   ALP in combination with ancillary ligands L1.1-L1.5

The *heteroleptic* dyes [Cu(**ALP**)(**L1.1-1.5**)]$^+$ show a gain in *Jsc* and *Voc* over the 4 day period. The best performing device on day 1 is achieved with **L1.3** producing an initial efficiency of 1.54%. On the last measuring day, the most efficient dye was with capping ligand **L1.1** reaching η = 1.65% and a relative energy conversion efficiency of 28% with respect to **N719** set to 100%. Due to the absence of phenylene spacers in the anchoring ligand **ALP**, the substituents in the 6,6'-positions of the ancillary ligand are relatively close to the TiO$_2$ surface. A possible reason for [Cu(**ALP**)(**L1.1**)]$^+$ exhibiting the highest efficiency might be that **L1.1** contains the least sterically demanding substituents in the 6,6'-positions. This might lead to a higher dye loading on the surface and a higher photon absorbance, which would then explain the higher *Jsc* and efficiency.
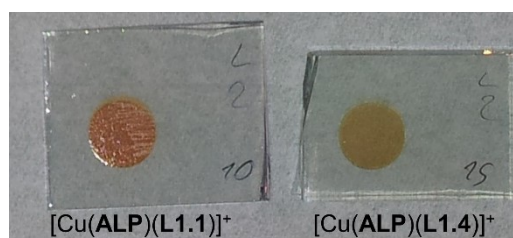
*Figure 77: Comparison of the photoanodes of heteroleptic dyes [Cu(**ALP**)(**L1.1**)]⁺ (left) and [Cu(**ALP**)(**L1.4**)]⁺ (right) on TiO₂.*

Figure 77 supports the suggestion that bulky substituents in the 6,6'-positions are the limiting factor for dye loading using anchoring ligand **ALP**. While the anode dyed with [Cu(**ALP**)(**L1.4**)]⁺ shows a rather pale colour, the photoanode stained with [Cu(**ALP**)(**L1.1**)]⁺ exhibits a much more intense colour. This difference in colour intensity is a hint that by using **ALP**, the limiting factor for dye uptake is the substituents in the 6,6'-positions.

II.6.2   ALP1 in combination with ancillary ligands L1.1-L1.6

The *heteroleptic* dyes [Cu(**ALP1**)(**L1.1-1.6**)]⁺ show an improvement in *Jsc* and *Voc* over the measuring period. The best performing dye on day 1 was [Cu(**ALP1**)(**L1.3**)]⁺ with an initial efficiency of 2.55% (or 38.5% relative to **N719**). The dye with the lowest η was [Cu(**ALP1**)(**L1.5**)]⁺ with an efficiency of 1.10%. On the last measuring day, [Cu(**ALP1**)(**L1.5**)]⁺ was the best dye with a conversion efficiency of 2.89% and a relative η of 48.5% with respect to **N719**. The dye exhibiting the lowest conversion efficiency was [Cu(**ALP1**)(**L1.6**)]⁺, which has the bulkiest substituents in the 6,6'-positions. In devices incorporating **ALP1** as anchoring ligand, the substituent's bulkiness does not seem to be the limiting factor for the cell performance. This could mean that by using **ALP1** in devices, we obtain information that relates directly to the potential of an implemented ancillary ligand whereas by using **ALP**, the results from devices simply reflect the bulkiness of the substituents in the 6,6'-positions.

II.7   Conclusion

The cell performance is enhanced by introducing a phenylene spacer in the anchoring ligands (e.g. on going from **ALP** to **APL1**). A comparison of anchoring ligands **ALP** and **ALP1** confirmed the results from Chapter I. Devices in which **ALP1** serves as anchoring ligand in all cases give better performances than their corresponding dyes with **ALP**. In order to save time, materials and costs, one can conclude that only **ALP1** from the currently available anchoring ligands should be used for future dye screenings.

The device performance was also significantly improved by using isobutyl (**L1.3**) or phenyl (**L1.5**) substituents in the 6,6'-positions of the ancillary ligand. It is important to note that devices containing the *heteroleptic* complex [Cu(**ALP1**)(**L1.5**)]$^+$ undergo a significant ripening effect and exhibit their full potential after a number of days. Whereas the introduction of phenyl substituents in the 6,6'-positions of the ancillary ligands leads to high performing devices, the further extension of the aromatic system in the 6,6'-substituents (e.g. on going from **L1.5** to **L1.6**) did not improve the efficiency and was, in fact, detrimental to device performance.

CHAPTER III: OPTIMIZING THE ATOM ECONOMY

III   Stepwise assembly on the surface

In this chapter the aim was to optimise the atom economy during the assembly process of Cu(I) based DSCs. Instead of using a solution of *homoleptic* copper(I) complex where during the ligand exchange process on the surface one equivalent of capping ligand is wasted, a two-step procedure was applied according to Hostettler[198].
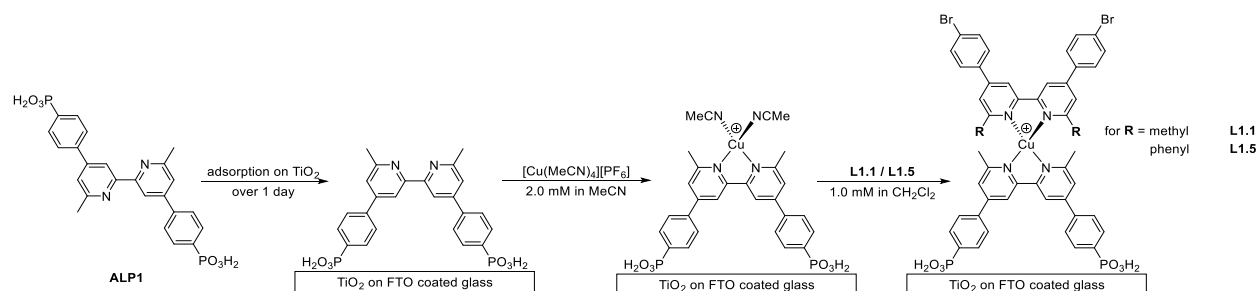
Scheme 17: Graphical representation of the stepwise assembly on the TiO₂ surface.

After the anchoring ligand is adsorbed on the TiO$_2$, the anode was immersed in a 2.0 mM solution of [Cu(MeCN)$_4$][PF$_6$] for 1 day. After removing the photoanode from the copper(I) solution and rinsing it with acetonitrile it was dried at 50°C with a heat gun. In the last step the anode was immersed in a 1.0 mM solution of ancillary ligand **L1.1** and **L1.5**.
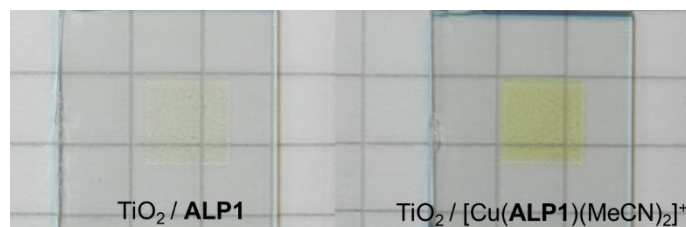
*Figure 78: Photoanodes treated with **ALP1** (left) and after the metallation with [Cu(MeCN)₄][PF₆] (right).*

Figure 78 shows the anode after the treatment in a solution of **ALP1** *vs.* that after metallation with [Cu(MeCN)$_4$][PF$_6$]. A clear difference in colour is observed from colourless to slightly yellow (e.g. on going from TiO$_2$/**ALP1** to TiO$_2$/**ALP1**/Cu/MeCN). This change in colour is a strong indication for copper(I) binding to the anchoring ligand. We propose the formation of [Cu(**ALP1**)(MeCN)$_2$]$^+$ as the intermediate surface bound complex. In the final step, the surface bound *heteroleptic* dye intermediate undergoes a ligand exchange by immersing the anodes in a 1.0 mM solutions of ancillary ligands (**L1.1** and **L1.5**). A change in colour was observed within a few minutes going from pale yellow to intense orange, forming the active dye [Cu(**ALP1**)(**L1.1/1.5**)]$^{+.}$

III.1 DSC performance

III.1.1 Parameters

dye	day	J_{sc} [mA/cm²]	V_{oc} [mV]	ff [%]	η [%]	rel. η [%]
[Cu(**L1.1**)(ALP)]⁺	**0**	5.98	498	73	2.17	27.2
[Cu(**L1.5**)(ALP1)]⁺	**0**	6.81	534	72	2.60	32.6
N719	**0**	16.97	660	71	7.98	100.0
[Cu(**L1.1**)(ALP)]⁺	**1**	6.30	512	73	2.36	28.5
[Cu(**L1.5**)(ALP1)]⁺	**1**	7.08	542	70	2.67	32.2
N719	**1**	16.93	681	72	8.29	100.0

Table 11: DSC parameters of cells made by the stepwise assembly for day 0 and day 1.

In Table 11 the parameters for DSCs that were prepared in a stepwise assembly are summarized. All cells exhibit a good *ff*. The device with capping ligand **L1.5** performs better than with **L1.1**, which is consistent with previous results (see Table 8 and Table 9). On going from day 0 to day 1, the cells improve slightly in performance. This improvement over time was also observed in earlier measurements (Table 8 and Table 9) for these dyes. For both cells, *Jsc* and *Voc* increase over time. More important than the increase in conversion efficiency is the gain in *Jsc*. While the device with **L1.1** starts with an initial $\eta = 2.17\%$ at day 0 and rises to $\eta = 2.36\%$ at day 1, the cell with ancillary ligand **L1.5** exhibits an initial efficiency of 2.60% which climbs to $\eta = 2.67\%$ on day 1.

Comparing the results from Table 11 with those from Table 8 and Table 9 one observes that devices that were prepared using the step-wise assembling approach show a higher initial efficiency than their corresponding cells where the convenient surface exchange was applied.

In both cases (stepwise and ligand exchange) the cells undergo an aging effect by showing an enhanced efficiency after some days compared to their initial conversion efficiency at day 0. Nevertheless, using the convenient methodology cells show a higher increase upon ripening. For ancillary ligand **L1.1** using the step-wise or the conventional assembly makes only a small difference in terms of efficiency. While using the step-wise approach, [Cu(**L1.1**)(ALP1)]⁺ reaches $\eta = 2.36\%$ or 28.5% relative to **N719**, compared to $\eta = 2.33\%$ or 28.4% rel. to **N719** (see Table 9) with the conventional methodology. For [Cu(**L1.5**)(ALP1)]⁺ there seems to be a difference for the two assembling strategies. Using the step-wise approach [Cu(**L1.5**)(ALP1)]⁺ reaches on day 1 a value of $\eta = 2.67\%$ (or 32.2% rel. to **N719**), while applying the classical ligand exchange method yields $\eta = 3.01\%$ (or 36.6% rel. to **N719** see Table 9).

III.1.2   JV and EQE curves
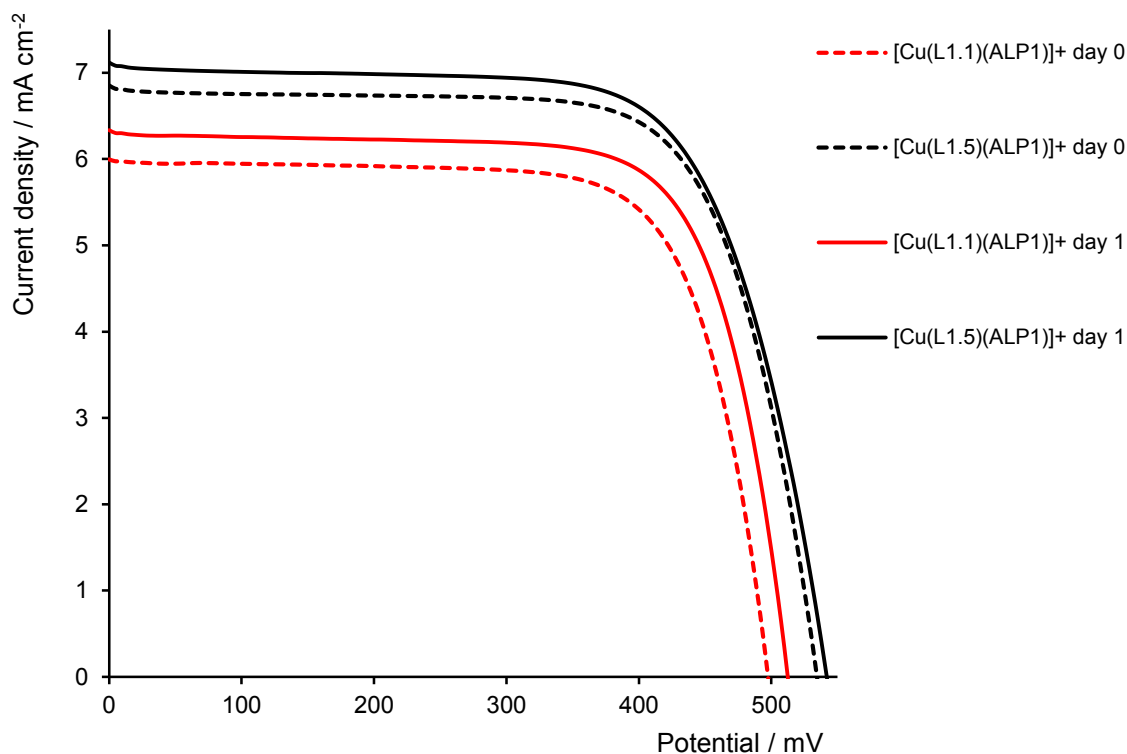
*Figure 79: JV-curves of [Cu(**ALP1**)(**L1.1**)]⁺ and [Cu(**ALP1**)(**L1.5**)]⁺ using the stepwise assembly method.*

The *JV*-curves in Figure 79 represent nicely the results from Table 11. The shape of the curves reflects the high fill factors for all cells. The slightly increasing *Jsc* and *Voc* represent the gain in efficiency over time, which is consistent with earlier results of these dyes (Table 9), although the initial increase in *Jsc* is much lower applying the stepwise assembly than using the conventional ligand exchange methodology (Figure 69).
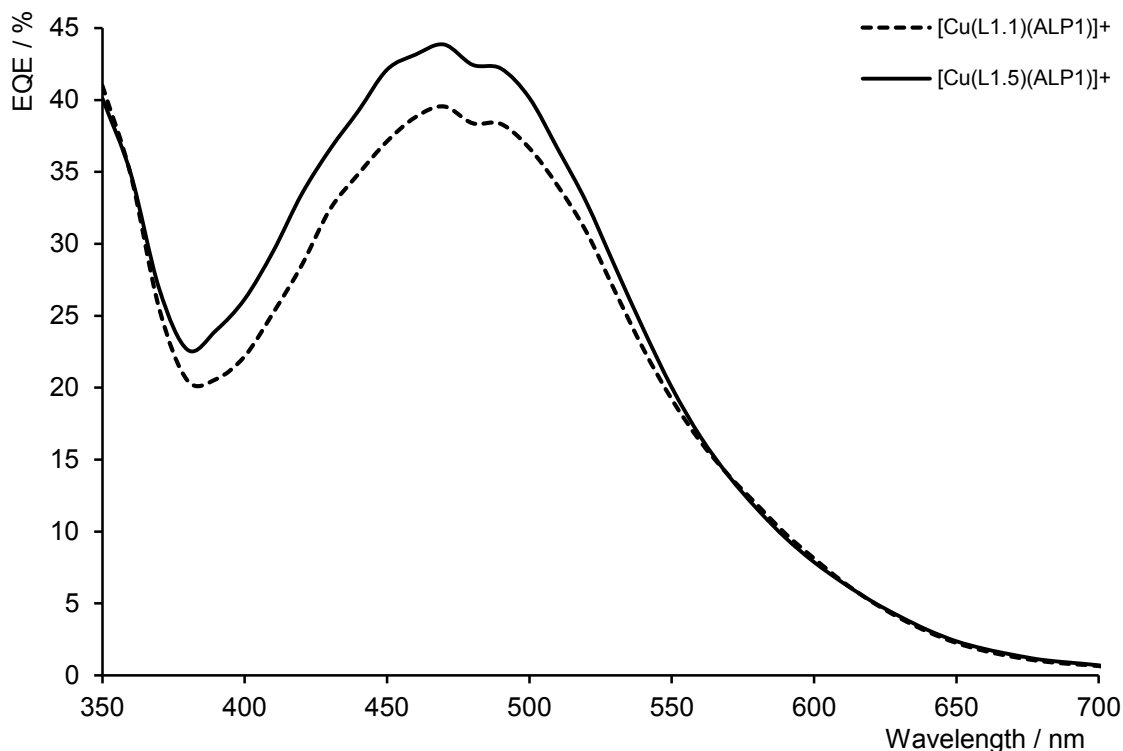
*Figure 80: EQE curves of [Cu(**ALP1**)(**L1.1**)]⁺ and [Cu(**ALP1**)(**L1.5**)]⁺ using the stepwise assembly method.*

Figure 80 reveals the origin of the enhanced performance of $[Cu(\mathbf{L1.5})(\mathbf{ALP1})]^+$ over $[Cu(\mathbf{L1.1})(\mathbf{ALP1})]^+$. The device with ancillary ligand **L1.5** exhibits a higher *EQE* over the whole spectrum than that with **L1.1**. This result is consistent with results obtained from the conventional ligand exchange method (see Figure 71). Independent of the assembling methodology applied for **L1.1**, the *EQE* λ_{max} at 470 nm exhibits ≈ 40% at day 0. In contrast, the DSC containing ancillary ligand **L1.5** shows a much higher *EQE* on day 0 using the stepwise assembly method than with the classical approach. While preparing the devices the classical way, **L1.5** exhibits an *EQE* of 28% at 470 nm, which is much lower than the *EQE* obtained from the stepwise assembly showing ≈ 44 % at 470 nm at day 0.

III.2   Discussion

The results obtained from the stepwise assembly show clearly that the initial performance of DSCs is significantly higher than compared to their corresponding devices obtained from the classical assembly. One of the reasons for this observation could be that the aggregation of dye molecules on the semiconductor surface is reduced by applying this new method.

In the last step of this methodology an appropriate solvent is chosen (CH_2Cl_2) to dissolve the ancillary ligand. Both copper(I) complexes ($[Cu(\mathbf{L1.1}/\mathbf{L1.5})_2)][PF_6]$) are soluble in CH_2Cl_2. While complex $[Cu(\mathbf{L1.5})_2][PF_6]$ was already dissolved in CH_2Cl_2 during the convenient ligand exchange procedure, for complex $[Cu(\mathbf{L1.1})_2][PF_6]$ acetonitrile was used during the ligand

exchange on the surface. In general, with any solvent that dissolves the free ancillary ligand, any accumulation or deposition of ligand on the semi-conductor surface or in the TiO$_2$ pores should be avoided. This is in contrast to the classical approach, applied for [Cu(**L1.1**)$_2$][PF$_6$] where the solvent (MeCN) was chosen to dissolve the *homoleptic* copper(I) complex but not the ligand on its own. Of course the solvent chosen to dissolve the complex would as well dissolve aggregations of the *homoleptic* complex. Since it was not chosen to dissolve the ligand on its own, the ancillary ligand that is lost during the ligand exchange might clog the pores of the semi-conductor. Any aggregation of *homoleptic* copper complex would then be hindered to be washed out of these pores due to the clogging. Another possible explanation for aggregation is the deposition of precipitated ligand on the TiO$_2$ which is released from the *homoleptic* complex during ligand exchange. This would not only block pores of the semi-conductor but would also cover already adsorbed dye molecules. While such aggregates and precipitates of free ligand would be detrimental to the device performance, one could assume a lower initial performance for cells prepared by the classical ligand exchange method than by the stepwise assembly. Since the assembled devices are filled with electrolyte that contains an ionic liquid, the aggregates and precipitations might be dissolved by this ionic liquid over time. This would lead to an increase in *Jsc* and global conversion efficiency. That is exactly what is seen by comparing the initial and final device performances of cells obtained from the stepwise assembly and the conventional ligand exchange method. The initial performances of devices prepared by applying the stepwise assembly are superior compared to those prepared by the classical method. Over time the cells prepared by the classical method improve much more than the ones obtained from the stepwise assembly. The final performances of the devices incorporating ancillary ligand **L1.1** are comparable in both methods. This leads to the assumption that aggregates formed using the classical setup are dissolved. The reason for the observation of ancillary ligand **L1.5** giving a lower conversion efficiency using the stepwise assembly is the much lower *Voc* compared to the classical approach (*i.e.* 542 mV with stepwise assembling *vs.* 611 mV with the classical approach). The origin of this reduced *Voc* could be due to enhanced charge recombination between oxidized species and electrons injected in TiO$_2$ electrodes.

Nevertheless, the device with ancillary ligand **L1.5** still shows a higher *Voc* upon applying the stepwise assembly than devices with **L1.1**. A possible explanation might be that the introduction of the phenyl groups in the 6,6'-positions has a positive effect on the electron lifetime due to a reduced molecular aggregation compared to **L1.1**. Similar effects upon the introduction of bulky substituents have been reported [199][200].

III.3   Conclusion

The stepwise assembly method is a valuable methodology to save material (ancillary ligand) that is wasted during the ligand exchange reaction on the surface with the classical approach. Another advantage is that devices start with a higher *Jsc* compared to those that are assembled using the classical fabrication. This leads to the conclusion that the structure of the functionally attached dyes on the surface is more ordered using the stepwise methodology than applying the classical ligand exchange. Nevertheless, the most important factor is the conversion efficiency. Since there was no difference for **L1.1** in the two methods, one can conclude that in terms of atom economy the stepwise assembly is the favoured way to attach the dye on the surface whereas for bulky substituents (**L1.5**) the higher conversion efficiency was obtained with the classical approach and therefore the stepwise assembly cannot be recommended.

III.4   Solar cell fabrication and characterisation III

The fabrication of DSCs was based on the method of Grätzel and coworkers[196]. The TiO_2 paste was prepared adapting the published method using a three-roll mill (50 EC, EXAKT, Germany), sonicator bath and terpineol (CAS: 8000-41-7). Each working electrode was made from an FTO glass plate (Solaronix TCO22-7, 2.2 mm thickness, sheet resistance $\approx 7\ \Omega$ square^{-1}), which was cleaned by sonicating in Hellmanex® surfactant (2% in milliQ water), and rinsed with milliQ water and EtOH. After a surface activation in a UV-O_3 system (Model 256-220, Jelight Company Inc) for 20 min, the FTO plates were immersed in aqueous $TiCl_4$ (40 mmol dm^{-3}) at 70 ºC for 30 min, and then washed with milliQ water and EtOH. The FTO plate was dried and a layer of TiO_2 paste was screen printed (90T, Serilith AG, Switzerland). The printed plate was kept in an EtOH chamber for 3 min to reduce surface irregularities of the printed layer and dried for 6 min at 125 ºC on a heating plate. The screen printing process was repeated 8 times and then the electrodes were gradually heated at 75 °C for 30 min, at 135 °C for 15 min, at 325 °C for 5 min, at 375 °C for 5 min, at 450 °C for 15 min and at 500 °C for 15 min. After the final sintering, the thickness of the TiO_2 layer was 14-16 μm (measured with Tencor Alpha-Step 500 profilometer). The annealed TiO_2 film was post-treated with 40 mM aqueous $TiCl_4$ solution (see above), rinsed with milliQ water and EtOH and sintered at 500 º C for 30 min.

The electrodes were cooled to ca. 80°C and immersed in a 1 mM DMSO solution of the anchoring ligand **ALP1** for 20 h. The colourless electrode was removed from the solution, washed with DMSO and EtOH and dried under a stream of N_2. After the anchoring ligand is adsorbed on the TiO_2, the anode was immersed in a 2.0 mM solution of [Cu(MeCN)$_4$][PF$_6$] for 1 day. After removing the photoanode from the copper(I) solution and rinsing it with

acetonitrile it was dried at 50 °C with a heat gun. In the last step the anode was immersed in a 1.0 mM CH$_2$Cl$_2$ solution of ancillary ligands **L1.1** and **L1.5**. The electrodes were removed from the solution and were washed with CH$_2$Cl$_2$ and dried under a stream of N$_2$. Each counter electrode was prepared from an FTO glass plate (Solaronix TCO22-7, 2.2 mm thickness, sheet resistance ≈7 Ω square^{-1}) with previously drilled hole. Residual organic impurities were removed by heating for 15 min at 500 ºC on a heating plate and the perforated plate was washed with water, then 0.1 M HCl solution in EtOH and finally ultrasonicated in an acetone bath for 15 min. It was dried on the heating plate at 500 °C for 15 min. The Pt catalyst was deposited on the FTO glass plate by coating with Platisol T (2 × 25.0 μL), obtained from Solaronix SA, and dried on a heating plate at 500 °C for 15 min. The dye-covered TiO$_2$ electrode and Pt counter-electrode were assembled using thermoplast hot-melt sealing foil (Solaronix, Meltonix 1170-25 Series, 25 microns thick) by heating while pressing them together. The electrolyte comprised LiI (0.1 mol dm^{-3}), I$_2$ (0.05 mol dm^{-3}), 1-methylbenzimidazole (0.5 mol dm^{-3}) and 1-butyl-3-methylimidazolinium iodide (0.6 mol dm^{-3}) in 3-methoxypropionitrile, and was introduced into the cell by vacuum backfilling. The hole on the counter electrode was finally sealed using the hot-melt sealing foil and a cover glass. The solar cell measurements and testing protocol were performed using fully masked cells. A black coloured copper sheet was used for masking with a single aperture of an average area of 0.06012 cm^2 (with a standard deviation of 1%) placed over the screen printed dye-sensitized TiO$_2$ circle. The area of the aperture in the mask was smaller than the active area of the dye-sensitized TiO$_2$ dot (0.288 cm^2). For complete masking, tape was also applied over the edges and rear of cell. Current density-voltage (IV) measurements were made by irradiating from behind using a light source SolarSim 150 (100 mW cm^{-2} = 1 sun). The power of the simulated light was calibrated by using a reference Si photodiode. The standard dye N719 was purchased from Solaronix. The quantum efficiency measurements were performed on a Spe-Quest quantum efficiency setup from Rera Systems (Netherlands) equipped with a 100 W halogen lamp (QTH) and a lambda 300 grating monochromator from Lot Oriel. The monochromatic light was modulated to 3Hz using a chopper wheel from ThorLabs. The cell response was amplified with a large dynamic range IV converter from CVI Melles Griot and then measured with a SR830 DSP Lock-In amplifier from Stanford Research.

CHAPTER IV: THE INFLUENCE OF DYE CONCENTRATION

IV A gradual change of dye concentration

In the literature,[191][192][193] the observed ripening effect of DSCs is a known phenomenon and is often explained in terms of reorganisation and disaggregation of dye molecules on the semi-conductor surface. Since it is desirable that DSCs exhibit their maximum performance immediately after assembling, it was decided to investigate whether aggregation could be avoided by using more dilute dye solutions.

Grätzel[191] states that dye aggregation of **N719** can be excluded and dyes can be adsorbed as monomers on the semi-conductor surface by using suitably dilute solutions of the ruthenium dyes. In this Chapter, our main attention is directed at the effect of different concentrations of *homoleptic* copper(I) dye solutions. A second variable was the time that photoanode was immersed in either the anchoring ligand **ALP1** or the homoleptic dye [Cu(**L2.1**)$_2$][PF$_6$].
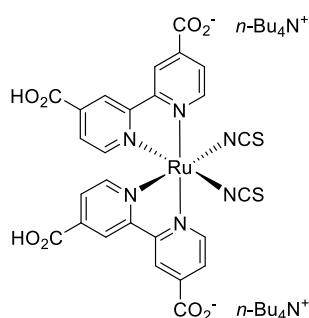
*Scheme 18: Ru(II) based dye, **N719**.*

IV.1 Set 1: 1 day in ALP1, 3 days in dye

In our first set of DSCs, the photoanode was immersed for 1 day in a 1.0 mM solution of **ALP1** in DMSO, followed by 3 days in an MeCN solution of [Cu(**L2.1**)$_2$][PF$_6$]. For the dye solution four different concentrations were chosen (2.0 mM, 1.0 mM, 0.5 mM and 0.1 mM).
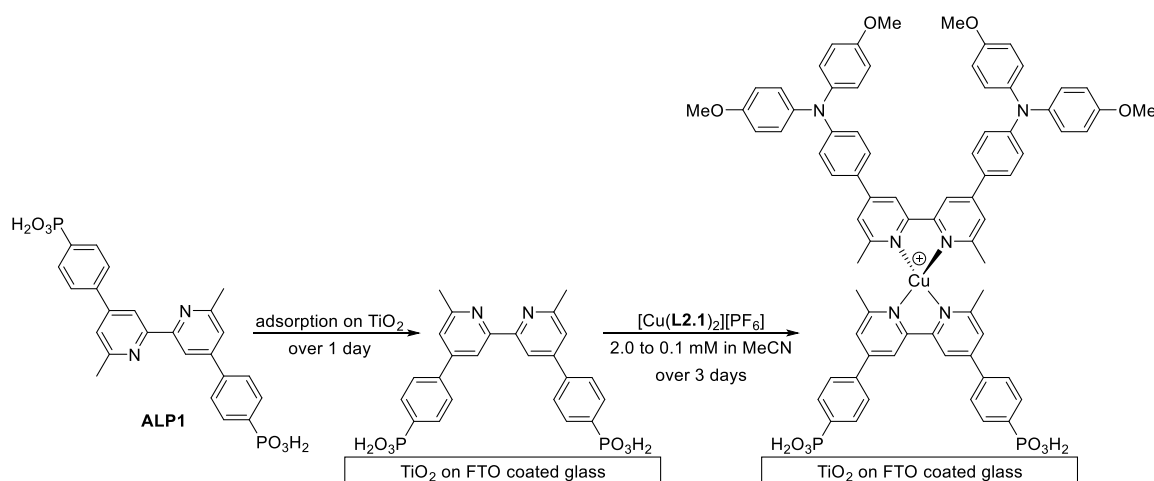
Scheme 19: Schematic presentation of the first trial.

In Scheme 19 a schematic summary of the first test set is represented. The anchoring ligand **ALP1** is adsorbed on the TiO$_2$ surface of a FTO coated glass plate. The *homoleptic* Cu(I)

complex [Cu(**L2.1**)$_2$][PF$_6$] undergoes an exchange with the anchoring ligand which is adsorbed on the semiconductor surface forming a new *heteroleptic* Cu(I) complex.

IV.1.1   DSC parameters set 1

Since Grätzel[191] suggests that the adsorption of Ru(II) dyes from dilute solutions (<0.4 mM) leads to an adsorbed monolayer of sensitizer on the TiO$_2$ surface, a 0.3 mM ethanol solution of **N719** was used for the preparation of the internal standard cell. In Table 12, the concentrations correspond to the *homoleptic* copper(I) dye and the **N719** solutions.

dye	conc. [mM]	day	J_{sc} [mA/cm^2]	V_{oc} [mV]	ff [%]	η [%]	rel. η [%]
[Cu(**L2.1**)(**ALP1**)]$^+$	**2.0**	**0**	2.10	535	72	0.81	10.0
[Cu(**L2.1**)(**ALP1**)]$^+$	**1.0**	**0**	3.24	511	73	1.21	14.9
[Cu(**L2.1**)(**ALP1**)]$^+$	**0.5**	**0**	4.09	501	73	1.51	18.5
[Cu(**L2.1**)(**ALP1**)]$^+$	**0.1**	**0**	4.55	489	72	1.61	19.7
N719	**0.3**	**0**	17.47	641	73	8.15	100.0
[Cu(**L2.1**)(**ALP1**)]$^+$	**2.0**	**1**	3.69	531	73	1.44	17.0
[Cu(**L2.1**)(**ALP1**)]$^+$	**1.0**	**1**	3.93	507	73	1.46	17.3
[Cu(**L2.1**)(**ALP1**)]$^+$	**0.5**	**1**	4.29	503	73	1.59	18.8
[Cu(**L2.1**)(**ALP1**)]$^+$	**0.1**	**1**	4.48	485	72	1.57	18.6
N719	**0.3**	**1**	17.45	663	73	8.45	100.0
[Cu(**L2.1**)(**ALP1**)]$^+$	**2.0**	**2**	3.67	516	73	1.39	16.9
[Cu(**L2.1**)(**ALP1**)]$^+$	**1.0**	**2**	3.90	503	73	1.44	17.5
[Cu(**L2.1**)(**ALP1**)]$^+$	**0.5**	**2**	4.37	509	73	1.63	19.9
[Cu(**L2.1**)(**ALP1**)]$^+$	**0.1**	**2**	4.57	494	72	1.62	19.7
N719	**0.3**	**2**	17.05	664	73	8.22	100.0
[Cu(**L2.1**)(**ALP1**)]$^+$	**2.0**	**3**	3.83	528	73	1.49	18.2
[Cu(**L2.1**)(**ALP1**)]$^+$	**1.0**	**3**	4.02	508	74	1.51	18.4
[Cu(**L2.1**)(**ALP1**)]$^+$	**0.5**	**3**	4.36	508	73	1.63	19.9
[Cu(**L2.1**)(**ALP1**)]$^+$	**0.1**	**3**	4.56	492	72	1.61	19.7
N719	**0.3**	**3**	17.02	665	72	8.19	100.0

*Table 12: Parameters for set 1. 1 day in a 1.0 mM solution of **ALP1** and 3 days in a solution of [Cu(**L2.1**)$_2$][PF$_6$].*

In Table 12 the DSCs' parameters are given over a measuring period of 4 days. Some clear trends arise from set 1. On day 0 the best efficiency is achieved with the most dilute dye solution (0.1 mM η = 1.61 %). The observed trend for day 0 is that the more dilute the dye solution is, the higher the values of *Jsc* and efficiency. In contrast, there is a direct correlation between dye concentration and *Voc*: the highest *Voc* was achieved with the most concentrated solutions. This

trend is more or less consistent over the whole measuring period. Another important observation is that while cells obtained from 2.0, 1.0 and 0.5 mM dye solutions improve over time (not only in *Jsc* but also in conversion efficiency), the device that was obtained from the most dilute solution (0.1 mM) exhibits a constant efficiency over the whole time.

Figure 81: 3D-bar diagram shows the evolution in efficiency over time (on going from day 0 to day 3).

In Figure 81 the improvement in efficiency over time for the different devices obtained from the four dye concentrations is displayed. One can clearly see that the device obtained from 0.1 mM solution exhibits a steady efficiency over the measuring period. For the cell prepared from the 0.5 mM solution of [Cu(**L2.1**)$_2$][PF$_6$], only a minor improvement in conversion efficiency is reported (*i.e.* on going from η = 1.51% to 1.63% for day 0 and day 3). For DSCs where a 1.0 mM solution of the *homoleptic* complex was used for the ligand exchange, a clear gain in efficiency is observed. It improves from η = 1.21 % on day 0 to η = 1.51 % on day 3. However its performance is still lower than for DSCs prepared from 0.5 and 0.1 mM solutions. The most drastic increase in efficiency occurs for the device prepared from the most concentrated dye solution (2.0 mM). Its initial conversion efficiency for day 0 was very poor and reached only η = 0.81 %. By day 1, it performed much better and exhibited an efficiency of 1.44%, which is 78% more than on day 0. Over the following days (on going from day 1 to day 3) the device only improved slightly and showed a final efficiency of 1.49%, which is comparable to the cell prepared from a 1.0 mM solution. Comparing the performance from day 3, one can say that devices obtained from 0.1 and 0.5 mM dye solutions perform on a similar level. Cells in which the more concentrated dye solutions were used (1.0 and 2.0 mM) exhibit a similar conversion efficiency.
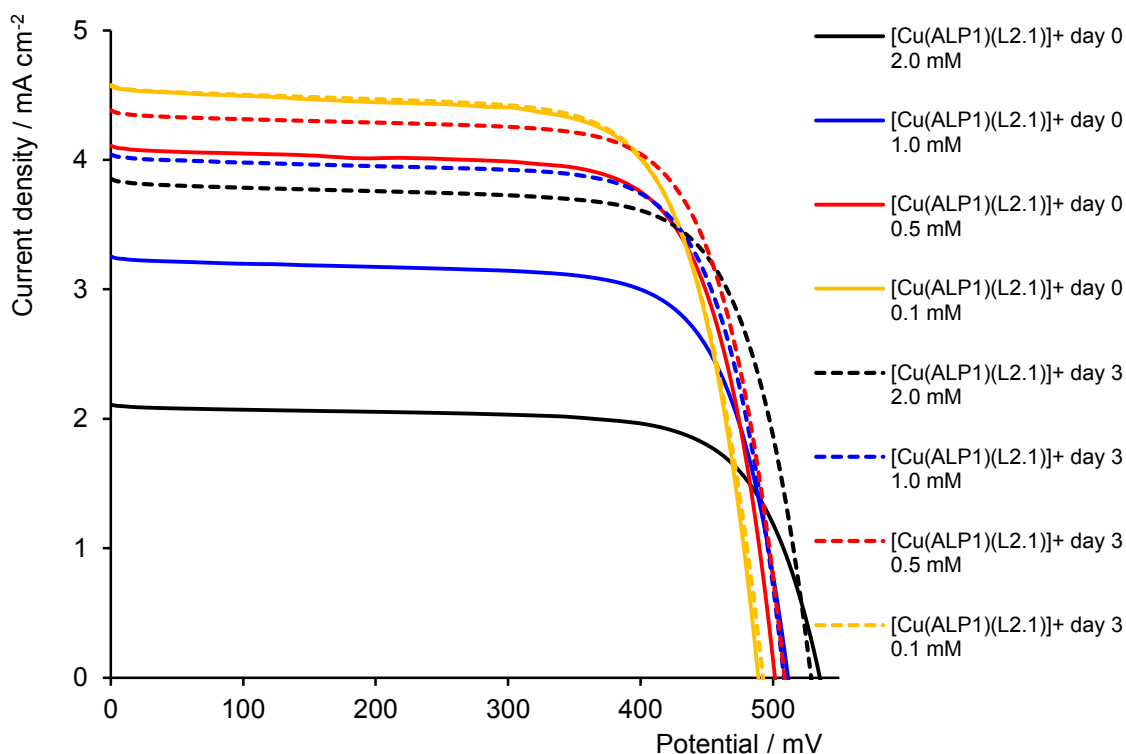
Figure 82: JV-curves of set 1. A comparison of performances on day 0 and day 3.

Figure 82 gives a more detailed insight into the improvement over time for set 1. Comparing values of *Jsc* from day 0 and day 3 the following order can be observed. The device prepared from the most concentrated solution (2.0 mM) improves more than any other cell. Its initial *Jsc* was measured as 2.10 mA cm^{-2} on day 0 and rose to 3.83 mA cm^{-2} on day 3. This is a gain of about 82% in short-circuit-current density. For the DSC prepared from a 1.0 mM solution of the *homoleptic* complex [Cu(**L2.1**)$_2$][PF$_6$], a clear improvement in *Jsc* was observed. On going from day 0 to day 3 it improved its initial *Jsc* from 3.24 mA cm^{-2} to 4.02 mA cm^{-2}. This corresponds to a gain in short-circuit-current density of ≈ 24%. The device obtained from a 0.5 mM solution shows only a minor increase in *Jsc*. On day 0 a short-circuit-current density of 4.09 mA cm^{-2} was measured and upon ripening a *Jsc* of 4.36 mA cm^{-2} was recorded. This corresponds to a relative increase of only ≈ 7% in *Jsc*. For the cell that was prepared from the most dilute solution of *homoleptic* complex [Cu(**L2.1**)$_2$][PF$_6$] (0.1 mM) no change in *Jsc* on going from day 0 to day 3 was recorded. On day 0, a short-circuit-current density of 4.55 mA cm^{-2} was measured, on day 3, 4.56 mA cm^{-2} was recorded.

When considering the open-circuit voltage, the following trends can be detected. On going from day 0 to day 3, the *Voc* for each device stayed approximately constant. Additionally, an ordering of *Voc* is noticed. The device produced from the most concentrated solution (2.0 mM) exhibits a *Voc* of 535 mV on day 0, which is higher than any other open-circuit voltage of the other cells. The lowest *Voc* of this set shows the cell prepared from a 0.1 mM dye solution.
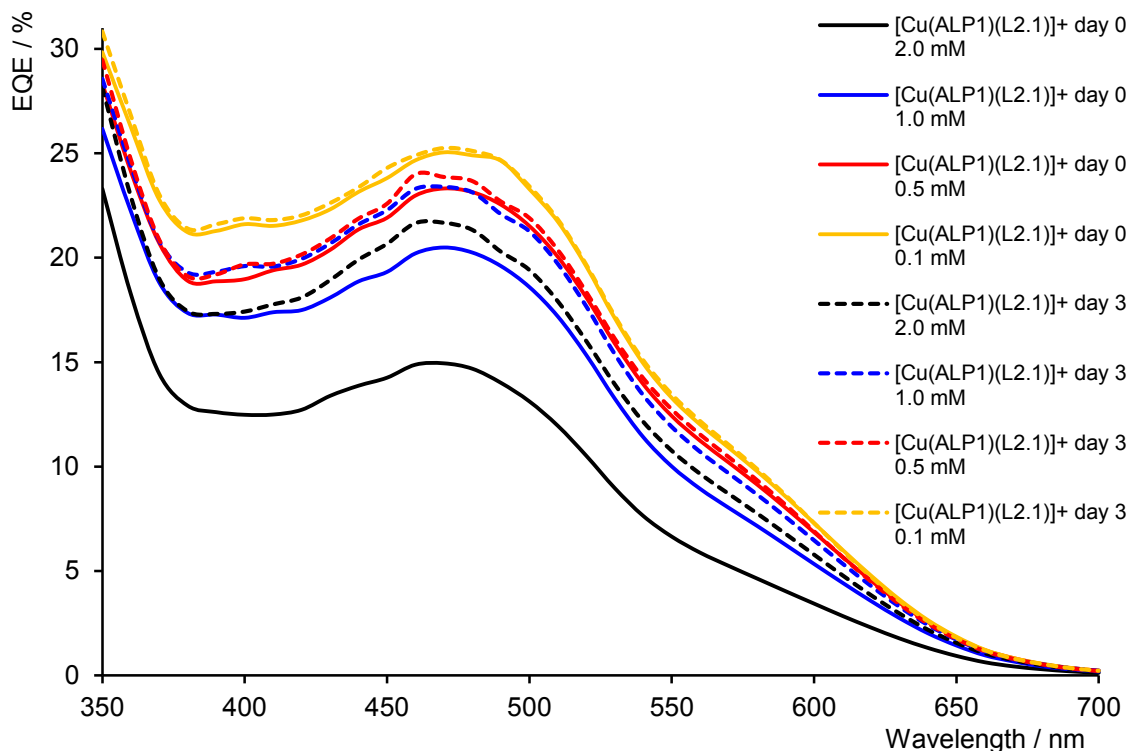
Figure 83: EQE curves for set 1. A comparison of day 0 and day 3.

The *EQE* curves of set 1 (see Figure 83) represent the evolution in *Jsc* over the measuring time. Comparing the curves for day 0 (solid lines) the following trends are observed. All cells exhibit a similar curve shape with a λ_{max} at 470 nm. The highest *EQE* over the whole spectrum is obtained by the device prepared from the most dilute dye solution (0.1 mM) where an *EQE* of ≈ 25% was measured at λ_{max} = 470 nm. The second highest *EQE* was achieved from the device prepared from a 0.5 mM dye solution, exhibiting an *EQE* of 23%. The second lowest *EQE* on day 0 was measured with the device prepared from a 1.0 mM dye solution showing an *EQE* of 20%. The lowest *EQE* was obtained from the cell prepared from the most concentrated dye solution exhibiting an *EQE* of only 15% on day 0. On day 3 the same order for *EQE* as for day 0 was observed. The highest *EQE* is obtained from the device prepared from a 0.1 mM dye solution but its *EQE* did not change on going from day 0 to day 3 (25% at 470 nm on both days). The *EQE* for the cell prepared from a 0.5 mM dye solution improves only slightly and rises to 24% on day 3. The DSC obtained from a 1.0 mM copper(I) complex solution clearly improves, showing an *EQE* of 23% on day 3. The most drastic increase in *EQE* is for the cell in which a 2.0 mM dye solution was used for the ligand exchange. Its *EQE* increased from 15% on day 0 to 22% on day 3. This increase in *EQE* over time is consistent with the increase *Jsc* on going from day 0 to day 3.

IV.2   Set 2: 3 days in ALP1, 1 day in dye

In the second set of cells, the photoanode was immersed for 3 days in a 1.0 mM solution of **ALP1** in DMSO, followed by 1 day in a solution of [Cu(**L2.1**)$_2$][PF$_6$] in acetonitrile. For the *homoleptic* copper(I) complex solution, four different concentrations were chosen (2.0 mM, 1.0 mM, 0.5 mM and 0.1 mM).

IV.2.1   DSC parameters set 2

dye	conc. [mM]	day	J_{sc} [mA/cm^2]	V_{oc} [mV]	ff [%]	η [%]	rel. η [%]
[Cu(**L2.1**)(**ALP1**)]$^+$	2.0	0	3.82	493	74	1.39	17.1
[Cu(**L2.1**)(**ALP1**)]$^+$	1.0	0	3.94	495	74	1.44	17.7
[Cu(**L2.1**)(**ALP1**)]$^+$	0.5	0	4.22	495	75	1.56	19.1
[Cu(**L2.1**)(**ALP1**)]$^+$	0.1	0	4.21	492	74	1.53	18.8
N719	0.3	0	17.28	650	72	8.14	100.0
[Cu(**L2.1**)(**ALP1**)]$^+$	2.0	1	4.01	517	74	1.54	18.7
[Cu(**L2.1**)(**ALP1**)]$^+$	1.0	1	4.23	495	74	1.55	18.7
[Cu(**L2.1**)(**ALP1**)]$^+$	0.5	1	4.36	495	74	1.60	19.4
[Cu(**L2.1**)(**ALP1**)]$^+$	0.1	1	4.22	497	74	1.56	18.9
N719	0.3	1	17.29	663	72	8.25	100.0
[Cu(**L2.1**)(**ALP1**)]$^+$	2.0	2	3.91	521	75	1.52	18.2
[Cu(**L2.1**)(**ALP1**)]$^+$	1.0	2	4.27	499	74	1.58	18.8
[Cu(**L2.1**)(**ALP1**)]$^+$	0.5	2	4.29	503	75	1.61	19.3
[Cu(**L2.1**)(**ALP1**)]$^+$	0.1	2	4.24	501	74	1.57	18.8
N719	0.3	2	17.27	668	73	8.37	100.0

*Table 13: Parameters for set 2. 3 days in a 1.0 mM solution of **ALP1** and 1 day in a solution of [Cu(**L2.1**)$_2$][PF$_6$].*

Parameters obtained for set 2 are given in Table 13. The range of measured efficiencies is very small. The only cell that did not improve its *Jsc* over time was that from the 0.1 mM dye solution. All devices gain in *Voc* over the measuring period and all DSCs show a high *ff* of 74-75%. While cells obtained from the 0.1 and 0.5 mM dye solutions only show a minor gain in conversion efficiency, devices from the 1.0 and 2.0 mM solutions improve much more over time. The best performing dye on day 0 was prepared from a 0.5 mM solution, exhibiting $\eta =$ 1.56%. The lowest efficiency on day 0 was obtained with the cell where a 2.0 mM solution was used for the ligand exchange on the surface. On day 2, the best performing cell is still obtained from a 0.5 mM dye solution exhibiting 1.61% conversion efficiency. Cells prepared from 0.1

and 1.0 mM solutions perform only slightly worse, showing $\eta = 1.57$ and 1.58%, respectively. The lowest efficiency was measured with the device prepared from a 2.0 mM dye solution.
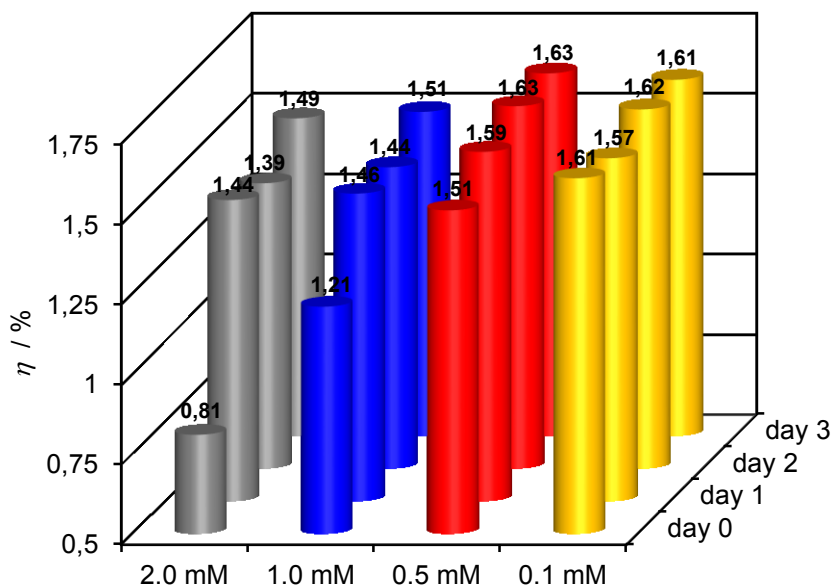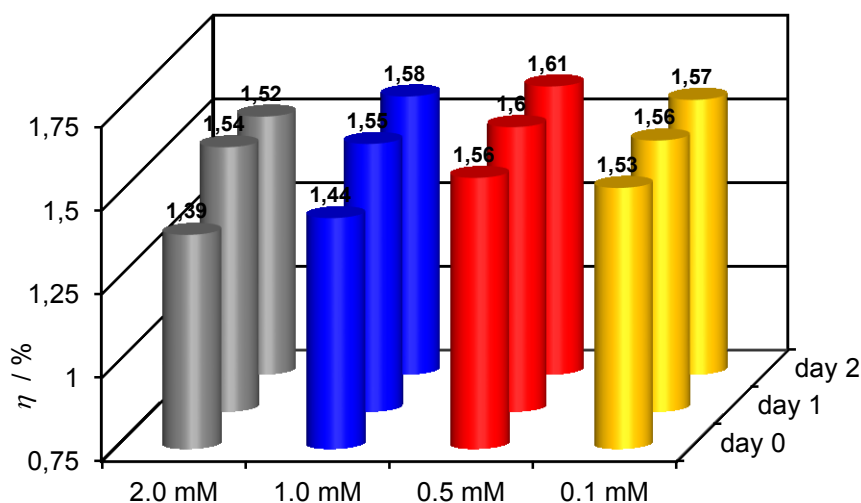

Figure 84: 3D-bar diagram shows the evolution in efficiency over time (on going from day 0 to day 2).

In Figure 84 the improvement in efficiency over time for the different devices obtained from the four dye concentrations is shown. It is obvious that devices obtained from 0.1 and 0.5 mM solutions of *homoleptic* complex [Cu(**L2.1**)$_2$][PF$_6$] show a higher initial efficiency at day 0 than those from 2.0 and 1.0 mM solutions. With ongoing time, cells where 2.0 and 1.0 mM dye solutions were used for the ligand exchange improve more in conversion efficiency than those obtained from 0.5 and 0.1 mM solutions. In fact, the improvement in η for the two lowest concentrations is very small and could be taken as statistically insignificant. The DSC prepared from the 2.0 mM solution shows an initial η of 1.39%, which increases to 1.52% on day 2. The cell from a 1.0 mM solution shows approximately the same increase in conversion efficiency going from $\eta = 1.44$ % on day 0 to 1.58% on day 2. The DSC prepared from a 0.5 mM dye solution is the best performing cell and shows an insignificant gain in η from 1.56% on day 0 to 1.61% on day 2. Similarly, the device prepared from a 0.1 mM dye solution only improves slightly from $\eta = 1.53$% on day 0 to 1.57% on day 2, again statistically not meaningful. On the final measuring day, three devices (from the 0.1, 0.5 and 1.0 mM dye solutions) show comparable performances and only the DSC prepared from the most concentrated solution (2.0 mM) exhibits a clearly reduced efficiency compared to the others.
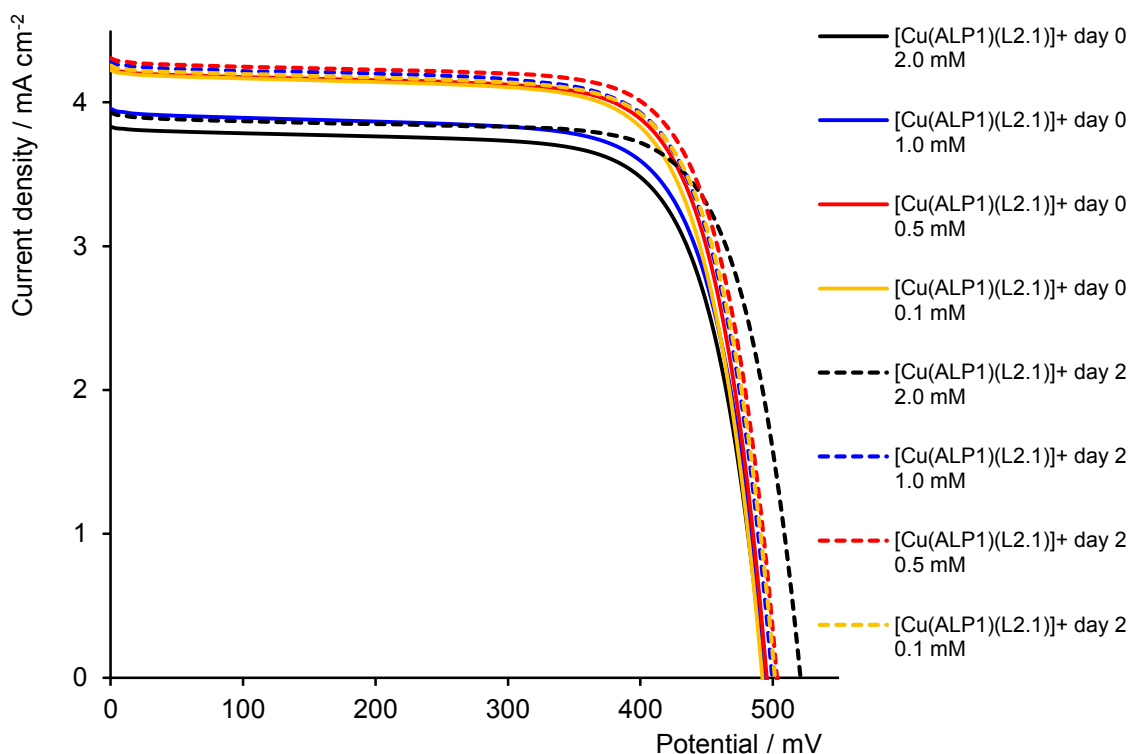
Figure 85: JV-curves of set 2. A comparison of performances on day 0 and day 2.

In the *JV*-curves for set 2, the improvement over time basically follows the gain in *Jsc* on going from day 0 to day 2. On day 0 (solid lines), cells from 0.1 and 0.5 mM copper(I) complex solutions show comparable *Jsc* values that are clearly higher than devices from 1.0 and 2.0 mM dye solutions. On day 2, only the cell prepared from the most concentrated solution (2.0 mM) exhibits a clearly reduced *Jsc* compared to the other cells.

Concentrating on day 0, *Voc* values for all cells are comparable (492 - 495 mV). On going from day 0 to day 2, the open-circuit voltage increases for all cells. While cells prepared with 0.1, 0.5 and 1.0 mM dye solutions show comparable *Voc* (499 – 503 mV), the device assembled with a 2.0 mM dye solution exhibits a higher *Voc* (521 mV) than the other cells. The shape of all curves reflects the general high *ff* of all devices.
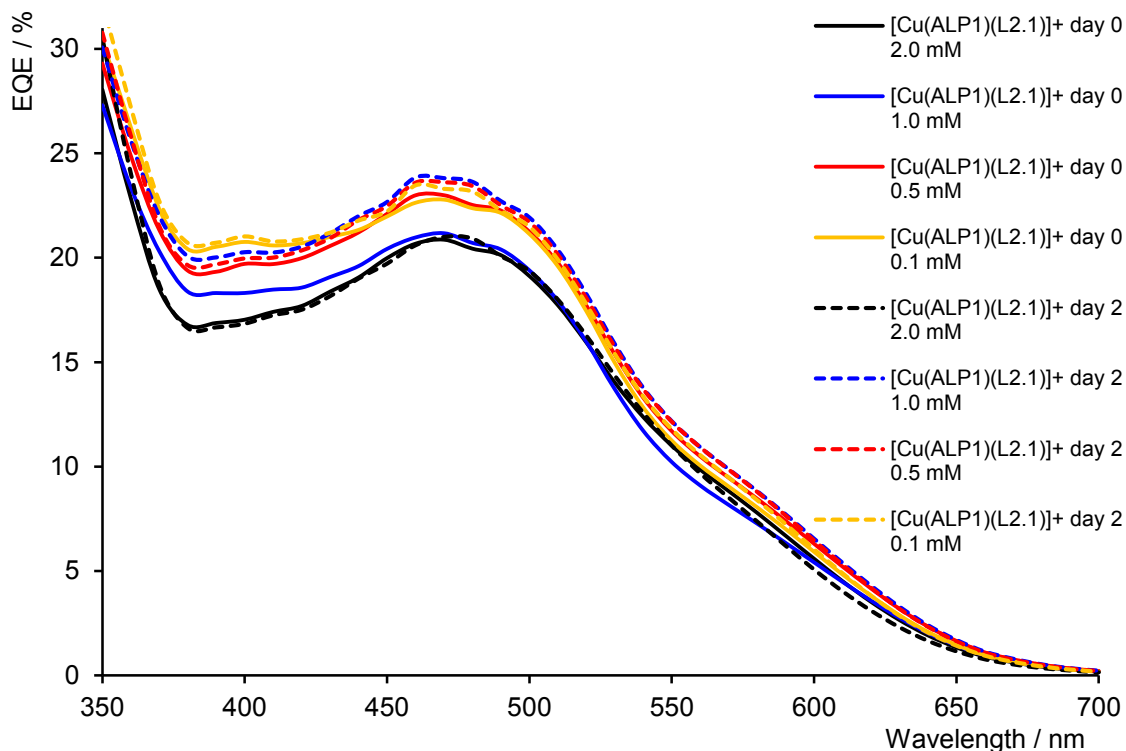
Figure 86: EQE curves for set 2. A comparison of day 0 and day 3

The *EQE* curves demonstrate the improvement in *Jsc* over time. All curves exhibit the same shape with a λ_{max} at $\approx$ 470 nm. On day 0 (solid lines), the cells obtained from 2.0 and 1.0 mM dye solutions show a lower *EQE* ($\approx$ 21%) than those obtained from 0.5 and 0.1 mM solutions ($\approx$ 23%). This observation is consistent with the measured *Jsc* on day 0 (see Table 13). On day 2 the device where a 2.0 mM dye solution was used for the ligand exchange displays the lowest *EQE* (21%) for all cells of this set. Its *EQE* stayed more or less constant over the whole spectrum, which is consistent with the observation that its *Jsc* did not change on going from day 0 to day 2. The DSC prepared from a 1.0 mM solution improved the most in *EQE* compared to the other cells of this set. It shows a max *EQE* of roughly 24% at day 2, the highest of this set, which is consistent with the measured *Jsc* of this cell and is the highest short-circuit-current density of these four cells. The cells obtained from 0.5 and 0.1 mM dye solutions show only a small change in their *EQE* maxima, displaying both about 23.5% *EQE* on day 2. Since there is only a minor gain in their *EQE*, this observation is consistent with the measured *Jsc* values, which also improve slightly on going from day 0 to day 2.

IV.3 Discussion

IV.3.1 Set 1

The results from set 1 for the copper(I) dyes are consistent with the literature[191] concerning ruthenium (II) dyes, *i.e.* electrodes which are exposed to less concentrated dye solutions exhibit higher short-circuit-current density. The observation of an increasing *Voc* upon using more concentrated dye solutions is also consistent with the literature[201]. The higher current observed for more dilute dye solutions indicates that dye aggregation on the semiconductor could be prevented. Minimizing aggregation of dye molecules on the surface is consistent with the adsorbed dye molecules being ordered immediately upon making the DSCs, and this leads to reduced intermolecular quenching [202] and therefore an increased injection of absorbed photons. Focusing on *Voc*, the results show that the open-circuit voltage increases upon using a more concentrated dye solution. A possible explanation could be the amount of non-anchored *homoleptic* copper(I) complex on the TiO_2 surface and in the TiO_2 pores increases. Any *homoleptic* complex near the semi-conductor surface could prevent the redox mediator (I^-/I_3^-) from reaching the TiO_2 surface [203][204]. This could have a positive effect on the *Voc* due to a possible blocking effect of the charge recombination between oxidized species and injected electrons. A significant retardation of charge recombination of injected electrons with oxidized species might then occur. Another reason could be a movement of the quasi *Fermi*-level of the semiconductor with respect to the redox potential of the electrolyte [205].

IV.3.2 Set 2

The results from set 2 illustrate that the trends in the short-circuit-current density are the same as those from set 1. The device prepared from the most concentrated dye solution (2.0 mM) exhibits the lowest *Jsc* for day 0 and day 2. The reason for this decreased *Jsc* could be that using a more concentrated dye solution leads to increased dye aggregation on TiO_2 and therefore to a reduced injection of electrons [202]. The reason for the enhanced *Voc* for the most concentrated dye solution could be the same as for set 1. The exposure to more *homoleptic* complex could lead to an increased aggregation of such molecules on the semi-conductor. These aggregates slow down the rate of charge recombination between electrons in TiO_2 and oxidized species [206].

IV.3.3 Comparison of set 1 vs. set 2

Comparing the data from set 1 with set 2 leads us to observe some similarities. In both cases the device from the most concentrated dye solution leads to the lowest short-circuit-current density but on the other hand, the highest open-circuit voltage. Devices in which a dilute dye concentration was applied for the ligand exchange reaction showed a more or less constant performance in terms of the conversion efficiency.

The effect of the dye concentration on the ripening effect was more obvious in set 1 but also visible in set 2. In both sets, the device which showed the most improvement over time was obtained from a 2.0 mM dye solution. While in set 1 the *Jsc* rose from 2.10 mA cm^{-2} on day 0 to 3.83 mA cm^{-2} on day 3 (a relative increase of 82%), in set 2 it rose from 3.82 mA cm^{-2} on day 0 to 3.91 mA cm^{-2} on day 2. A possible reason for the reduced impact of the dye concentration upon the ripening effect is probably the difference in the exposure time. While set 1 was immersed for 3 days in a solution of *homoleptic* Cu(I) complex, set 2 was only treated for 1 day with the dye solution. During the elongated treatment time of the photoanode in the solution more aggregates might have formed. This would explain the higher initial conversion efficiency from the most concentrated dye solution from set 2 compared to the one from set 1. By using the more dilute copper(I) complex solutions, the aggregation of molecules tends to be avoided in both sets.

IV.4 Conclusion

An influence of the concentration upon initial and final DSC performance was reported. By using a 0.1 mM solution of *homoleptic* copper(I) complex for the ligand exchange, the devices exhibit their full potential from the first measurement onwards. Cells from these dilute solutions performed with an approximately steady conversion efficiency over the whole measuring period of three days. The more concentrated the dye solution was, the lower was the initial performance of a device. Although the cells from the 2.0 mM dye solutions improved over time, they could not reach the level of efficiency as those prepared from the most dilute solutions.

In conclusion, it is an advantage to use more dilute copper(I) dye solutions for the ligand exchange because these devices reveal their full potential from the beginning. Another advantage of employing more dilute solutions is the reduced demand of materials (*e.g.* *homoleptic* complex to prepare a solution).

IV.5 DSC fabrication and measurements

DSCs were prepared adapting the method of Grätzel and coworkers [196][197]. For the photoelectrode, Solaronix Test Cell Titania Electrodes made from TCO22-7 FTO coated glass, prepared by screen-printing for a homogenous surface using Ti-Nanoxide pastes, active layer from Ti-Nanoxide T/SP covered by a reflective layer of Ti-Nanoxide R/SP, active area: 6×6 mm, thickness: titania layer 9 μm plus scattering layer 3 μm were used. The electrodes were rinsed with EtOH and sintered at 450 °C for 30 min, then cooled to ca. 80 °C and immersed in a 1 mM DMSO solution of the anchoring ligand **ALP1** for 24 h. The colourless electrode was removed from the solution, washed with DMSO and EtOH and dried with a heat gun at 60 °C. The electrode with adsorbed anchoring ligand was immersed in either a 2.0, 1.0, 0.5 or 0.1 mM CH_2Cl_2 solution of each homoleptic copper(I) complex for ca. 68 h. Each reference cell was prepared by dipping a commercial electrode in a 0.3 mM EtOH solution of standard dye N719 (Solaronix) for ca. 68 h. The electrodes were removed from the solution and were washed with the corresponding solvent and dried with a heat gun at 60 °C.

For the counter electrode, Solaronix Test Cell Platinum Electrodes (made from TCO22-7 FTO coated glass) were used. Residual organic impurities were removed by heating for 30 min at 450 °C on a heating plate.

The dye-covered TiO_2 electrode and Pt counter-electrode were assembled using thermoplast hot-melt sealing foil (Solaronix Test Cell Gaskets) by heating while pressing them together. The electrolyte was a mixture of LiI (0.1 mol dm^{-3}), I_2 (0.05 mol dm^{-3}), 1-methylbenzimidazole (0.5 mol dm^{-3}) and 1-butyl-3-methylimidazolinium iodide (0.6 mol dm^{-3}) in 3-methoxypropionitrile; it was introduced into the DSC by vacuum backfilling. The hole on the counter electrode was sealed using hot-melt sealing foil (Solaronix Test Cell Sealings) and a cover glass (Solaronix Test Cell Caps).

The solar cell measurements and testing protocol were performed using fully masked cells. A black coloured copper sheet was used for masking with a single aperture of an average area of 0.06012 cm^2 (with a standard deviation of 1%) placed over the screen printed dye-sensitized TiO_2 circle. The area of the aperture in the mask was smaller than the active area of the dye-sensitized TiO_2 dot (0.36 cm^2). For complete masking, tape was also applied over the edges and rear of cell.

Measurements were made by irradiating from behind using a light source SolarSim 150 (100 mW cm^{-2} = 1 sun). The power of the simulated light was calibrated by using a reference Si cell. The quantum efficiency measurements were performed on a Spe-Quest quantum efficiency setup from Rera Systems (Netherlands) equipped with a 100 W halogen lamp (QTH) and a

lambda 300 grating monochromator from Lot Oriel. The monochromatic light was modulated to 3Hz using a chopper wheel from ThorLabs. The cell response was amplified with a large dynamic range IV converter from CVI Melles Griot and then measured with a SR830 DSP Lock-In amplifier from Stanford Research.

CHAPTER V: ENHANCING THE PHOTON ABSORBANCE

V Extending the aromatic system

In this chapter the extension of the π-system of the ancillary ligand by introduction of first (**L2.1-2.6**) and second generation dendrimers (**L3.1-3.6**) and their incorporation in copper(I) dyes in DSCs is described. Triarylamines are widely used in organic dyes for solar cells in order to achieve high molar extinction coefficients and broad spectral absorption of visible light[207][208].

In addition to extending the π-system, the substitution pattern in the 6,6'-positions of the bipyridine of the ancillary ligand is also changed. These groups are required for the stabilization of the copper(I) centre[209].

For L2 series: for R_1 = methyl **L2.1**, n-butyl **L2.2**, isobutyl **L2.3**, n-hexyl **L2.4**, phenyl **L2.5**, 2-naphthyl **L2.6**

For L3 series: for R_1 = methyl **L3.1**, n-butyl **L3.2**, isobutyl **L3.3**, n-hexyl **L3.4**, phenyl **L3.5**, 2-naphthyl **L3.6**
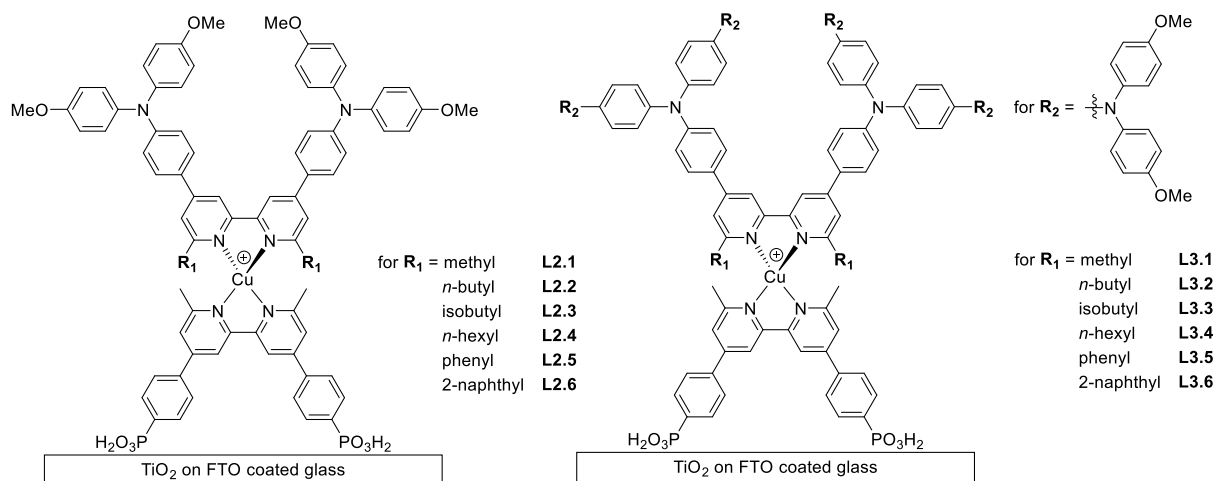
*Scheme 20: Schematic representation of anchored dyes [Cu(**ALP1**)(**L2.1-3.6**)]$^+$ on TiO2.*

In the previous chapters, it has been established that the introduction of a phenylene spacer between the bipyridine unit and the phosphonic acids significantly enhances the photoresponse. Additionally, the results from dye concentration tests leads to the conclusion that the use of 0.1 mM solutions of a labile *homoleptic* copper(I) complex[209][210][211] for the ligand exchange reaction on the surface leads to optimal performance.

V.1   Dendrimer 1ˢᵗ generation

V.1.1   DSC parameters

dye	day	J_{sc} [mA/cm²]	V_{oc} [mV]	ff [%]	η [%]	rel. η [%]
[Cu(**ALP1**)(**L2.1**)]⁺	0	5.47	490	69.4	1.86	25.1
[Cu(**ALP1**)(**L2.2**)]⁺	0	4.65	475	69.8	1.54	20.8
[Cu(**ALP1**)(**L2.3**)]⁺	0	3.94	479	69.6	1.31	17.7
[Cu(**ALP1**)(**L2.4**)]⁺	0	4.07	491	71.8	1.43	19.4
[Cu(**ALP1**)(**L2.5**)]⁺	0	5.35	492	70.4	1.85	25.0
[Cu(**ALP1**)(**L2.6**)]⁺	0	2.94	485	68.3	0.97	13.1
N719	0	16.31	637	71.3	7.41	100.0
[Cu(**ALP1**)(**L2.1**)]⁺	1	5.12	492	69.56	1.75	22.7
[Cu(**ALP1**)(**L2.2**)]⁺	1	4.04	474	69.81	1.34	17.3
[Cu(**ALP1**)(**L2.3**)]⁺	1	3.51	483	69.80	1.18	15.3
[Cu(**ALP1**)(**L2.4**)]⁺	1	3.92	501	70.69	1.39	18.0
[Cu(**ALP1**)(**L2.5**)]⁺	1	5.11	494	70.33	1.78	23.0
[Cu(**ALP1**)(**L2.6**)]⁺	1	3.09	496	67.68	1.04	13.5
N719	1	16.55	663	70.3	7.71	100.0
[Cu(**ALP1**)(**L2.1**)]⁺	15	5.17	508	70.1	1.84	23.2
[Cu(**ALP1**)(**L2.2**)]⁺	15	4.30	518	69.9	1.55	19.6
[Cu(**ALP1**)(**L2.3**)]⁺	15	3.97	525	70.2	1.46	18.5
[Cu(**ALP1**)(**L2.4**)]⁺	15	3.77	526	72.7	1.44	18.2
[Cu(**ALP1**)(**L2.5**)]⁺	15	5.54	545	71.8	2.17	27.4
[Cu(**ALP1**)(**L2.6**)]⁺	15	2.82	498	70.7	0.99	12.5
N719	24	15.86	698	71.6	7.92	100.0

*Table 14: Parameters over 2 weeks. [Cu(**ALP1**)(**L2.1-2.6**)]⁺ obtained from 0.1 mM dye solution in CH₂Cl₂.*

The data for the 1ˢᵗ generation dendrimers incorporated in DSCs are given in Table 14. For the ligand exchange reaction, a 0.1 mM solution of *homoleptic* copper(I) complex in CH₂Cl₂ was used. The cells were measured over a period of three weeks. All cells exhibit a good fill factor between 68 and 72%. On the day of sealing (day 0), the cell with capping ligand **L2.1** and **L2.5** achieve the highest J_{sc} of 5.47 mA cm⁻² and 5.35 mA cm⁻², respectively. The device containing ancillary ligand **L2.2** reaches the third highest J_{sc} of 4.65 mA cm⁻². Comparable, but lower, short-circuit-current densities are obtained with devices containing capping ligands **L2.3** and **L2.4**. By far the lowest J_{sc} was measured with the DSC containing ancillary ligand **L2.6**, which yielded only 2.96 mA cm⁻². For all cells, comparable values of *Voc* were measured between 475 and 492 mV. In terms of efficiency, on day 0 the cells with capping ligand **L2.1** and **L2.5** showed the best performance (η = 1.86 and 1.85%, respectively). The second highest efficiency was obtained with the device containing ancillary ligand **L2.2**, followed by cells with **L2.4** and **L2.3**. The poorest performance exhibited the DSC with **L2.6**, which only achieved η = 0.97%.

Upon aging (*e.g.* on going from day 0 to day 15), all cells gained in *Voc*. After two weeks (day 15) the highest *Voc* was measured with the device containing capping ligand **L2.5**, which improved from 492 mV on day 0 to 545 mV on day 15. The devices with ancillary ligands **L2.4** and **L2.3** achieved 526 mV and 525 mV. A slightly lower open-circuit voltage was obtained with **L2.2**, which rose from 475 mV on day 0 to 518 mV on day 15. For the device containing capping ligand **L2.1**, a *Voc* of 508 mV was measured after two weeks. The lowest potential was exhibited by the cell with ancillary ligand **L2.6**, which showed a *Voc* of 498 mV after two weeks.

For the short-circuit-current density only the cell with ancillary ligand **L2.5** improved; *Jsc* increased to 5.54 mA cm^{-2}. The other cells either did not change in *Jsc* or showed only a minor decrease in short-circuit-current density after 15 days.

Concerning the efficiency, a clear increase for the device with ancillary ligand **L2.5** on going from day 0 to day 15 was observed. Its efficiency increased to 2.17% and shows the best conversion efficiency for this set of DSCs. For the cell containing capping ligand **L2.1** the efficiency stayed constant over 15 days. Also, the conversion efficiency of the DSCs with topping ligands **L2.2** and **L2.4** did not change within 2 weeks. A slight improvement in efficiency was measured for **L2.3**, showing $\eta = 1.46\%$ on day 15. The lowest efficiency was still obtained for **L2.6**.

V.1.2   JV-curves
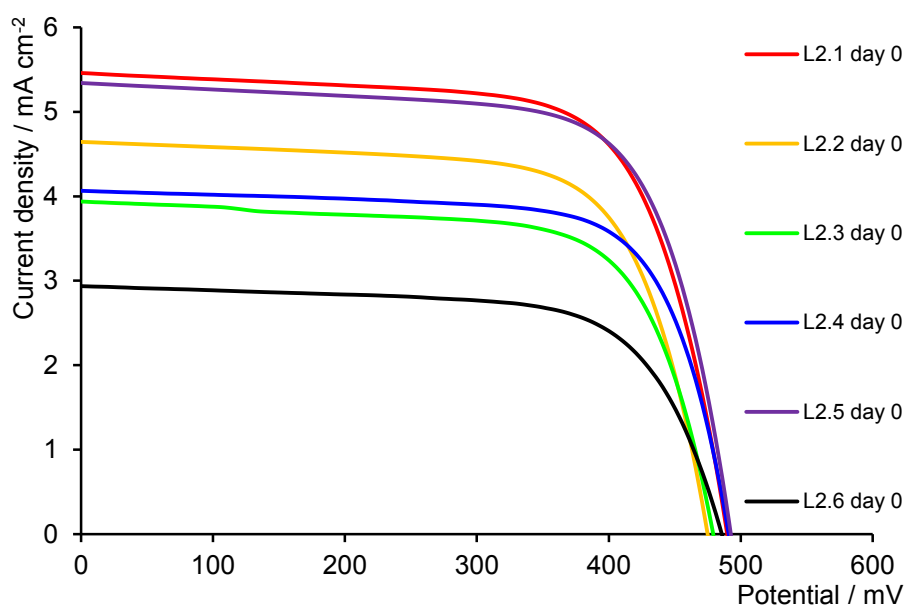
*Figure 87: JV-curves of [Cu(**ALP1**)(**L2.1-2.6**)]$^+$ on day 0.*

The *JV*-curves on day 0 for the 1st generation of dendrimers (Figure 87) show comparable *Voc* for all cells. It is clear to see that cells with ancillary ligands **L2.1** and **L2.5** are similar in performance and the best performing dyes of this set on day 0. While their *Voc* is similar to the other cells, their *Jsc* is much higher than any of the other cells. While the device containing capping ligand **L2.6** also exhibits a similar *Voc* as the other dyes, its *Jsc* is by far the lowest of all as Figure 87 shows.
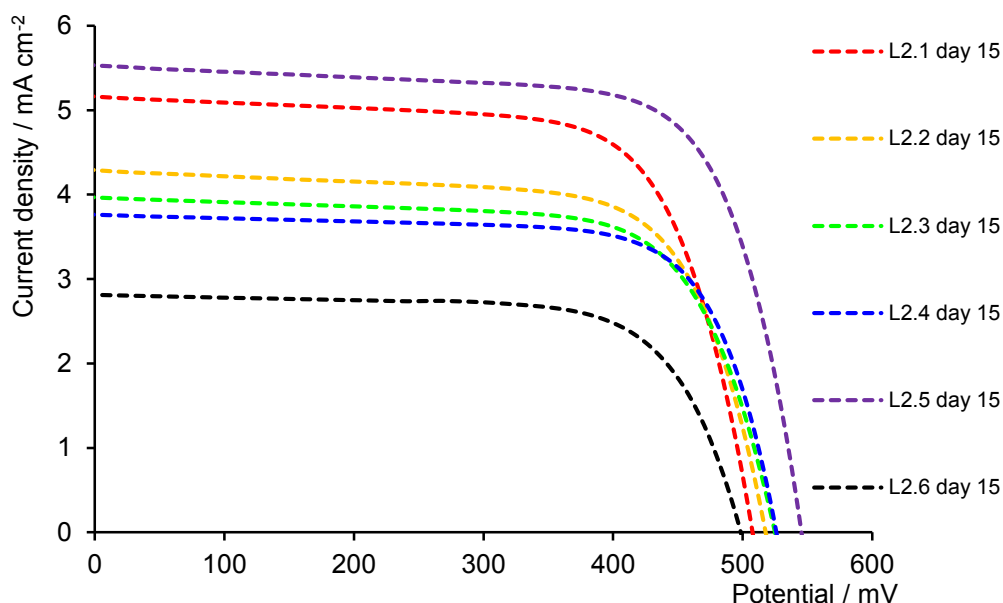
*Figure 88: JV-curves of [Cu(**ALP1**)(**L2.1-2.6**)]+ for day 15.*

The open-circuit-voltages on day 15 (Figure 88) are not as similar as on day 0 for the six dyes. While on day 0 all *Voc* values were below 500 mV, on day 15 only the device with ancillary ligand **L2.6** shows a *Voc* lower than 500 mV. Although all cells improved in *Voc* during two weeks, the device with **L2.5** gained the most. It clearly exhibits the highest *Voc* on day 15. Concerning the short-circuit-current density, the DSC with capping ligand **L2.6** still shows the lowest *Jsc*. The *Jsc* values for DSCs containing capping ligands **L2.2**, **L2.3** and **L2.4** are between 3.77 and 4.30 mA cm^{-2}, those for **L2.1** and **L2.5** are higher than 5.0 mA cm^{-2}. However, all cells improved in *Voc* over two weeks, the device with **L2.5** is the only one that gained in *Jsc*.
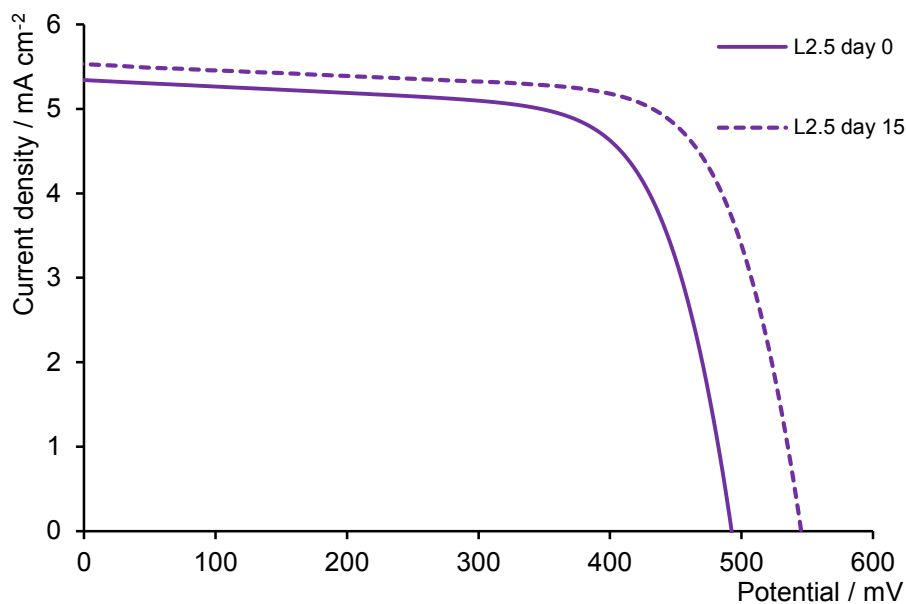
*Figure 89: JV-curves of [Cu(**ALP1**)(**2.5**)]⁺ for day 0 and day 15.*

The data reveal that the device with **L2.5** improves in conversion efficiency over time. Comparing the *JV*-curves on day 0 and day 15 (Figure 89), it is clear that not only the increase in *Jsc* contributes to the higher efficiency but also the much higher *Voc*.

V.1.3   EQE
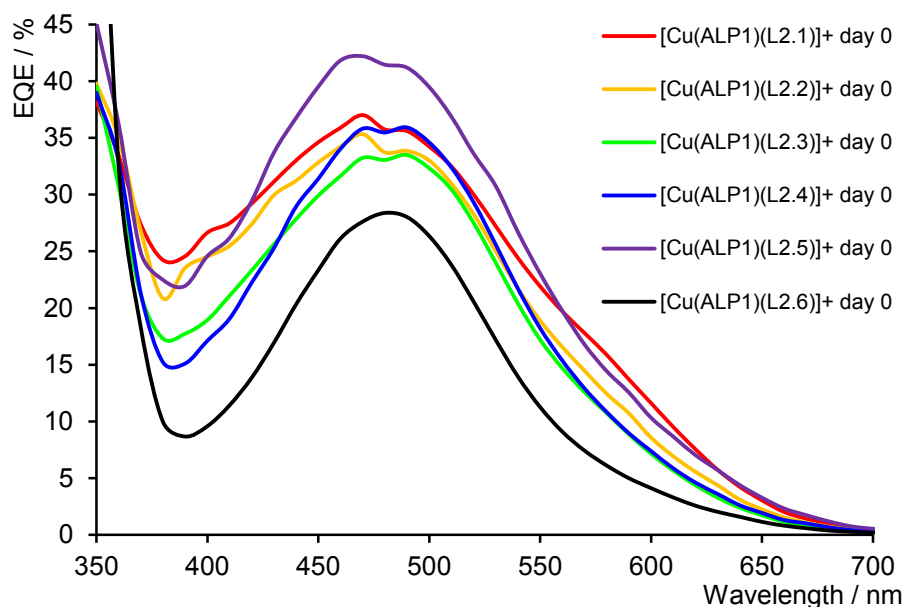
*Figure 90: EQE curves for [Cu(**ALP1**)(**L2.1-2.6**)]⁺ on day 0*

The integration of the *EQE* curves over a simulated sunlight (ASTM-G173-3) reveals the same trend in *Jsc* as the trend obtained from Table 14. The two cells with the highest *Jsc* output contain ancillary ligands **L2.5** and **L2.1**. A slightly higher *Jsc* was calculated for **L2.2** than for

L2.4 and **L2.3**. The lowest short-circuit-current density was obtained with the device containing capping ligand **L2.6**.

All cells exhibit a similar curve shape with a λ_{max} at $\approx$ 470 nm. While the device with **L2.5** has the highest *EQE* of 41%, the cell with capping ligand **L2.1** shows an enhanced photoresponse in the red region of the spectrum (>560 nm). The DSC containing ancillary ligand **L2.1** has a maximum *EQE* of 37%, which is similar to the cell with **L2.4**. A slightly lower *EQE* is observed for the cells with ancillary ligands **L2.2** and **L2.3**, which have maxima *EQE* of 35% and 34%, respectively. The lowest external quantum efficiency is seen for the cell with **L2.6** and corresponds to the low overall efficiency.

V.1.4   Solid state UV-vis spectra

The *heteroleptic* dyes were assembled by stepwise adsorption of the anchoring ligand (**ALP1**) on the photoanode (without scattering layer), followed by treatment with a solution of *homoleptic* copper(I) complex, which causes a ligand exchange forming the *heteroleptic* dye.
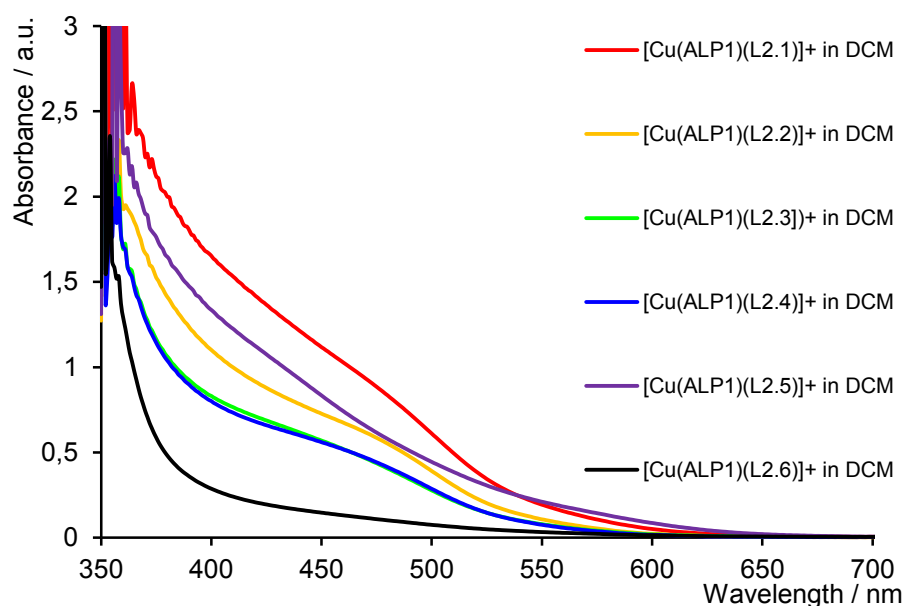
Figure 91: Solid-state UV-vis spectra of anodes with adsorbed heteroleptic copper(I) complexes.

All photoelectrodes containing an ancillary ligand with alkyl substituents in the 6,6'-positions (**L2.1**, **L2.2**, **L2.3** and **L2.4**) show a similar curve shape with a shoulder at $\approx$ 480 nm. The spectrum of the anode containing capping ligand **L2.5** shows a continuous decrease in absorbance at lower energy with a very weak shoulder at $\approx$ 440 nm. The curve for the electrode with ancillary ligand **L2.6** exhibits a drastic drop in absorbance on going from 350 to 380 nm and a continuous reduction in absorption.

The most intense absorbance between 350 and 540 nm is obtained with ancillary ligand **L2.1**, whereas the cell with **L2.5** exhibits the broadest absorption > 540 nm. Overall, the anode containing capping ligand **L2.5** gives the second most intense absorbance. The anode with **L2.2** exhibits a slightly lower absorbance compared to **L2.5**. Photoanodes with **L2.3** and **L2.4** show the same intense absorption over the whole spectrum. The weakest absorption is exhibited by the electrode with ancillary ligand **L2.6**.
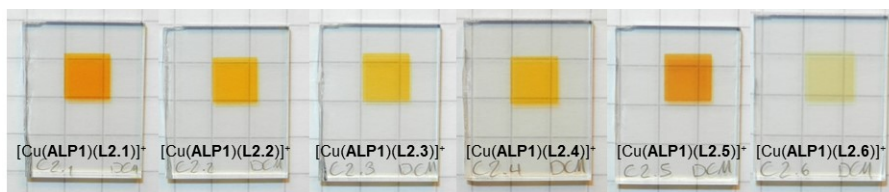
Figure 92: Photoanodes after the treatment with homoleptic Cu(I) complexes in CH₂Cl₂.

By comparing the photoanodes with the naked eye (Figure 92), the difference in absorption intensity can be detected. While the anode with ancillary ligand **L2.1** exhibits the strongest orange colour of the alkyl substituents in the 6,6'-positions, cells with **L2.2**, **L2.3** and **L2.4** show a much paler colour of the dyed TiO_2. In contrast, the anode with **L2.5** shows again a strong colour, whereas the cell with capping ligand **L2.6** is barely coloured.

V.2 Discussion

V.2.1 Dye concentration

Using dilute solutions of *homoleptic* copper(I) complexes (0.1mM) leads to the results that all devices showed their highest *Jsc* on day 0, except for **L2.5** which increased in *Jsc* over time. By applying dilute dye solutions the aggregation during the ligand exchange reaction is minimized. Since the initial *Jsc* is high, it appears that the photon absorbance and the electron injection (charge separation) are optimized right from the start after cell fabrication[206].

V.2.2 Voc

The initial *Voc* values of all the cells are similar. Upon aging, the *Voc* of all devices increased. After 2 weeks there is a general trend: the larger the substituents in the 6,6'-positions, the higher the *Voc*. This trend is true for all but the dye with capping ligand **L2.6**. This gain in *Voc* can be attributed to a reduction of charge recombination[206]. The addition of bulkier substituents may lead to a barrier or interlinked chains between the sensitizer and the electrolyte. This barrier can then block, or at least retard, the charge recombination between injected electrons and oxidized electrolyte (I_3^-). In other words, a longer electron lifetime is achieved. Grätzel[212] not only showed that the introduction of alkyl chains is beneficial to the *Voc* but also showed that the

introduction of such alkyl chains not only reduces the recombination but also protects the dye from desorption[204]. The device with **L2.6** exhibits the lowest *Voc* although its substituents are the bulkiest of this set. A possible justification can be found by looking at the solid state absorbance spectrum. Since the absorbance is by far weakest, one can say that there is the least dye adsorbed on TiO₂ compared to the other dyes. Due to this lack of adsorbed dye, the substituents in the 6,6'-positions are not capable of forming such an insulating layer to slow down the charge recombination. On the other hand, poor performance may simply be due to very low dye loading.

V.2.3   Jsc

Compared to earlier presented results, all the cells except the one with **L2.5** showed their highest *Jsc* on day 0. The obtained short-circuit-current density correlates with the absorption intensity in the solid-state UV-vis. For **L2.1** and **L2.5**, the highest current and the strongest absorptions were measured. Devices with ancillary ligands **L2.3** and **L2.4** show essentially the same *Jsc* on day 15 (1.46 and 1.44 mA cm^{-2}, respectively) as well as the same intensity in the solid-state absorption spectrum over the whole region. Additionally, the order of measured *Jsc* (Table 14) on day 15 is consistent with the calculated *Jsc* from the *EQE* curves.

Order of measured *Jsc*:   **L2.5** > **L2.1** > **L2.2** > **L2.3** > **L2.4** > **L2.6**

Order of calculated *Jsc*:   **L2.5** > **L2.1** > **L2.2** > **L2.3** > **L2.4** > **L2.6**

Calc. *Jsc* [mA cm^{-2}]:   4.18 (**L2.5**) > 3.77 (**L2.1**) > 3.36 (**L2.2**) > 2.97 (**L2.3**)> 2.91 (**L2.4**) > 2.08 (**L2.6**)

Another observation is that the initial *Jsc* on day 0 was, for all cells except one, the highest over the measuring period. Only the device with **L2.5** improved its *Jsc* during a two week period after being assembled (*i.e.* on going from day 0 to day 15, from 5.35 mA cm^{-2} to 5.54 mA cm^{-2}). This leads to the assumption that only in the device with **L2.5** is a reorganisation of dye molecules on the surface taking place. The increase in *Jsc* for **L2.5** is a hint for improved electron injection. A possible reason could be the reorganisation of dye molecules over time[200].

V.2.4   Solid-state absorption

For the solid state absorption, the order of absorption intensity generally follows the size of the 6,6'-substituents. However, the photoanode with ancillary ligand **L2.5** does not fit into the order since its substituent is the second largest/bulkiest but its absorbance is the second most intense. The size of the substituents in the 6,6'-positions seems to be the limiting factor for the dye loading on TiO₂. No steric hindrance (**L2.1**) leads to the highest dye loading, but even going

from **L2.1** (methyl) to **L2.2** (*n*-butyl) apparently leads to a reduction in absorption/surface coverage. With isobutyl and *n*-hexyl, the dye loading is even more limited. For phenyl substituents, there seems to be a favoured interaction between the ancillary ligands of neighbouring dye molecules which leads to higher dye loading. With the biggest substituents the lowest absorption in the solid state UV-vis was measured and therefore the lowest dye loading is assumed.

V.3 Dendrimer 2nd generation

V.3.1 DSC parameter

dye	day	J_{sc} [mA/cm²]	V_{oc} [mV]	ff [%]	η [%]	rel. η [%]
[Cu(**ALP1**)(**L3.1**)]⁺	0	4.32	509	68.1	1.50	20.2
[Cu(**ALP1**)(**L3.2**)]⁺	0	4.08	469	67.9	1.30	17.6
[Cu(**ALP1**)(**L3.3**)]⁺	0	2.60	428	65.3	0.73	9.8
[Cu(**ALP1**)(**L3.4**)]⁺	0	2.73	459	68.5	0.86	11.6
[Cu(**ALP1**)(**L3.5**)]⁺	0	1.78	418	67.2	0.50	6.8
[Cu(**ALP1**)(**L3.6**)]⁺	0	1.29	413	63.3	0.34	4.6
N719	0	16.44	647	69.5	7.40	100.0
[Cu(**ALP1**)(**L3.1**)]⁺	1	5.07	532	68.3	1.84	22.7
[Cu(**ALP1**)(**L3.2**)]⁺	1	4.64	505	69.6	1.63	20.1
[Cu(**ALP1**)(**L3.3**)]⁺	1	3.10	456	68.6	0.97	12.0
[Cu(**ALP1**)(**L3.4**)]⁺	1	3.09	479	69.7	1.03	12.7
[Cu(**ALP1**)(**L3.5**)]⁺	1	2.31	440	69.0	0.70	8.6
[Cu(**ALP1**)(**L3.6**)]⁺	1	1.57	436	67.6	0.46	5.7
N719	1	17.02	681	70.0	8.11	100.0
[Cu(**ALP1**)(**L3.1**)]⁺	15	5.09	551	69.6	1.95	25.4
[Cu(**ALP1**)(**L3.2**)]⁺	15	4.49	509	70.3	1.61	20.8
[Cu(**ALP1**)(**L3.3**)]⁺	15	3.59	497	68.9	1.23	15.9
[Cu(**ALP1**)(**L3.4**)]⁺	15	3.58	523	69.1	1.29	16.8
[Cu(**ALP1**)(**L3.5**)]⁺	15	2.68	449	68.7	0.83	10.7
[Cu(**ALP1**)(**L3.6**)]⁺	15	1.87	459	69.8	0.60	7.8
N719	15	16.02	691	69.6	7.71	100.0
[Cu(**ALP1**)(**L3.1**)]⁺	22	5.17	561	69.4	2.01	25.4
[Cu(**ALP1**)(**L3.2**)]⁺	22	4.54	512	70.0	1.63	20.5
[Cu(**ALP1**)(**L3.3**)]⁺	22	3.43	484	70.1	1.16	14.7
[Cu(**ALP1**)(**L3.4**)]⁺	22	3.71	522	68.1	1.32	16.6
[Cu(**ALP1**)(**L3.5**)]⁺	22	2.83	449	69.1	0.88	11.1
[Cu(**ALP1**)(**L3.6**)]⁺	22	2.03	463	69.2	0.65	8.2
N719	22	16.16	709	69.3	7.94	100.0

Table 15: Parameters over 3 weeks. [Cu(ALP1)(L3.1-3.6)]⁺ obtained from 0.1 mM dye solution in CH₂Cl₂.

The data for the 2nd generation dendrimers incorporated in DSCs are given in Table 15. All cells exhibit *ff* between 63% and 72%. On the day of sealing (day 0) the highest *Jsc* of 4.32 mA cm⁻² was measured for the cell with ancillary ligand **L3.1**, followed by the device with **L3.2**, which showed a *Jsc* of 4.08 mA cm⁻². For the DSCs with capping ligands **L3.3** and **L3.4**, similar *Jsc* values of 2.60 and 2.73 mA cm⁻² were obtained. For the ancillary ligands with aromatic substituents in the 6,6'-positions (**L3.5** and **L3.6**), very low short-circuit-current densities of 1.78 and 1.29 mA cm⁻² were obtained.

For values of *Voc* on day 0, the data in Table 15 reveal the same trend as for the *Jsc*. The highest *Voc* of 509 mV was measured for the device with capping ligand **L3.1**, followed by the cell with **L3.2** achieving 469 mV. A slightly lower *Voc* of 459 mV was measured for **L3.4**. For the isobutyl ancillary ligand an even more reduced *Voc* of 428 mV was obtained. The dyes containing **L3.5** and **L3.6** show similar, but low, *Voc*'s of 418 and 413 mV, respectively.

Concerning the efficiency on day 0, the trend is consistent with trends in *Voc* and *Jsc*. The cell with capping ligand **L3.1** gives the highest η (1.50%), followed by **L3.2** (η = 1.30%). Cells with **L3.4** and **L3.3** gave much lower efficiencies of 0.86 and 0.73 %. The poorest conversion efficiencies were measured for DSCs with ancillary ligands **L3.5** and **L3.6**.

During the measuring period of 3 weeks, the cells underwent an aging effect. Not only did all cells increase in *Jsc*, but values of *Voc* also increased. As a result of the gain in these two parameters, the efficiency of each cell increased on going from day 0 to day 22. The order for the measured *Jsc* values did not change compared to the day of sealing. The DSC with **L3.1** increased for 0.85 mA cm^{-2} to 5.17 mA cm^{-2}. The cell with capping ligand **L3.2** increased to 4.54 mA cm^{-2}. A significantly lower *Jsc* was measured for cells with capping ligands **L3.4** and **L3.3** (3.71 and 3.43 mA cm^{-2}, respectively). Although after three weeks DSCs with ancillary ligands **L3.5** and **L3.6** still exhibit the lowest *Jsc* values, it is noteworthly that the values improved to 2.83 and 2.03 mA cm^{-2}, respectively, compared to the day of sealing the cells.

The device with ancillary ligand **L3.1** gained 52 mV in *Voc*, yielding 561 mV on day 22. For the cell with **L3.4**, the highest increase in *Voc* (63 mV) was achieved (522 mV on day 22). For the DSC with **L3.2**, only a slightly lower *Voc* of 512 mV was obtained. With **L3.3** the *Voc* rose by 56 mV to 484 mV on day 22. Again the devices with capping ligands **L3.5** and **L3.6** (*Voc* of 449 and 463 mV on day 22), represent the lowest values of this set.

Since the efficiency depends on the key factors *Jsc* and *Voc*, the conversion efficiency improved for all cells during the measuring period of 3 weeks. The order of the efficiencies obtained on the day of sealing did not change over these three weeks. The best performance was obtained for the dye with ancillary ligand **L3.1** (η = 2.01 % and a relative efficiency of 25.4 % to **N719**). The cell with capping ligand **L3.2**, which is the second most efficient dye of this set, shows a quite drastically reduced efficiency of 1.63% compared to **L3.1**. With **L3.4**, an efficiency of 1.32 % was obtained after 3 weeks. For the device containing the isobutyl ancillary ligand (**L3.3**), the efficiency increased from 0.73 to 1.16 %. The poorest sunlight to power conversion efficiencies were measured with **L3.5** and **L3.6**, which achieved only 0.88 % and 0.65 % after three weeks and correlate to relative efficiencies of only 11% and 8% compared to **N719** set at 100%.

V.3.2 JV-curves
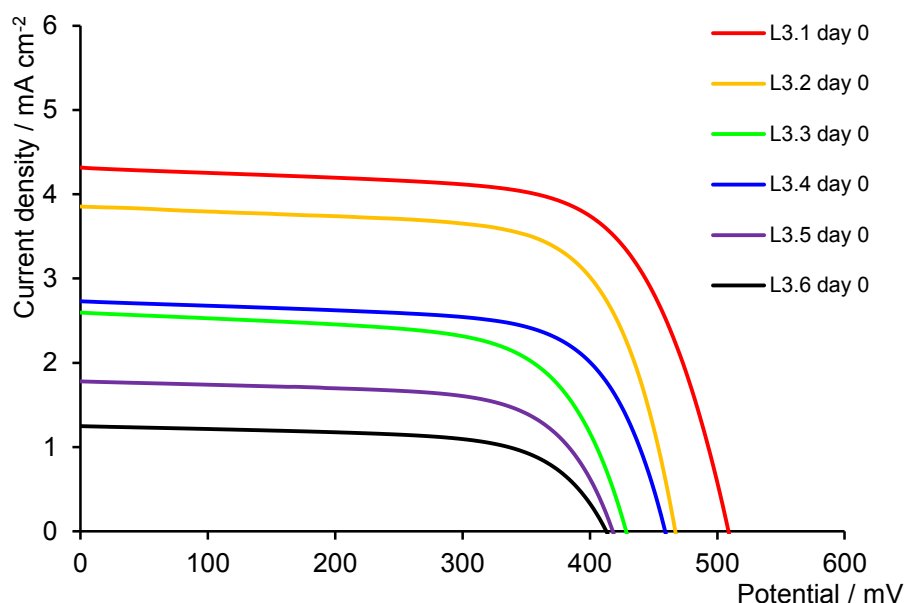
Figure 93: JV-curves on day 0 of 2ⁿᵈ generation of dendrimers.

In the *JV*-curves of the 2nd generation dendrimers on day 0 of the 2nd generation dendrimers (Figure 93), the wide distribution of *Voc* and *Jsc* values is displayed. This large variation in values correlates to a large variation in conversion efficiencies. It is obvious to see that the sequence in *Jsc* follows the same order as the sequence in *Voc*. The order follows more or less the size/bulkiness/steric hindrance of the 6,6'-substituents. While with methyl and *n*-butyl groups moderately high *Jsc* values were obtained, cells containing capping ligands **L3.3** and **L3.4** show a reduced but comparable *Jsc*. The devices with **L2.5** and **L2.6** show again an additional drop in *Jsc*.

For *Voc*, the device with **L3.1** exhibits the highest potential. Cells with **L3.2** and **L3.4** (linear alkyl substituents in the 6,6'-positions) show similar values for *Voc*. A further loss in *Voc* is observed by the insertion of branched alkyl (**L3.3**) or aromatic substituents.
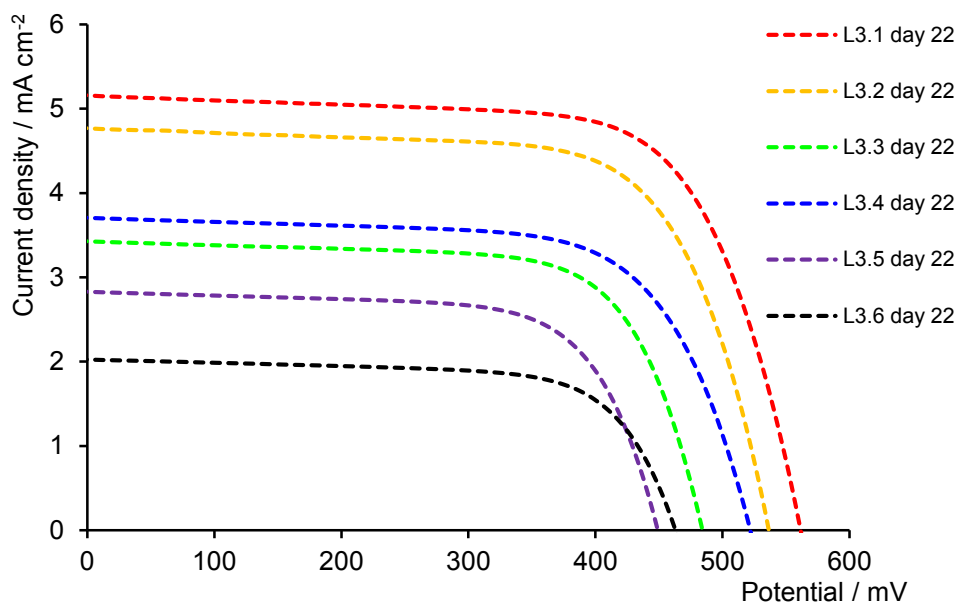
Figure 94: JV-curves on day 22 of 2nd generation of dendrimers

As already mentioned, all cells with the 2nd generation of dendrimers improved in *Jsc* and *Voc* with ongoing measuring time. This becomes obvious by comparing their *JV*-curves obtained on the day of sealing and after 3 weeks (compare Figure 93 and Figure 94). While the highest *Jsc* on day 0 was 4.32 mA cm^{-2}, after 3 weeks it increased to 5.17 mA cm^{-2}. The lowest *Jsc* on day 0 (**L3.6**, 1.29 mA cm^{-2}) increased to 2.03 mA cm^{-2}. The same is observed comparing the data for day 0 and day 22. The cells gained in *Voc* between 31 and 63 mV during the measuring period of 3 weeks.
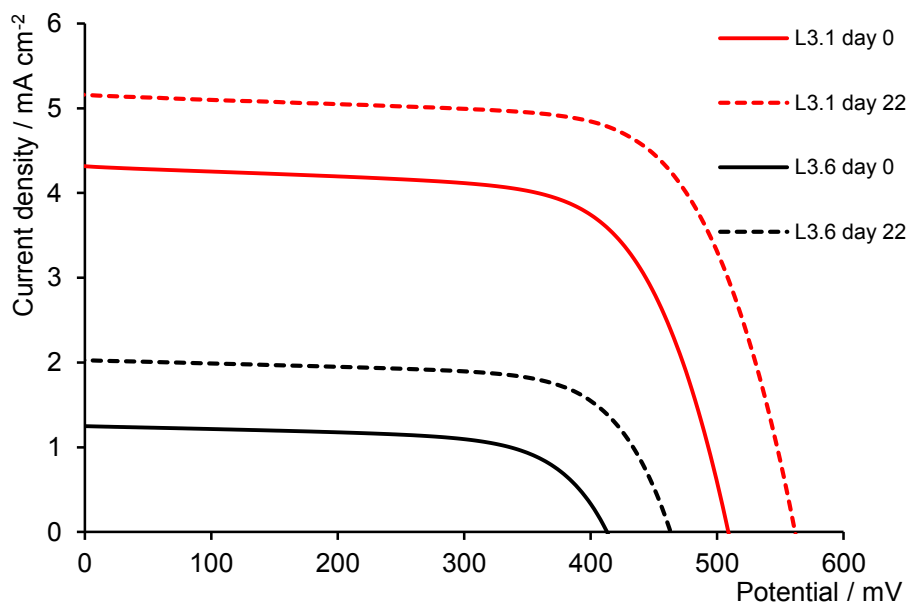
*Figure 95: JV-curves of [Cu(**ALP1**)(**L3.1**)]$^{+}$ and [Cu(**ALP1**)(**L3.6**)]$^{+}$ on day 0 (solid line) and day 22 (dashed line).*

V.3.3   EQE
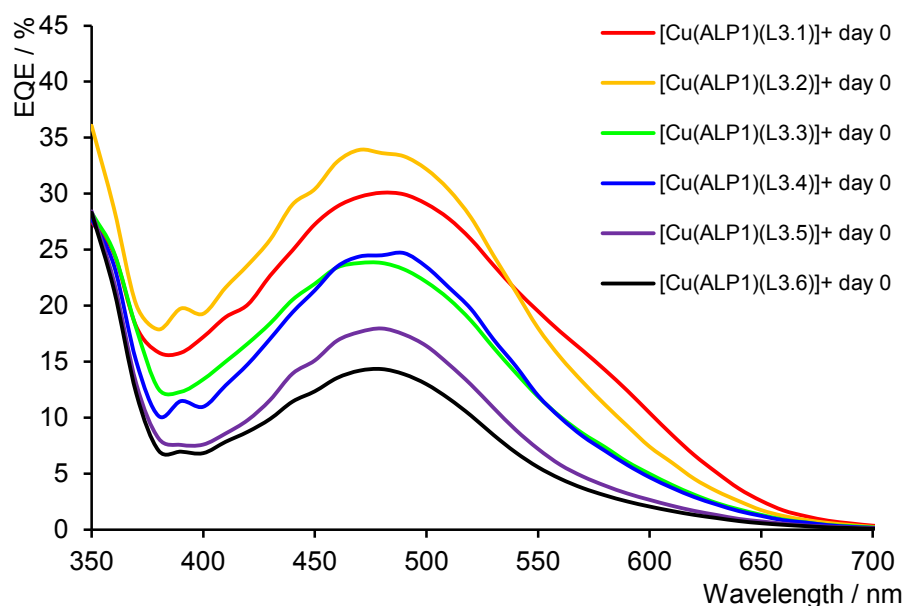
*Figure 96: EQE curves for [Cu(**ALP1**)(**L3.1-3.6**)]$^+$ on day 0.*

All *EQE* curves exhibit the same λ_{max} at 470-480 nm. On day 0, the device with ancillary ligand **L3.2** had the highest *EQE* of 34%. For the DSC containing capping ligand **L3.1** the second highest *EQE* of 30% at 470 nm was obtained. In addition, the cell with **L3.1** exhibits an improved photoresponse at longer wavelength (>550 nm) compared to any other cell of this set. The DSCs with capping ligands **L3.3** and **L3.4** show nearly the same *EQE* over the whole spectrum. A much lower *EQE* was obtained for devices containing capping ligands **L3.5** and **L3.6**, which only achieved 18% and 14% at their λ_{max}.
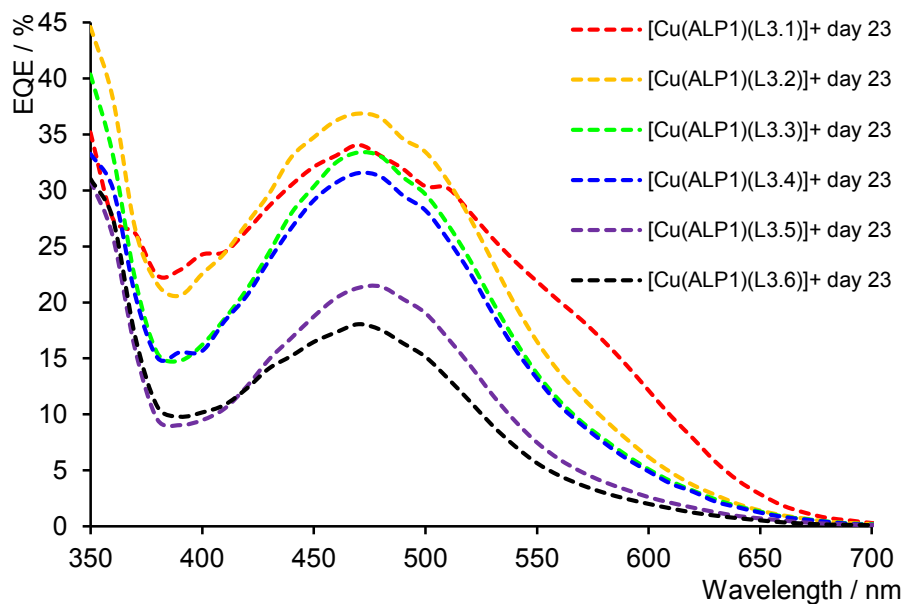
*Figure 97: EQE curves for [Cu(**ALP1**)(**L3.1-3.6**)]⁺ on day 23.*

The improvement in *Jsc* during the measuring period can also be seen by comparing the *EQE* curves on day 0 and day 23 for the 2nd generation dendrimers (compare Figure 96 and Figure 97). All cells exhibit the same λ$_{max}$ at 470-480 nm. After three weeks, the *EQE* for the cell containing ancillary ligand **L3.2** increased from 34 to 36%. The *EQE* for the DSC with **L3.1** rose from 30% to 34%. The increased photoresponse at lower energy (>550 nm) is even more pronounced after three weeks than on the day of sealing. The measured *EQE* on day 23 increased for devices containing ancillary ligands **L3.3** and **L3.4** from initial values of ≈ 25% to 34% and 32%, respectively. For the poor performing DSCs incorporating **L3.5** and **L3.6**, *EQE* of 22% and 18% were obtained.

V.3.4   Solid state UV-vis spectra
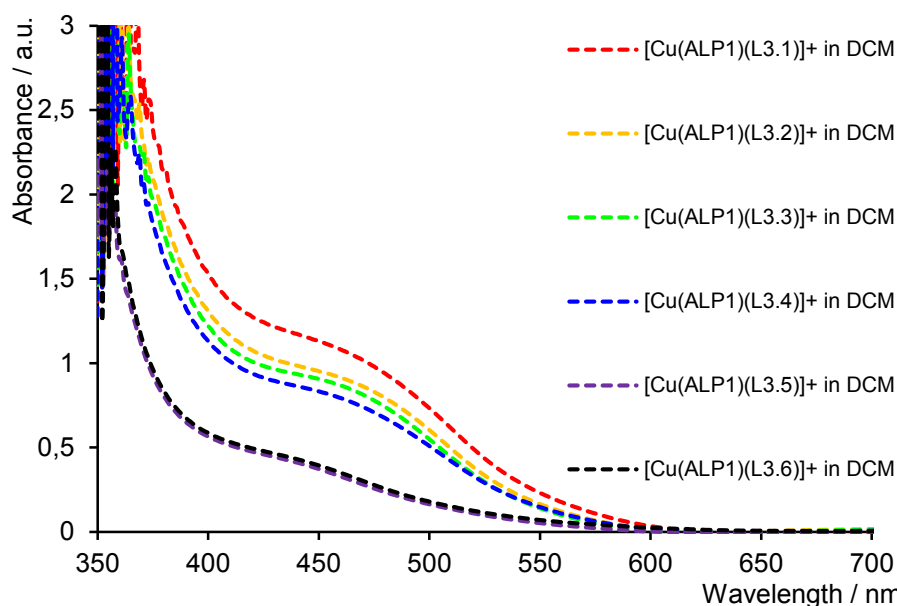
*Figure 98: Solid-state UV-VIS of photoanodes dyed with [Cu(**ALP1**)(**L3.1-3.6**)]$^+$ from CH$_2$Cl$_2$ solutions.*

Anodes with ancillary ligands **L3.1**-**L3.4** show the same curve shape in their solid state absorption spectra with a shoulder at 460-470 nm (Figure 98). For the photoanodes with capping ligands **L3.5** and **L3.6**, only an indication of a shoulder at ≈ 450 nm can be detected. The steric hindrance of the substituents in the 6,6'-positions of the capping ligands affects the dye loading and therefore the solid-state absorption is lower for anodes containing ancillary ligands with bulky substituents. While the device with capping ligand **L3.1** had the strongest absorption, the intensity drops by enlarging the substituents in the *ortho*-positions to the nitrogen atoms of the bipyridine unit. The photoanodes containing ancillary ligands **L3.5** and **L3.6** show the same absorption intensity over the whole spectrum.
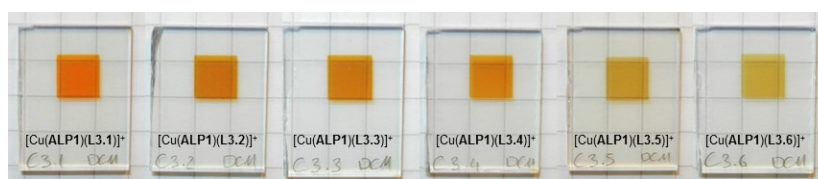
*Figure 99: Photoanodes with adsorbed [Cu(**ALP1**)(**L3.1-3.6**)]$^+$ from CH$_2$Cl$_2$ solutions.*

A comparison of the photoanodes with the naked eye clearly shows a difference in absorption intensity (see Figure 99). While the anode with capping ligand **L3.1** exhibits the strongest orange colour, the other cells show a much paler colour of the dyed TiO$_2$.

V.4   Discussion

V.4.1   Dye concentration

Although for the ligand exchange reaction a dilute solution (0.1 mM) of *homoleptic* copper(I) complex was used, the cells showed a ripening effect as they gained not only in *Voc* but also in *Jsc* over the measuring period. This observation is in contrast to the 1st generation dendrimers, which showed their highest *Jsc* on day 0 and only gained in *Voc*. This leads to the conclusion that even at low concentrations an aggregation of dye molecules arises due to the large and bulky dendrimer structure of the ancillary ligand. To obtain an efficient device concerning photocurrent generation, π-stacking/aggregation should be avoided [213]. The triphenylamine moiety of the ancillary ligand should contain a twisted arrangement of the three arene rings and this should supress aggregation between neighbouring ancillary ligands [214].

V.4.2   Voc

Since *Voc* increases over the measuring period of three weeks, this implies that a rearrangement process of dye molecules functionally anchored to the semiconductor takes place with ongoing time. The increase in *Voc* is normally attributed to a longer electron lifetime in the semiconductor and a slower recombination with either the oxidized dye or I_3^-[215].

The trends in open-circuit voltage more or less correspond to the literature, which states that the presence of alkyl chains retards the charge recombination and therefore raises *Voc* [206]. Although the device with **L3.1** has the least steric hindrance, it achieves the highest *Voc*. This is probably due to the highest dye loading on TiO$_2$ for this set of dyes [201][216]. The cell with ancillary ligand **L3.4** (*n*-hexyl groups) reaches a *Voc* of 522 mV, which is higher than for **L3.2** and **L3.3**, although dyes with *n*-butyl and isobutyl capping ligands exhibit a higher dye adsorption. Again, this observation correlates with findings from the literature where alkyl chains were added in order to reduce aggregation and slow down charge recombination [217]. The devices with capping ligands **L3.5** and **L3.6** have even bulkier substituents in the 6,6'-positions, and one would expect their *Voc* to be higher than for the other dyes because they might be able to form a barrier to block charge recombination and avoid aggregation[218]. However, since they exhibit a very poor absorbance on TiO$_2$, their dye loading is regarded to be very low too. This poor adsorption on the semiconductor is not compensated by the presence of phenyl and 2-naphthyl substituents and it appears that the weak coverage leads to holes between the dye molecules where charge recombination cannot be blocked.

V.4.3   Jsc

The differences in *Jsc* values can, on the one hand, be explained by the differences in dye loading on the surface, where more dye on the TiO$_2$ yields more current; devices with a poorly covered semi-conductor exhibit a much lower *Jsc*[201][216]. On the other hand, a plausible reason for the increase in *Jsc* over the measuring period is the continuous reorganisation or the dissolving of aggregates at the backbone of the capping ligand. This structural and electronic optimization over time leads to an enhanced photon absorption coupled with an improved dye regeneration by I⁻, which is no longer blocked by aggregates to reduce the oxidized dye.

V.4.4   Solid state UV-vis spectra

The solid state UV-vis gives a feedback on how much dye is adsorbed on the TiO$_2$ surface. The order of absorption intensity correlates with the steric hindrance of the substituents in the 6,6'-positions on the ancillary ligand. While alkylated capping ligands show a much stronger absorbance, the anodes with capping ligands **L3.5** and **L3.5** show a very weak absorption on the semi-conductor. This sequence of absorption intensity correlates with the order of measured efficiencies and *Jsc*.

V.4.5   Efficiency

As the two key factors for the efficiency are *Voc* and *Jsc*, the global efficiency is increases with enhanced *Jsc* and *Voc*. The order of efficiency correlates with the obtained sequence for *Jsc*, as well as with the solid state absorption.

V.5   Conclusion

For the set of the 2nd generation dendrimers, the influence of the 6,6'-substituents and the extension of the aromatic system on the open-circuit-voltage in combination with the *Jsc* and the dye loading capacity has been explored. With the extension of the π-system, the dyes appear to aggregate on the surface and therefore show an increase in *Jsc* over time as molecular reorganisation takes place. The different bulky substituents had an influence on the *Voc* and the dye loading. While the dye absorption decreased with larger substituents in the 6,6'-positions, the efficiency decreased too. The highest $\eta = 2.01\%$ was achieved with the DSC containing ancillary ligand **L3.1** but the introduction of bulky substituents in the 6,6'-positions did not yield in higher efficiencies.

V.6 Comparison of 1st and 2nd generation dendrimers

On comparing 1st and 2nd generation dendrimers incorporated in DSCs, attention was turned to see whether the increase in absorptivity on going from the 1st to the 2nd generation leads to an enhanced cell performance.

V.6.1 JV-curves
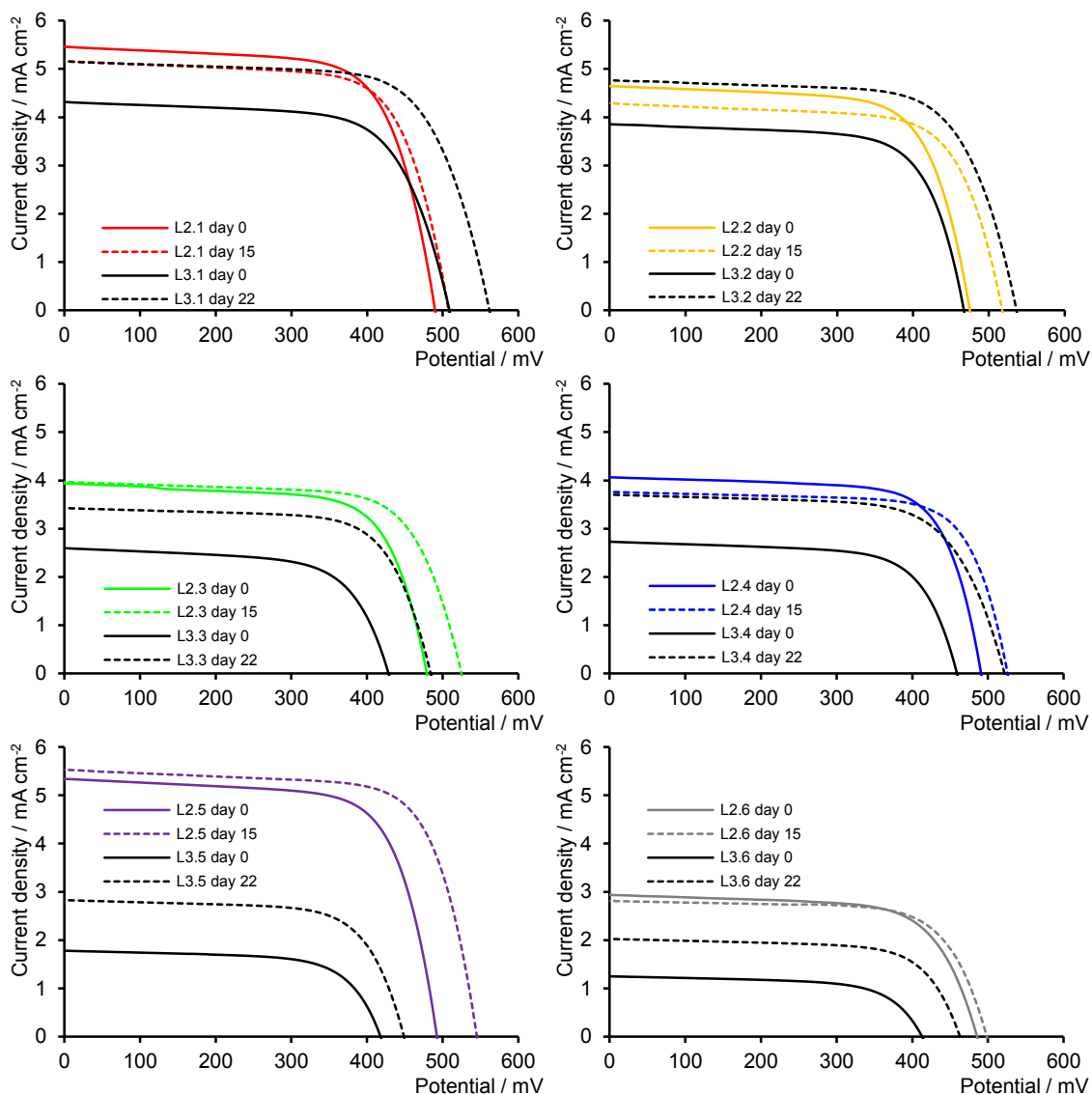
*Figure 100: A comparison of JV-curves of copper(I) dyes containing 1st (**L2.1-2.6**) vs. 2nd (**L3.1-3.6**) generation dendrimers and their behaviour over time.*

The data for the DSC performance of the 1st and 2nd generations are presented in Table 14 and Table 15 (see sections V.1.1 and V.3.1). Focusing on the evolution of *Jsc* over the measuring period (Figure 100) it can be observed that the cells of the 2nd generation all gain in *Jsc* over time, whereas for the 1st generation, only the cell with capping ligand **L2.5** shows a minor increase in *Jsc*. Concerning the *Voc*, all cells of 1st and 2nd generations gain in potential with ongoing measuring time.

On the day of sealing the DSCs, all devices with 1st generation capping ligands exceed the 2nd generation in efficiency. After two to three weeks, only dyes with **L3.1** and **L3.2** exhibit a higher efficiency than their corresponding 1st generation devices. In all other cases, the 1st generation device shows an enhanced performance.

For ancillary ligands with methyl groups in the 6,6'-positions, the dye with **L2.1** shows a much higher *Jsc* than that with **L3.1** on day 0. While with time the cell with **L3.1** gained in *Jsc*, for **L2.1** a drop in *Jsc* was recorded. The *Voc* values of dyes containing **L2.1** and **L3.1** are similar on day 0, while with ongoing time the device with **L3.1** gained much more in *Voc* than **L2.1**. For **L2.1**, the overall efficiency did not change but for **L3.1** it increased from $\eta = 1.50\%$ on day 0 to 2.01% on day 22.

For dyes with **L2.2** and **L3.2**, the results present the same trend. On day 0, **L2.2** exhibits a higher *Jsc* than **L3.2**, but their *Voc* values are similar. After two to three weeks, the dye with **L3.2** exceeds the device with **L2.2** in terms of performance due to an increased *Jsc* and higher *Voc* than the cell with **L2.2**.

The DSC with 1st generation isobutyl capping ligand (**L2.3**) achieves a higher *Jsc* and higher *Voc* than the cell with **L3.3**. With time, the *Jsc* for the dye with **L2.3** did not change, whereas it increased for **L3.3**. Both cells gain in potential but the device with capping ligand **L2.3** still exhibits the higher *Voc*.

For the dye containing **L2.4** on day 0, improved *Jsc* and *Voc* were obtained compared to **L3.4**. While **L2.4** lost in *Jsc*, **L3.4** gained in *Jsc* over time. Both cells showed the same *Jsc* after two to three weeks. Also **L2.4** and **L3.4** improved in *Voc*, leading to the dye containing **L3.4** showing the same *Voc* after the measuring period as **L2.4**. Only the low *ff* is responsible for **L3.4** exhibiting a lower efficiency than **L2.4**.

Also for **L2.6** a higher *Jsc* and *Voc* were reported on day 0 than for **L3.6**. While the cell with **L2.6** shows only a slight decrease in *Jsc* and a minor gain in *Voc* over time, the device with ancillary ligand **L3.6** improves in both *Jsc* and *Voc*. Nevertheless, the DSC with **L2.6** exhibits the higher efficiency on day 0 and with ongoing time compared to that with capping ligand **L3.6**.

For the cell with **L2.5**, the value of *Jsc* increased clearly over time, whereas for **L2.5** only a minor gain was recorded. Concerning the *Voc*, both cells with capping ligands **L2.5** and **L3.5** gain in potential with ongoing time. The most striking difference on going from 1st to 2nd generation capping ligands was exhibited by these two cells. While the device with **L3.5** shows a poor efficiency of 0.55% on day 0 and 0.88% in day 22, the cell with **L2.5** exhibits a good

efficiency of 1.85% on day 0 and an increased conversion efficiency of 2.17% on day 15. The DSC with **L2.5** achieved the highest efficiency of all dyes in this comparison.

V.6.2   EQE

The *EQE* gives direct information about how much of the incident sunlight is converted to electric power. The higher the integral of an *EQE* curve, the higher is the current that can be obtained with a device.
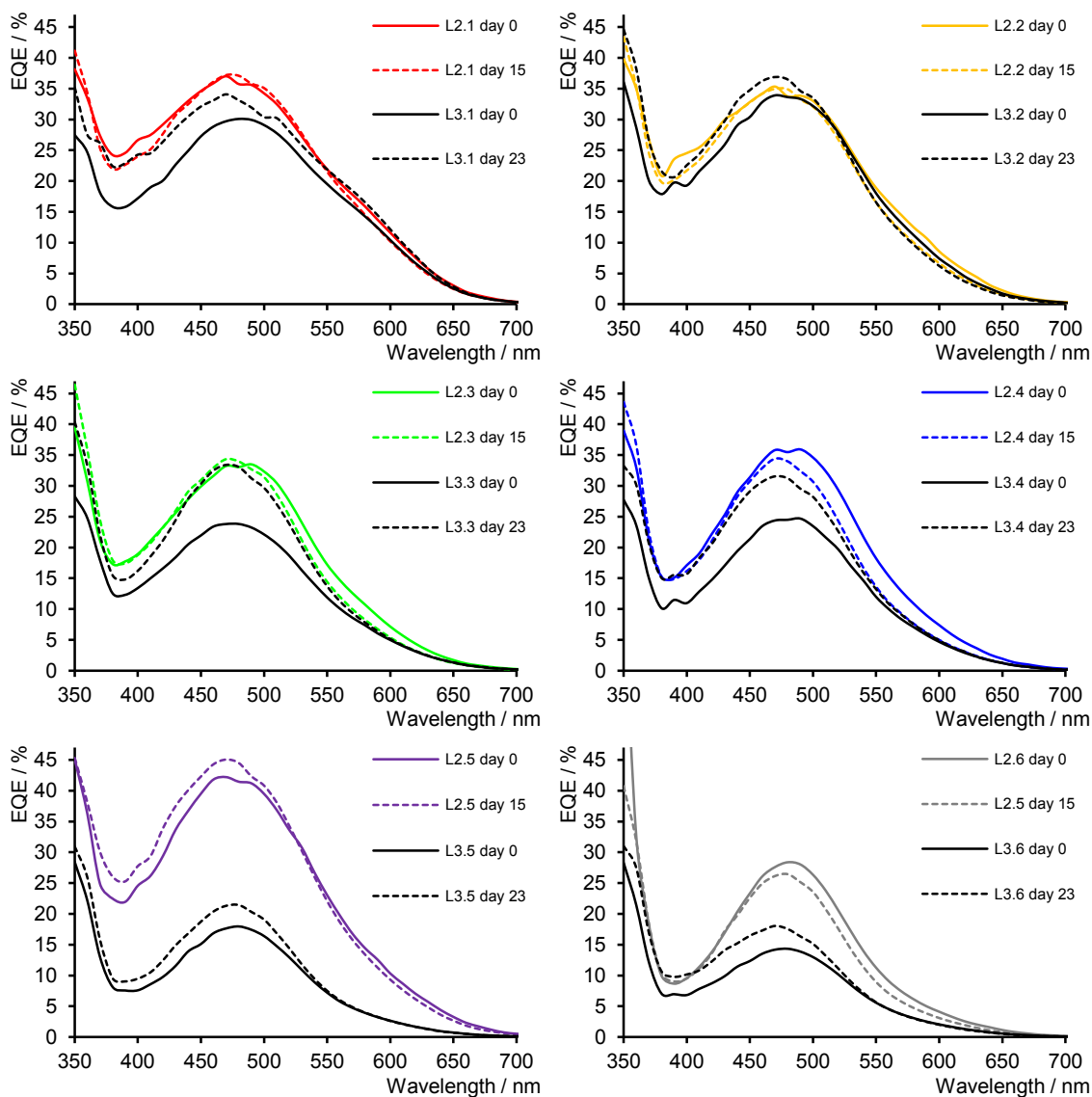
*Figure 101: A comparison of EQE data for devices containing dyes with 1st (**L2.1-2.6**) and 2nd (**L3.1-3.6**) generation dendrimers.*

The *EQE* curves of the 1st and 2nd generations reveal the same trend as already seen in the *JV* curves. For the 1st generation, *Jsc* only increased for **L2.5** with ongoing measuring time. For the 2nd generation, all cells exhibit an enhanced *EQE* after three weeks. All devices exhibit the same λ_{max} at ≈ 470 nm. All DSCs show the same curve shape, except for **L2.1** and **L3.1**, which

exhibit a broader photoresponse. The response is especially enhanced at longer wavelengths (>550 nm) compared to the other dyes. For **L2.1**, the *EQE* does not change from day 0 to day 15, while for **L3.1** an increase in *EQE* can be seen over the whole spectrum on going from day 0 to day 23. For the device with **L2.2**, only a minor decrease in *EQE* was measured, which is consistent with *JV*-measurements. For **L3.2** an increase in *EQE* over the measuring period was detected. On day 0, the DSC with **L2.3** exhibits a much higher *EQE* than with **L3.3**. Over the measuring time the device with **L2.3** did not change in *EQE* whereas the cell with **L3.3** improved quite drastically, showing nearly the same *EQE* as with **L2.3**. Also, for **L3.4** the *EQE* on day 0 is much lower than for **L2.4**. Over time, the cell with **L3.4** gained in *EQE* whereas the cell with **L2.4** decreased in *EQE*. For the cells with **L2.6** and **L3.6**, the same trend is observed. While the device with **L2.6** decreases in *EQE* over time, the DSC with **L3.6** gains in *EQE*. For **L2.5** and **L3.5** the same trend as in the *JV*-curves can be seen. Both cells gain in *EQE*/current over time. While the cell with **L3.5** exhibits a poor *EQE* of 21% at 480 nm, an *EQE* of 45% at 470 nm was measured for the device with **L2.5**.

V.6.3 Solid state absorbance on TiO₂
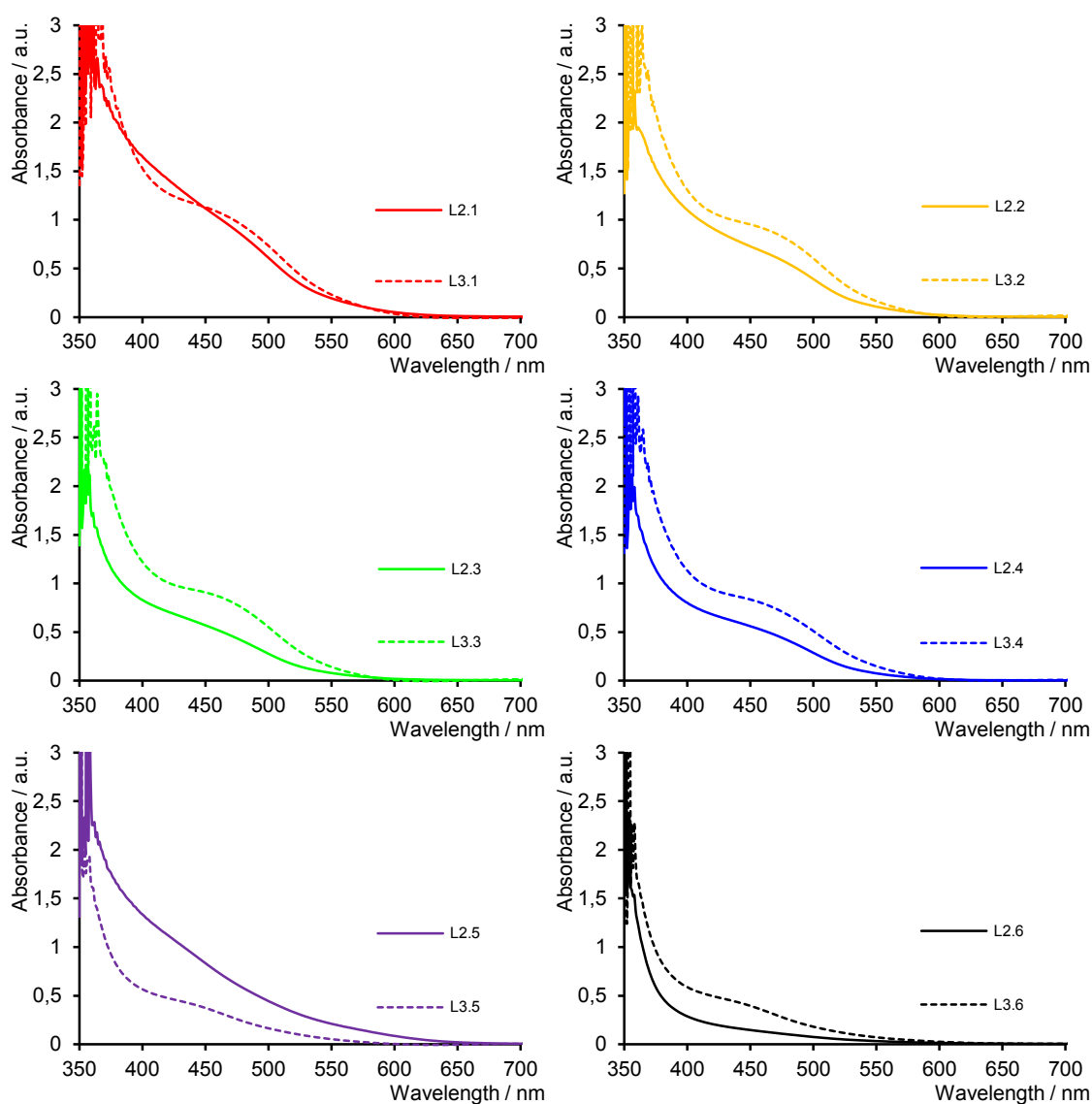
Figure 102: Solid state absorption spectra of heteroleptic dyes adsorbed on TiO₂. For the ligand exchange reaction, a CH₂Cl₂ solution of homoleptic copper(I) complex was used.

The solid-state absorption spectra of the cells were recorded, each spectrum being corrected for the background spectrum of a blank DSC (TiO₂).
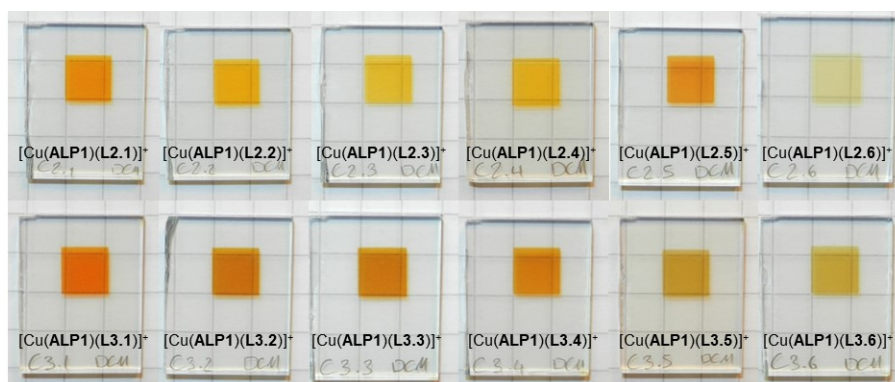
*Figure 103: Cells after immersing in CH₂Cl₂ solution of homoleptic complexes [Cu(**L2.1-2.6**)₂][PF₆] (**top**) and [Cu(**L3.1-3.6**)₂][PF₆] (**bottom**). Left to right **L2.1-2.6**, **L3.1-3.6** respectively.*

In general all photoanodes of the 2nd generation show a stronger intensity in absorbance than the 1st generation, except for **L2.5**, where the 1st generation exhibits a much stronger absorption than with **L3.5**. Concerning the shape of the curve, it is observed that the 2nd generations featuring a more distinct shoulder at $\approx$ 480nm than the 1st generation.

Even by the naked eye, a clear difference in colour intensity can be observed by comparing dyed photoanodes of the 1st and 2nd generation.

V.7   Discussion

Dyes of the 2nd generation undergo an increase in *Jsc* over time, which can be attributed to enhanced photon collection due to reorganisation of dye molecules.

Although the extension of the absorption is a desired feature that a dye should possess for efficient light harvesting and improved photocurrent, aggregation of molecules should be avoided because such molecular aggregations can decrease the electron injection efficiency[219]. Aggregation leads to unfavourable back electron transfer and decreases the *Voc* of the device[220].

Although the absorbance could be increased on going from the 1st to the 2nd generation, only devices with ancillary ligands **L3.1** and **L3.2** yield efficiencies surpassing their 1st generation analogues.

Not only do the substituents in the 6,6'-positions have an effect on the *Voc*, but also on the dye uptake on TiO2. One reason as already mentioned is the steric hindrance of the 2nd generation dendrimer backbone, leading to a much more hindered ligand exchange reaction when there are bigger substituents in the 6,6'-positions of the ancillary ligand. Besides the aggregates, the low packing density of chromophores on the surface, which allows less hindered recombination of injected electrons and I_3^-[221], is responsible for the lower performance.

The increase in *Voc* with increasing dye adsorption can be explained by a reduced charge recombination at the TiO2 - electrolyte interface. Where there is a higher adsorbed amount of dye on the TiO2 surface, it can act as an insulting layer that protects the TiO2 from the electrolyte and decreases the electron transfer from the semi-conductor to the oxidized electrolyte (I_3^-) (charge recombination), causing a gain in *Voc*[222][223].

However, O'Regan[224] and co-workers have recently pointed out that care must be taken in relating the dye loading to *Voc*, since the presence of the dye also shifts the TiO2 conduction band edge, which in itself has an effect on *Voc*[225].

V.8   Conclusion

Cells with ancillary ligands **L2.1** and **L3.1** perform well, showing higher *Jsc* and η values than other dyes. Their *EQE* spectra extend further into the red region than for other dyes. The *EQE* measurements also indicate that dyes containing **L2.6** and **L3.6** (2-naphthyl groups) show the lowest injection efficiency, which is consistent with the low *Jsc* values measured. Therefore the introduction of these large substituents is unfavourable for the device performance. Nevertheless, after two weeks the 1st generation with **L2.5** (phenyl groups) performs even better than the cells with **L2.1** and **L3.1**. However the performance drops on going to the 2nd generation analogue.

The final conclusion is that the dyes with ancillary ligands **L2.1**, **L2.5** and **L3.1** are the most promising dyes.

V.9   DSC fabrication and measurements

DSCs were prepared adapting the method of Grätzel and coworkers[196][197]. For the photoelectrode, Solaronix Test Cell Titania Electrodes made from TCO22-7 FTO coated glass, prepared by screen-printing for a homogenous surface using Ti-Nanoxide pastes, active layer from Ti-Nanoxide T/SP covered by a reflective layer of Ti-Nanoxide R/SP, active area: 6×6 mm, thickness: titania layer 9 μm plus scattering layer 3 μm were used. The electrodes were rinsed with EtOH and sintered at 450 °C for 30 min, then cooled to ca. 80 °C and immersed in a 1 mM DMSO solution of the anchoring ligand **ALP1** for 24 h. The colourless electrode was removed from the solution, washed with DMSO and EtOH and dried with a heat gun at 60 °C. The electrode with adsorbed anchoring ligand was immersed in 0.1 mM CH_2Cl_2 solution of each homoleptic copper(I) complex for ca. 68 h. Each reference cell was prepared by dipping a commercial electrode in a 0.3 mM EtOH solution of standard dye N719 (Solaronix) for ca. 68 h. The electrodes were removed from the solution and were washed with the corresponding solvent and dried with a heat gun at 60 °C. For the counter electrode Solaronix Test Cell Platinum Electrodes (made from TCO22-7 FTO coated glass) were used. Residual organic impurities were removed by heating for 30 min at 450 °C on a heating plate.

The dye-covered TiO_2 electrode and Pt counter-electrode were assembled using thermoplast hot-melt sealing foil (Solaronix Test Cell Gaskets) by heating while pressing them together. The electrolyte was a mixture of LiI (0.1 mol dm^{-3}), I_2 (0.05 mol dm^{-3}), 1-methylbenzimidazole (0.5 mol dm^{-3}) and 1-butyl-3-methylimidazolinium iodide (0.6 mol dm^{-3}) in 3-methoxypropionitrile; it was introduced into the DSC by vacuum backfilling. The hole on the

counter electrode was sealed using hot-melt sealing foil (Solaronix Test Cell Sealings) and a cover glass (Solaronix Test Cell Caps).

The solar cell measurements and testing protocol was performed using fully masked cells. A black coloured copper sheet was used for masking with a single aperture of an average area of 0.06012 cm^2 (with a standard deviation of 1%) placed over the screen printed dye-sensitized TiO$_2$ circle. The area of the aperture in the mask was smaller than the active area of the dye-sensitized TiO$_2$ dot (0.36 cm^2). For complete masking, tape was also applied over the edges and rear of cell.

Measurements were made by irradiating from behind using a light source SolarSim 150 (100 mW cm^{-2} = 1 sun). The power of the simulated light was calibrated by using a reference Si cell. The quantum efficiency measurements were performed on a Spe-Quest quantum efficiency setup from Rera Systems (Netherlands) equipped with a 100 W halogen lamp (QTH) and a lambda 300 grating monochromator from Lot Oriel. The monochromatic light was modulated to 3Hz using a chopper wheel from ThorLabs. The cell response was amplified with a large dynamic range IV converter from CVI Melles Griot and then measured with a SR830 DSP Lock-In amplifier from Stanford Research.

CHAPTER VI: SOLVENT EFFECT ON DSC PERFORMANCE

VI   Acetone solutions for *homoleptic* copper(I) complexes

In this chapter the performance of DSCs incorporating the same dyes as in Chapter V is investigated. However, during the ligand exchange reaction, the *homoleptic* Cu(I) complexes were dissolved in acetone (whereas in chapter V they were dissolved in CH_2Cl_2). To avoid overestimation of the efficiencies, all cells were masked. The DSC sets of 1st and 2nd generation dendrimers were measured over a period of three weeks with respect to **N719**.

for **L2.1-L2.6** R_2 = OMe

for **L3.1-L3.6** R_2 =

for R_1 = methyl	**L2.1 / 3.1**
n-butyl	**L2.2 / 3.2**
isobutyl	**L2.3 / 3.3**
n-hexyl	**L2.4 / 3.4**
phenyl	**L2.5 / 3.5**
2-naphthyl	**L2.6 / 3.6**
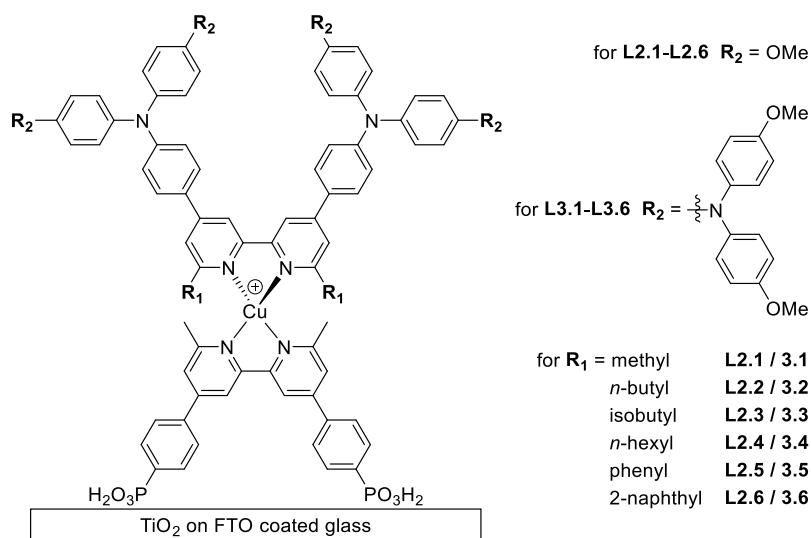
Scheme 21: 1st and 2nd generation dendrimers incorporated in DSCs.

It is known from the literature that the solvent of the dye solution affects the dye uptake on TiO_2[216]. When a dye (a copper(I) salt) is dissolved in a solvent, the interactions between complex cation and solvent depend on the latter, which could cause changes in the physical and chemical properties of the dye and semiconductor surface[226]. Additionally, it is known that acetone can bind to TiO_2, which could also have an influence of the performance[227].

Since the 1st and 2nd generation capping ligands contain arylamines, the *homoleptic* complexes [Cu(**L2.1-2.6**)₂][PF₆] and [Cu(**L3.1-3.6**)₂][PF₆] were chosen for trials in acetone. This solvent is supposed to be milder than the previously used CH_2Cl_2 in terms of pH and therefore, more tolerated by amines.

VI.1   DSC parameters 1st and 2nd generations

dye 1st generation	day	J_{sc} [mA/cm²]	V_{oc} [mV]	ff [%]	η [%]	rel. η [%]	dye 2nd generation	day	J_{sc} [mA/cm²]	V_{oc} [mV]	ff [%]	η [%]	rel. η [%]
[Cu(ALP1)(L2.1)]⁺	0	6.00	510	70.3	2.15	29.4	[Cu(ALP1)(L3.1)]⁺	0	6.46	515	67.9	2.26	32.7
[Cu(ALP1)(L2.2)]⁺	0	4.41	482	69.4	1.48	20.2	[Cu(ALP1)(L3.2)]⁺	0	6.08	506	70.8	2.18	31.6
[Cu(ALP1)(L2.3)]⁺	0	4.22	475	69.6	1.39	19.0	[Cu(ALP1)(L3.3)]⁺	0	5.48	475	69.9	1.82	26.4
[Cu(ALP1)(L2.4)]⁺	0	5.60	542	71.8	2.18	29.8	[Cu(ALP1)(L3.4)]⁺	0	5.25	488	70.9	1.81	26.3
[Cu(ALP1)(L2.5)]⁺	0	3.22	468	68.6	1.03	14.1	[Cu(ALP1)(L3.5)]⁺	0	4.01	459	70.2	1.29	18.7
[Cu(ALP1)(L2.6)]⁺	0	4.29	508	67.0	1.46	19.9	[Cu(ALP1)(L3.6)]⁺	0	3.04	444	69.2	0.93	13.5
N719	0	16.72	641	68.4	7.32	100.0	**N719**	0	16.52	608	68.8	6.90	100.0
[Cu(ALP1)(L2.1)]⁺	18	5.27	520	71.1	1.94	24.5	[Cu(ALP1)(L3.1)]⁺	22	5.94	536	70.3	2.23	27.5
[Cu(ALP1)(L2.2)]⁺	22	4.42	516	70.7	1.61	20.3	[Cu(ALP1)(L3.2)]⁺	22	5.97	532	71.6	2.27	28.0
[Cu(ALP1)(L2.3)]⁺	22	4.18	487	69.6	1.42	17.8	[Cu(ALP1)(L3.3)]⁺	22	6.31	541	71.0	2.42	29.9
[Cu(ALP1)(L2.4)]⁺	22	5.05	532	70.8	1.90	23.9	[Cu(ALP1)(L3.4)]⁺	22	5.47	522	70.6	2.02	24.9
[Cu(ALP1)(L2.5)]⁺	22	4.00	485	69.9	1.36	17.1	[Cu(ALP1)(L3.5)]⁺	22	4.99	487	71.3	1.73	21.4
[Cu(ALP1)(L2.6)]⁺	22	4.10	504	68.0	1.41	17.7	[Cu(ALP1)(L3.6)]⁺	22	2.77	466	70.2	0.91	11.2
N719	22	16.65	671	71.2	7.95	100.0	**N719**	22	16.98	674	70.9	8.11	100.0

*Table 16: DSC parameters for [Cu(**L2.1-2.6**)₂]⁺ and [Cu(**L3.1-3.6**)₂]⁺ over 3 weeks prepared from acetone solutions.*

The data for the 1st and 2nd generation dendrimers incorporated in DSCs from acetone solutions of *homoleptic* copper(I) complexes are given in Table 16. All devices exhibit a satisfactory fill factor between 68% and 72%. They are measured with respect to **N719**, which is set to $\eta = 100\%$, to allow an assessment of relative efficiencies.

VI.1.1   1st Generation

We concentrate first on the 1st generation of dendrimers acting as ancillary ligands (**L2.1-2.6**). On the day of sealing (day 0), the devices with capping ligands **L2.1** and **L2.4** exhibit the highest efficiencies of $\eta = 2.15$ and 2.18%, respectively. A much lower performance is shown by cells with **L2.2** and **L2.6**, which achieve $\eta = 1.48$ and 1.46%, respectively. A slightly reduced efficiency was obtained for the DSC with **L2.3** as capping ligand, yielding $\eta = 1.39\%$. The lowest efficiency was obtained with capping ligand **L2.5**, reaching only 1.03% on day 0.

Focusing on the short-circuit-current density, the highest *Jsc* was measured with ancillary ligand **L2.1**, reaching 6.00 mA cm⁻². For the device with capping ligand **L2.4**, a *Jsc* of 5.60 mA cm⁻² was measured. The fact that the highest *Jsc* values were obtained for these two cells is consistent with their efficiencies also being the highest of this set. With devices containing

ancillary ligands **L2.2**, **L2.6** and **L2.3**, comparable *Jsc* values of 4.41, 4.29 and 4.22 mA cm^{-2} were obtained. The poorest *Jsc* was measured for **L2.5**.

Comparing their *Voc* values the cell with **L2.4** reached by far the highest value with 542 mV on day 0. For devices with ancillary ligands **L2.1** and **L2.6**, similar *Voc* values of 510 and 508 mV were obtained. With capping ligands **L2.2** and **L2.3**, a lowered *Voc* of 482 mV and 475 mV respectively was measured. The lowest open-circuit voltage value was obtained for **L2.5**, which only reached 468 mV.

Upon aging, devices with capping ligands **L2.1**, **L2.4** and **L2.6** showed slightly decreased efficiency, whereas for cells with ancillary ligands **L2.2**, **L2.3** and **L2.5**, an increased efficiency was measured.

After 3 weeks, all devices (except the cell with capping ligand **L2.5**), decreased in *Jsc*. The obtained order in *Jsc* does not differ from the order obtained for day 0. The highest *Jsc* was still obtained with **L2.1**, followed by the device with ancillary ligand **L2.4**. With ancillary ligand **L2.2**, a *Jsc* value of 4.42 mA cm^{-2} was obtained. For devices containing capping ligands **L2.3**, **L2.6** and **L2.5**, similar *Jsc* values of 4.18, 4.10 and 4.00 mA cm^{-2} were measured.

Except for the devices with capping ligands **L2.4** and **L2.6**, cells gained in open-circuit voltage on going from day 0 to day 22.

VI.1.2   2nd Generation

For the 2nd generation dendrimers as capping ligands in DSCs, the following order of efficiencies was obtained for day 0. As a general trend on the day of sealing, the larger the substituents in the 6,6'-positions in the ancillary ligands, the lower the efficiency of the device. The highest conversion efficiencies were achieved with capping ligand **L3.1** and **L3.2**, which reached η = 2.26 and 2.18%. For devices with ancillary ligands **L3.3** and **L3.4**, similar efficiencies of 1.82 and 1.81% were measured. Much poorer performances were obtained for cells incorporating **L3.5** and **L3.6** as capping ligands. These cells only reached 1.29% and 0.93%, respectively.

The same trend can be seen for the short-circuit-current density, where the order also follows the size of the substituents in the 6,6'-positions in the ancillary ligands. The devices with **L3.1** and **L3.2** reached *Jsc* of 6.46 mA cm^{-2} and 6.08 mA cm^{-2}, respectively. Much lower *Jsc* values were obtained for cells with capping ligands **L3.3** and **L3.4**, for which 5.48 mA cm^{-2} and 5.25 mA cm^{-2} were measured, respectively. The lowest *Jsc* values were measured for ancillary ligands with aromatic substituents in the 6,6'-positions. While the cell with **L3.5** reached 4.01 mA cm^{-2}, the device with capping ligand **L3.6** achieved only 3.04 mA cm^{-2}.

For values of *Voc* on day 0, a similar order was found. The bulkier the substituents in the 6,6'-positions in the ancillary ligands, the lower the *Voc* value. Only the device with **L3.4** exhibited a higher *Voc* value than **L3.3**. All devices show *ff* between 68 and 71% on day 0.

With ongoing measurement time (on going from day 0 to day 22), the order in efficiencies becomes less clear. While some devices did not change in efficiency, some increased in their performance. The devices with **L3.1** and **L3.6** did not change much in efficiency over time. A small increase in efficiency was measured for the device with ancillary ligand **L3.2**. The cells with capping ligands **L3.3**, **L3.4** and **L3.5** exhibited a much higher efficiency on day 22 than on day 0. The best efficiency was measured for the device with capping ligand **L3.3**, which showed $\eta = 2.42\%$.

The observations for the change in *Jsc* over time are consistent with the changes made in the conversion efficiency. Cells which showed an increased efficiency after 22 days also showed a higher *Jsc* on day 22 than on day 0. In contrast, devices with a reduced efficiency on day 22 compared to day 0 also exhibit a lower *Jsc* value on day 22 than on the day of sealing. While devices with capping ligands **L3.1** and **L3.6** show a clear drop in *Jsc*, the cell with ancillary ligand **L3.2** exhibits only minor reduced *Jsc* compared to day 0. The DSCs with capping ligands **L3.3**, **L3.4** and **L3.5** exhibited a much higher *Jsc* on day 22 than on day 0. The highest *Jsc* was measured for the device with ancillary ligand **L3.3**.

Nevertheless, all devices gained in *Voc* over time and the highest measured *Voc* was obtained for the device with capping ligand **L3.3**.

VI.1.3   1st *vs.* 2nd Generations

In general on the day of sealing the 2nd generation performs better than the 1st generation. The exceptions are the *n*-hexyl and the 2-naphthyl substituted capping ligands, where the devices with ancillary ligand **L2.4** and **L2.6** exhibit a higher efficiency than the 2nd generation. The same trend is observed for *Jsc*, where only cells with capping ligands **L2.4** and **L2.6** show an improved *Jsc* compared to their corresponding 2nd generation device. The trend in *Voc* is almost consistent with the trends for *Jsc* and the efficiencies. While the DSCs with ancillary ligands **L2.4** and **L2.6** exhibit a higher *Voc* than their 2nd generation devices, the dye with **L2.5** shows a slightly higher *Voc* than **L3.5**.

After 3 weeks, the difference between the 1st and 2nd generation dyes becomes more obvious. Except for the device with ancillary ligand **L2.6**, the 2nd generation dye reaches higher efficiencies and higher short-circuit-current densities. This trend is almost consistent with the obtained sequence in *Voc* for day 22. There as well, only the cell with capping ligand **L2.6**

achieves a higher *Voc* than with **L3.6**; additionally the device with ancillary ligand **L2.4** reaches a slightly higher *Voc* than with **L3.4**.

VI.2   JV-curves
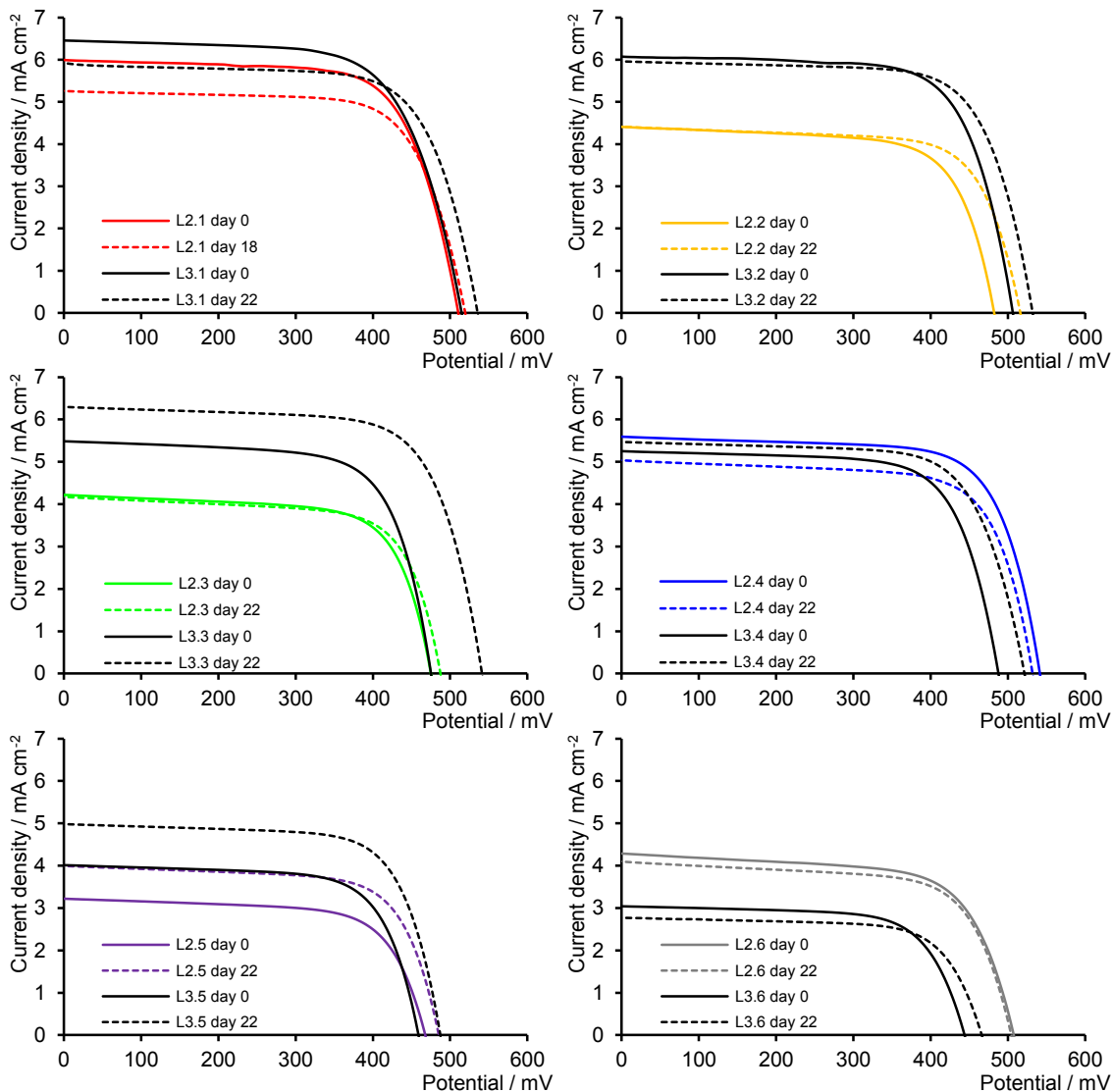
Figure 104: JV-curves for day 0 and day 22, comparing ancillary ligands of 1ˢᵗ and 2ⁿᵈ generations implemented in DSCs.

The *JV*-curves of DSCs with the 1ˢᵗ and 2ⁿᵈ generation ancillary ligands are shown in Figure 104. It is obvious to see that the DSC with ancillary ligand **L2.5** is the only one of the 1ˢᵗ generation that improves in *Jsc* over time. All other devices with the 1ˢᵗ generation dendrimer decrease or stay constant in *Jsc* over time. For the second generation dendrimers acting as capping ligands, devices with **L3.3**, **L3.4** and **L3.5** improve in *Jsc*, whereas the other ancillary ligands exhibit a drop in *Jsc* over time. It is also obvious that only the cell with capping **L2.6** shows a higher *Jsc* after 22 days than its corresponding 2ⁿᵈ generation device. In all other devices, the 2ⁿᵈ generation ancillary ligands yield a higher *Jsc*.

All DSCs gain in *Voc* on going from day 0 to day 22. Here as well for the 2nd generation ancillary ligands, higher *Voc* values are generally achieved compared with the 1st generation. Only **L2.4** gives a slightly higher *Voc* than **L3.4** and with capping ligand **L2.6**, a much higher *Voc* is obtained than with **L3.6**.

VI.3 EQE
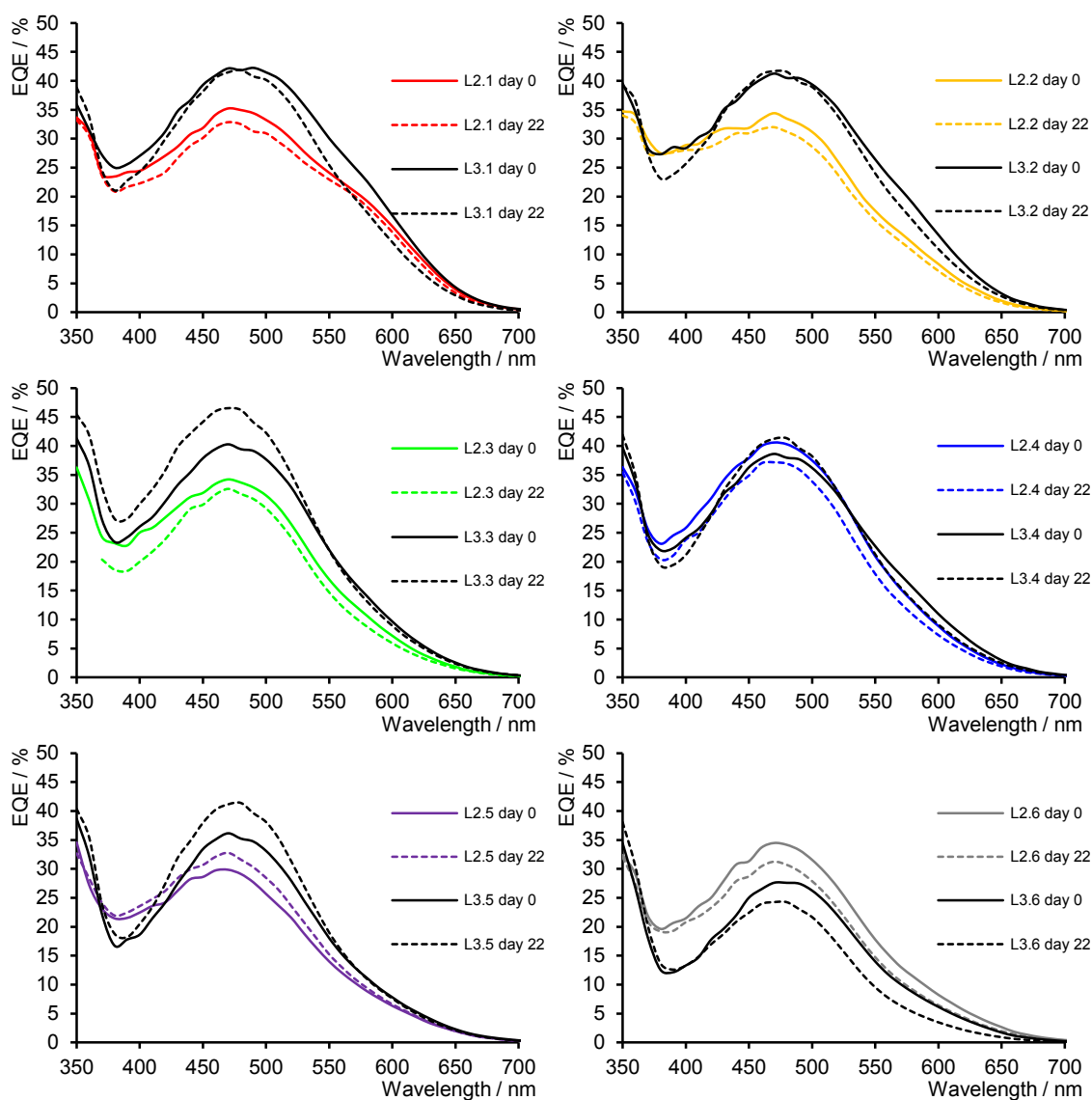
*Figure 105: EQE curves of [Cu(**ALP1**)(**L2.1-L2.6**)]⁺ and [Cu(**ALP1**)(**L3.1-L3.6**)]⁺ over 3 weeks prepared from acetone solutions.*

The external-quantum-efficiency (*EQE*) curves roughly exhibit the same shape with a λ_{max} at ≈ 470 nm (Figure 105). The devices with ancillary ligands **L2.1** and **L3.1** show an improved photoresponse at lower energy, and especially the cell with capping ligand **L3.1** exhibits a shoulder at 590 nm on day 0. In general, an improvement in *EQE* was measured for the second generation compared to the corresponding 1st generation dye. Only for the devices with capping

ligands **L2.4** and **L3.4** was a similar *EQE* measured, and for the capping ligand **L2.6**, a higher *EQE* was obtained than for the 2nd generation dye. These observations correspond to the measured efficiencies, where the cells with 2nd generation ancillary ligands exhibited an enhanced efficiency. For devices containing **L2.4** and **L2.6,** a similar and a higher efficiency, respectively, was measured for the 1st generation compared to their corresponding 2nd generation dye.

VI.4 Solid-state absorbance

FTO/TiO$_2$ electrodes without scattering layer and with adsorbed dye from acetone solutions of *homoleptic* copper(I) complexes were prepared and their solid state absorption spectra were recorded. The spectra were corrected for a background spectrum of a pristine electrode.
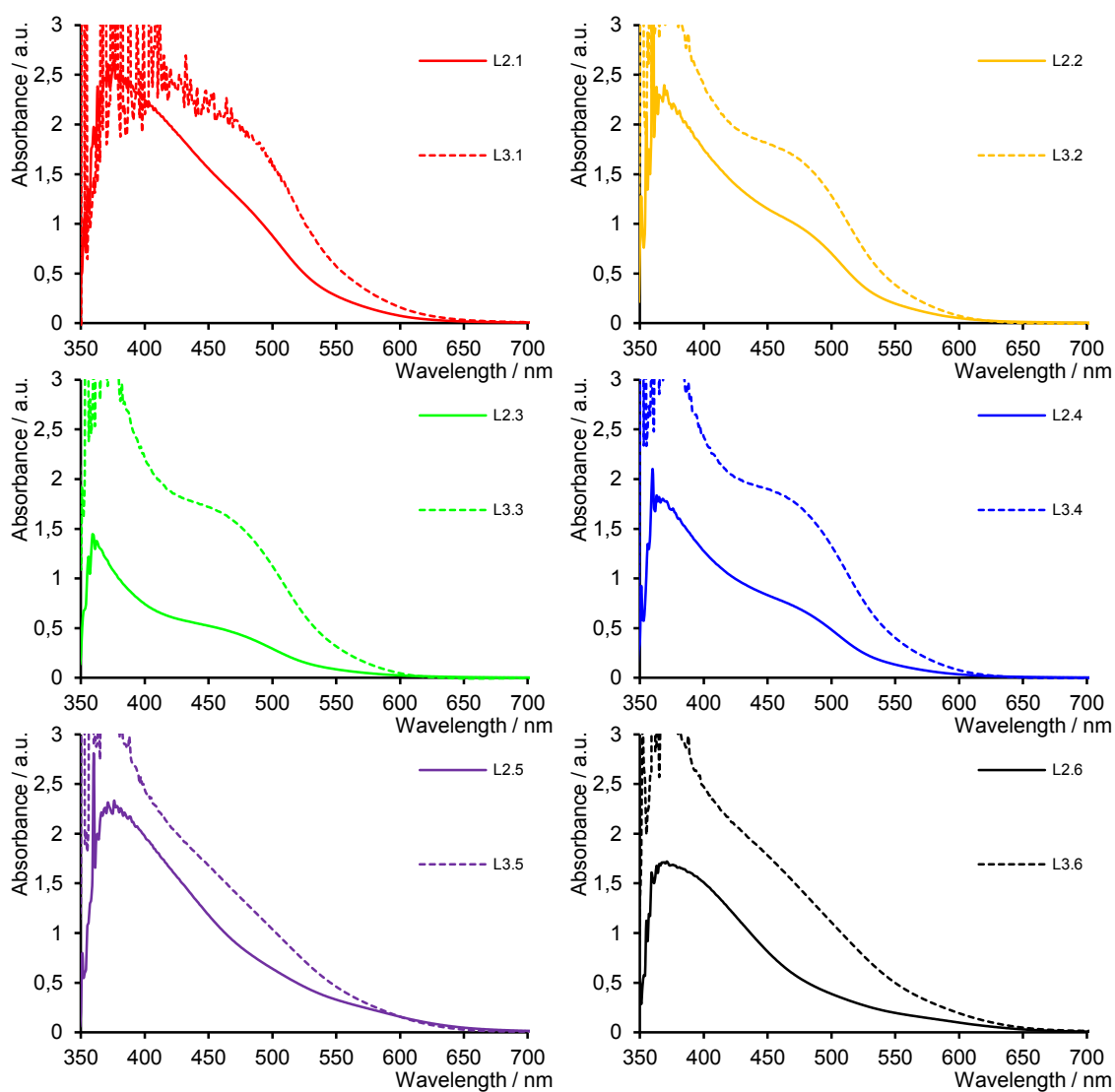
*Figure 106: Solid state absorbance of [Cu(**ALP1**)(**L2.1-L2.6**)]$^+$ and [Cu(**ALP1**)(**L3.1-L3.6**)]$^+$ adsorbed on TiO$_2$ prepared from acetone solutions.*

The solid state absorption spectra for devices containing alkyl substituents in the 6,6'-positions in the ancillary ligands all exhibit a shoulder at 480-490 nm. For the cells with aromatic substituents in the 6,6'-positions in the capping ligand, no low energy shoulder can be seen (see Figure 106). The photoanodes with 2nd generation dendrimers as ancillary ligands always exhibit a stronger absorption than the analogous 1st generation dyes.
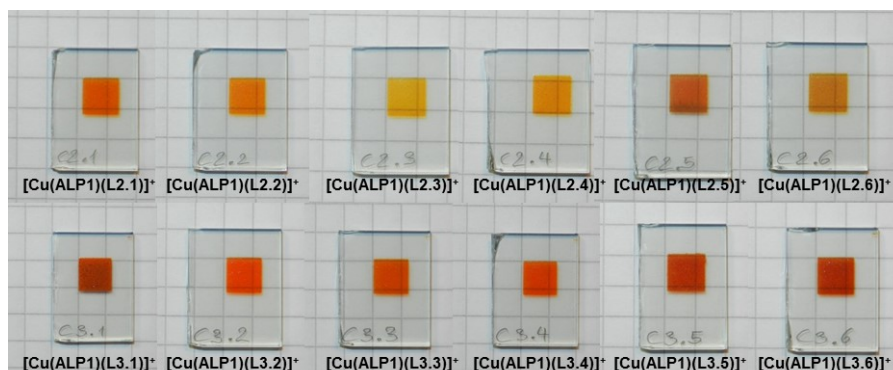
Figure 107: Dyed photoanodes with [Cu(**ALP1**)(**L2.1-L2.6**)]$^+$ and [Cu(**ALP1**)(**L3.1-L3.6**)]$^+$ obtained from acetone solutions of homoleptic copper(I) complexes.

By the naked eye, an obvious difference in absorption intensity can be observed on going from 1st to 2nd generation dendrimers acting as capping ligands (Figure 107). All photoanodes with 2nd generation dendrimers incorporated into the dyes exhibit a stronger coloured TiO$_2$ surface than those of the first generation.

VI.5   Discussion

While using an acetone solution of *homoleptic* copper(I) complexes during the ligand exchange reaction, some important observations were made.

For the 1st generation, the highest *Voc* was obtained with **L2.4**. This correlates with the literature where the introduction of alkyl chains reduced charge recombination and therefore an increased *Voc* was obtained[206]. For the device with **L2.3**, a low *Voc* was obtained. This correlates with findings from the literature, which state that by increasing the dye loading, an improved *Voc* can be obtained[201][216]. For dyes containing ancillary ligands with methyl, *n*-butyl and isobutyl substituents, an increase in *Voc* was observed on going from 1st to 2nd generation dendrimers. Similar results have been reported in the literature[228][215], where a longer lifetime of injected electrons was given as the reason for the increased *Voc* on going from 1st to 2nd generation dendrimers.

For the 1st generation, only the device containing capping ligand **L2.5** showed an improvement in *Jsc* over time. This is consistent with *EQE* measurements, which showed an enhanced *EQE*

after 22 days. This gain in current can be attributed to an improved photon absorbance upon a reorganisation / structural optimization among the phenyl substituents with time.

In general a higher current was obtained with 2nd generation dendrimers as ancillary ligands. This correlated with the increased absorption on TiO_2 and the improved *EQE*. Only for the 2-naphthyl substituents in the 6,6'-positions did the 1st generation yield higher *Jsc*, *Voc* and, therefore, an improved efficiency. The introduction of such bulky substituents in the 2nd generation seems to be detrimental to cell performance.

Unfortunately, the absolute dye loading on the surface cannot be determined because only the extinction coefficient of the *homoleptic* copper(I) complexes is known and not the extinction coefficient of the *heteroleptic* dyes adsorbed on TiO_2. Therefore it is not possible to obtain any information as to whether more dye molecules are present on the photoanode using the 1st or 2nd generation dendrimers and if the increase in absorption is mainly due to a higher dye loading on the surface or because of the more conjugated system. This would be helpful in order to calculate the effective efficiency of a single molecule.

VI.6   Conclusion

Upon using acetone solutions of copper(I) complexes during the ligand exchange, the introduction of the more conjugated 2nd generation ancillary ligands leads to higher conversion efficiencies. With the 2nd generation dendrimers as ancillary ligands, higher *Jsc* and *Voc* values were obtained. The dyes that incorporate the sterically demanding 2-naphthyl groups exhibit a poorer cell performance than other dyes. This is associated with lower *Jsc* and *EQE* values. The data also suggest that the extension of the dendron on going from **L2.6** to **L3.6** is detrimental to the dye performance. The highest efficiency was obtained for the dye [Cu(**ALP1**)(**L3.3**)]$^+$, yielding $\eta = 2.42\%$, which compares to 29.9% relative to **N719** (100%).

VI.7   DSC fabrication and measurements

The DSC fabrication and characterization applies to the above mentioned procedure (section V.9), except that for the dye solutions, a 0.1 mM acetone solution of each *homoleptic* copper(I) complex was used instead of CH_2Cl_2.

VI.8   Acetone vs. CH₂Cl₂ solutions of copper(I) complexes

In this part, the focus is on the influence of two different solvents (*e.g.* acetone and CH_2Cl_2) used for the solution of the *homoleptic* copper(I) complex, which is used to perform the ligand exchange on the surface.
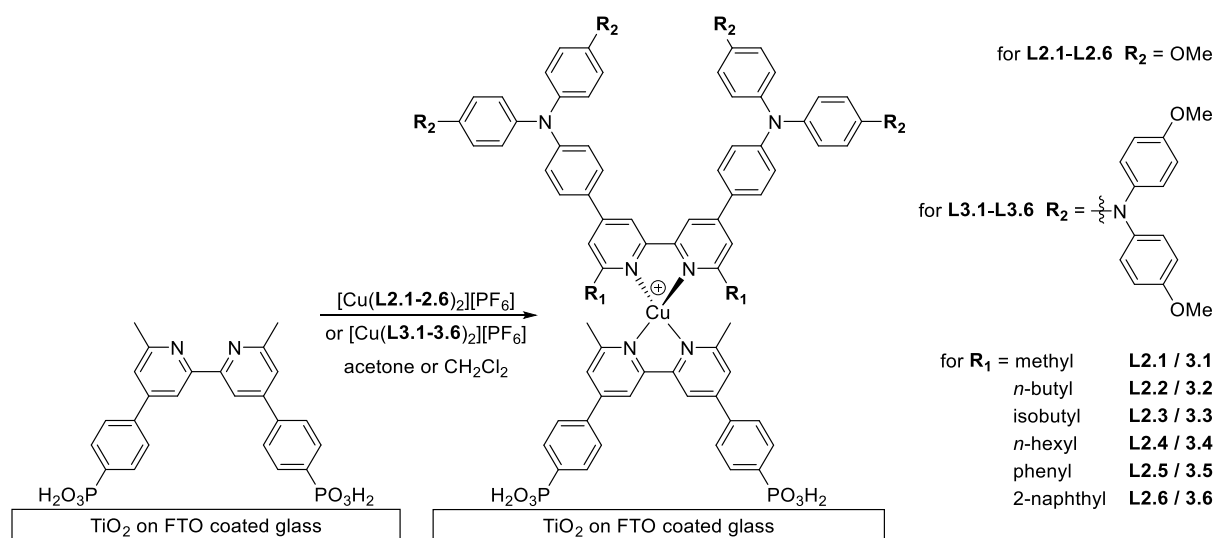
Scheme 22: Ligand exchange on a TiO₂ surface to form the heteroleptic adsorbed dye.

It is known from the literature[216] that the solvent can affect the amount of dye, that is adsorbed on the surface. On the other hand, the dye loading itself has a crucial influence on the device performance[201].

The main interest in this study was to see if one of the solvents would influence the dye adsorption and whether any other issues such as dye aggregation could be avoided by using one or the other solvent.

VI.9   1st Generation: Acetone *vs.* CH₂Cl₂

We return to the influence of the solvent during the dye dipping cycle when making the solar cells. The data for DSCs incorporating the 1st generation dendrons that are fabricated using acetone and methylenechloride solutions of *homoleptic* copper(I) complexes are represented in Table 17. The devices were measured over two and three weeks respectively.

Acetone							CH₂Cl₂						
dye 1st generation	day	J_{sc} [mA/cm²]	V_{oc} [mV]	*ff* [%]	η [%]	rel. η [%]	dye 1st generation	day	J_{sc} [mA/cm²]	V_{oc} [mV]	*ff* [%]	η [%]	rel. η [%]
[Cu(**ALP1**)(**L2.1**)]⁺	0	6.00	510	70.3	2.15	29.4	[Cu(**ALP1**)(**L2.1**)]⁺	0	5.47	490	69.4	1.86	25.4
[Cu(**ALP1**)(**L2.2**)]⁺	0	4.41	482	69.4	1.48	20.2	[Cu(**ALP1**)(**L2.2**)]⁺	0	4.65	475	69.8	1.54	21.0
[Cu(**ALP1**)(**L2.3**)]⁺	0	4.22	475	69.6	1.39	19.0	[Cu(**ALP1**)(**L2.3**)]⁺	0	3.94	479	69.6	1.31	17.9
[Cu(**ALP1**)(**L2.4**)]⁺	0	5.60	542	71.8	2.18	29.8	[Cu(**ALP1**)(**L2.4**)]⁺	0	4.07	491	71.8	1.43	19.6
[Cu(**ALP1**)(**L2.5**)]⁺	0	3.22	468	68.6	1.03	14.1	[Cu(**ALP1**)(**L2.5**)]⁺	0	5.35	492	70.4	1.85	25.3
[Cu(**ALP1**)(**L2.6**)]⁺	0	4.29	508	67.0	1.46	19.9	[Cu(**ALP1**)(**L2.6**)]⁺	0	2.94	485	68.3	0.97	13.3
N719	0	16.72	641	68.4	7.32	100.0	N719	0	16.31	637	71.3	7.41	101.2
[Cu(**ALP1**)(**L2.1**)]⁺	18	5.27	520	71.1	1.94	24.5	[Cu(**ALP1**)(**L2.1**)]⁺	15	5.17	508	70.1	1.84	23.2
[Cu(**ALP1**)(**L2.2**)]⁺	22	4.42	516	70.7	1.61	20.3	[Cu(**ALP1**)(**L2.2**)]⁺	15	4.30	518	69.9	1.55	19.6
[Cu(**ALP1**)(**L2.3**)]⁺	22	4.18	487	69.6	1.42	17.8	[Cu(**ALP1**)(**L2.3**)]⁺	15	3.97	525	70.2	1.46	18.5
[Cu(**ALP1**)(**L2.4**)]⁺	22	5.05	532	70.8	1.90	23.9	[Cu(**ALP1**)(**L2.4**)]⁺	15	3.77	526	72.7	1.44	18.2
[Cu(**ALP1**)(**L2.5**)]⁺	22	4.00	485	69.9	1.36	17.1	[Cu(**ALP1**)(**L2.5**)]⁺	15	5.54	545	71.8	2.17	27.4
[Cu(**ALP1**)(**L2.6**)]⁺	22	4.10	504	68.0	1.41	17.7	[Cu(**ALP1**)(**L2.6**)]⁺	15	2.82	498	70.7	0.99	12.5
N719	22	16.65	671	71.2	7.95	100.0	N719	24	15.86	698	71.6	7.92	100.0

*Table 17: DSC parameters for [Cu(**ALP1**)(**L2.1-2.6**)]⁺ obtained from acetone (left) and CH₂Cl₂ (right) solutions of the homoleptic copper (I) complexes.*

For the ancillary ligands **L2.1**, the cell performs better when acetone is used during the dipping cycle. The device obtained from an acetone solution exhibits a higher *Jsc*, *Voc* and efficiency, independent of the measuring day. Both cells lost in *Jsc* over time but gained in *Voc*. For the devices with capping ligand **L2.2**, the cell from CH₂Cl₂ solution performs better on day 0 than the one obtained from an acetone solution. The difference between these cells is very small and can only be attributed to the difference in initial *Jsc*. Over time both cells improve in *Voc*, but whereas the CH₂Cl₂ cells decrease in *Jsc* over time, the DSCs from acetone solution do not lose in current. Therefore, after three weeks the cell with capping ligand **L2.2** obtained from an acetone solution yields a higher efficiency than the one from CH₂Cl₂ solution. With ancillary ligand **L2.3**, the cell obtained from acetone solution performs only slightly better than the one from a CH₂Cl₂ solution. They both exhibit a similar *Voc* and the device from the acetone solution shows a slightly higher *Jsc* on day 0. Over time they both improve in *Voc* but the cell

obtained from CH_2Cl_2 solution improves much more than the one from acetone solution. In *Jsc*, the devices containing ancillary ligand **L2.3** do not change over time. Due to the much higher *Voc* on the last measuring day, the cell from the CH_2Cl_2 solution performs better than the device obtained from an acetone solution. Cells with capping ligand **L2.4** show a much higher efficiency on day 0 when prepared from an acetone solution instead of a CH_2Cl_2 solution. This can be attributed to the increased *Jsc* and *Voc*. Over time they both lose in *Jsc*. While the cell prepared from an acetone solution loses some of its initial high *Voc*, the CH_2Cl_2 cell improves in *Voc*. Nevertheless this gain cannot compensate for the lack of current, so on the last measuring day the acetone cell still gives a higher efficiency. For the capping ligand **L2.5**, the device using a CH_2Cl_2 solution achieves a much higher efficiency on day 0 than the cell obtained from an acetone solution. It is exhibits a higher *Voc* and *Jsc*. Both cells improve in *Jsc* over time. The increase in *Voc* is much higher for the cell obtained from CH_2Cl_2 solution than for the cell obtained from an acetone solution. On the last day, the device with **L2.5** where a CH_2Cl_2 solution was used, showed the highest *Voc*, *Jsc* and best conversion efficiency for the 1st generation dendrons incorporated in DSCs. The lowest efficiencies for both solvents were obtained for the capping ligand **L2.6**. On day 0, the cell using acetone showed an increased efficiency compared to the CH_2Cl_2 cell. Over time, the device obtained from acetone solution loses in *Jsc* and slightly in *Voc*. On the other hand, the cell from CH_2Cl_2 only decreased in *Jsc* but gained in *Voc*. Over time the acetone cell decreased slightly, whereas for the cell obtained from a CH_2Cl_2 solution a minor increase in efficiency was observed.

An important conclusion is that, in general, higher conversion efficiencies are obtained when acetone is used during the cell fabrication, but no unambiguous trend can be seen. What is obvious is that with capping ligands **L2.1**, good efficiencies are always obtained. However the worst performing devices contained the bulky ancillary ligands **L2.6**.

VI.9.1 JV-curves
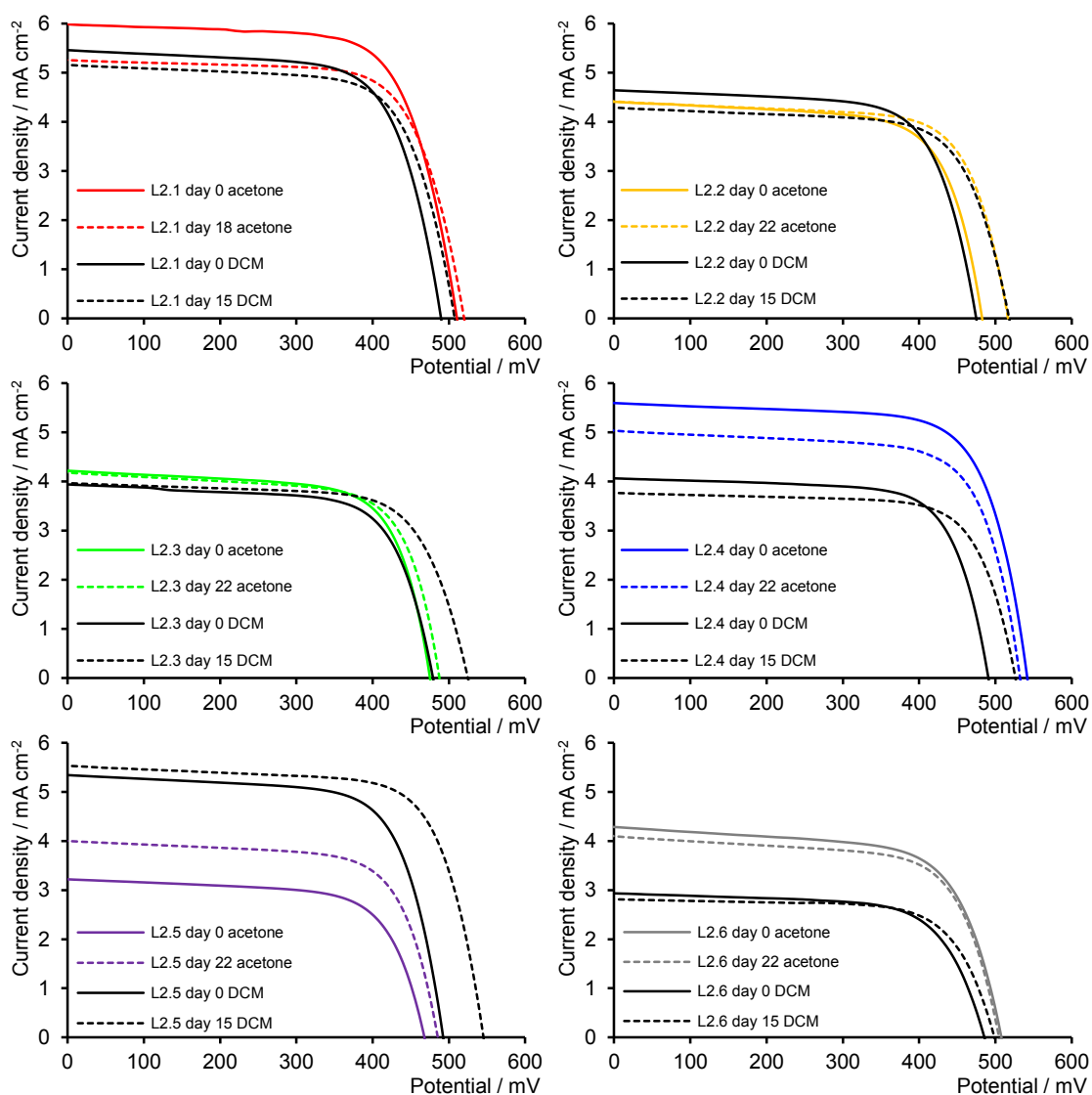
*Figure 108: JV curves for [Cu(**ALP1**)(**L2.1-2.6**)]⁺ obtained from acetone (coloured lines) and CH₂Cl₂ (black lines) solutions of the homoleptic copper (I) complexes.*

By comparing the *JV*-curves for the devices obtained from acetone and CH$_2$Cl$_2$ solutions of the *homoleptic* dyes (see Figure 108), it is obvious that on the last measuring day, devices obtained from acetone solutions exhibit a higher *Jsc* than those prepared by using CH$_2$Cl$_2$. The exception is for ancillary ligand **L2.5**, where the cell using CH$_2$Cl$_2$ reaches a much higher *Jsc* and *Voc* than the one prepared from an acetone solution. Another trend which can be detected is that only for devices with ancillary ligand **L2.5** an obvious increase in *Jsc* was obtained over time. All other devices hardly changed or even decreased in *Jsc* over time.

VI.9.2 EQE
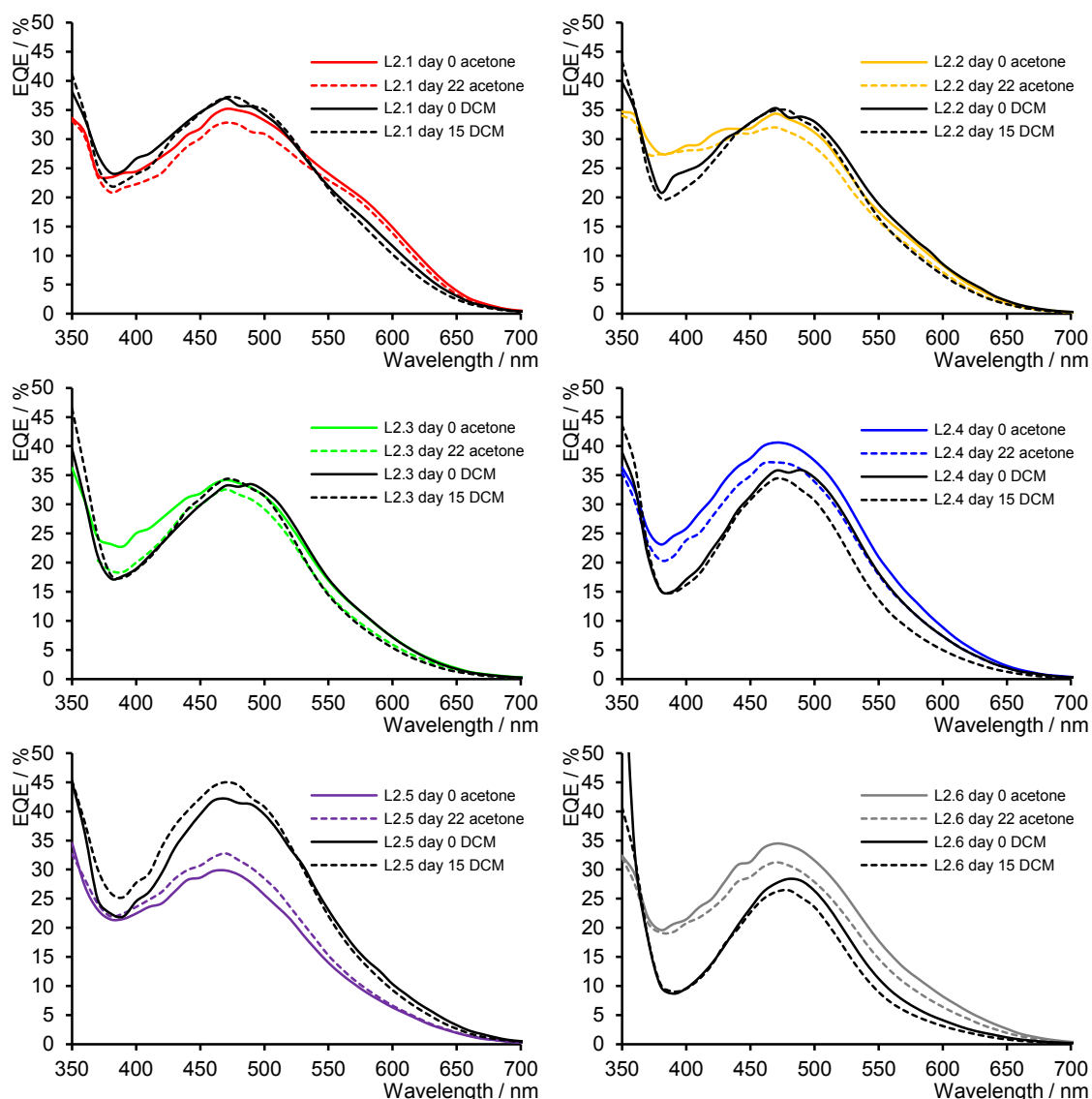
*Figure 109: EQE curves for [Cu(**ALP1**)(**L2.1-2.6**)]$^{+}$ obtained from acetone and CH$_2$Cl$_2$ solutions of homoleptic dyes.*

All *EQE* curves exhibit their λ_{max} at $\approx$ 470 nm. Only for the capping ligand **L2.1** is a clear difference in the curve shape observed. While the device prepared by using an acetone solution shows a lower *EQE* of 35% at 470 nm compared to the one prepared from a CH$_2$Cl$_2$ solution, its *EQE* performance is clearly enhanced over 550 nm. Additionally, the *EQE* trend for capping ligand **L2.5** is consistent with the *JV*-curves. They reveal a much lower quantum efficiency for the device prepared from an acetone solution than for the one where a CH$_2$Cl$_2$ solution of *homoleptic* dye was used. In general, the *EQE* curves are consistent with the measured *Jsc* and its behaviour over time.

VI.9.3 Solid-state absorption

FTO/TiO$_2$ electrodes without scattering layer and with adsorbed dye from acetone solutions of the *homoleptic* copper(I) complexes were prepared and their solid state absorption spectra were recorded. The spectra were corrected for a background spectrum of a bare electrode.
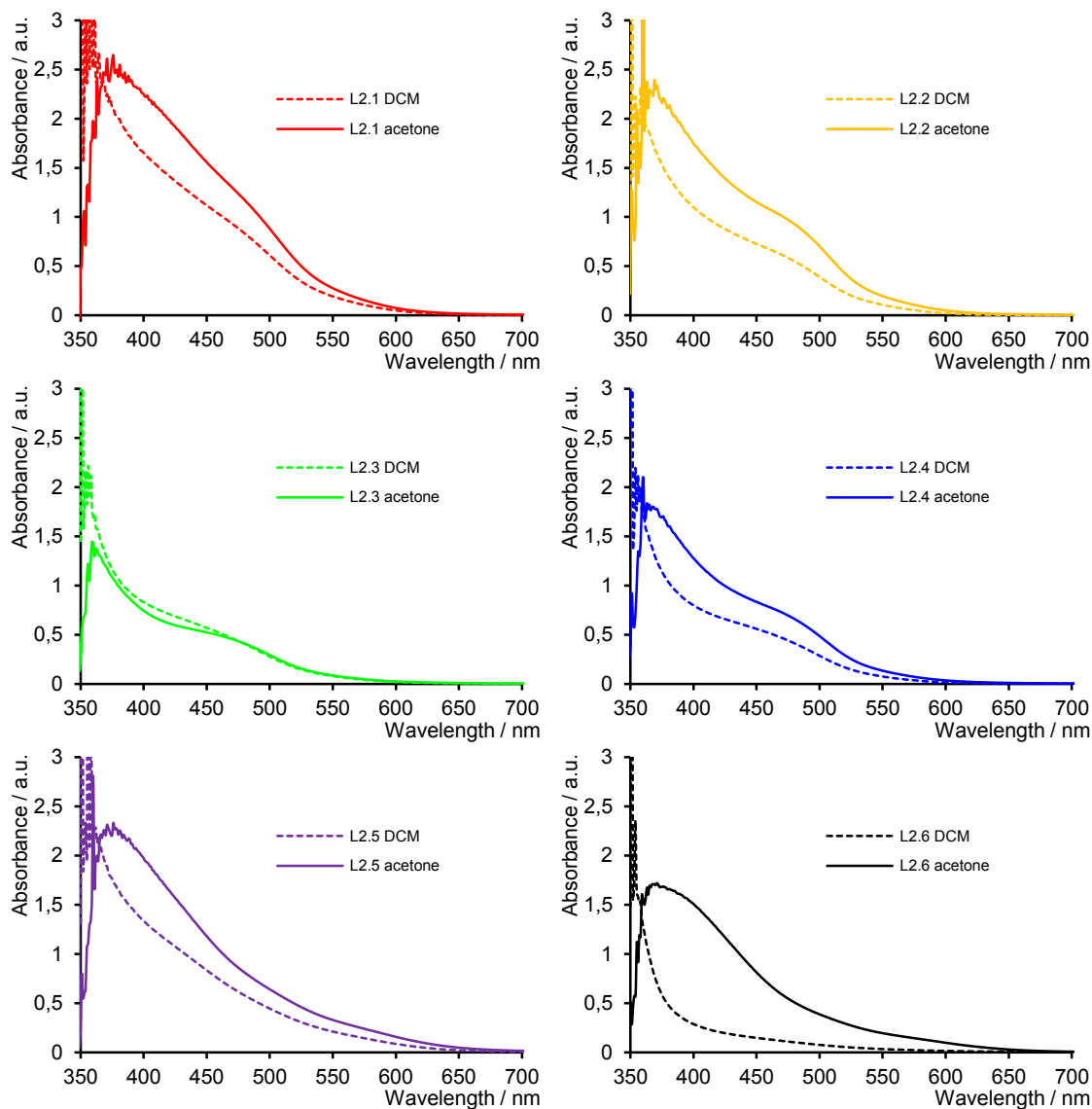
*Figure 110: Solid state absorption for [Cu(**ALP1**)(**L2.1-2.6**)]$^+$ obtained from acetone and CH$_2$Cl$_2$ solutions of homoleptic dyes.*

In all cases, using acetone during the dipping cycle of the cell preparation leads to stronger absorption over the whole spectrum. Except for the ancillary ligand **L2.3**, a similar absorption intensity was obtained independent of the solvent. This is consistent for this anchoring ligand, since for these cells comparable efficiencies and *Jsc* were obtained.
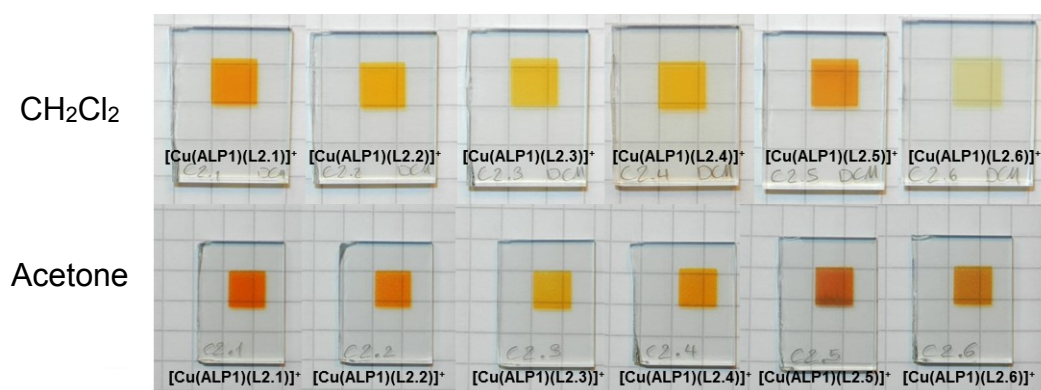
*Figure 111: Dyed photoanodes of adsorbed [Cu(**ALP1**)(**L2.1-2.6**)]⁺ on TiO₂.For the dipping cycle solutions of homoleptic dye in acetone (bottom) and CH₂Cl₂ (top) were used.*

By eye, there is, in general, an enhanced absorption by using acetone solutions instead of methylene chloride solutions of the complexes. By eye, cells with ancillary ligands **L2.3** look very similar, but there is a striking difference with the capping ligand **L2.6** when using acetone or CH₂Cl₂ during the dipping cycle.

VI.10 Discussion

With ancillary ligand **L2.1**, devices obtained from both solvents, acetone and CH₂Cl₂, achieve high efficiencies. The cell from acetone solution exhibits a higher *Voc*, *Jsc* and efficiency. Due to the stronger absorption from the acetone dipped photoanode, it can be assumed that more dye is present on TiO₂ when acetone is used during the dipping cycle instead of CH₂Cl₂. The enhanced dye loading is consistent with retarded charge recombination[201][222][229], which raises the *Voc*, and higher photon absorption, which leads to a higher *Jsc*[225]. With capping ligand **L2.2**, the device where acetone was used during the dipping cycle yields a slightly higher efficiency than the one obtained from CH₂Cl₂ solution and this is mainly due to a higher *Jsc*. The *Voc* values are very similar. The higher *Jsc* value is attributed to the higher dye loading. The comparable *Voc* values can be explained by substituents in the 6,6'-positions of the ancillary ligands[218]. The *n*-butyl substituents seem to be able to compensate for the difference in dye loading and reduce/slow down the charge recombination[217], leading to similar *Voc* values. For the photoanode containing capping ligand **L2.3**, the same intensity of absorbance was obtained, no matter which solvent was used during the ligand exchange reaction. The overall efficiency on the last measuring day was slightly higher for the cell obtained from a CH₂Cl₂ solution. While the measured *Jsc* was higher for the DSC obtained from an acetone solution, the *Voc* was much higher for the cell from the CH₂Cl₂ solution. Additionally, the device from the CH₂Cl₂ solution gained drastically in *Voc* over time. Structural reorganisation of the isobutyl groups (blocking the electrolyte accessing the TiO₂/dye interface) might be the

reason for this gain in *Voc* over time. For the cells containing capping ligand **L2.4**, a relatively strong difference in performance was obtained for cells prepared from the two different dye solutions. While the device prepared from the acetone solution achieves $\eta = 1.90\%$ on the last measuring day, the device where a CH_2Cl_2 solution was used only reaches $\eta = 1.44\%$. This difference arises due to a much higher *Jsc* obtained from the cell using an acetone solution during the dipping cycle of the cell preparation. This is consistent with the higher dye loading by using the acetone solution, which is assumed by comparison of the solid state absorption spectra. Both cells exhibit a similar *Voc* value on the last measuring day, indicating that the *n*-hexyl substituents are able to reduce the charge recombination by the same amount for both cells[206][230]. The DSCs with ancillary ligands **L2.5** also show very different performances upon using different solvents for the ligand exchange step. Although the cell prepared from an acetone solution shows a stronger absorbance on the photoanode, its *Jsc*, *Voc* and efficiency are much lower than obtained for the cell using a CH_2Cl_2 solution of *homoleptic* copper(I) complex. This observation is supported by the *EQE* curves, which present a much lower *EQE* over the spectrum for the acetone cell than for the CH_2Cl_2 cell. A plausible reason might be that by using CH_2Cl_2 during the dipping cycle a saturated/optimized dye loading is achieved. By using the acetone solution, more dye can be bound to the surface but this may not be as ordered on the surface as for CH_2Cl_2. Therefore the aggregation of dye molecules increased, causing a less efficient photon absorption (self quenching). With capping ligand **L2.6** in the devices, the higher *Jsc* and efficiency was obtained for the cell using an acetone solution during the dipping cycle. The increased efficiency for the device using an acetone solution during the ligand exchange is consistent with its higher absorption on TiO_2 and the higher *EQE* over the whole spectrum.

VI.11 Conclusion

In general, higher *Jsc* values were obtained for devices when an acetone solution of *homoleptic* copper(I) complexes ($[Cu(\textbf{L2.1-2.6})_2][PF_6]$) was used for the ligand exchange reaction on the surface, than the ones prepared from a CH_2Cl_2 solution. Only for the capping ligand **L2.5**, much higher *Jsc*, *Voc* and efficiency was achieved upon using a CH_2Cl_2 solution of homoleptic dye during the dipping cycle. For both solvents, the dyes containing methyl substituents perform well (**L2.1**) and the worst performing dye contains the very bulky 2-naphthyl groups on the ancillary ligand.

VI.12 2nd Generation: Acetone *vs.* CH$_2$Cl$_2$

Acetone							CH$_2$Cl$_2$						
dye 2nd generation	day	J_{sc} [mA/cm^2]	V_{oc} [mV]	*ff* [%]	η [%]	rel. η [%]	dye 2nd generation	day	J_{sc} [mA/cm^2]	V_{oc} [mV]	*ff* [%]	η [%]	rel. η [%]
[Cu(**ALP1**)(**L3.1**)]$^+$	0	6.46	515	67.9	2.26	32.7	[Cu(**ALP1**)(**L3.1**)]$^+$	0	4.32	509	68.1	1.50	20.2
[Cu(**ALP1**)(**L3.2**)]$^+$	0	6.08	506	70.8	2.18	31.6	[Cu(**ALP1**)(**L3.2**)]$^+$	0	4.08	469	67.9	1.30	17.6
[Cu(**ALP1**)(**L3.3**)]$^+$	0	5.48	475	69.9	1.82	26.4	[Cu(**ALP1**)(**L3.3**)]$^+$	0	2.60	428	65.3	0.73	9.8
[Cu(**ALP1**)(**L3.4**)]$^+$	0	5.25	488	70.9	1.81	26.3	[Cu(**ALP1**)(**L3.4**)]$^+$	0	2.73	459	68.5	0.86	11.6
[Cu(**ALP1**)(**L3.5**)]$^+$	0	4.01	459	70.2	1.29	18.7	[Cu(**ALP1**)(**L3.5**)]$^+$	0	1.78	418	67.2	0.50	6.8
[Cu(**ALP1**)(**L3.6**)]$^+$	0	3.04	444	69.2	0.93	13.5	[Cu(**ALP1**)(**L3.6**)]$^+$	0	1.29	413	63.3	0.34	4.6
N719	0	16.52	608	68.8	6.90	100.0	**N719**	0	16.44	647	69.5	7.40	100.0
[Cu(**ALP1**)(**L3.1**)]$^+$	22	5.94	536	70.3	2.23	27.5	[Cu(**ALP1**)(**L3.1**)]$^+$	22	5.17	561	69.4	2.01	25.4
[Cu(**ALP1**)(**L3.2**)]$^+$	22	5.97	532	71.6	2.27	28.0	[Cu(**ALP1**)(**L3.2**)]$^+$	22	4.54	512	70.0	1.63	20.5
[Cu(**ALP1**)(**L3.3**)]$^+$	22	6.31	541	71.0	2.42	29.9	[Cu(**ALP1**)(**L3.3**)]$^+$	22	3.43	484	70.1	1.16	14.7
[Cu(**ALP1**)(**L3.4**)]$^+$	22	5.47	522	70.6	2.02	24.9	[Cu(**ALP1**)(**L3.4**)]$^+$	22	3.71	522	68.1	1.32	16.6
[Cu(**ALP1**)(**L3.5**)]$^+$	22	4.99	487	71.3	1.73	21.4	[Cu(**ALP1**)(**L3.5**)]$^+$	22	2.83	449	69.1	0.88	11.1
[Cu(**ALP1**)(**L3.6**)]$^+$	22	2.77	466	70.2	0.91	11.2	[Cu(**ALP1**)(**L3.6**)]$^+$	22	2.03	463	69.2	0.65	8.2
N719	22	16.98	674	70.9	8.11	100.0	**N719**	22	16.16	709	69.3	7.94	100.0

*Table 18: DSC parameters for [Cu(**ALP1**)(**L3.1-3.6**)]$^+$ using acetone (left) and CH$_2$Cl$_2$ (right) solutions of the homoleptic copper(I) complexes.*

The DSCs containing ancillary ligands **L3.1**-**L3.6** were measured over three weeks (Table 18). As a general trend it can be observed that all cells, without exception, prepared from acetone solutions exhibited a higher efficiency than those prepared using a CH$_2$Cl$_2$ solution of the *homoleptic* dye during the dipping cycle. All cells prepared using acetone solutions show higher *Jsc* and *Voc* values on day 0 than devices prepared from CH$_2$Cl$_2$ solutions. After 3 weeks, only the device with capping ligand **L3.1** obtained from a CH$_2$Cl$_2$ solution exhibits a higher *Voc* value than the one prepared using an acetone solution. While the set obtained from CH$_2$Cl$_2$ solutions gains in *Voc* and *Jsc*, the set from acetone improves also in *Voc* but only the cells containing capping ligand **L3.3, L3.4** and **L3.5** gain in *Jsc* over time.

On day 0, independent of the solvent, the DSC performance corresponds quite well to the steric demands of the 6,6'-substituents on the capping ligands. Whereas after three weeks the order in efficiencies for the acetone cells was unclear, the sequence for the cells using a CH$_2$Cl$_2$ solution did not change. On day 0 for both sets, the best performance was achieved with dyes containing capping ligand **L3.1**. The lowest efficiency on day 0 was measured for both sets with the DSC containing ancillary ligand **L3.6**. After three weeks, the cells with capping ligand **L3.6** exhibit the worst efficiencies. For the cells obtained from acetone solutions, the highest

efficiency after three weeks was obtained with the device incorporating ancillary ligand **L3.3** and reached η = 2.42% (or 29.9% relative to **N719** (100%)). For the CH₂Cl₂ set, the best performing dye after three weeks was still the cell with capping ligand **L3.1**, which achieved η = 2.01% (or 25.4% relative to **N719**).

VI.12.1 JV-curves
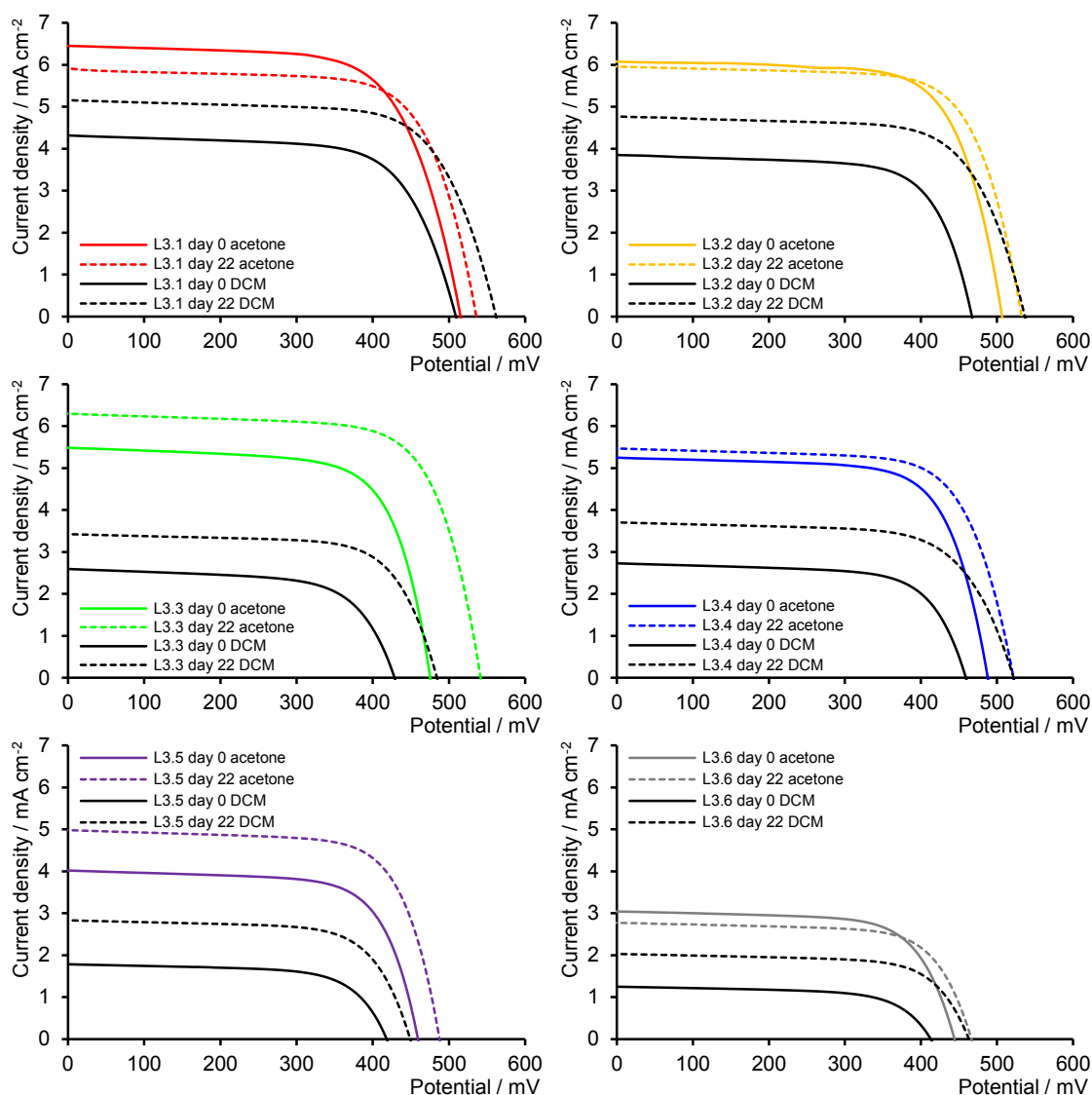
*Figure 112: JV curves for [Cu(**ALP1**)(**L3.1-3.6**)]⁺ using acetone and CH₂Cl₂ solutions of the homoleptic dyes.*

In the *JV*-curves, comparing the two sets obtained from different solvents (Figure 112), it is obvious that devices obtained from acetone solutions (coloured lines) all show higher *Jsc* values than those obtained from CH₂Cl₂ solutions. While all cells of the CH₂Cl₂ set gain in *Jsc* over time, only cells from the acetone set with capping ligands **L3.3, L3.4** and **L3.5** gain in *Jsc* over the measuring period. Nevertheless, all cells of both sets increase in *Voc* over time.

VI.12.2 EQE
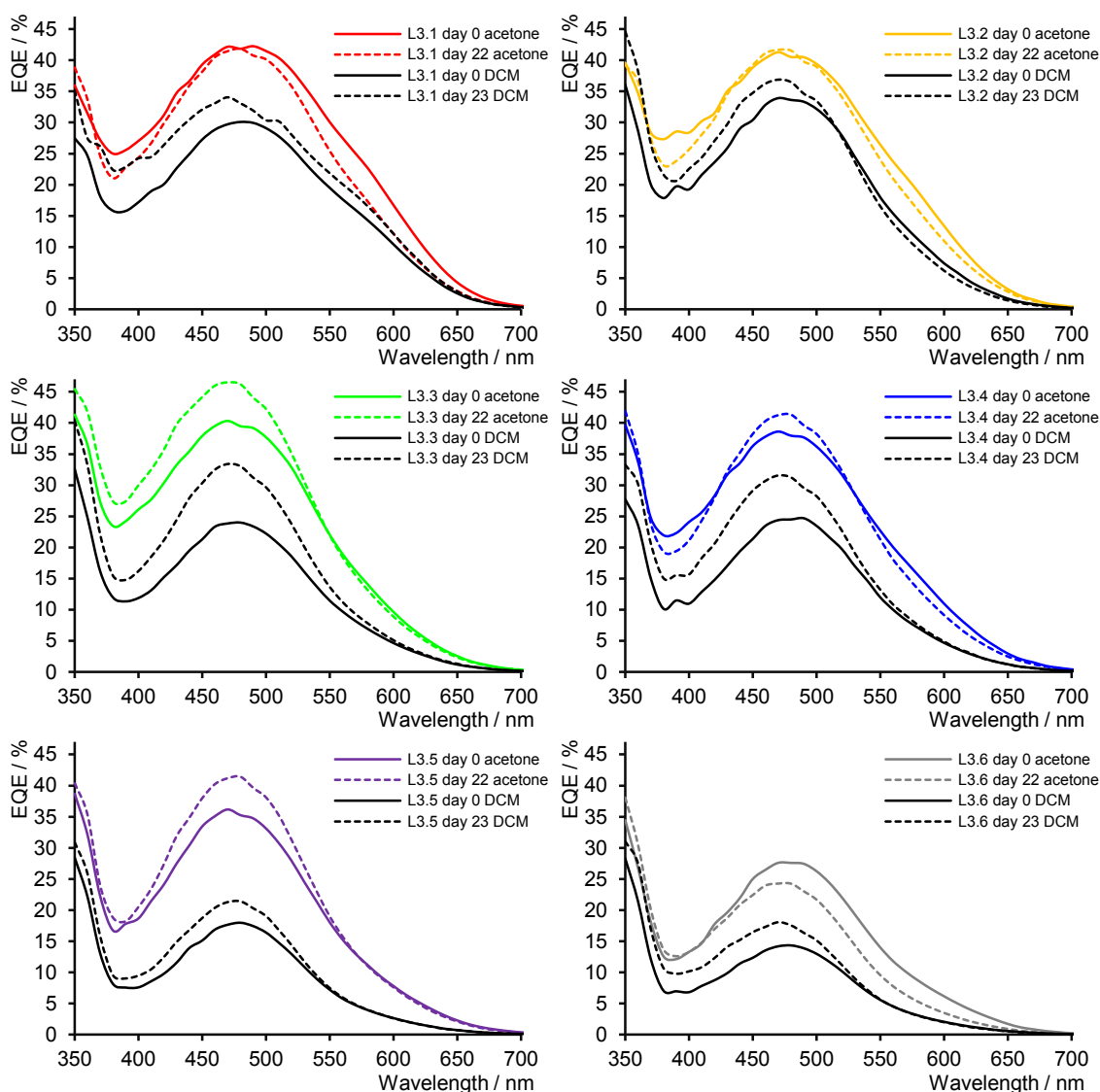
*Figure 113: EQE curves for [Cu(**ALP1**)(**L3.1-3.6**)]$^+$ obtained from acetone and CH$_2$Cl$_2$ solutions of homoleptic dyes.*

The *EQE*-curves comparing the two sets over the measuring time correlate nicely with the *JV*-curves. In all cases the device obtained from the acetone solution surpasses the cell obtained from CH$_2$Cl$_2$ solution. All DSCs exhibit their λ_{max} at 470-480 nm. For the devices containing ancillary ligands **L3.1**, a distinct shoulder can be detected at 590 nm. This is consistent with the *EQE*-curves obtained for their corresponding 1st generation dendrimers (see Figure 109). The curves also display an increase in current over time for the CH$_2$Cl$_2$ set. Additionally, the EQE over the whole spectrum correlates with the measured efficiency for the devices (see Table 18). The lowest *EQE* for both sets was measured for the devices containing ancillary ligand **L3.6**.

VI.12.3 Solid-state absorption

FTO/TiO$_2$ electrodes without scattering layer and with adsorbed dye from acetone and CH$_2$Cl$_2$ solutions of *homoleptic* copper(I) complexes were prepared and their solid state absorption spectra were recorded. The spectra were corrected with a background spectrum of a bare electrode.
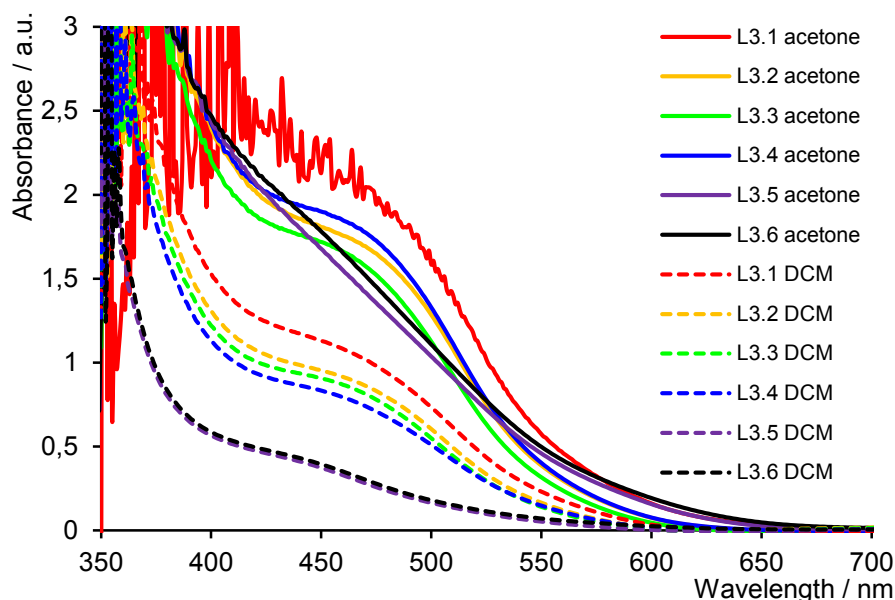
*Figure 114: Solid state absorption spectra for anchored [Cu(**ALP1**)(**L3.1-3.6**)]$^+$ on TiO$_2$ obtained from acetone and CH$_2$Cl$_2$ solutions of homoleptic dyes.*

From the solid state absorption spectra of the anodes containing the 2nd generation dendrimers obtained from different solvents a clear trend can be seen. The photoanode prepared from an acetone solution of *homoleptic* dye always shows a stronger absorbance than the one obtained using a CH$_2$Cl$_2$ solution. In the set where a CH$_2$Cl$_2$ solution was used, the order in absorbance measured on TiO$_2$ correlates with the steric hindrance of the 6,6'-substituents of the ancillary ligands. By using acetone, this effect seems to vanish. For the cell obtained from CH$_2$Cl$_2$ solutions, the devices containing capping ligands **L3.1**, **L3.2**, **L3.3** and **L3.4** exhibit the same curve shape with a shoulder at ≈460 nm, whereas the cells with capping ligands **L2.5** and **L2.6** show a reduced absorption with a shoulder at ≈ 440 nm.

For the cell obtained from acetone solutions the devices containing capping ligands **L3.1**, **L3.2**, **L3.3** and **L3.4** exhibit again the same curve shape with a shoulder at ≈470 nm, while anodes with ancillary ligands **L3.5** and **L3.6** do not show a shoulder but a steady decrease in intensity.
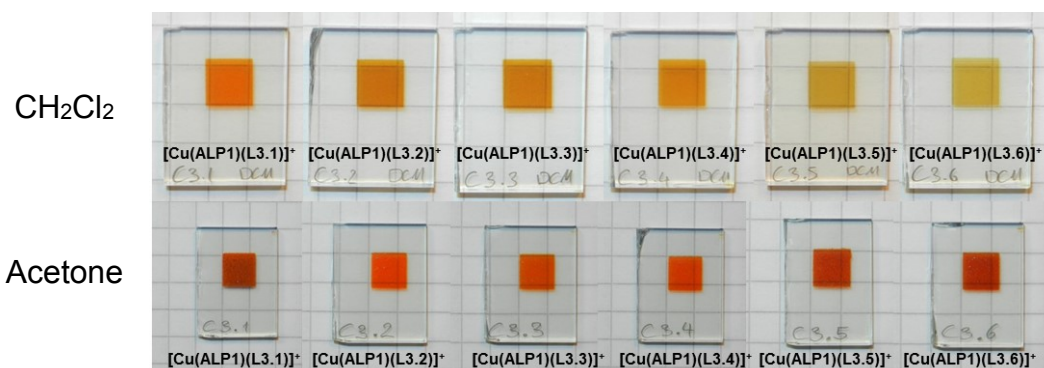
*Figure 115: Dyed photoanodes of adsorbed [Cu(**ALP1**)(**L3.1-3.6**)]⁺ on TiO₂ for the dipping cycle solutions of homoleptic dye in acetone (bottom) and CH₂Cl₂ (top) were used.*

Comparing the colour of photoanodes with adsorbed dyes from CH₂Cl₂ and acetone solutions, a remarkable difference not only in colour intensity but also in the colour itself can be seen (Figure 115). While anodes obtained from the treatment with CH₂Cl₂ solutions show colours from orange to pale orange, the electrodes where acetone was used during the dipping cycle exhibit an orange to red colour. A possible reason for this stronger colouring could be the increased dye loading.

VI.13 Discussion

The supreme performance of devices obtained using acetone solutions of *homoleptic* copper(I) complexes for the ligand exchange is mainly due to the higher dye loading on the semiconductor. For devices containing ancillary ligands **L2.1** (no bulky substituents in the 6,6'-positions) the strongest absorbance was obtained and their performances after three weeks were almost comparable, although the device from acetone showed a much stronger absorption. This leads to the conclusion that upon using acetone solutions during the dipping cycle, most of the dye molecules that contribute to the absorption are not functionally attached to TiO₂ and therefore cannot inject electrons, or that a high amount of dye molecules are aggregating. For cells with capping ligands **L3.2**, **L3.3**, **L3.4** and **L3.5**, the efficiencies of the acetone set is much higher than those for the CH₂Cl₂ set. Again, one reason for this improved performance is the amount of dye on the semiconductor. On the other hand, with acetone the aggregation of the dendrons with the substituents in the 6,6'-positions seems to be reduced. With the capping ligand **L3.6**, both sets perform poorly, although by using acetone during the dipping cycle the absorption was increased drastically. Again this suggests that with the presence of the bulky 2-naphthyl groups severe aggregation occurs, which is detrimental to the cell performance.

A reason for the increased dye uptake by using acetone solutions in the dipping cycle could be that acetone is able to coordinate and, therefore stabilize, a copper(I)-intermediate complex,

which leads to a better accessibility of non saturated anchoring ligands through dye molecules that already performed the ligand exchange on the surface.

VI.14 Conclusion

In order to obtain good efficiencies with the 2nd generation dendrimers, it is mandatory to use acetone solutions of *homoleptic* copper(I) complexes during the ligand exchange reaction. For devices prepared from CH$_2$Cl$_2$ solutions, only with ancillary ligand **L3.1** was an efficiency over 2% achieved.

Whether the extension of the dendrimers (*e.g.* on going from 1st to 2nd generation) was a useful tool to enhance the efficiency one has to differentiate between the solvents which are used during the dipping cycle.

For devices where acetone solutions are used for the ligand exchange, the extension of the aromatic system yielded higher efficiencies, except for the bulky 2-naphthyl groups, where the 1st generation achieved a higher efficiency.

For cells obtained from CH$_2$Cl$_2$ solutions, the trend looks completely different. In general, devices with the 1st generation dendrimers reach higher efficiencies than the 2nd generation. Only for the methyl substituents in the 6,6'-positions in the ancillary ligand (*e.g.* on going from **L2.1** to **L3.1**) a higher efficiency was obtained with the more conjugated capping ligand.

This leads to the conclusion that although more photons are absorbed fewer electrons are injected on going from 1st to the 2nd generation in CH$_2$Cl$_2$.

This leads us to investigate the effect of adding co-adsorbants, which should minimize intermolecular aggregation and thereby optimize the photon absorption, electron injection and reduce the charge recombination[231].

CHAPTER VII: AVOIDING AGGREGATION

VII The effect of a co-adsorbant and solvent

From the previous chapter we assume that a major issue for reduced device performance is dye aggregation. In 1993 Grätzel[232] et al. investigated the effect of different co-adsorbants on DSC
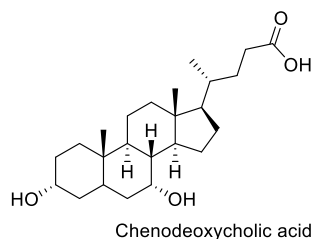
Scheme 23: Structure of cheno-deoxycholic acid (cheno).

performance containing chlorophyll derivatives. In the literature,[231] the effect of cheno-deoxycholic acid (subsequently named cheno) has already been investigated. The addition of cheno leads to an increase in efficiency for Ru(II) based dyes. This increase in efficiency was attributed to enhanced *Voc* and *Jsc* values.[233] The disaggregation of dye molecules leads to reduced back electron transfer/charge recombination and increases the *Voc* value of the device.[220][234]

Cheno can be used in various concentrations during the dyeing process of the electrode and is co-adsorbed on the TiO$_2$ surface along with the dye to reduce dye/dye intermolecular interactions, which can lower the DSCs performances[235][236][237][238]. On the one hand, coadsorption of cheno dissociates the dye aggregates and reduces the dye loading on TiO$_2$, but on the other hand it improves the electron injection yield and therefore the *Jsc*.[215] Hagfeldt et. al [239] additionally proposed that cheno may act as a proton buffer for the dye, assisting dye adsorption on the semi-conductor surface.
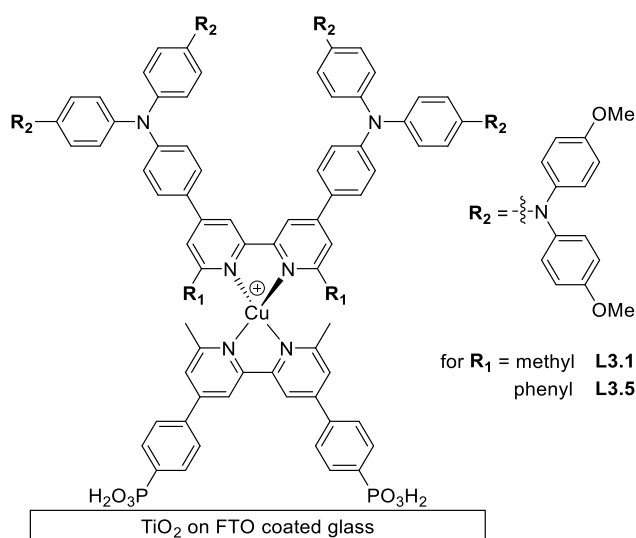
Scheme 24: Heteroleptic dyes, which are investigated in this chapter.

In this chapter, the 2nd generation ancillary ligands **L3.1** and **L3.5** were chosen to be investigated for the influence of coadsorbants upon device performance. Since for the DSCs containing capping ligand **L3.1** high efficiencies were obtained, the idea was to see whether the

addition of cheno could improve the performance even more. The capping ligand **L3.5** was chosen because its phenyl groups lower the efficiency compared to **L3.1**. This lower efficiency was assumed to be due to aggregation of the phenyl groups and the dendrons of the ancillary ligands. Our hope was to reduce the aggregation for devices containing **L3.5** and increase their performances.

VII.1 DSC parameters

The DSCs were prepared by immersing the photoanodes in a solution of **ALP1** (1.0 mM in DMSO), followed by a dipping cycle in CH_2Cl_2 or acetone solutions containing a 1:1 mixture of cheno and either $[Cu(\textbf{L3.1})_2][PF_6]$ or $[Cu(\textbf{L3.5})_2][PF_6]$ (0.1 mM each). The cells were measured over a period of three weeks.

cheno							no cheno						
CH_2Cl_2							CH_2Cl_2						
dye 2nd generation	day	J_{sc} [mA/cm²]	V_{oc} [mV]	ff [%]	η [%]	rel. η [%]	dye 2nd generation	day	J_{sc} [mA/cm²]	V_{oc} [mV]	ff [%]	η [%]	rel. η [%]
$[Cu(ALP1)(L3.1)]^+$	0	6.02	531	69.6	2.23	28.0	$[Cu(ALP1)(L3.1)]^+$	0	4.32	509	68.1	1.50	20.2
$[Cu(ALP1)(L3.5)]^+$	0	3.74	493	67.1	1.24	15.5	$[Cu(ALP1)(L3.5)]^+$	0	1.78	418	67.2	0.50	6.8
N719	0	16.73	669	71.2	7.96	100.0	N719	0	16.44	647	69.5	7.40	100.0
$[Cu(ALP1)(L3.1)]^+$	22	6.18	572	70.0	2.47	30.1	$[Cu(ALP1)(L3.1)]^+$	22	5.17	561	69.4	2.01	25.4
$[Cu(ALP1)(L3.5)]^+$	22	4.95	555	68.3	1.87	22.8	$[Cu(ALP1)(L3.5)]^+$	22	2.83	449	69.1	0.88	11.1
N719	22	16.34	704	71.4	8.22	100.0	N719	22	16.16	709	69.3	7.94	100.0
acetone							acetone						
dye 2nd generation	day	J_{sc} [mA/cm²]	V_{oc} [mV]	ff [%]	η [%]	rel. η [%]	dye 2nd generation	day	J_{sc} [mA/cm²]	V_{oc} [mV]	ff [%]	η [%]	rel. η [%]
$[Cu(ALP1)(L3.1)]^+$	0	6.72	520	60.9	2.13	26.7	$[Cu(ALP1)(L3.1)]^+$	0	6.46	515	67.9	2.26	32.7
$[Cu(ALP1)(L3.5)]^+$	0	6.34	546	70.8	2.45	30.8	$[Cu(ALP1)(L3.5)]^+$	0	4.01	459	70.2	1.29	18.7
N719	0	16.73	669	71.2	7.96	100.0	N719	0	16.52	608	68.8	6.90	100.0
$[Cu(ALP1)(L3.1)]^+$	22	6.27	553	60.1	2.08	25.3	$[Cu(ALP1)(L3.1)]^+$	22	5.94	536	70.3	2.23	27.5
$[Cu(ALP1)(L3.5)]^+$	22	6.33	552	70.9	2.48	30.1	$[Cu(ALP1)(L3.5)]^+$	22	4.99	487	71.3	1.73	21.4
N719	22	16.34	704	71.4	8.22	100.0	N719	22	16.98	674	70.9	8.11	100.0

*Table 19: DSC performance data for cells containing dyes [Cu(**ALP1**)(**L3.1**)]⁺ and [Cu(**ALP1**)(**L3.5**)]⁺. Relative efficiencies (last columns) are with respect to 100% for **N719**, measured under the same conditions. The cells were prepared from either CH_2Cl_2 or acetone solutions of homoleptic dyes. DSCs containing cheno are compared with cell where no cheno was co-adsorbed.*

VII.1.1 Cells with co-adsorbant

In general the addition of cheno improves the cell performance of devices containing ancillary ligands **L3.1** and **L3.5** (see Table 19). All cells containing cheno exhibit an improved *Jsc* and a higher *Voc* value than without cheno. DSCs originating from a CH$_2$Cl$_2$ dye solution and containing cheno gain in *Voc* and *Jsc* over time. While the device containing **L3.1** increases its *Jsc* from 6.02 to 6.18 mA cm^{-2}, the cell with capping ligand **L3.5** increases from 3.74 to 4.95 mA cm^{-2}. Also the increase in *Voc* is larger for the DSC containing capping ligand **L3.5** (493 mV to 555 mV) than for the cell with **L3.1** (531 mV to 572 mV). The efficiencies for cells containing ancillary ligands **L3.1** and **L3.5** rise from initially η = 2.23% and 1.24%, respectively, on day 0 to η = 2.47% and 1.87%.

DSCs originating from an acetone dye solution and containing cheno gain in *Voc* but *Jsc* stays constant or decreases over the measuring period. Whereas the cell containing capping ligand **L3.1** loses *Jsc* (6.72 mA cm^{-2} to 6.27 mA cm^{-2}), the device with capping ligand **L3.5** does not change in *Jsc*, exhibiting 6.33 mA cm^{-2} on day 0 and 6.34 mA cm^{-2} on day 22. While the cell containing **L3.1** shows an increase in *Voc* of 33 mV over time, the cell with capping ligand **L3.5** exhibits a minor gain in *Voc* of 6 mV. While the efficiency for the device containing ancillary ligand **L3.1** slightly decreases, the efficiency of the cell with capping ligand **L3.5** slightly increases.

Now we focus on differences between cells originating from acetone and CH$_2$Cl$_2$ solutions containing cheno. For the cells containing ancillary ligand **L3.1**, the main differences between the devices from the two different solvents are as follows. The cell using a CH$_2$Cl$_2$ solution improves in *Jsc* and *Voc* over time, whereas the DSC obtained from an acetone solution only gains in *Voc* but loses in *Jsc* over time. On day 0, the cell originating from the CH$_2$Cl$_2$ solution reached a slightly higher efficiency (η = 2.23%) than the one obtained from the acetone dye solution (η = 2.13%). Over the measuring period the DSC using the CH$_2$Cl$_2$ solution, clearly improved up to η = 2.47% on day 22, whereas the efficiency of the cell obtained from the acetone solution essentially did not change (η = 2.08%).

For the devices containing ancillary ligand **L3.5** originating from the two different solvents, the differences in performance are as follows. While the cell using CH$_2$Cl$_2$ during the dipping cycle shows a gain in *Voc* and *Jsc* over time, the device where an acetone solution of dye was used showed an increase in *Voc* but *Jsc* stayed unchanged over the measuring period. The cell obtained from the acetone solution leads to the higher efficiency on day 0 and after three weeks than the cell obtained from a CH$_2$Cl$_2$ dye solution. The cell originating from the CH$_2$Cl$_2$ solution increases its efficiency from an initial η = 1.24% on day 0 to 1.87% on day 22. The DSC

obtained from the acetone dye solution reached an efficiency on day 0 of $\eta = 2.45\%$ and after three weeks its efficiency was still the same ($\eta = 2.48\%$).

VII.1.2 Cells with cheno *vs.* cells without cheno

For DSCs with dyes [Cu(**ALP1**)(**L3.1/3.5**)]$^+$ originating from CH_2Cl_2 dye solutions, the addition of cheno during the dipping cycle improved the performance. Cells without cheno show the same trend as those with cheno: a gain in *Jsc* and *Voc* and an increase in efficiency over time. The parameters of the devices containing cheno (*Jsc* and *Voc*) exceed those without cheno.

For the dyes originating from acetone dye solutions, the addition of cheno during the ligand exchange only enhanced the efficiency for the device which contains ancillary ligand **L3.5**. For the cell with capping ligand **L3.1** the addition did not improve the performance, although higher *Jsc* and *Voc* values were reached by the addition of cheno. The low *ff* of this cell was detrimental to obtaining an enhanced performance. The *ff* relates directly to the total series resistance of a DSC. When the electrons can be transported quickly (without a large resistance) the value of the fill factor increases, otherwise the value decreases.[240]

VII.2 JV-curves
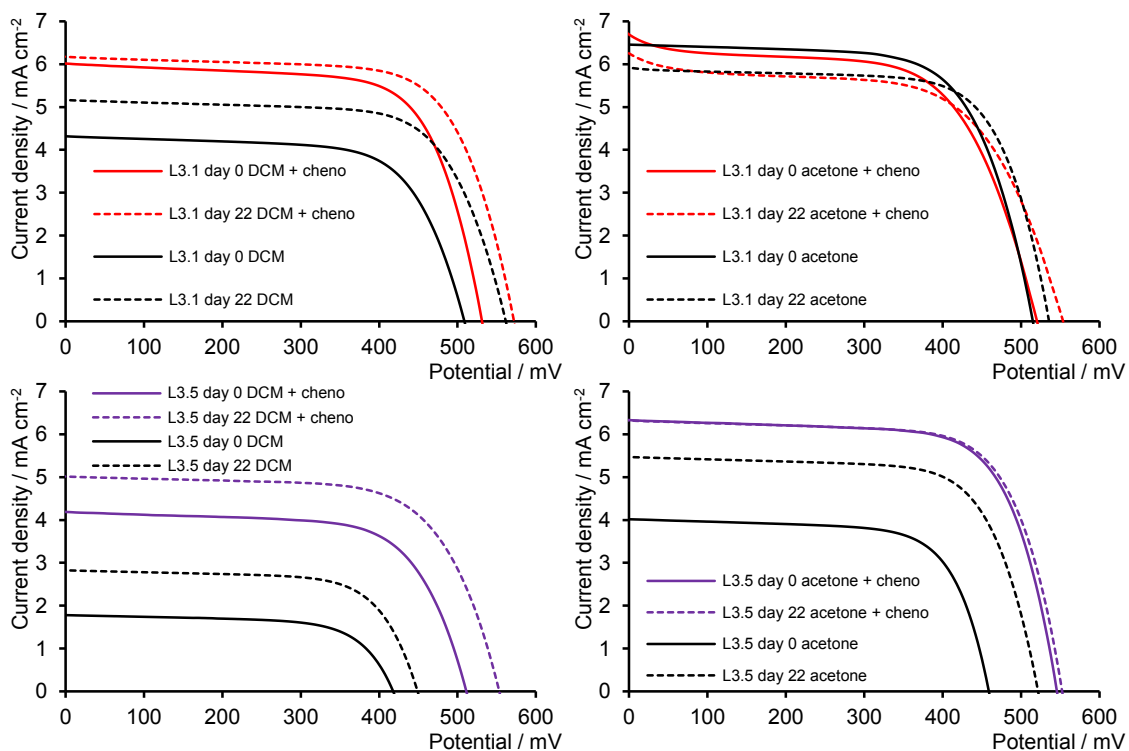
*Figure 116: JV-curves for [Cu(**ALP1**)(**L3.1**)]$^+$ and [Cu(**ALP1**)(**L3.5**)]$^+$ originating from CH_2Cl_2 dye solutions (top) and from acetone solutions (bottom), on day 0 and after 22 days, with and without co-adsorbant cheno.*

From the *JV*-curves (Figure 116) the effect of the co-adsorbant is obvious. In all cases except one (**L3.1**, acetone + cheno), higher *Voc* and *Jsc* values were measured with an ongoing increase in efficiency. For the devices containing capping ligand **L3.1** originating from CH_2Cl_2 dye solutions (Figure 116, top left), the addition of cheno resulted in an increase in the initial *Jsc*, which then only slightly increases over time, whereas the cell without cheno undergoes a larger increase in *Jsc* over time. Both DSCs gain in *Voc* over time.

For the cells with ancillary ligand **L3.1** originating from acetone solutions (Figure 116, top right), no clear trend can be seen. Both devices with and without cheno show similar *Jsc* values for day 0 and day 22. They exhibit comparable *Voc* values on day 0, whereas on day 22 the device with cheno shows a slightly higher *Voc* value than the cell without co-adsorbant. For both cells a drop in *Jsc* and a gain in *Voc* over time was measured.

Now we focus on DSCs containing ancillary ligand **L3.5** originating from the two different solvents with and without cheno. For the cells where a CH_2Cl_2 solution of *homoleptic* dye was used during the dipping cycle (Figure 116, bottom left), the same trend can be seen over time. Both cells gain in *Voc* and *Jsc* with an ongoing improvement in efficiency over time. The device containing cheno surpasses the efficiency of the cell without co-adsorbant by more than a factor of 2.

For the DSCs with ancillary ligand **L3.5** using acetone solutions of $[Cu(\textbf{L3.5})_2][PF_6]$ during the dipping cycle (Figure 116, bottom right), a clear increase in efficiency is obtained by the addition of cheno. While the device without cheno improves in *Voc* and *Jsc* over time, the device with co-adsorbant exhibits an enhanced efficiency that is maintained over three weeks.

VII.3   EQE
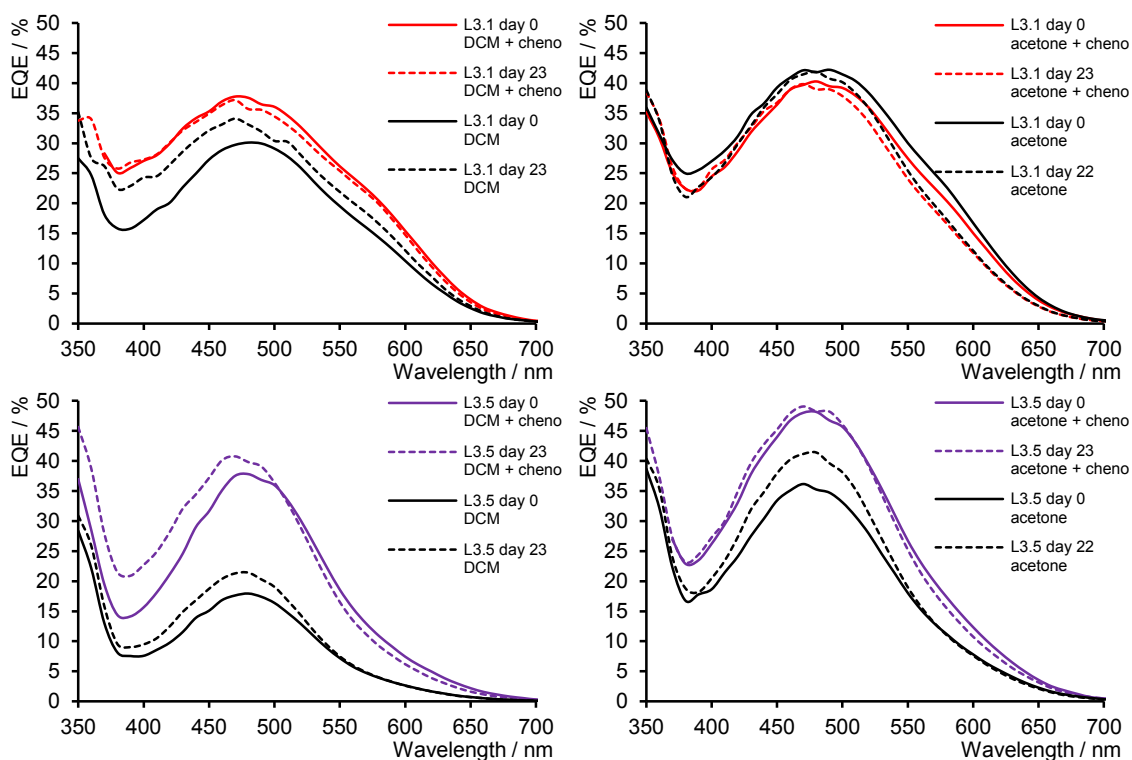
*Figure 117: Dependence of EQE for dyes [Cu(**ALP1**)(**L3.1**)]$^+$ and [Cu(**ALP1**)(**L3.5**)]$^+$ originating from CH$_2$Cl$_2$ and acetone dye solutions, on day 0 and after 22 days, with and without co-adsorbant cheno.*

The *EQE*-curves (Figure 117) confirm the results from the *JV* measurements. All devices exhibit their highest *EQE* at $\lambda_{max} \approx 480$ nm.

For the DSCs containing capping ligand **L3.1** where a CH$_2$Cl$_2$ dye solution was used (Figure 117, top left), the same curve shape was obtained for devices with and without cheno. While the device without cheno gains in *EQE* over time, the cell with cheno shows no increase in *EQE* over the measuring period. Significantly, the DSC containing cheno shows an enhanced *EQE* compared to the cell without co-adsorbant.

For devices with ancillary ligand **L3.1** originating from acetone dye solutions (Figure 117, top right) no increase in cell performance was achieved by the addition of cheno. The cells with and without cheno show comparable *EQE* values over the whole spectrum. They also both slightly decrease in *EQE* over time.

Concerning the cells originating from CH$_2$Cl$_2$ dye solutions containing ancillary ligand **L3.5** (Figure 117, bottom left), both cells exhibit the same behaviour over time. They gain in *EQE* (current) over the measuring period of three weeks. While the cell without any co-adsorbant exhibits a rather low *EQE* (18% on day 0 and 21% on day 22), the device with cheno shows a drastically enhanced *EQE* (38% on day 0 and 41% on day 22).

For the DSCs originating from acetone dye solutions containing ancillary ligand **L3.5**, (Figure 117, bottom right), the following observations were made. While the device containing cheno exhibits a constant *EQE* over three weeks, the cell without cheno gain in *EQE* during the measuring period. For the device with co-adsorbant a higher *EQE* was measured (49% on day 0 and 48% on day 23) as compared to the cell without cheno (36% on day 0 and 41% on day 23).

VII.4 Solid-state absorbance
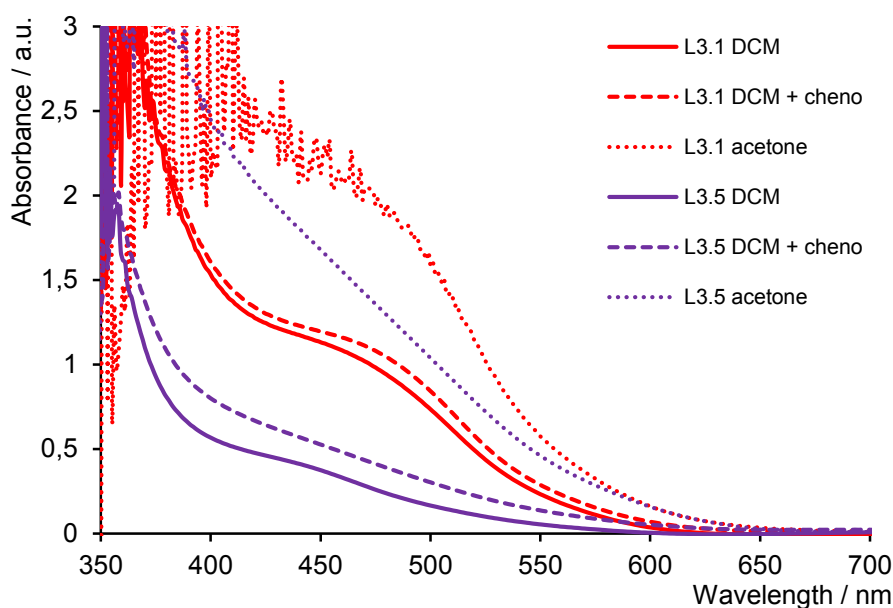
*Figure 118: Solid-state absorption spectra of electrodes with anchored [Cu(**ALP1**)(**L3.1**)]$^+$ and [Cu(**ALP1**)(**L3.5**)]$^+$ with and without cheno. The electrode with anchored dye were prepared using CH$_2$Cl$_2$ or acetone solutions of [Cu(**L3.1/3.5**)$_2$][PF$_6$].*

In the solid state absorption spectra (see Figure 118) an unexpected observation was made. Photoanodes containing cheno exhibited a higher absorption than their corresponding electrodes without co-adsorbant. This is rather unexpected, since the presence of cheno typically means that there is less area available on TiO$_2$ for the dye to bind. In the literature, it has been observed that the dye loading decreases in the presence of cheno.[232][234][237][241][242][243][244][245] Significantly, photoanodes originating from acetone dye solutions without cheno show a much higher absorption than devices originating from CH$_2$Cl$_2$ dye solution containing cheno.

VII.5   Discussion

The addition of cheno improves the performance of dyes [Cu(**ALP1**)(**L3.1**)]$^+$ and [Cu(**ALP1**)(**L3.5**)]$^+$ originating from CH$_2$Cl$_2$ dye solutions. For devices originating from acetone solutions the implementation of a co-adsorbant only leads to an increase in performance for the DSCs containing ancillary ligand **L3.5**. With capping ligand **L3.1**, the addition of cheno did not lead to an improved efficiency.

The increase in efficiency is mainly due to higher *Jsc* and *Voc* values. The increase in voltage (*Voc*) is achieved by either reducing or retarding the charge recombination, or via the adsorption of cheno on the TiO$_2$ surface, thereby changing the semi-conductor's quasi Fermi level under illumination.[33][231][241][242][244][33]
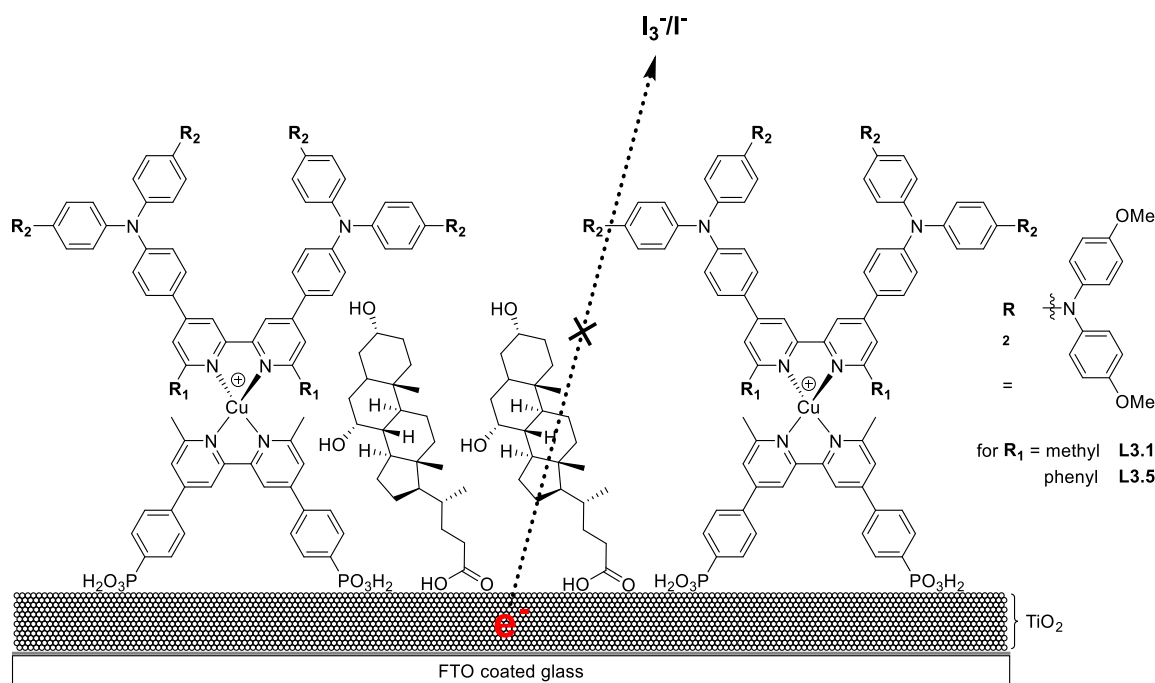
Scheme 25: Representation of the blocking effect of adsorbed cheno. The oxidized electrolyte (I$_3^-$) cannot approach closely to the semi-conductor surface because of the insulating cheno layer.

Since aggregates do not contribute to the photocurrent [238][246], the gain in *Jsc* is attributed to a reduction of dye aggregation upon cheno coadsoption and therefore there is improved electron injection. [205][214][219][232][237][247][248]

Since the addition of cheno to the acetone solution of [Cu(**L3.1**)$_2$][PF$_6$] did not yield an improvement of the device performance, an obvious assumption is that upon using acetone during the dipping cycle aggregation of the ancillary ligand **L3.1** is already minimized. This assumption is supported by the cell data (see Table 19) for capping ligand **L3.1** derived from acetone dye solution without cheno. For this device, no gain in *Jsc* was observed over time, which correlates with no disaggregation process that would enhance the photon absorption and electron injection over time.

VII.6   Conclusion

The addition of cheno during the dipping cycle is important for optimizing the DSC performance. With the addition of cheno to the device, the DSC efficiency of dyes [Cu(**ALP1**)(**L3.1**)]$^+$ and [Cu(**ALP1**)(**L3.5**)]$^+$ originating from CH$_2$Cl$_2$ dye solutions was improved. They exhibited higher *Voc* and *Jsc* values than cells without co-adsorbant. Additionally the *EQE* values of these cells surpassed those of cells without cheno.

For the dye [Cu(**ALP1**)(**L3.5**)]$^+$ originating from acetone dye solution, an improvement in efficiency was achieved by the addition of cheno. This dye exhibited a constant efficiency over the whole measuring period.

In contrast, no gain in performance was observed for the dye [Cu(**ALP1**)(**L3.1**)]$^+$ originating from acetone dye solution. This led us to conclude that using an ancillary ligand with sterically non-hindering methyl groups in the 6,6'-positions of the capping ligand and using acetone during the dipping cycle means that an aggregation of dye molecules is successfully avoided.

VII.7   DSC fabrication and measurements

The DSC fabrication and characterization discussed previously applies to the above mentioned procedure (section V.9). For the experiments with co-adsorbant chenodeoxycholic acid, the procedure was as above but using a 1 : 1 dye : cheno solution (each 0.1 mM) during the dye-dipping cycle.

Summary

Within this study, 18 ligands (**L1.1-L3.6**) and their *homoleptic* copper(I) complexes [Cu(**L1.1-L3.6**)$_2$][PF$_6$] have been synthesized. They were fully characterized by ^{1}H and ^{13}C NMR, mass spectrometry, solution absorption spectrometry, melting point, elemental analysis and infrared spectrometry. Furthermore, all *homoleptic* Cu(I) complexes were electrochemically analysed by cyclic voltammetry and square-wave voltammetry.

By increasing the aromatic system in the ligands (Scheme 26), the light harvesting was effectively enhanced (e.g. going from **L1.1**→**L2.1**→**L3.1**). An increase in absorption by extending the aryl system was achieved in the *homoleptic* Cu(I) complexes, with an extinction of about twice that the free ligands.
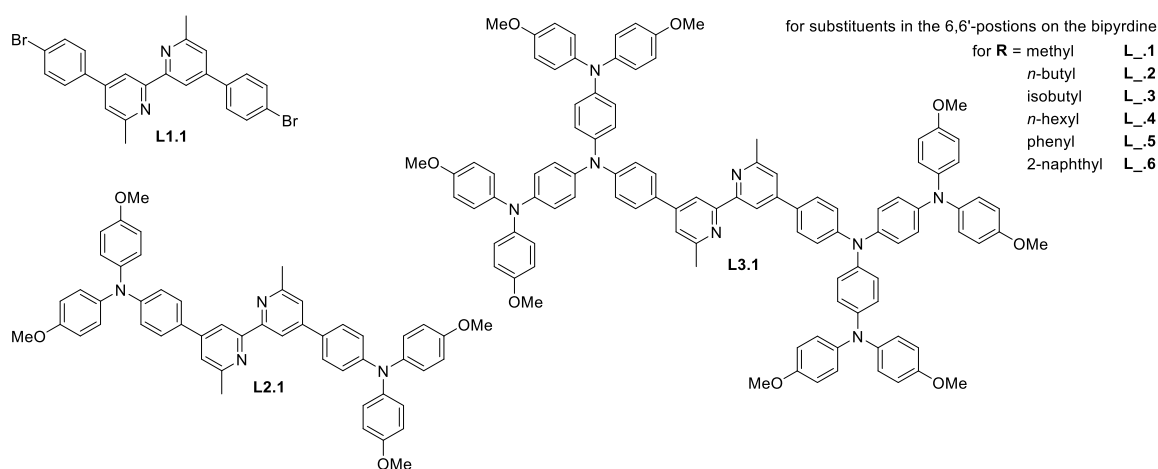
Scheme 26: Representative ligands to illustrate the extension of the aryl system.

Furthermore, the substituents in the 6,6′-positions on the bipyridine were varied within each ligand generation (Scheme 26). All complexes were incorporated in DSCs.

In Chapter I, the first focus is on the influence of the anchoring ligand on the performance of a DSC. For this study, two representative capping ligands were introduced by treating an anchoring ligand covered photoanode with complexes [Cu(**L2.1**)$_2$][PF$_6$] and [Cu(**L3.1**)$_2$][PF$_6$]. By using these two example dyes, a set of four anchoring ligands was screened to identify the one that yielded the best conversion efficiency in the device.
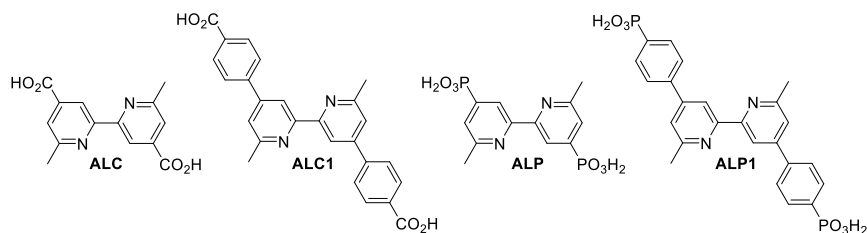
Scheme 27: Set of anchoring ligands with phosphonic and carboxylic acids as anchoring groups.

It turned out that devices with anchoring ligands decorated with phosphonic acids (**ALP** and **ALP1**) generally achieve higher efficiencies than those with carboxylic acids (**ALC** and **ALC1**). Additionally, the influence of the extended aryl system on the ancillary ligands (**L2.1** *vs.* **L3.1**) was examined in this set. Indeed, higher conversion efficiencies were obtained from devices incorporating the more conjugated ancillary ligand **L3.1** compared to **L2.1**.

for **R** =	methyl	**L1.1**
	n-butyl	**L1.2**
	isobutyl	**L1.3**
	n-hexyl	**L1.4**
	phenyl	**L1.5**
	2-naphthyl	**L1.6**
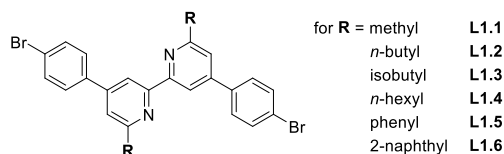
*Scheme 28: Ancillary ligands **L1.1-L1.6** examined in Chapter II.*

In Chapter II, the influence of 6 different substituents in the 6,6'-positions of the bipyridine ancillary ligands (Scheme 28) in combination with anchoring ligands **ALP** and **ALP1** was examined. It was found that DSCs incorporating anchoring ligands **ALP1** reach much higher conversion efficiencies than those with **ALP**. Ancillary ligands **L1.3** and **L1.5** reached remarkably higher efficiencies, which was attributed to the reduced charge recombination rate.
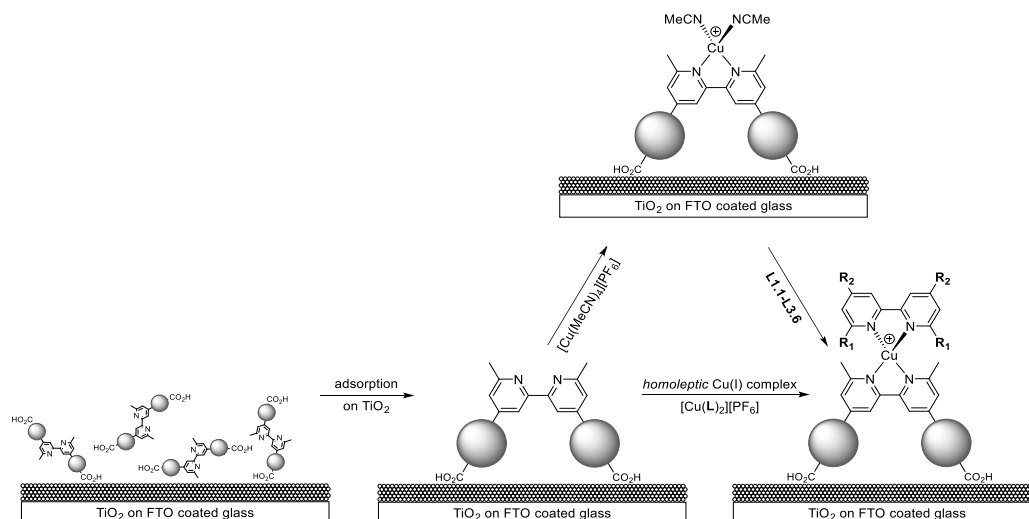
Scheme 29: Two approaches to introduce a copper metal ion and an ancillary ligand on a TiO₂ coated photoanode.

In Chapter III, a new strategy for incorporating *heteroleptic* complexes on the TiO₂ surface was tested and compared with the state of the art methodology. The state of the art method works as followed. After an anchoring ligand has been adsorbed on a semiconductor surface, the photoanode is immersed in a solution of homoleptic Cu(I) complex. Due to the labile nature of Cu(I) complexes, a ligand exchange with the previously anchored ligand occurs, leaving with *heteroleptic* copper dye on the surface.

In the second methodology it becomes needless to prepare the *homoleptic* Cu(I) complex beforehand. By using the new method (stepwise methodology), an additional step during the dyeing process is required. Nevertheless, it is more economic than the conventional process.

After the anchoring ligand is bound to the TiO_2 surface, the anode is immersed in a solution of $[Cu(MeCN)_4][PF_6]$. At this stage the copper(I) binds to the anchoring ligand and it is assumed that a *heteroleptic* complex with two coordinating acetonitrile molecules is formed. In the last step, the anode with the intermediate heteroleptic complex on the surface is immersed in a solution of pure ligand, which replaces the acetonitrile molecules due to the chelating effect. The main outcome of this survey was that devices prepared by the state of the art method achieve a higher final conversion efficiency than those prepared from the stepwise assembly. However, using this new method, devices exhibited a higher initial efficiency than those prepared from the old method.

In Chapter IV, devices were prepared from four different concentrations of dye solutions ($[Cu(\textbf{L2.1})_2][PF]$ in CH_2Cl_2 at 2.0, 1.0, 0.5 and 0.1 mM). Their initial efficiencies and their development over several days were compared. The results showed that devices prepared from the least concentrated dye solutions reached their maximum efficiency immediately after assembling the cells and this efficiency was maintained over the whole measuring period. Additionally, it was found that DSCs prepared from the more dilute dye solutions reach a higher maximum conversion efficiency than those prepared from concentrated dye solutions.

In Chapter V, the focus was on the change in device performance by extending the aromatic systems of the ancillary ligands. Ligands **L2.1-2.6** and **L3.1-3.6** were introduced into the DSCs by applying the state of the art ligand exchange method using complexes $[Cu(\textbf{L2.1-2.6})_2][PF_6]$ and $[Cu(\textbf{L3.1-3.6})_2][PF_6]$. Except for ancillary ligand **L3.1**, no increase in efficiency was recorded by extending the aromatic system and increasing the absorption. Although the solid state UV-vis absorption spectra of the photoanodes showed an increase in absorption intensity, no gain in *Jsc* was achieved.

Chapter VI addresses the use of two different solvents during the dyeing process of the photoanodes. The cells were prepared either from acetone or CH_2Cl_2 dye solutions of $[Cu(\textbf{L2.1-2.6})_2][PF_6]$ and $[Cu(\textbf{L3.1-3.6})_2][PF_6]$. By measuring solid state absorption spectra of dye loaded photoanodes, it turned out that upon using acetone during the dyeing process a severe increase of dye adsorption on the TiO_2 surface was achieved. Moreover, by using acetone dye solutions the devices incorporating the more conjugated ancillary ligands (**L3.1-3.6**) reach generally higher efficiencies than cells with ligands **L2.1-L2.6**. DSCs prepared from acetone dye solutions containing capping ligands **L3.1-3.6** also exhibit higher efficiencies than those with

the same ancillary ligands prepared from CH_2Cl_2 solutions. For devices with capping ligands **L2.1-2.6**, no clear trend could be discovered by comparing cells prepared from acetone and CH_2Cl_2 dye solutions.

In Chapter VII, the main attempt was to minimize the dye aggregation on the surface by adding a co-adsorbant (chenodeoxycholic acid) to the dye solution during the dyeing process of the photoanode. The *homoleptic* complexes $[Cu(\mathbf{L3.1})_2][PF_6]$ and $[Cu(\mathbf{L3.5})_2][PF_6]$ served as example dyes. Additionally, cells were prepared again from acetone and CH_2Cl_2 dye solutions. Interestingly, all devices prepared from CH_2Cl_2 in the presence of cheno showed a clear increase in efficiency compared to the control devices without co-adsorbant. Furthermore, the device with ancillary ligand **L3.5** prepared from acetone dye solution with cheno showed a higher conversion efficiency than its control cell. The device with the capping ligand **L3.1** obtained from an acetone dye solution with cheno did not show an increased performance.

CONCLUSION

It has been shown that by increasing the aromatic system of the ancillary ligand, a gain in absorption intensity and an increase in conversion efficiency was achieved under certain circumstances. The studies revealed the huge number of possible tuning sites of DSCs, such as structural properties of the dye, dye concentration and solvent used during the dyeing cycle, and aggregation issues concerning the molecular size of the dye. Nevertheless, this work showed that a dye that does not seem to yield a reasonable conversion efficiency at first might reveal its full potential after some time. Screening of dyes is quite delicate because it is simply impossible to know the optimal conditions for every dye and it is likely to miss a potentially good dye.

OUTLOOK

For the future, one may want to think to test more solvents during the dyeing process of the photoanode in order to obtain even higher device performances. Additionally, it might be reasonable to add a co-adsorbant to all of the synthesized dyes during the dyeing process of the photoanode in order to reduce dye aggregation, reduce charge recombination and increase the efficiency. Furthermore, that it is also sensible to test new electrolytes in combination with these dyes in attempt to obtain, for example, a higher *Voc*.

SYNTHESIS

6 Experimental Part

6.1 Ligand Precursors

For the pyrdinium salts and ligand precursors the synthetical procedure according to [137][139][140][141] was applied.

6.1.1 1-(2-Oxopropyl)pyridinium chloride: S1

SB117
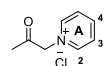
Chloroacetone (25.0 mL, 29.0 g, 313 mmol, 1.0 eq.) and pyridine (25.3 mL, 24.8 g, 313 mmol, 1.0 eq.) were dissolved in diethyl ether (100 mL) and heated under reflux for 6h. The white solid that formed was filtered off, washed with cold diethyl ether and dried under vacuum. The product was isolated as a colourless solid yielding **S1** (42.0 g, 246 mmol, 79%). The crude material was used without purification for the preparation of ligand **L1.1**.

^{1}H NMR (500 MHz, CDCl$_3$, 25°C, TMS) δ/ppm: 9.41 – 9.28 (m, 2H, H^{A2}), 8.50 – 8.39 (m, 1H, H^{A4}), 8.03 (dd, J = 7.5, 6.2 Hz, 2H, H^{A3}), 6.69 (s, 2H, H^{CH2}), 2.50 (s, 2H, H^{CH3}).
^{13}C NMR (126 MHz, CDCl$_3$, 25°C, TMS) δ/ppm: 198.3 (C$^{C=O}$), 146.6 (C^{A2}), 145.1 (C^{A4}), 127.5 (C^{A3}), 68.8 (C^{CH2}), 27.8 (C^{CH3}).

6.1.2 1-(2-Oxohexyl)pyridinium iodide: S2

SB244, SB309
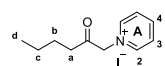
Iodine (25.6 g, 101 mmol) was dissolved in vigorously stirring pyridine (40.8 mL, 39.9 g, 505 mmol) to which hexan-2-one (13 mL, 101 mmol) was added dropwise over a period of 5 min. The reaction mixture was heated at reflux overnight. The solvent was removed under reduced pressure and the crude material was used without further purification for the preparation of ligand **L1.2**.

^{1}H NMR (400 MHz, CDCl$_3$, 25°C, TMS) δ/ppm: 9.17 (d, J = 5.5 Hz, 2H, H^{A2}), 8.50 (m, 1H, H^{A4}), 8.06 (m, 2H, H^{A3}), 6.52 (s, 2H, H^{NCH2}), 2.85 (t, J = 7.4 Hz, 2H, H^a), 1.68 (m, 2H, H^b), 1.38 (m, 2H, H^c), 0.93 (t, J = 7.3 Hz, 2H, H^d).

6.1.3 1-(4-Methyl-2-oxopentyl)pyridinium iodide: S3

SB271
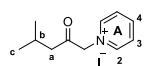
Iodine (30.4 g, 120 mmol) was dissolved in vigorously stirring pyridine (48.5 mL, 47.4 g, 599 mmol) to which 4-methylpentan-2-one (15.0 mL, 120 mmol) was added dropwise over a period of 5 min. The reaction mixture was heated at reflux overnight, after which time it was cooled slowly (over 1 h) to room temperature. The solvent was removed under reduced pressure. Diethyl ether was added and the mixture poured into a flask. The liquid phase was decanted and the solid residue was dissolved in CHCl$_3$. After filtration, solvent was removed under reduced pressure. The crude material was used without purification for the synthesis of ligand **L1.3**.

^{1}H NMR (400 MHz, CDCl$_3$, 25°C, TMS) δ/ppm: 9.22 (d, J = 5.7 Hz, 2H, H^{A2}), 8.58 (t, J = 7.8 Hz, 1H, H^{A4}), 8.09 (m, 2H, H^{A3}), 6.38 (s, 2H, H^{NCH2}), 2.70 (d, J = 6.8 Hz, 2H, H^a), 2.20 (m, 1H, H^b), 0.93 (d, J = 6.7 Hz, 6H, H^c).

6.1.4 1-(2-Oxooctyl)pyridinium iodide: S4

SB285
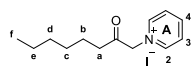
Iodine (16.2 g, 63.9 mmol) was dissolved in vigorously stirring pyridine (25.8 mL, 25.2 g, 319 mmol) to which octan-2-one (10.0 mL, 63.9 mmol) was addeddrop wise over a period of 5 min. The reaction mixture was heated to reflux overnight. The reaction mixture was cooled to room temperature over 1 h and the solvent was removed under reduced pressure. The crude material was used without purification for the synthesis of ligand **L1.4**.

^{1}H NMR (400 MHz, CDCl$_3$, 25°C, TMS) δ/ppm: 9.24 (d, J = 5.8 Hz, 2H, H^{A2}), 8.54 (m, 1H, H^{A4}), 8.07 (m, 2H, H^{A3}), 6.47 (s, 2H, H^{NCH2}), 2.82 (t, J = 7.4 Hz, 2H, H^a), 1.65 (m, 2H, H^b), 1.27 (overlapping m, 6H, H^{c,d,e}), 0.85 (t, J = 6.5 Hz, 2H, H^f).

6.1.5 *N*-[2-Oxoethyl-2-phenyl]pyridinium iodide: S5

SB3
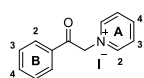
Iodine (38.2 g, 150 mmol, 1.0 eq.) was dissolved in pyridine (75.0 mL, 73.7 g, 932 mmol, 6.2 eq.). The solution was stirred until all I$_2$ had dissolved. Acetophenone (17.5 mL, 18.0 g, 150 mmol, 1.0 eq.) was added to the solution, which was then heated to reflux for 1 h. The heating was stopped and the solution was cooled to rt. The remaining pyridine was

removed under vacuum. The solid was washed with ice water, acetone and dried under vacuum. Yielding **S5** 1-(2-phenyl-2-oxoethyl)pyridinium iodide as an off-white solid (43.6 g, 134 mmol, 90%).

^{1}H NMR (500 MHz, CD$_3$CN, 25°C, TMS) δ/ppm: 8.75 (dd, J = 6.6, 1.5 Hz, 2H, H^{A2}), 8.64 (tt, J = 7.9, 1.4 Hz, 1H, H^{A4}), 8.14 (dd, , J = 8.0, 6.6 Hz, 2H, H^{A3}), 8.09 (dd, J = 8.4, 1.3 Hz, 2H, H^{B2}), 7.84 – 7.71 (m, 1H, H^{B4}), 7.69 – 7.59 (m, 2H, H^{B3}), 6.36 (s, 2H, H^{CH2}).

^{13}C NMR (126 MHz, CD$_3$CN, 25°C, TMS) δ/ppm: 190.7 (C$^{C=O}$), 147.7 (C^{A4}), 147.0 (C^{A2}), 135.9 (C^{B4}), 134.3 (C^{B1})130.2 (C^{B3}), 129.3 (C^{B2}), 128.9 (C^{A3}), 67.3 (C^{CH2}).

6.1.6   *N*-[2-Oxoethyl-2-naphthyl]pyridinium iodide: S6

SB279
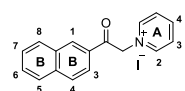
2-Naphthylmethylketone (12.0 g, 70.0 mmol, 1.0 eq.) and iodine (17.3 mL, 17.8 g, 70.0 mmol, 1.0 eq.) were heated in pyridine (100 mL) under reflux for 1 h. The resulting orange solid was filtered off, washed with cold diethyl ether and dried under vacuum. The product **S6** was isolated as an orange solid (20.2 g, 53.8 mmol, 76.7%). The crude material was used without purification for the preparation of ligand **L1.5**.

^{1}H NMR (500 MHz, CD$_3$CN, 25°C, TMS) δ/ppm: 8.78 – 8.76 (m, 1H, H^{B1}), 8.74 (tt, J = 6.7, 1.5 Hz, 2H, H^{A2}), 8.68 – 8.63 (m, 1H, H^{A4}), 8.20 – 8.12 (m, 3H, H^{A3,B3}), 8.11 – 8.01 (m, 3H, H$^{B4,B5+B8}$), 7.75 (ddd, J = 8.3, 6.9, 1.3 Hz, 1H, H^{B7}), 7.70 (ddd, J = 8.1, 6.9, 1.3 Hz, 1H, H^{C6}), 6.42 (s, 2H, H^{CH2}).

^{13}C NMR (126 MHz, CD$_3$CN, 25°C, TMS) δ/ppm: 190.6 (C$^{C=O}$), 147.7 (C^{A4}), 147.1 (C^{A2}), 137.1 (C$^{B4a/B8a}$), 133.2 (C$^{B4a/B8a}$), 131.7 (C^{B1}), 130.6 (C^{B3,B7}), 130.0 (C^{B4}), 129.0 (C^{A3}), 128.8 (C^{B8}), 128.5 (C^{B6}), 123.9 (C^{B2,B5}), 67.3 (C^{CH2}).

6.1.7   (1*E*,5*E*)-1,6-Bis(4-bromophenyl)hexa-1,5-diene-3,4-dione: Diketone1

SB144, SB146, SB284
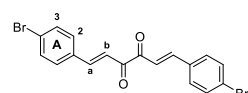
The synthesis is adapted from the general method of Kröhnke[137]. To a vigorously stirred solution of 4-bromobenzaldehyde (36.7 g, 198 mmol, 2.0 eq.) and piperidine (1.96 mL, 19.8 mmol, 0.2 eq.) in MeOH (100 mL), a solution of 2,3-butanedione (8.53 mL, 99.1 mmol, 1.0 eq.) in MeOH (30 mL) was added drop wise using a dropping funnel over 90 min.. The reaction mixture was heated under reflux for 4 h. The solution was slowly cooled to room temperature while stirring and was cooled in an ice bath.

The precipitate was removed by filtration and washed with Et$_2$O yielding (1E,5E)-1,6-bis(4-bromophenyl)hexa-1,5-diene-3,4-dione (8.54 g, 20.3 mmol, 20.5%) as a yellow solid.

^{1}H NMR (400 MHz, CDCl$_3$, 25°C, TMS) δ/ppm: 7.81 (d, J = 16.1 Hz, 2H, H^a), 7.57 (d$_{AB}$, J = 9.0 Hz, 4H, H$^{A2/A3}$), 7.52 (d$_{AB}$, J = 8.9 Hz, 4H, H$^{A2/A3}$) overlapping with 7.49 (d, J = 16.1 Hz, 2H, H^b).

EI MS (m/z): 419.9 m.u. [M]$^+$ (calc. 419.9 m.u.).

6.2   Ligands I: L1.1-1.6

6.2.1   4,4'-Bis(4-bromophenyl)-6,6'-dimethyl-2,2'-bipyridine: L1.1

SB146, SB182, SB222, SB225
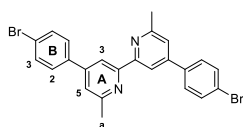
In a 500 mL one-necked flask **diketone1** (4.01 g, 9.54 mmol, 1.0 eq.), **S1** (3.27 g, 19.1 mmol, 2.0 eq.) and ammonium acetate (22.5 g, 286 mmol, 30 eq.) were suspended in EtOH (200 mL). The suspension was heated to reflux and EtOH (200 mL) was added until the reactants had dissolved. The solution was heated at reflux overnight, after which time the reaction mixture was allowed to cool to rt. The precipitate was removed by filtration and washed with Et$_2$O yielding **L1.1** (3.1 g, 6.28 mmol, 65.8%) as a colorless solid.

^{1}H NMR (500 MHz, CDCl$_3$, 25°C, TMS) δ/ppm: 8.48 (d, J = 1.8 Hz, 2H, H^{A3}), 7.63 (m, 8H, H^{B2,B3}), 7.37 (d, J = 1.6 Hz, 2H, H^{A5}), 2.73 (s, 6H, H^a).

^{13}C NMR (126 MHz, CDCl$_3$, 25°C, TMS) δ/ppm: 158.5 (C^{A6}), 155.9 (C^{A2}), 148.5 (C^{A4}), 137.7 (C^{B1}), 132.2 (C$^{B2/B3}$), 128.6 (C$^{B2/B3}$), 123.3 (C^{B4}), 121.0 (C^{53}), 116.5 (C^{A3}), 24.1 (C^a).

IR ($\tilde{v}$/cm^{-1}): 3053 (w), 3033 (w), 2957 (w), 2918 (w), 1597 (m), 1545 (m), 1488 (m), 1379 (m), 1008 (s), 821, (s), 748 (s), 477 (s).

Mp. [°C]: decomposition > 294.

EI MS (m/z): 494.0 m.u. [M]$^+$ (calc. 493.9 m.u.).

UV-VIS (CH$_2$Cl$_2$, 1.0 × 10^{-5} mol dm^{-3}): λ$_{abs}$ / nm 256 (ε / dm^3 mol^{-1} cm^{-1} 45100), 300 $sh.$ (17300).

Found: C, 58.19, H, 3.56, N, 5.61; C$_{24}$H$_{18}$Br$_2$N$_2$ requires C, 58.33, H, 3.67, N, 5.67.

6.2.2   4,4'-Bis(4-bromophenyl)-6,6'-dibutyl-2,2'-bipyridine: L1.2

SB246, SB311
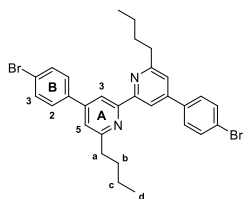
S2 (3.00 g, 9.83 mmol) was dissolved in EtOH (60 mL) under vigorous stirring. (1*E*,5*E*)-1,6-bis(4-bromophenyl)hexa-1,5-diene-3,4-dione (1.03 g, 2.46 mmol) and NH_4OAc (2.84 g, 36.9 mmol) were added followed by EtOH (30 mL). The reaction mixture was heated at reflux for 2 d and was then allowed to cool rt while being stirred. The precipitate was collected by filtration and washed with cold EtOH. The brown needles were dried under a stream of air. The product was recrystallized twice from EtOH, then from MeOH. Ligand **L1.2** was isolated as an off-white solid (0.630 g, 1.09 mmol, 44.3%)

^{1}H NMR (500 MHz, $CDCl_3$, 25°C, TMS) δ/ppm: 8.48 (d, J = 1.6 Hz, 2H, H^{A3}), 7.63 (m, 8H, H^{B2,B3}), 7.34 (d, J = 1.7 Hz, 2H, H^{A5}), 2.94 (t, J = 7.8 Hz, 4H, H^a), 1.83 (m, 4H, H^b), 1.47 (m, 4H, H^c), 0.99 (t, J = 7.4 Hz, 6H, H^d).

^{13}C NMR (126 MHz, $CDCl_3$, 25°C, TMS) δ/ppm: 162.8 (C^{A6}), 156.7 (C^{A2}), 148.3 (C^{A4}), 138.1 (C^{B1}), 132.3 (C$^{B2/3}$), 128.9 (C$^{B2/3}$), 123.3 (C^{B4}), 120.4 (C^{A2}), 116.6 (C^{A3}), 38.7 (C^a), 32.2 (C^b), 22.7 (C^c), 14.2 (C^d).

IR ($\tilde{v}$/cm^{-1}): 2949 (w), 2918 (w), 2869 (w), 2853 (w), 1595 (m), 1544 (m), 1488 (m), 1404 (m), 1274 (m), 1298 (w), 1098 (w), 1008 (m), 821, (s), 758 (m), 480 (s).

ESI MS (*m/z*): 579.1 m.u. [M+H]$^+$ (calc. 579.1 m.u.).

Mp. [°C]: 157.

UV-VIS (CH_2Cl_2, 1.0×10^{-5} mol dm^{-3}): λ / nm 255 (ε / dm^3 mol^{-1} cm^{-1} 53400), 301 *sh.* (18400).

Found: C 61.04, H 5.22, N 4.94; $C_{30}H_{30}Br_2N_2 \cdot {}^1/_2H_2O$ requires C 61.34, H 5.32, N 4.77%.

6.2.3   4,4'-Bis(4-bromophenyl)-6,6'-di-isobutyl-2,2'-bipyridine: L1.3

SB264
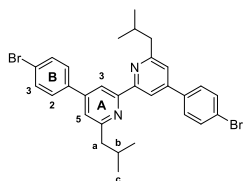
L1.3 was prepared in the same manner as ligand **L1.1**, starting with 1-(4-methyl-2-oxopentyl)pyridinium iodide (13.4 g, 43.8 mmol, 9.0 eq.) and (1*E*,5*E*)-1,6-bis(4-bromophenyl)hexa-1,5-diene-3,4-dione (2.04 g, 4.87 mmol, 1.0 eq.) and NH$_4$OAc (7.50 g, 97.4 mmol, 20 eq.). The reaction time at reflux was 1 d. Ligand **L1.3** was isolated as an off-white solid (1.18 g, 2.04 mmol, 42.0%)

^{1}H NMR (500 MHz, CDCl$_3$, 25°C, TMS) δ/ppm: 8.48 (d, *J* = 1.7 Hz, 2H, H^{A3}), 7.63 (m, 8H, H^{B2,B3}), 7.30 (d, *J* = 1.7 Hz, 2H, H^{A5}), 2.80 (d, *J* = 7.2 Hz, 4H, H^a), 2.27 (m, 2H, H^b), 1.01 (d, J = 6.6 Hz, 12H, H^c).

^{13}C NMR (126 MHz, CDCl$_3$, 25°C, TMS) δ/ppm: 161.6 (C^{A6}), 156.5 (C^{A2}), 148.1 (C^{A4}), 137.8 (C^{B1}), 132.1 (C$^{B2/B3}$), 128.8 (C$^{B2/B3}$), 123.1 (C^{B4}), 121.1 (C^{A5}), 116.5 (C^{A3}), 47.5 (C^a), 29.0 (C^b), 22.4 (C^c).

IR (ṽ/cm^{-1}): 3082(w), 3053 (w), 2954 (m), 2928 (m), 2913 (w), 2864 (m), 1599 (m), 1543 (m), 1491 (m), 1462 (m), 1376 (m), 1326 (m), 1165 (m), 1010 (s),896 (m), 828 (s), 814 (s), 765 (s), 744 (m), 658 (m), 590 (m), 526 (s).

Mp. [°C]: 181.

ESI MS (*m/z*): 579.1 m.u. [M+H]$^+$ (calc. 579.1 m.u.).

UV-VIS (CH$_2$Cl$_2$, 1.0 × 10^{-5} mol dm^{-3}): λ / nm 256 (ε / dm^3 mol^{-1} cm^{-1} 53600), 302 *sh.* (16800).

Found: C 62.03, H 5.11, N 5.16; C$_{30}$H$_{30}$Br$_2$N$_2$ requires C 62.30, H 5.23, N 4.84%.

6.2.4 4,4'-Bis(4-bromophenyl)-6,6'-dihexyl-2,2'-bipyridine: L1.4

SB262, SB286
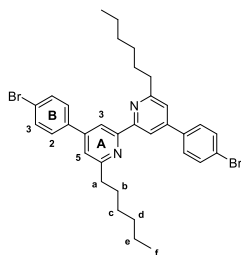
L1.4 was prepared in the same manner as ligand **L1.1** starting with **S4** 1-(2-oxooctyl)pyridinium iodide (10.3 g, 30.9 mmol, 4.0 eq.), **diketone1** (1*E*,5*E*)-1,6-bis(4-bromophenyl)hexa-1,5-diene-3,4-dione (3.24 g, 7.72 mmol, 1.0 eq.) and NH$_4$OAc (4.95 g, 77.2 mmo, 10 eq.). The reaction was heated overnight at reflux. Ligand **1.4** was isolated as an off-white solid (1.23 g, 1.94 mmol, 25.1%).

^{1}H NMR (500 MHz, CDCl$_3$, 25°C, TMS) δ/ppm: 8.48 (d, *J* = 1.7 Hz, 2H, H^{A3}), 7.63 (m, 8H, H^{B2,B3}), 7.33 (d, *J* = 1.7 Hz, 2H, H^{A5}), 2.93 (t, *J* = 7.8 Hz, 4H, H^a), 1.85 (m, 4H, H^b), 1.44 (m, 4H, H^c), 1.35 (m, 8H, H^{d+e}), 0.99 (t, *J* = 7.1 Hz, 6H, H^f).

^{13}C NMR (126 MHz, CDCl$_3$, 25°C, TMS) δ/ppm: 162.8 (C^{A6}), 156.7 (C^{A2}), 148.3 (C^{A4}), 138.1 (C^{B1}), 132.3 (C$^{B2/B3}$), 128.9 (C$^{B2/3}$), 123.3 (C^{B4}), 120.4 (C^{A2}), 116.6 (C^{A3}), 38.65 (C^a), 31.92 (C^b), 29.99 (C^c), 29.29 (C^d), 22.80 (C^e), 14.29 (C^f).

IR (ṽ/cm^{-1}): 2949 (m), 2924 (m), 2866 (w), 2853 (m), 1597 (m), 1545 (m), 1490 (m), 1462 (m), 1407 (m), 1377 (m), 1069 (m), 1009 (m), 892 (m), 824, (s), 754 (m), 655 (m), 515 (m), 485 (m).

Mp. [°C]: 135.

ESI MS(*m/z*): 635.1 m.u. [M+H]$^+$ (calc. 635.1m.u).

UV-VIS (CH$_2$Cl$_2$, 1.0 × 10^{-5} mol dm^{-3}): λ / nm 256 (ε / dm^3 mol^{-1} cm^{-1} 43900), 302 *sh.* (14200).

Found: C 62.91, H 5.86, N 4.62; C$_{34}$H$_{38}$Br$_2$N$_2$·H$_2$O requires C 62.58, H 6.18, N 4.29%.

6.2.5   4,4'-Bis(4-bromophenyl)-6,6'-diphenyl-2,2'-bipyridine: L1.5

SB267, SB282
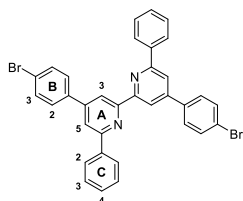
Ligand **L1.5** was prepared in the same manner as ligand **L1.2** starting with **S5** (1.61 g, 4.95 mmol, 2.0 eq.), **diketone1** (1E,5E)-1,6-bis(4-bromophenyl)hexa-1,5-diene-3,4- dione (1.04 g, 2.48 mmol, 1.0 eq.) and NH$_4$OAc (2.68 g, 37.1 mmol, 7.5 eq.). Reaction time at reflux was 1 d. Ligand **L1.5** was isolated as an off-white solid (0.443 g, 0.718 mmol, 29.0%).

^{1}H NMR (500 MHz, CD$_2$Cl$_2$, 25°C, TMS) δ/ppm: 8.91 (d, J = 1.5 Hz, 2H, H^{A3}), 8.23 (m, 4H, H^{C2}), 8.04 (d, J = 1.6 Hz, 2H, H^{A5}), 7.81 (m, 4H, H^{B2}), 7.72 (m, 4H, H^{B3}), 7.57 (m, 4H, H^{C3}), 7.52 (m, 2H, H^{C4}).

^{13}C NMR (126 MHz, CD$_2$Cl$_2$, 25°C, TMS) δ/ppm: 157.6 (C^{A6}), 155.6 (C^{A2}), 150.1 (C^{A4}), 138.8 (C^{C1}), 137.9 (C^{B1}), 132.7 (C^{B3}), 129.8 (C^{C4}), 129.5 (C^{B2}), 129.2 (C^{C3}), 127.6 (C^{C2}), 124.2 (C^{B4}), 119.5 (C^{A5}), 118.9 (C^{A3}).

IR (ṽ/cm^{-1}): 3061 (w), 3035 (w), 1594 (s), 1571 (m), 1542 (s), 1488 (s), 1405 (m), 1375 (m), 1238 (w), 1181 (w), 1074 (m), 1025 (m), 1008 (m), 884 (m), 818 (s), 775 (s), 739 (s), 690 (s), 637 (m), 557 (m), 538 (m), 476 (m).

Mp. [°C]: 318.

ESI MS (m/z): 619.1 m.u. [M+H]$^+$ (calc. 619.0 m.u.).

UV-VIS (CH$_2$Cl$_2$, 1.0 × 10^{-5} mol dm^{-3}): λ / nm 265 (ε / dm^3 mol^{-1} cm^{-1} 79400), 320 (16500).

Found: C 64.86, H 3.67, N 4.54; C$_{34}$H$_{22}$Br$_2$N$_2$·^{1}/$_2$H$_2$O requires C 65.09, H 3.70, N 4.47%.

6.2.6 4,4'-Bis(4-bromophenyl)-6,6'-di(2-naphthyl)-2,2'-bipyridine: L1.6

SB280, SB312
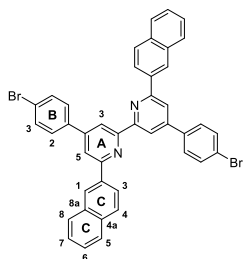
Ligand **1.6** was prepared in the same manner as **L1.2** starting with **S6** (5.10 g, 13.6 mmol, 2.0 eq.), **diketone1** (2.85 g, 6.79 mmol, 1.0 eq.) and NH$_4$OAc (5.23 g, 67. mmol, 10 eq.). The reaction time at reflux was 1 d. As solvents ethanol (30 mL), 2-propanol (100 mL) and toluene (150 mL) were used. Ligand **L1.6** was isolated as an off-white solid (1.77 g, 2.46 mmol, 36.3%).

^{1}H NMR (500 MHz, d-TFA, 25°C, TMS) δ/ppm: 8.68 (d, J = 1.8 Hz, 2H, H^{A3}), 8.66 (d, J = 1.8 Hz, 2H, H^{A5}), 8.41 (d, J = 2.1 Hz, 2H, H^{C1}), 8.06 (d, J = 8.6 Hz, 2H, H^{C4}), 7.90 – 7.87 (m, 4H, H^{C5,C8}), 7.83 (dd, J = 8.7, 2.0 Hz, 2H, H^{C3}), 7.82 – 7.78 (m, 4H, H^{B2}), 7.77 – 7.74 (m, 4H, H^{B3}), 7.63 (ddd, J = 8.1, 6.9, 1.3 Hz, 2H, H$^{C6/C7}$), 7.58 (ddd, J = 8.2, 6.9, 1.3 Hz, 2H, H$^{C6/C7}$).

^{13}C NMR (126 MHz, d-TFA, 25°C, TMS) δ/ppm: 162.0 (C^{B4}), 159.0 (C^{A6}), 144.6 (C^{A4}), 137.9 (C$^{C4a/C8a}$), 135.8 (C^{B3}), 135.2 (C$^{C4a/C8a}$), 134.1 (C^{A4}), 133.0 (C^{C4}), 132.2 (C$^{C1,C6/C7}$), 131.7 (C^{B1}), 131.2 (C^{B2}), 130.9 (C$^{C5/C8}$), 130.5 (C$^{C6/C7}$), 130.0 (C$^{C5/C8}$), 128.4 (C^{B2}), 126.9 (C^{A5}), 126.0 (C^{A3}), 124.3 (C^{C3}).

IR (ṽ/cm^{-1}): 3051 (w), 3018 (w), 2970 (w), 1589 (m), 1574 (m), 1542 (s), 1489 (m), 1405 (m), 1379 (m), 1075 (m), 1007 (m), 863 (m), 812 (s), 785 (m), 775 (s), 757 (s), 732 (s), 718 (m), 570 (m), 470 (s).

Mp. [°C]: decomposition > 322.

ESI MS (*m/z*): 719.1 m.u. [M+H]$^+$ (calc. 719.1 m.u.).

UV-VIS (CH$_2$Cl$_2$, 1.0 × 10^{-5} mol dm^{-3}): λ/nm 237 (ε / dm^3 mol^{-1} cm^{-1} 73500), 263 (105300), sh 320 (24300), 350 *sh.* (9900).

UV-VIS (CH$_2$Cl$_2$ + 1%TFA, 1.0 × 10^{-5} mol dm^{-3}): λ / nm 227 (ε / dm^3 mol^{-1} cm^{-1} 81700), 262 (61600), 311 (43400), 400 *sh.* (15300).

Found: C 68.93, H 3.62, N 4.01; C$_{42}$H$_{26}$Br$_2$N$_2$·^{1}/$_2$H$_2$O requires C 69.34, H 3.74, N 3.85%.

6.3 Copper(I) complexes I: C1.1-1.6

General procedure I

In a typical reaction, the ligand (1.0 eq.) was dissolved in a 1:1 mixture of MeCN and CH_2Cl_2 and $[Cu(MeCN)_4][PF_6]$ (0.5 eq.) was added. The solution turned red immediately for **L1.1-L1.4** and green-black for **L1.5** and **L1.6** respectively. The solution was stirred overnight at rt after which time the volume of the solvent was reduced *in vacuo* and the product was precipitated by addition of diethyl ether. The solid was filtered off and washed with Et_2O and dried in a stream of air.

6.3.1 $[Cu(L1.1)_2][PF_6]$: C1.1

SB250
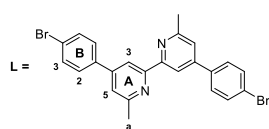
$[Cu(MeCN)_4][PF_6]$ (85.0 mg, 0.228 mmol) was reacted with ligand **L1.1** (225 mg, 0.456 mmol) in MeCN (4 mL) and CH_2Cl_2 (16 mL). Complex **C1.1** was isolated as a dark red solid (217 mg, 0.181 mmol, 79.6%).

^1H NMR (500 MHz, CD_3CN, 25°C, TMS) δ/ppm: 8.66 (br, 4H, H^{A3}), 7.88 (d, $J = 7.9$ Hz, 8H, $H^{B2/B3}$), 7.83 (br, 4H, H^{A5}), 7.78 (d, $J = 7.7$ Hz, 8H, $H^{B2/B3}$), 2.37 (s, 12H, H^a).

^{13}C NMR (126 MHz, CD_3CN, 25°C, TMS) δ/ppm: 165.1 (C^{A6}), 153.7 (C^{A2}), 149.8 (C^{A4}), 137.1 (C^{B1}), 133.3 ($C^{B2/B3}$), 130.2 ($C^{B2/B3}$), 124.5 (C^{B4}), 124.8 (C^{A5}), 118.7 (C^{A3}), 25.1 (C^a).

Mp. [°C]: decomposition > 320.

ESI MS (*m/z*): 1050.8 m.u. $[M–PF_6]^+$ (calc. 1050.9 m.u.), 495.0 m.u. $[\textbf{L1.1}+H]^+$ (calc. 495.0 m.u.).

UV-VIS (CH_2Cl_2, 1.0×10^{-5} mol dm^{-3}): λ / nm 279 (ε / dm^3 mol^{-1} cm^{-1} 77200), 323 (39300), 486 (10400).

Found: C 47.55, H 3.16, N 4.93; $C_{48}H_{36}Br_4CuF_6N_4P·H_2O$ requires C 47.45, H 3.15, N 4.61%.

6.3.2   [Cu(L1.2)$_2$][PF$_6$]: C1.2
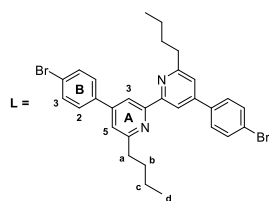
[Cu(MeCN)$_4$][PF$_6$] (36.1 mg, 0.097 mmol) was reacted with ligand **L1.2** (112 mg, 0.194 mmol) in MeCN (10 mL) and CH$_2$Cl$_2$ (10 mL). Complex **C1.2** was isolated as a dark red solid (50.9 mg, 0.037 mmol, 38.5%).

^{1}H NMR (500 MHz, CD$_3$CN, 25°C, TMS) δ/ppm: 8.67 (broadened d, 4H, H^{A3}), 7.89 (d, $J = 8.6$ Hz, 8H, H^{B2}), 7.84 (d, $J = 1.5$ Hz, 4H, H^{A5}), 7.78 (d, $J = 8.6$ Hz, H^{B3}), 2.70 (br, 8H, H^a), 1.40 (br, 8H, H^b), 0.88 (br, 8H, H^c), 0.44 (br, 12H, H^d).

^{13}C NMR (126 MHz, CD$_3$CN, 25°C, TMS) δ/ppm: 163.0 (C^{A6}), 153.6 (C^{A2}), 150.1 (C^{A4}), 137.1 (C^{B1}), 133.4 (C^{B3}), 130.3 (C^{B2}), 125.0 (C^{B4}), 124.1 (C^{A5}), 119.1 (C^{A3}), 40.3 (C^a), 32.6 (C^b), 23.3 (C^c), 13.7 (C^d).

Mp. [°C]: decomposition > 308.

ESI MS (*m/z*): 1219.0 m.u. [M–PF$_6$]$^+$ (calc. 1219.1 m.u.), 579.1 m.u. [**L1.2**+H]$^+$ (calc. 579.1 m.u.).

UV-VIS (CH$_2$Cl$_2$, 1.0×10^{-5} mol dm^{-3}): λ / nm 281 (ε / dm^3 mol^{-1} cm^{-1} 79600), 324 (38700), 483 (9900).

Found: C 52.08, H 4.53, N 4.29; C$_{60}$H$_{60}$Br$_4$CuF$_6$N$_4$P·H$_2$O requires C 52.10, H 4.52, N 4.05%.

6.3.3 [Cu(L1.3)$_2$][PF$_6$]: C1.3
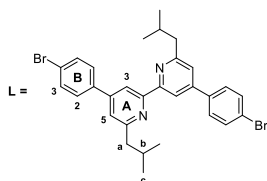
[Cu(MeCN)$_4$][PF$_6$] (58.7 mg, 0.158 mmol) was reacted with ligand **L1.3** (182 mg, 0.315 mmol) in MeCN (10 mL) and CH$_2$Cl$_2$ (10 mL). Complex **C1.3** was isolated as a dark red solid (186 mg, 0.136 mmol, 86.4%).

^{1}H NMR (500 MHz, DMSO-d$_6$, 25°C, TMS) δ/ppm: 9.08 (d, J = 1.4 Hz, 4H, H^{A3}), 8.08 (m, 8H, H^{B2}), 8.03 (d, J = 1.4 Hz, 4H, H^{A5}), 7.85 (m, 8H, H^{B3}), 2.52 (s, 8H, H^a), 1.72 (septet, d, J = 6.8 Hz, 4H, H^b), 0.47 (d, J = 6.6 Hz, 24H, H^c).

^{1}H NMR (500 MHz, CD$_3$CN, 25°C, TMS) δ/ppm: 8.68 (broadened s, 4H, H^{A3}), 7.89 (d, J = 8.5 Hz, 8H, H^{B2}), 7.80 - 7.78 (m, 12H, H^{A5}, H^{B3}), 2.55 (broadened s, 8H, H^a), 1.76 (broadened s, 4H, H^b), 0.53 (broadened s, 24H, H^c).

^{13}C NMR (126 MHz, DMSO-d$_6$, 25°C, TMS) δ/ppm: 160.6 (C^{A6}), 153.3 (C^{A2}), 148.7 (C^{A4}), 135.9 (C^{B1}), 132.7 (C^{B3}), 130.2 (C^{B2}), 124.3 (C^{B4}), 123.5 (C^{A5}), 118.1 (C^{A3}), 47.6 (C^a), 27.5 (C^b), 21.5 (C^c).

Mp. [°C]: 338.

ESI MS (*m/z*): 1219.1 m.u. [M–PF$_6$]$^+$ (calc. 1219.1 m.u.), 579.1 m.u. [**L1.3**+H]$^+$ (calc. 579.1 m.u.).

UV-VIS (CH$_2$Cl$_2$, 1.0 × 10^{-5} mol dm^{-3}): λ / nm 281 (ε / dm^3 mol^{-1} cm^{-1} 82300), 319 (38700), 476 (10100).

Found: C 52.51, H 4.52, N 4.38; C$_{60}$H$_{60}$Br$_4$CuF$_6$N$_4$P requires C 52.78, H 4.43, N 4.10%.

6.3.4   [Cu(L1.4)₂][PF₆]: C1.4

$L = $

[Cu(MeCN)₄][PF₆] (27.4 mg, 0.074 mmol) was reacted with ligand **L1.4** (93.4 mg, 0.147 mmol) in MeCN (10 mL) and CH₂Cl₂ (10 mL). Complex **C1.4** was isolated as a dark red solid (40.2 mg, 0.027 mmol, 37.0%).

^{1}H NMR (500 MHz, CD₃CN, 25°C, TMS) δ/ppm: 8.70 (s, 4H, H^{A3}), 7.90 (d, J = 8.5 Hz, 8H, H^{B2}), 7.85 (s, 4H, H^{A5}), 7.79 (d, J = 8.5 Hz, 8H, H^{B3}), 2.68 (s, 8H, H^a), 1.41 (s, 8H, H^b), 0.89 (s, 8H, H^e), 0.84 (s, 8H, H^c), 0.72 (s, 8H, H^d), 0.55 (t, J = 6.6 Hz, 12H, H^f).

^{13}C NMR (126 MHz, CD₃CN, 25°C, TMS) δ/ppm: 163.2 (C^{A6}), 153.6 (C^{A2}), 150.1 (C^{A4}), 137.0 (C^{B1}), 133.3 (C^{B3}), 130.2 (C^{B2}), 124.9 (C^{B4}), 124.1 (C^{A5}), 118.9 (C^{A3}), 40.7 (C^a), 32.0 (C^d), 30.6 (C^b), 30.0 (C^c), 22.9 (C^e), 14.0 (C^f).

Mp. [°C]: 270.

ESI MS (*m/z*): 1331.0 m.u. [M–PF₆]$^+$ (calc. 1331.2 m.u.), 635.2 m.u. [**L1.4**+H]$^+$ (calc. 635.1 m.u.).

UV-VIS (CH₂Cl₂, 1.0 × 10^{-5} mol dm^{-3}): λ / nm 281 (ε / dm³ mol^{-1} cm^{-1} 83400), 325 (39600), 482 (11300).

Found: C 55.44, H 5.21, N 4.18; C₆₈H₇₆Br₄CuF₆N₄P·^{1}/₂MeCN requires C 55.32, H 5.21, N 4.21%.

6.3.5 [Cu(L1.5)$_2$][PF$_6$]: C1.5

[Cu(MeCN)$_4$][PF$_6$] (90.4 mg, 0.243 mmol, 1.0 eq.) was reacted with ligand **L1.5** (300 mg, 0.485 mmol, 2.0 eq.) in MeCN (5 mL) and CH$_2$Cl$_2$ (40 mL). Complex **C1.5** was isolated as a black solid (206 mg, 0.143 mmol, 58.9%).

^{1}H NMR (500 MHz, CDCl$_3$, 25°C, TMS) δ/ppm: 8.23 (d, J = 1.2 Hz, 2H, H^{A3}), 7.77 (overlapping m, 8H, H^{B2+B3}), 7.64 (d, J = 1.2 Hz, 2H, H^{A5}), 7.62 (d, J = 7.5 Hz, 4H, H^{C2}), 7.05 (t, J = 7.4 Hz, 2H, H^{C4}), 6.93 (t, J = 7.6 Hz, H^{C3}).

^{13}C NMR (126 MHz, CDCl$_3$, 25°C, TMS) δ/ppm: 156.9 (C^{A6}), 153.6 (C^{A2}), 149.5 (C^{B1}), 137.9 (C^{C1}), 135.6 (C^{A4}), 132.9 (C$^{B2/3}$), 129.5 (C^{C4}), 128.9 (C$^{B2/3}$), 127.7 (C^{C3}), 127.6 (C^{C2}), 124.8 (C^{B4}), 122.5 (C^{A5}), 119.4 (C^{A3}).

Mp. [°C]: decomposition > 325.

ESI MS (m/z): 1299.2 m.u. [M–PF$_6$]$^+$ (calc. 1399.0 m.u.), 618.8 m.u. [**L1.5**+H]$^+$ (calc. 619.0 m.u.).

UV-VIS (CH$_2$Cl$_2$, 1.0 × 10^{-5} mol dm^{-3}): λ / nm 272 (ε/dm^3 mol^{-1} cm^{-1} 73500), 292 (76200), 337 (29600), 424 (5900), 573 (4400).

Found: C 55.02, H 3.20, N 4.14; C$_{68}$H$_{44}$Br$_4$CuF$_6$N$_4$P·2H$_2$O requires C 55.14, H 3.27, N 3.78%.

6.3.6 [Cu(L1.6)₂][PF₆]: C1.6

SB283
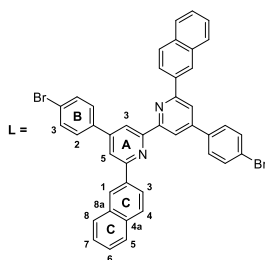
[Cu(MeCN)₄][PF₆] (75.9 mg, 0.204 mmol, 1.0 eq.) was reacted with ligand **L1.6** (293 mg, 0.408 mmol, 2.0 eq.) in CH_2Cl_2 (40 mL). Complex **C1.6** was isolated as a green/black solid (283 mg, 0.172 mmol, 84.4%).

^{1}H NMR (500 MHz, CD_2Cl_2, 25°C, TMS) δ/ppm: 8.39 (d, J = 1.8 Hz, 2H, H^{C1}), 7.79 (dd, J = 8.5, 1.9 Hz, 2H, H^{C3}), 7.75 (d, J = 8.4 Hz, 4H, H^{B3}), 7.66 (d, J = 1.5 Hz, 2H, H^{A5}), 7.57 (d, J = 8.0 Hz, 2H, H^{C5}), 7.55 (d, J = 1.6 Hz, 2H, H^{A3}), 7.52 (d, J = 8.4 Hz, 2H, H^{C4}), 7.38 (d, J = 8.5 Hz, 4H, H^{B2}), 7.38 – 7.33 (m, 2H, H^{C2}), 7.30 – 7.24 (m, 4H, H^{C6,C8}).

^{13}C NMR (126 MHz, CD_2Cl_2, 25°C, TMS) δ/ppm: 156.7 (C^{A6}), 153.5 (C^{A2}), 149.3 (C^{B4}), 135.6 (C^{A4}), 133.3 (C^{C2}), 132.9 (C^{B3}), 131.9 (C^{C8a}), 129.2 (C^{B2}), 128.3 (C^{C8}), 128.2 (C^{C1}), 127.9 (C^{C7}), 127.8 (C^{C4,C5}), 127.4 (C^{C4a}), 127.1 (C^{C6}), 125.4 (C^{C3}), 124.7 (C^{B1}), 122.6 (C^{A5}), 119.0 (C^{A3}).

Mp. [°C]: decomposition > 330.

ESI MS (m/z): 1501.7 m.u. [M–PF₆]$^+$ (calc. 1501.0 m.u.), 145.0 m.u. [PF₆]$^-$ (calc. 145.0 m.u.).

UV-VIS (CH_2Cl_2, 1.0 × 10^{-5} mol dm^{-3}): λ/nm 240 (ε/dm^3 mol^{-1} cm^{-1} 160400), 287 (114600), 250 *sh.* (31800), 437 (6700), 587 (4200).

IR (ṽ/cm^{-1}): 3059 (w), 1608 (m), 1536 (m), 1490 (m), 1386 (m), 1069 (m), 1008 (m), 849 (s), 811 (s), 755 (s), 557 (s), 475 (s).

Found: C 60.46, H 3.38, N 3.70; $C_{84}H_{52}Br_4CuF_6N_4P·H_2O$ requires C 60.65, H 3.27, N 3.37%.

6.4   Ligands II: L2.1-2.6

6.4.1   4,4'-(6,6'-Dimethyl-[2,2'-bipyridine]-4,4'-diyl)bis(N,N-bis(4-methoxyphenyl)aniline): L2.1
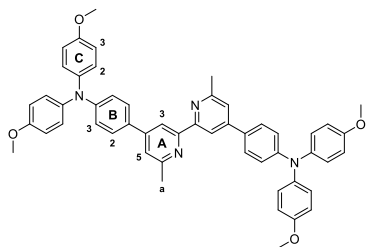
4,4'-Bis(4-bromophenyl)-6,6'-dimethyl-2,2'-bipyridine (460 mg, 0.91 mmol, 1.0 eq.) and bis(4-methoxyphenyl)amine (640 mg, 2.74 mmol, 2.0 eq.) were suspended in dry toluene (60 mL) under argon, and NaO^{t}Bu (289 mg, 3.01 mmol, 3.3 eq.) was added. To a suspension of Pd(bda)$_2$ (21.0 mg, 0.037 mmol, 4.0 mol%, 0.04 eq.) in dry toluene (4 mL), a 1M toluene solution of P^{t}Bu$_3$ (0.037 mL, 0.037 mmol, 4.0 mol%) was added. The active catalyst suspension was added to the reaction mixture. The mixture was heated at 100°C for 16 h, after which time it was filtered hot. The solvent of the filtrate was removed and the resulting solid was boiled in EtOH (100 mL) until a homogeneous suspension was obtained. The solid was filtered hot and washed with diethyl ether (30 mL). Compound **L2.1** was isolated as a greenish solid (543 mg, 0.69 mmol, 75%).

^{1}H NMR (500 MHz, CDCl$_3$, 25°C, TMS) δ/ppm: 8.39 (d, J = 1.7 Hz, 2H, H^{A3}), 7.59 (d, J = 8.7 Hz, 4H, H^{B2}), 7.33 (d, J = 1.7 Hz, 2H, H^{A5}), 7.11 (d, J = 8.9 Hz, 8H, H^{C2}), 7.00 (d, J = 8.7 Hz, 4H, H^{B3}), 6.86 (d, J = 8.9 Hz, 8H, H^{C3}), 3.81 (s, 12H, H^{OMe}), 2.67 (s, 6H, H^a).

^{13}C NMR (126 MHz, CDCl$_3$, 25°C, TMS) δ/ppm: 158.3 (C^{A6}), 156.8 (C^{A2}), 156.3 (C^{C4}), 149.6 (C^{B4}), 149.0 (C^{A4}), 140.6 (C^{C1}), 130.1 (C^{B1}), 127.8 (C^{B2}), 127.1 (C^{C2}), 120.2 (C^{A5+B3}), 116.0 (C^{A3}), 114.9 (C^{C3}), 55.6 (C^{OMe}), 25.0 (C^a).

IR (solid, ṽ/cm^{-1}): 2954 (w), 2941 (w), 2831 (w), 1585 (s), 1495 (s), 1384 (m), 1322 (s), 1237 (s), 1107 (m), 1033 (s), 838 (s), 822 (s).

Mp. [°C]: decomposition > 280.

ESI MS (*m/z*): 791.5 m.u. [M+H]$^+$ (calc. 791.4 m.u.).

UV-VIS (THF, 1.0 × 10^{-5} mol dm^{-3}): λ_{abs}/nm 245 (ε/dm^3 mol^{-1} cm^{-1} 50800), 294 (48100), 359 (50700).

UV-VIS (CH$_2$Cl$_2$, 1.0 × 10^{-5} mol dm^{-3}): λ_{abs}/nm 240 *sh.* (ε/dm^3 mol^{-1} cm^{-1} 48100), 297 (37400), 360 (38700).

Found: C, 77.84; H, 5.92; N, 7.21; C$_{52}$H$_{46}$N$_4$O$_4$·^{1}/$_2$H$_2$O requires C, 78.07; H, 5.92; N, 7.00.

6.4.2 4,4'-(6,6'-Di-*n*-butyl-[2,2'-bipyridine]-4,4'-diyl)bis(N,N-bis(4-methoxyphenyl)aniline): L2.2

SB289
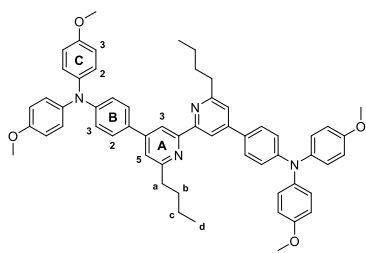
Ligand **L2.2** was prepared and purified in the same manner as **L2.1** starting with 4,4'-bis(4-bromophenyl)-6,6'-di-*n*-butyl-2,2'-bipyridine (422 mg, 0.73 mmol, 1.0 eq.), bis(4-methoxyphenyl)amine (376 mg, 1.61 mmol, 2.2 eq.) and NaO^{t}Bu (231 mg, 2.41 mmol, 3.3 eq.) in dry toluene (40 mL). For the preparation of the catalyst suspension Pd(bda)$_2$ (16.8 mg, 0.029 mmol, 4.0 mol%), dry toluene (15 mL) and 1M toluene solution of P^{t}Bu$_3$ (29.2 μL, 0.029 mmol, 4.0 mol%) were used. Reaction time at 100°C was 16 h. Ligand **L2.2** was isolated as yellow-green solid (563 mg, 0.64 mmol, 88 %).

^{1}H NMR (500 MHz, CDCl$_3$, 25°C, TMS) δ/ppm: 8.44 (d, J = 1.6 Hz, 2H, H^{A3}), 7.60 (d, J = 8.7 Hz, 4H, H^{B2}), 7.31 (d, J = 1.7 Hz, 2H, H^{A5}), 7.11 (d, J = 8.9 Hz, 8H, H^{C2}), 7.01 (d, J = 8.7 Hz, 4H, H^{B3}), 6.86 (d, J = 8.9 Hz, 8H, H^{C3}), 3.82 (s, 12H, OMe), 2.90 (t, J = 7.8 Hz, 4H, H^a), 1.85 – 1.78 (m, 4H, H^b), 1.45 (tq, J = 14.7, 7.4 Hz, 4H, H^c), 0.97 (t, J = 7.4 Hz, 6H, H^d).

^{13}C NMR (126 MHz, CDCl$_3$, 25°C, TMS) δ/ppm: 162.3 (C^{A6}), 156.8 (C^{A2}), 156.3 (C^{C4}), 149.5 (C^{B4}), 148.8 (C^{B1}), 140.7 (C^{C1}), 130.4 (C^{A4}), 127.8 (C^{B2}), 127.1 (C^{C2}), 120.2 (C^{B3}), 119.6 (C^{A5}), 116.1 (C^{A3}), 114.9 (C^{C3}), 55.7 (C^{OMe}), 38.44 (C^a), 32.2 (C^b), 22.7 (C^c), 14.2 (C^d).

IR (ṽ/cm^{-1}): 3036 (w), 3002 (w), 2952 (w), 2926 (w), 2855 (w), 2832 (w), 1588 (m), 1501 (s), 1461 (m), 1285 (m), 1238 (s), 1178 (m), 1105 (m), 1029 (s), 823 (s), 780 (m), 662 (m), 574 (m), 527 (m).

Mp. [°C]: 165.

ESI MS (*m/z*): 875.5 m.u. [M+H]$^+$, (calc. 875.5 m.u.).

UV-VIS (CH$_2$Cl$_2$, 1.0 × 10^{-5} mol dm^{-3}): λ$_{abs}$/nm 240 *sh*. (ε/dm^3 mol^{-1} cm^{-1} 48600), 296 (41400), 359 (47500).

Found: C, 78.08; H, 6.54; N, 6.31; C$_{58}$H$_{58}$N$_4$O$_4$·H$_2$O requires C, 78.00; H, 6.77; N, 6.27.

6.4.3 4,4'-(6,6'-Di-isobutyl-[2,2'-bipyridine]-4,4'-diyl)bis(N,N-bis(4-methoxyphenyl)aniline): L2.3
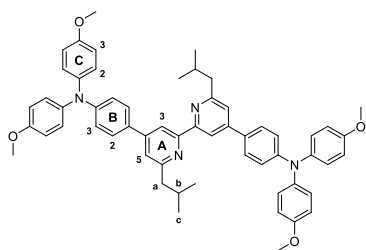
Ligand **L2.3** was prepared and purified in the same manner as **L2.1** starting with 4,4'-bis(4-bromophenyl)-6,6'-di-*iso*-butyl-2,2'-bipyridine (400 mg, 0.69 mmol, 1.0 eq.), bis(4-methoxyphenyl)amine (356 mg, 1.52 mmol, 2.2 eq.) and NaO^{t}Bu (219 mg, 2.28 mmol, 3.3 eq.) in dry toluene (60 mL). For the preparation of the catalyst suspension Pd(bda)$_2$ (15.9 mg, 0.027 mmol, 4.0 mol%), dry toluene (25 mL) and 1M toluene solution of P^{t}Bu$_3$ (27.7 µL, 0.027 mmol, 4.0 mol%) were used. Reaction time at 100°C was 16 h. Ligand **L2.3** was isolated as yellow-green solid (520 mg, 0.59 mmol, 86 %).

^{1}H NMR (500 MHz, CDCl$_3$, 25°C, TMS) δ/ppm: 8.46 (d, J = 1.3 Hz, 2H, H^{A3}), 7.60 (d, J = 8.8 Hz, 4H, H^{B2}), 7.28 (d, J = 1.6 Hz, 2H, H^{A5}), 7.12 (d, J = 9.0 Hz, 8H, H^{C2}), 7.02 (d, J = 8.8 Hz, 4H, H^{B3}), 6.87 (d, J = 9.0 Hz, 8H, H^{C3}), 3.82 (s, 12H, H^{OMe}), 2.76 (d, J = 7.2 Hz, 4H, H^a), 2.26 (ts, J = 13.6, 6.8 Hz, 2H, H^b), 0.99 (d, J = 6.6 Hz, 12H, H^c).

^{13}C NMR (126 MHz, CDCl$_3$, 25°C, TMS) δ/ppm: 161.3 (C^{A6}), 156.8 (C^{A2}), 156.3 (C^{C4}), 149.6 (C^{B4}), 148.6 (C^{B1}), 140.7 (C^{C1}), 130.4 (C^{A4}), 127.8 (C^{B2}), 127.1 (C^{C2}), 120.4 (C^{A5}), 120.2 (C^{B3}), 116.0 (C^{A3}), 114.9 (C^{C3}), 55.7 (C^{OMe}), 47.9 (C^a), 29.2 (C^b), 22.7 (C^c).

IR (ṽ/cm^{-1}): 3063 (w), 3033 (w), 3003 (w), 2950 (w), 2926 (w), 2899 (w), 2866 (w), 2831 (w), 1587 (m), 1502 (s), 1319 (m), 1240 (s), 1181 (m), 1166 (m), 1029 (m), 825 (s), 661 (m), 592 (m), 573 (m).

Mp. [°C]: 238.

ESI MS (*m/z*): 875.6 m.u. [M+H]$^+$, (calc. 875.5 m.u.).

UV-VIS (CH$_2$Cl$_2$, 1.0 × 10^{-5} mol dm^{-3}): λ$_{abs}$/nm 240 *sh.* (ε/dm^3 mol^{-1} cm^{-1} 48500), 296 (40400), 360 (45300).

Found: C, 78.29; H, 6.63; N, 6.15; C$_{58}$H$_{58}$N$_4$O$_4$·H$_2$O requires C, 78.00; H, 6.77; N, 6.27.

6.4.4 4,4'-(6,6'-Di-*n*-hexyl-[2,2'-bipyridine]-4,4'-diyl)bis(N,N-bis(4-methoxyphenyl)aniline): L2.4

SB288
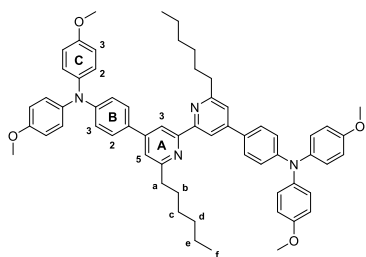
Ligand **L2.4** was prepared and purified in the same manner as **L2.1** starting with 4,4'-bis(4-bromophenyl)-6,6'-di-*n*-hexyl-2,2'-bipyridine (482 mg, 0.76 mmol, 1.0 eq.), bis(4-methoxyphenyl)amine (391 mg, 1.67 mmol, 2.2 eq.) and NaO^{t}Bu (241 mg, 2.51 mmol, 3.3 eq.) in dry toluene (50 mL). For the preparation of the catalyst suspension Pd(bda)$_2$ (17.5 mg, 0.030 mmol, 4.0 mol%), dry toluene (15 mL) and 1M toluene solution of P^{t}Bu$_3$ (30.4 μL, 0.030 mmol, 4.0 mol%) were used. Reaction time at 100°C was 16 h. Ligand **L2.4** was isolated as yellow-green solid (608 mg, 0.65 mmol, 86 %).

^{1}H NMR (500 MHz, CDCl$_3$, 25°C, TMS) δ/ppm: 8.44 (d, J = 1.7 Hz, 2H, H^{A3}), 7.60 (d, J = 8.8 Hz, 4H, H^{B2}), 7.31 (d, J = 1.7 Hz, 2H, H^{A5}), 7.11 (d, J = 8.9 Hz, 8H, H^{C2}), 7.01 (d, J = 8.8 Hz, 4H, H^{B3}), 6.87 (d, J = 9.0 Hz, 8H, H^{C3}), 3.82 (s, 12H, H^{OMe}), 2.89 (t, J = 7.8 Hz, 4H, H^a), 1.83 (tt, J = 15.4, 7.6 Hz, 4H, H^b), 1.55 – 1.39 (m, 4H, H^c), 1.39 – 1.24 (m, 8H, H^d, H^e), 0.88 (t, J = 7.0 Hz, 6H, H^f).

^{13}C NMR (126 MHz, CDCl$_3$, 25°C, TMS) δ/ppm: 162.4 (C^{A6}), 156.8 (C^{A2}), 156.3 (C^{C4}), 149.5 (C^{B4}), 148.9 (C^{B1}), 140.7 (C^{C1}), 130.4 (C^{A4}), 127.8 (C^{B2}), 127.0 (C^{C2}), 120.2 (C^{B3}), 119.6 (C^{A5}), 116.1 (C^{A3}), 114.9 (C^{C3}), 55.7 (C^{OMe}), 38.7 (C^a), 32.0 (C^b), 30.0 (C^c), 29.3 (C^d), 22.8 (C^e), 14.3 (C^f).

IR (ṽ/cm^{-1}): 3036 (w), 2997 (w), 2950 (w), 2921 (w), 2851 (w), 2827 (w), 1591 (m), 1504 (s), 1461 (m), 1439 (m), 1321 (m), 1291 (m), 1239 (s), 1194 (m), 1167 (m), 1038 (m), 826 (s), 660 (m), 597 (m), 571 (m), 530 (m).

Mp. [°C]: 179.

ESI MS (*m/z*): 931.6 m.u. [M+H]$^+$, (calc. 931.5 m.u.).

UV-VIS (CH$_2$Cl$_2$, 1.0 × 10^{-5} mol dm^{-3}): λ$_{abs}$/nm 240 *sh.* (ε/dm^3 mol^{-1} cm^{-1} 47300), 297 (41100), 359 (46600).

Found: C, 77.22; H, 6.91; N, 5.99; C$_{62}$H$_{66}$N$_4$O$_4$·2H$_2$O requires C, 76.99; H, 7.29; N, 5.79.

6.4.5 4,4'-(6,6'-Diphenyl-[2,2'-bipyridine]-4,4'-diyl)bis(N,N-bis(4-methoxyphenyl)aniline): L2.5

SB287
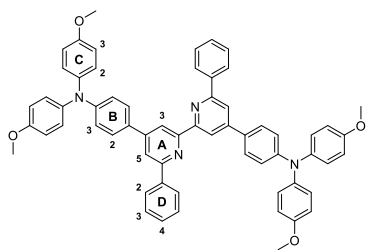
Ligand **L2.5** was prepared and purified in the same manner as **L2.1** starting with 4,4'-bis(4-bromophenyl)-6,6'-diphenyl-2,2'-bipyridine (432 mg, 0.70 mmol, 1.0 eq.), bis(4-methoxyphenyl)amine (359 mg, 1.54 mmol, 2.2 eq.) and NaO^{t}Bu (221 mg, 2.30 mmol, 3.3 eq.) in dry toluene (50 mL). For the preparation of the catalyst suspension Pd(bda)$_2$ (16.1 mg, 0.028 mmol, 4.0 mol%), dry toluene (15 mL) and 1M toluene solution of P^{t}Bu$_3$ (29.7 μL, 0.028 mmol, 4.0 mol%) were used. Reaction time at 100°C was 16 h. Ligand **L2.5** was isolated as yellow-green solid (552 mg, 0.60 mmol, 86 %).

^{1}H NMR (500 MHz, CDCl$_3$, 25°C, TMS) δ/ppm: 8.82 (d, J = 1.4 Hz, 2H, H^{A3}), 8.22 (d, J = 7.2 Hz, 4H, H^{D2}), 7.95 (d, J = 1.4 Hz, 2H, H^{A5}), 7.69 (d, J = 8.8 Hz, 4H, H^{B2}), 7.56 – 7.51 (m, 4H, H^{D3}), 7.48 – 7.43 (m, 2H, H^{D4}), 7.15 (d, J = 8.9 Hz, 8H, H^{C2}), 7.06 (d, J = 8.7 Hz, 4H, H^{B3}), 6.89 (d, J = 9.0 Hz, 8H, H^{C3}), 3.83 (s, 12H, OMe).

^{13}C NMR (126 MHz, CDCl$_3$, 25°C, TMS) δ/ppm: 157.0 (C^{A6}), 156.7 (C^{A2}), 156.4 (C^{C4}), 149.8 (C^{B4}), 149.7 (C^{B1}), 140.6 (C^{C1}), 140.0 (C^{D1}), 130.2 (C^{A4}), 128.8 (C^{D4}), 128.4 (C^{D3}), 127.9 (C^{B2}), 127.2 (C^{D2}), 127.2 (C^{C2}), 120.1 (C^{B3}), 117.8 (C^{A5}), 117.2 (C^{A3}), 115.0 (C^{C3}), 55.7 (OMe).

IR (ṽ/cm^{-1}): 3033 (w), 2952 (w), 2929 (w), 2903 (w), 2832 (w), 1590 (m), 1503 (s), 1462 (m), 1441 (m), 1239 (s), 1194 (m), 1180 (m), 1165 (m), 1032 (m), 824 (m), 774 (m), 688 (m), 660 (m), 576 (m), 537 (m).

Mp. [°C]: decomposition >172.

ESI MS (*m/z*): 915.5 m.u. [M+H]$^+$, (calc. 915.4 m.u.).

UV-VIS (CH$_2$Cl$_2$, 1.0 × 10^{-5} mol dm^{-3}): λ$_{abs}$/nm 254 (ε/dm^3 mol^{-1} cm^{-1} 60500), 290 *sh.* (44100), 369 (37300).

Found: C, 78.08; H, 5.36; N, 5.88; C$_{62}$H$_{50}$N$_4$O$_4$·H$_2$O requires C, 78.29; H, 5.72; N, 5.89.

6.4.6 4,4'-(6,6'-Di(2-naphthyl)-[2,2'-bipyridine]-4,4'-diyl)bis(N,N-bis(4-methoxyphenyl) aniline): L2.6
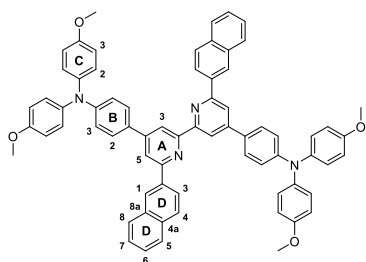
Ligand **L2.6** was prepared and purified in the same manner as **L2.1** starting with 4,4'-bis(4-bromophenyl)-6,6'-di(naphthalen-2-yl)-2,2'-bipyridine (460 mg, 0.64 mmol, 1.0 eq.), bis(4-methoxyphenyl)amine (330 mg, 1.41 mmol, 2.2 eq.) and NaO^{t}Bu (203 mg, 2.11 mmol, 3.3 eq.) in dry toluene (70 mL). For the preparation of the catalyst suspension Pd(bda)$_2$ (14.7 mg, 0.026 mmol, 4.0 mol%), dry toluene (10 mL) and 1M toluene solution of P^{t}Bu$_3$ (25.6 μL, 0.026 mmol, 4.0 mol%) were used. Reaction time at 100°C was 24 h. Ligand **L2.6** was isolated as yellow-green solid (393 mg, 0.39 mmol, 60%).

^{1}H NMR (500 MHz, CDCl$_3$, 25°C, TMS) δ/ppm: 8.89 (d, J = 1.5 Hz, 2H, H^{A3}), 8.67 – 8.64 (m, 2H, H^{D1}), 8.42 (dd, J = 8.6, 1.7 Hz, 2H, H^{D3}), 8.11 (d, J = 1.6 Hz, 2H, H^{A5}), 8.03 – 7.99 (m, 4H, H^{D5}, H^{D8}), 7.94 – 7.88 (m, 2H, H^{D4}), 7.75 (d, J = 8.8 Hz, 4H, H^{B2}), 7.55 – 7.51 (m, 4H, H^{D7}, H^{D6}), 7.16 (d, J = 9.0 Hz, 8H, H^{C2}), 7.09 (d, J = 8.8 Hz, 4H, H^{B3}), 6.89 (d, J = 9.0 Hz, 8H, H^{C3}), 3.83 (s, 12H, OMe).

^{13}C NMR (126 MHz, CDCl$_3$, 25°C, TMS) δ/ppm: 157.0 (C^{A6}), 156.9 (C^{A2}), 156.4 (C^{C4}), 149.9 (C^{B4}), 149.8 (C^{B1}), 140.6 (C^{C1}), 137.4 (C^{D2}), 133.8 (C^{D4a}), 133.7 (C^{D8a}), 130.2 (C^{A4}), 128.9 (C$^{D4/D5/D8}$), 128.5 (C$^{D4/D5/D8}$), 128.0 (C^{B2}), 127.9 (C^{D4}), 127.2 (C^{C2}), 126.6 (C$^{D6/D7}$), 126,5 (C^{D1}), 126.4 (C$^{D6/D7}$), 125.2 (C^{D3}), 120.2 (C^{B3}), 118.2 (C^{A5}), 117.4 (C^{A3}), 115.0 (C^{C3}), 55.7 (OMe).

IR (ṽ/cm^{-1}): 3059 (w), 3038 (w), 2999 (w), 2950 (w), 2929 (w), 2905 (w), 2830 (w), 1587 (m), 1502 (s), 1463 (m), 1439 (m), 1283 (m), 1239 (s), 1180 (m), 1035 (m), 820 (s), 755 (m), 575 (m), 533 (m), 476 (m).

Mp. [°C]: decomposition >320.

ESI MS (m/z): 1015.5 m.u. [M+H]$^+$, (calc. 1015.4 m.u.).

UV-VIS (CH$_2$Cl$_2$, 1.0 × 10^{-5} mol dm^{-3}): λ$_{abs}$/nm 234 (ε/dm^3 mol^{-1} cm^{-1} 84000), 255 (82900), 297 (55400), 370 (36500).

Found: C, 79.28; H, 5.30; N, 5.47; C$_{70}$H$_{54}$N$_4$O$_4$·2.5H$_2$O requires C, 79.30; H, 5.61; N, 5.28.

6.5 Copper(I) complexes II: C2.1-2.6

General procedure II

In a typical reaction, the ligand (1.0 eq.) was dissolved in a 1:1 mixture of MeCN and CH_2Cl_2 (only CH_2Cl_2 for **L2.5** and **L2.6**) and [Cu(MeCN)$_4$][PF$_6$] (0.5 eq.) was added. The solution turned red immediately for **L2.1-L2.4** and green-black for **L2.5** and **L2.6** respectively. The solution was stirred over night at r.t. after which time, the volume of the solvent was reduced *in vacuo* and the product was precipitated by addition of Et$_2$O. The solid was filtered off and washed with Et$_2$O and dried in a stream of air.

6.5.1 [Cu(L2.1)$_2$][PF$_6$]: C2.1

SB218, SB252, SB300
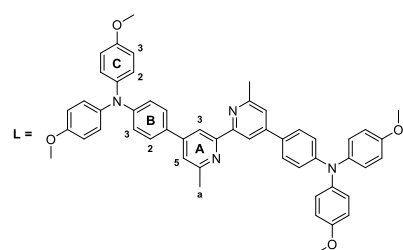
[Cu(MeCN)$_4$][PF$_6$] (118 mg, 0.316 mmol, 0.5 eq.) was reacted with **L2.1** (500 mg, 0.632 mmol, 1.0 eq.) in MeCN (30 mL) and CH_2Cl_2 (30 mL). **C2.1** was isolated as a red solid (471 mg, 0.263 mmol, 83%).

^{1}H NMR (500 MHz, CDCl$_3$, 25°C, TMS) δ/ppm: 8.25 (s, 4H, H^{A3}), 7.59 (s, 4H, H^{A5}) overlapping with 7.58 (m, 8H, H^{B2}), 7.13 (d, J = 8.7 Hz, 16H, H^{C2}), 7.02 (m, 8H, H^{B3}), 6.89 (d, J = 8.8 Hz, 16H, H^{C3}), 3.83 (s, 24H, H^{OMe}), 2.31 (s, 12H, H^a).

^{13}C NMR (126 MHz, CDCl$_3$, 25°C, TMS) δ/ppm: 157.1 (C^{A6}), 152.1 (C^{A2}), 156.2 (C^{C4}), 150.5 (C^{B4}), 139.7 (C^{C1}), 127.7 (C^{A5}), 127.4 (C^{C2}), 127.1 (C^{B1}), 122.3 (C^{B2}), 119.3 (C^{B3}), 115.9 (C^{A3}), 114.5 (C^{C3}), 55.4 (C^{OMe}), 25.4 (C^a); signal for C^{A4} not resolved at r.t..

Mp. [°C]: decomposition > 136.

ESI MS (*m/z*): 1644.6 m.u. [M–PF$_6$]$^+$ (calc. 1644.6 m.u.), 791.5 m.u. [**L1**+H]$^+$ (base peak, calc. 791.4 m.u.), 145.0 m.u. [PF$_6$]$^-$, (calc. 145.0 m.u.).

UV-VIS (CH$_2$Cl$_2$, 1.0 × 10^{-5} mol dm^{-3}): λ$_{abs}$/nm 306 (ε/dm^3 mol^{-1} cm^{-1} 65400), 392 (57300), 480 *sh.* (27200).

IR (ṽ/cm^{-1}): 3052 (w), 3032 (w), 1591 (s), 1498 (s), 1324 (m), 1239 (s), 1171 (m), 1030 (m), 822 (s), 746 (s), 691 (s).

Found: C, 67.54; H, 5.14; N, 6.34; C$_{104}$H$_{92}$CuF$_6$N$_8$O$_8$P·3H$_2$O requires C, 67.72; H, 5.36; N, 6.08.

6.5.2 [Cu(L2.2)₂][PF₆]: C2.2

SB291
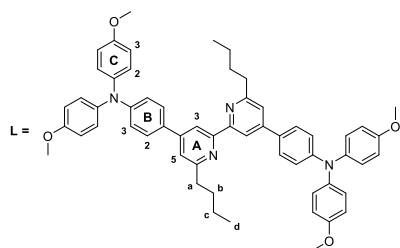
[Cu(MeCN)₄][PF₆] (35.2 mg, 0.094 mmol, 0.5 eq.) was reacted with **L2.2** (165 mg, 0.189 mmol, 1.0 eq.) in MeCN (15 mL) and CH₂Cl₂ (15 mL). **C2.2** was isolated as a red solid (145 mg, 0.074 mmol, 78%).

^{1}H NMR (500 MHz, CDCl₃, 25°C, TMS) δ/ppm: 8.27 (d, J = 1.2 Hz, 4H, H^{A3}), 7.59 (d, J = 8.8 Hz, 8H, H^{B2}), 7.57 (d, J = 1.2 Hz, 4H, H^{A5}), 7.14 (d, J = 9.0 Hz, 16H, H^{C2}), 7.02 (d, J = 8.8 Hz, 8H, H^{B3}), 6.89 (d, J = 9.0 Hz, 16H, H^{C3}), 3.83 (s, 24H, OMe), 2.62 (t, J = 8.2 Hz, 8H, H^a), 1.44 – 1.32 (m, 8H, H^b), 0.90 (tq, J = 7.4 Hz, 8H, H^c), 0.48 (t, J = 7.4 Hz, 12H, H^d).

^{13}C NMR (126 MHz, CDCl₃, 25°C, TMS) δ/ppm: 161.5 (C^{A6}), 156.8 (C^{C4}), 152.6 (C^{A2}), 150.8 (C^{B4}), 150.2 (C^{B1}), 139.8 (C^{C1}), 127.8 (C^{B2}), 127.5 (C^{C2}), 127.3 (C^{A4}), 121.8 (C^{A5}), 119.4 (C^{B3}), 116.3 (C^{A3}), 115.1 (C^{C3}), 55.7 (O^{Me}), 39.8 (C^a), 31.9 (C^b), 22.7 (C^c), 13.6 (C^d).

IR (ṽ/cm^{-1}): 3187 (w), 3036 (w), 2997 (w), 2952 (w), 2924 (w), 2866 (w), 2853 (w), 2832 (w), 1595 (s), 1501 (s), 1462 (m), 1440 (m), 1321 (m), 1237 (s), 1195 (m), 1179 (m), 1102 (m), 1031 (m), 838 (s), 824 (s), 728 (m), 574 (m), 557 (m), 527 (m).

Mp. [°C]: 136.

ESI MS (m/z): 1813.8 m.u. [M-PF₆]$^+$, (calc. 1813.8 m.u.), 144.9 m.u. [PF₆]$^-$, (calc. 145.0 m.u.).

UV-VIS (CH₂Cl₂, 1.0 × 10^{-5} mol dm^{-3}): λ$_{abs}$/nm 306 (ε/dm^3 mol^{-1} cm^{-1} 67500), 386 (60400), 480 $sh.$ (27500).

Found: C, 71.69; H, 6.32; N, 5.52; C₁₁₆H₁₁₆N₈O₈CuPF₆ requires C, 71.13; H, 5.97; N, 5.72.

6.5.3 [Cu(L2.3)₂][PF₆]: C2.3

SB276
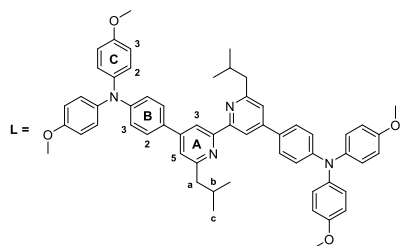
[Cu(MeCN)₄][PF₆] (47.9 mg, 0.128 mmol, 0.5 eq.) was reacted with **L2.3** (225 mg, 0.257 mmol, 1.0 eq.) in MeCN (15 mL) and CH_2Cl_2 (15 mL). **C2.3** was isolated as a red solid (105 mg, 0.054 mmol, 42%).

^{1}H NMR (500 MHz, CDCl₃, 25°C, TMS) δ/ppm: 8.27 (s, 4H, H^{A3}), 7.60 (d, J = 8.5 Hz, 8H, H^{B2}), 7.52 (s, 4H, H^{A5}), 7.14 (d, J = 8.7 Hz, 16H, H^{C2}), 7.02 (d, J = 8.6 Hz, 8H, H^{B3}), 6.89 (d, J = 8.4 Hz, 16H, H^{C3}), 3.83 (s, 24H, OMe), 2.47 (d, J = 7.4 Hz, 8H, H^a), 1.69 (qs, J = 13.4, 6.7 Hz, 4H, H^b), 0.54 (d, J = 6.7 Hz, 24H, H^c).

^{13}C NMR (126 MHz, CDCl₃, 25°C, TMS) δ/ppm: 160.5 (C^{A6}), 156.9 (C^{C4}), 153.1 (C^{A2}), 149.9 (C^{B1}, C^{B4}), 139.9 (C^{C1}), 127.9 (C^{B2}), 127.6 (C^{A4}, C^{C2}), 122.8 (C^{A5}), 119.5 (C^{B3}), 116.5 (C^{A3}), 115.1 (C^{C3}), 55.7 (OMe), 48.8 (C^a), 28.5 (C^b), 22.2 (C^c).

IR (ṽ/cm⁻¹): 3190 (w), 3033 (w), 2997 (w), 2953 (w), 2929 (w), 2866 (w), 2834 (w), 1594 (s), 1504 (s), 1463 (m), 1440 (m), 1322 (m), 1289 (m), 1239 (s), 1196 (m), 1179 (m), 1102 (m), 1032 (m), 825 (s), 597 (m), 574 (m), 557 (m), 531 (m).

Mp. [°C]: 178.

ESI MS (*m/z*): 1814.8 m.u. [M-PF₆]$^+$ (calc. 1813.8 m.u.), 875.6 m.u. [L+H]$^+$(base peak, calc. 875.5 m.u.), 144.9 m.u. [PF₆]$^-$ (calc. 145.0 m.u.).

UV-VIS (CH₂Cl₂, 1.0×10^{-5} mol dm⁻³): λ_{abs}/nm 305 (ε/dm³ mol⁻¹ cm⁻¹ 63000), 393 (58700), 480 *sh.* (28200).

Found: C, 70.14; H, 6.30; N, 5.48; $C_{116}H_{116}N_8O_8CuPF_6 \cdot H_2O$ requires C, 70.48; H, 6.02; N, 5.67.

6.5.4 [Cu(L2.4)₂][PF₆]: C2.4
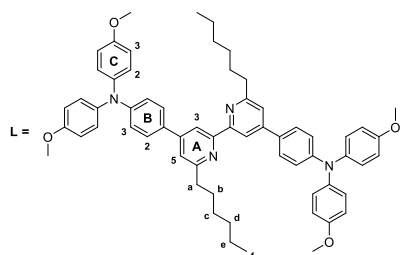
[Cu(MeCN)₄][PF₆] (31.7 mg, 0.085 mmol, 0.5 eq.) was reacted with **L2.4** (158 mg, 0.17 mmol, 1.0 eq.) in MeCN (15 mL) and CH₂Cl₂ (15 mL). **C2.4** was isolated as a red solid (153 mg, 0.074 mmol, 86%).

^{1}H NMR (500 MHz, CDCl₃, 25°C, TMS) δ/ppm: 8.26 (d, J = 1.4 Hz, 4H, H^{A3}), 7.58 (d, J = 8.9 Hz, 8H, H^{B2}), 7.56 (d, J = 1.4 Hz, 4H, H^{A5}), 7.13 (d, J = 9.0 Hz, 16H, H^{C2}), 7.02 (d, J = 8.9 Hz, 8H, H^{B3}), 6.89 (d, J = 9.0 Hz, 16H, H^{C3}), 3.83 (s, 24H, OMe), 2.61 (t, J = 8.2 Hz, 8H, H^a), 1.38 (tt, J = 8.0, 7.9 Hz, 8H, H^b), 0.95 (tt, J = 7.0 Hz, 8H, H^c), 0.90 – 0.82 (m, 8H, H^d), 0.82 – 0.73 (m, 8H, H^e), 0.62 (t, J = 7.3 Hz, 12H, H^f).

^{13}C NMR (126 MHz, CDCl₃, 25°C, TMS) δ/ppm: 161.6 (C^{A6}), 156.8 (C^{C4}), 152.6 (C^{A2}), 150.8 (C^{B4}), 150.2 (C^{B1}), 139.8 (C^{C1}), 127.8 (C^{B2}), 127.5 (C^{C2}), 127.2 (C^{A4}), 121.8 (C^{A5}), 119.4 (C^{B3}), 116.2 (C^{A3}), 115.1 (C^{C3}), 55.7 (OMe), 40.1 (C^a), 31.5 (C^b), 30.0 (C^c), 29.5 (C^d), 22.6 (C^e), 14.1 (C^f).

IR (ṽ/cm^{-1}): 3187 (w), 3036 (w), 2997 (w), 2947 (w), 2924 (w), 2853 (w), 2835 (w), 1594 (s), 1504 (s), 1461 (m), 1327 (m), 1294 (m), 1239 (s), 1200 (m), 1179 (m), 1102 (m), 1031 (m), 838 (s), 825 (s), 729 (m), 663 (m), 573 (m), 557 (m), 535 (m).

Mp. [°C]: decomposition >250.

ESI MS (m/z): 1926.0 m.u. [M-PF₆]$^+$ (base peak, calc. 1924.5 m.u.), 932.2 m.u. [L+H]$^+$(calc. 931.5 m.u.), 144.9 m.u. [PF₆]$^-$ (calc. 145.0 m.u.).

UV-VIS (CH₂Cl₂, 1.0 × 10^{-5} mol dm^{-3}): λ$_{abs}$/nm 306 (ε/dm^3 mol^{-1} cm^{-1} 65700), 388 (60000), 480 *sh.* (28000).

Found: C, 68.93; H, 6.12; N, 5.46; C₁₂₄H₁₃₂N₈O₈CuPF₆·4H₂O requires C, 69.50; H, 6.58; N, 5.23.

6.5.5   [Cu(L2.5)$_2$][PF$_6$]: C2.5

L =
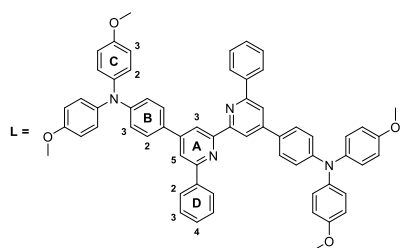
[Cu(MeCN)$_4$][PF$_6$] (45.9 mg, 0.123 mmol, 0.5 eq.) was reacted with **L2.5** (225 mg, 0.246 mmol, 1.0 eq.) in CH$_2$Cl$_2$ (40 mL). **C2.5** was isolated as a green-black solid (225 mg, 0.11 mmol, 90%).

^{1}H NMR (500 MHz, CDCl$_3$, 25°C, TMS) δ/ppm: 7.95 (d, J = 1.2 Hz, 4H, H^{A3}), 7.61 (d, J = 1.2 Hz, 4H, H^{A5}), 7.60 – 7.57 (m, 8H, H^{D2}), 7.56 (d, J = 8.8 Hz, 8H, H^{B2}), 7.17 (d, J = 9.0 Hz, 16H, H^{C2}), 7.05 (d, J = 8.8 Hz, 8H, H^{B3}), 7.05 – 7.01 (m, 4H, H^{D4}), 6.92 (d, J = 9.0 Hz, 16H, H^{C3}), 7.06 – 7.01 (m, 8H, H^{D3}), 3.84 (s, 24H, OMe).

^{13}C NMR (126 MHz, CDCl$_3$, 25°C, TMS) δ/ppm: 157.0 (C^{A6}), 156.9 (C^{C4}), 153.6 (C^{A2}), 150.9 (C^{B4}), 149.9 (C^{B1}), 139.8 (C^{C1}), 138.7 (C^{D1}), 129.2 (C^{D4}), 127.8 (C^{B2}), 127.7 (C^{D2}, C^{D3}), 127.6 (C^{C2}), 127.2 (C^{A4}), 121.5 (C^{A5}), 119.4 (C^{B3}), 117.8 (C^{A3}), 115.1 (C^{C3}), 55.7 (OMe).

IR (ṽ/cm^{-1}): 3036 (w), 2999 (w), 2950 (w), 2931 (w), 2903 (w), 2832 (w), 1593 (s), 1504 (s), 1321 (m), 1238 (s), 1196 (m), 1179 (m), 1104 (m), 1030 (m), 824 (s), 773 (m), 741 (m), 729 (m), 696 (m), 576 (m), 557 (m), 527 (m).

Mp. [°C]: decomposition >185.

ESI MS (m/z): 1894.4 m.u. [M-PF$_6$]$^+$ (calc. 1893.7 m.u.), 915.9 m.u. [L+H]$^+$(base peak, calc. 915.4 m.u.).

UV-VIS (CH$_2$Cl$_2$, 1.0 × 10^{-5} mol dm^{-3}): λ$_{abs}$/nm 286 (ε/dm^3 mol^{-1} cm^{-1} 79300), 331 (51600), 401 (55600), 560 $sh.$ (7000).

Found: C, 73.04; H, 5.39; N, 5.30; C$_{124}$H$_{100}$N$_8$O$_8$CuPF$_6$ requires C, 73.05; H, 4.94; N, 5.50.

6.5.6 [Cu(L2.6)₂][PF₆]: C2.6
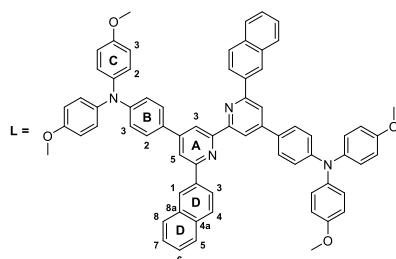
[Cu(MeCN)₄][PF₆] (27.6 mg, 0.074 mmol, 0.5 eq.) was reacted with **L2.6** (150 mg, 0.148 mmol, 1.0 eq.) in CH₂Cl₂ (40 mL). **C2.6** was isolated as a green-black solid (153 mg, 0.068 mmol, 92%).

^{1}H NMR (500 MHz, CDCl₃, 25°C, TMS) δ/ppm: 8.22 (s, 4H, H^{D1}), 7.64 – 7.60 (m, 4H, H^{D3}), 7.59 – 7.55 (m, 8H, H^{A5}, H$^{D5/D8}$), 7.43 (d, J = 8.6 Hz, 4H, H^{D4}), 7.36 – 7.29 (m, 16H, H^{A3},H^{B2}, H$^{D6/D7}$), 7.20 (d, J = 8.9 Hz, 16H, H^{C2}), 7.17 – 7.11 (m, 8H, H$^{D5/D8}$, H$^{D7/D8}$), 7.03 (d, J = 8.7 Hz, 8H, H^{B3}), 6.95 (d, J = 9.0 Hz, 16H, H^{C3}), 3.86 (s, 24H, OMe).

^{13}C NMR (126 MHz, CDCl₃, 25°C, TMS) δ/ppm: 156.9 (C^{C4}), 156.5 (C^{A6}), 153.5 (C^{A2}), 150.8 (C^{B4}), 149.8 (C^{B1}), 139.9 (C^{C1}), 136.0 (C^{D2}), 133.3 (C$^{D4a/D8a}$), 132.2 (C$^{D4a/D8a}$), 128.1 (C$^{D5/D6/D7/D8}$), 127.9 (C^{B2}), 127.6 (C^{C2}), 127.5 (C^{D1}, C^{D4}, C$^{D5/D8}$), 127.2 (C^{A4}), 127.1 (C$^{D6/D7}$), 126.4 (C$^{D5/D6/D7/D8}$), 125.1 (C^{D3}), 121.2 (C^{A5}), 119.2 (C^{B3}), 117.4 (C^{A3}), 115.2 (C^{C3}), 55.7 (OMe).

IR (ṽ/cm^{-1}): 3038 (w), 2999 (w), 2950 (w), 2929 (w), 2905 (w), 2832 (w), 1592 (s), 1504 (s), 1320 (m), 1239 (m), 1196 (m), 1179 (m), 1102 (m), 1032 (m), 824 (s), 781 (m), 755 (m), 741 (m), 576 (m), 557 (m), 533 (m), 477 (m).

Mp. [°C]: decomposition >185.

ESI MS (*m/z*): 2094.8 m.u. [M-PF₆]$^+$ (base peak, calc. 2093.8 m.u.), 1016.1 m.u. [L+H]$^+$(calc. 1015.4 m.u.).

UV-VIS (CH₂Cl₂, 1.0 × 10^{-5} mol dm^{-3}): λ$_{abs}$/nm 290 (ε/dm^3 mol^{-1} cm^{-1} 103100), 340 *sh.* (55400), 408 (58000), 576 (5900).

Found: C, 73.11; H, 5.18; N, 4.98; C₁₄₀H₁₀₈N₈O₈CuPF₆·3H₂O requires C, 73.33; H, 5.01; N, 4.89.

6.6 Dendrimer precursors

6.6.1 *tert*-Butyl-bis(4-bromophenyl)carbamate: carbamate1

SB230, SB328
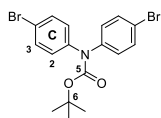
The synthesis is adapted from the general method of Ito et al.[169][249][250] and Müllen et al. [251] .To a solution of bis(4-bromophenyl)amine (4.00 g, 11.9 mmol, 1.0 eq.) and (Boc)$_2$O (2.91 g, 13.1 mmol, 1.1 eq.) in dry THF (25 mL), dimethylaminopyridine (293.mg, 2.37 mmol, 0.2 eq.) was added and the color changed from blue to yellow. The mixture was refluxed for 18 h under argon. The solution was filtered hot and the solvent was removed. To the yellowish oil, hexane (20 mL) was added and the mixture was cooled in an ice bath. Upon cooling white crystals formed which were removed by filtration washed again with hexane (10 mL). The crystals were collected and dried yielding (2.81g, 0.0066 mmol, 55%) of a first fraction of pure protected amine. The solvent of the mother liquor was removed. The yellowish solid was purified via column chromatography (Al$_2$O$_3$, 100% CHCl$_3$) to give a second fraction of pure product (1.79 g, 0.0042 mmol, 35%).

^{1}H NMR (500 MHz, CDCl$_3$, 25°C, TMS) δ/ppm: 7.43 (d, J = 8.7 Hz, 4H, H^{C2}), 7.06 (d, J = 8.7 Hz, 4H, H^{C3}), 1.44 (s, 9H, ^{t}Bu).

^{13}C NMR (126 MHz, CDCl$_3$, 25°C, TMS) δ/ppm: 153.2 (C^{C5}), 141.8 (C^{C1}), 132.0 (C^{C3}), 128.6 (C^{C2}), 119.4 (C^{C4}), 82.0 (C^{C6}), 28.3 (C^{Me}).

EI MS (*m/z*): 427.0 m.u. [M]$^+$ (calc. 426.9 m.u.), 370.9 m.u. [M-^{t}Bu]$^+$ (calc. 370.9 m.u.), 57.1 m.u. [^{t}Bu]$^+$ (calc. 57.1 m.u.).

IR (ATR, ṽ/cm^{-1}): 2982 (w), 2971 (w), 1705 (s), 1452 (s), 1388 (m), 1249 (s), 1098 (m), 954 (s), 844 (s), 822 (s), 799 (s), 694 (s).

6.6.2 *tert*-Butyl bis(4-(bis(4-methoxyphenyl)amino)phenyl)carbamate: carbamate2

SB239, SB329
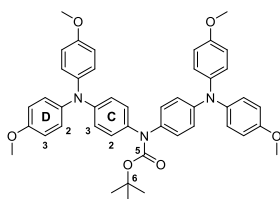
In a three-necked round-bottomed flask, bis(4-methoxyphenyl)amine (3.49 g, 15.2 mmol, 2.5 eq.), NaO^{t}Bu (1.75 g, 18.3 mmol, 3.0 eq.) and *N*-Boc-bis(4-bromophenyl)amine (2.59 g, 6.09 mmol, 1.0 eq.) were dissolved in dry toluene (20 mL). In a separate flask, flushed with N$_2$,

P^{t}Bu$_3$ (0.30 mL, 1.0 M in toluene) and Pd(bda)$_2$ (175 mg, 0.30 mmol) were suspended in dry toluene (10 mL). The freshly prepared solution of the catalyst was added to the reaction mixture and heated to reflux overnight. The reaction mixture was filtered hot in order to remove insoluble solids. The solvent was removed. The resulting black oil was purified by column chromatography (Al$_2$O$_3$, EtOAc). The dark solid was recrystallized from hexane to give a white solid. A little acetone was added to the mother liquor and upon the addition of hexane, a white precipitate formed. These two fractions were collected to give *tert*-butyl bis(4-(bis(4-methoxyphenyl)amino)phenyl)carbamate (**carbamate2**) as a colourless solid (3.66 g, 5.05 mmol, 83%).

^{1}H NMR (500 MHz, CDCl$_3$, 25°C, TMS) δ/ppm: 7.02 (m, 12H, H^{D2+C2}), 6.85 (d, J = 8.9 Hz, 4H, H^{C3}), 6.81 (d, J = 9.0 Hz, 8H, H^{D3}), 3.79 (s, 12H, C^{OMe}), 1.45 (s, 9H, C^{Me}).

^{13}C NMR (126 MHz, CDCl$_3$, 25°C, TMS) δ/ppm: 155.8 (C^{D4}), 154.5 (C^5), 146.3 (C^{C4}), 141.2 (C^{D1}), 136.1 (C^{C1}), 127.5 (C^{C2}), 126.5 (C^{D2}), 120.9 (C^{C3}), 114.7 (C^{D3}), 80.8 (C^6), 55.4 (C^{OMe}), 28.3 (C^{Me}).

EI MS (*m/z*): 723.3 m.u. [M]$^+$ (calc. 723.3 m.u.), 623.3 m.u. [M − Boc]$^+$ (calc. 623.3 m.u.).

IR (solid, ṽ/cm^{-1}): 3037 (w), 2965 (w), 2930 (w), 1696 (s), 1499 (s), 1234 (s), 1156 (s), 1034 (s), 825 (s), 690 (m).

6.6.3 N¹-(4-(Bis(4-methoxyphenyl)amino)phenyl)-N⁴,N⁴-bis(4-methoxyphenyl)benzene-1,4-diamine: amine2

SB240, SB317, SB330
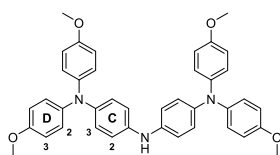
Tert-Butyl-bis(4-(bis-(4-methoxyphenyl)-amino)-phenyl)-carbamate (**carbamate2**) (323 mg, 0.446 mmol, 1.0 eq.) was dissolved in acetone (20 mL) and concentrated trifluoroacetic acid (5 mL, 7.40 g, 64.8 mmol, 145 eq.) was added. The reaction mixture was stirred at room temperature overnight. The solvent was then removed and the solid was purified by column chromatography (Al$_2$O$_3$, EtOAc). The resulting solid was suspended in hexane (50 mL) and the mixture was heated to reflux until a fine suspension was obtained. **Amine2** was isolated by filtration (243 mg, 0.39 mmol, 88%).

^{1}H NMR (500 MHz, acetone-d$_6$ + TFA, 25°C, TMS) δ/ppm: 7.38 (d, J = 9.0 Hz, 4H, H$^{C2/C3}$), 7.16 (d, J = 8.9 Hz, 8H, H$^{D2/D3}$), 6.95 (d, J = 8.9 Hz, 8H, H$^{D2/D3}$), 6.84 (d, J = 9.0 Hz, 4H, H$^{C2/C3}$), 4.01 (br, H^{NH}), 3.79 (s, 12H, H^{OMe}).

^{13}C NMR (126 MHz, acetone-d$_6$ + TFA, 25°C, TMS) δ/ppm: 158.4 (C^{D4}), 151.6 (C^{C4}), 139.9 (C^{D1}), 134.1 (C^{C1}), 129.0 (C^{D2}), 125.9 (C^{C2}), 118.4 (C^{C3}), 116.0 (C^{D3}), 55.6 (C^{OMe}).

EI MS (*m/z*): 623.3 m.u. [M]$^+$ (calc. 623.3 m.u.).

IR (ATR, ṽ/cm^{-1}): 3036 (w), 2999 (w), 2960 (w), 2900 (w), 2830 (w), 1587 (w), 1490 (s), 1266 (s), 1233 (s), 1101 (m), 815 (s), 798 (m), 572 (m).

6.7 Ligands III: L3.1-3.6

6.7.1 N^1,N$^{1''}$-((6,6'-Dimethyl-[2,2'-bipyridine]-4,4'-diyl)bis(4,1-phenylene))bis(N^1-(4-(bis(4-methoxyphenyl)amino)phenyl)-N^4,N^4-bis(4-methoxyphenyl)benzene-1,4-diamine): L3.1

SB241, SB243
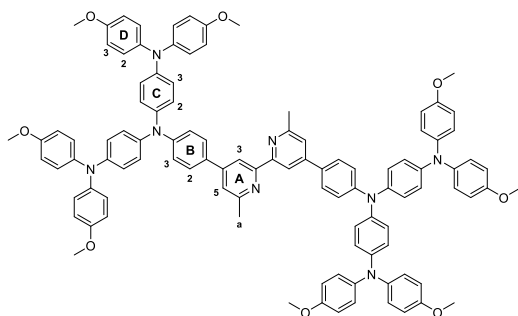
4,4'-Bis(4-bromophenyl)-6,6'-dimethyl-2,2'-bipyridine (**L1.1**) (365 mg, 0.74 mmol, 1.0 eq.), **amine2** (1.15 g, 1.85 mmol, 2.5 eq.) and NaO^{t}Bu (402 mg, 4.06 mmol, 5.5 eq.) were suspended in dry toluene (60 mL). To a suspension of Pd(bda)$_2$ (42.5 mg, 0.074 mmol, 10 mol%) and dry toluene (20 mL), a 1M solution of P^{t}Bu$_3$ in toluene (0.07 mL, 0.074 mmol, 10 mol%) was added. The freshly prepared catalyst suspension was added to the reaction mixture which was then heated to 100°C for 16 h. The reaction mixture was filtered hot to remove insoluble solids. The solvent was removed and the resulting solid was boiled in EtOH until a homogeneous suspension was obtained. After filtration ligand **L3.1** was isolated as a fine yellow powder (865 mg, 0.547 mmol, 74%).

^{1}H NMR (500 MHz, CDCl$_3$, 25°C, TMS) δ/ppm: 8.40 (d, J = 1.2 Hz, 2H, H^{A3}), 7.61 (d, J = 8.7 Hz, 4H, H^{B2}), 7.33 (d, J = 1.4 Hz, 2H, H^{A5}), 7.09 (d, J = 8.7 Hz, 4H, H^{B3}), 7.06 (d, J = 9.0 Hz, 16H, H^{D2}), 6.99 (d, J = 8.8 Hz, 8H, H^{C2}), 6.89 (d, J = 8.9 Hz, 8H, H^{C3}), 6.83 (d, J = 9.0 Hz, 16H, H^{D3}), 3.79 (s, 24H, H^{OMe}), 2.66 (s, 6H, H^a).

^{13}C NMR (126 MHz, CDCl$_3$, 25°C, TMS) δ/ppm: 158.1 (C^{A6}), 156.6 (C^{A2}), 155.5 (C^{D4}), 149.0 (C^{B1,4}), 144.6 (C^{C4}), 141.2 (C^{D1}), 140.3 (C^{C1}), 130.2 (C^{A4}), 127.6 (C^{B2}), 126.1 (C^{D2}), 126.0 (C^{C2}), 122.2 (C^{C3}), 120.7 (C^{B3}), 120.0 (C^{A5}), 115.9 (C^{A3}), 114.6 (C^{D3}), 55.4 (C^{OMe}), 24.7 (C^a).

IR (ṽ/cm^{-1}): 3045 (w), 3036 (w), 2931 (w), 2836 (w), 1589 (s), 1495 (s), 1318 (m), 1268 (m), 1239 (s), 1177 (m), 1109 (m), 1037 (s), 881 (m), 822 (s), 698 (m).

Mp. [°C]: decomposition > 220 °C.

ESI MS (m/z): 1580.5 m.u. [M+H]$_+$ (calc. 1580.7 m.u.).

UV-VIS (CH$_2$Cl$_2$, 1.0 × 10^{-5} mol dm^{-3}): λ$_{abs}$/nm 226 (ε/dm^3 mol^{-1} cm^{-1} 98900), 307 (86200), 343 (73800).

Found: C, 76.48; H, 5.68; N, 6.41; C$_{104}$H$_{90}$N$_8$O$_8$·3H$_2$O requires C, 76.45; H, 5.92; N, 6.86.

6.7.2 N^1,N$^{1'}$-((6,6'-Di-*n*-butyl-[2,2'-bipyridine]-4,4'-diyl)bis(4,1-phenylene))bis(N^1-(4-(bis(4-methoxyphenyl)amino)phenyl)-N^4,N^4-bis(4-methoxyphenyl)benzene-1,4-diamine): L3.2

SB314, SB331
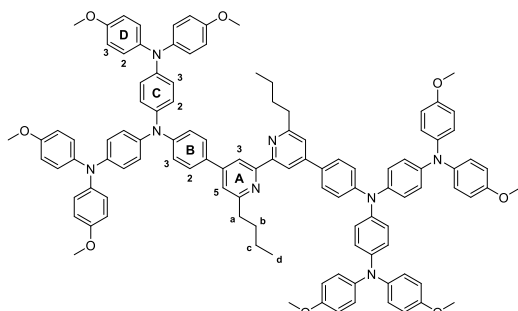
Ligand **L3.2** was prepared and purified in the same manner as **L3.1** starting with 4,4'-bis(4-bromophenyl)-6,6'-di-*n*-butyl-2,2'-bipyridine (69.9 mg, 0.12 mmol, 1.0 eq.), **amine2** (166 mg, 0.26 mmol, 2.2 eq.) and NaO^{t}Bu (63.9 mg, 0.67 mmol, 5.5 eq.) in dry toluene (30 mL). For the preparation of the catalyst suspension Pd(bda)$_2$ (6.95 mg, 0.012 mmol, 10 mol%), dry toluene (10 mL) and 1M toluene solution of P^{t}Bu$_3$ (10.0 μL, 0.012 mmol, 10 mol%) were used. Reaction time at 100°C was 16 h. Ligand **L3.2** was isolated as yellow-green solid (143 mg, 85.9 μmol, 71 %).

^{1}H NMR (500 MHz, CDCl$_3$, 25°C, TMS) δ/ppm: 8.46 (d, *J* = 1.7 Hz, 2H, H^{A3}), 7.62 (d, *J* = 8.8 Hz, 4H, H^{B2}), 7.32 (d, *J* = 1.7 Hz, 2H, H^{A5}), 7.11 (d, *J* = 8.7 Hz, 4H, H^{B3}), 7.07 (d, *J* = 8.9 Hz, 16H, H^{D2}), 7.00 (d, *J* = 8.9 Hz, 8H, H^{C2}), 6.90 (d, *J* = 8.9 Hz, 8H, H^{C3}), 6.83 (d, *J* = 9.0 Hz, 16H, H^{D3}), 3.80 (s, 24H, H^{OMe}), 2.90 (t, *J* = 7.8 Hz, 4H, H^a), 1.86 – 1.78 (m, 4H, H^b), 1.54 – 1.40 (m, 4H, H^c), 0.98 (t, *J* = 7.3 Hz, 6H, H^d).

^{13}C NMR (126 MHz, CDCl$_3$, 25°C, TMS) δ/ppm: 162.3 (C^{A6}), 156.8 (C^{A2}), 155.7 (C^{D4}), 149.2 (C^{B4}), 148.8 (C^{B1}), 144.8 (C^{C4}), 141.4 (C^{D1}), 140.5 (C^{C1}), 130.7 (C^{A4}), 127.8 (C^{B2}), 126.2 (C$^{D2, C2}$), 122.3 (C^{C3}), 120.9 (C^{B3}), 119.6 (C^{A5}), 116.1 (C^{A3}), 114.8 (C^{D3}), 55.6 (C^{OMe}), 38.5 (C^a), 32.2 (C^b), 22.7 (C^c),14.2 (C^d).

IR (ṽ/cm^{-1}): 3038 (w), 2997 (w), 2929 (w), 2833 (w), 1591 (m), 1499 (s), 1238 (s), 1038 (m), 825 (s), 574 (m), 527 (m).

Mp. [°C]: decomposition > 305.

ESI MS (*m/z*): 832.3 m.u. [L3.2+2H]$^{2+}$, (calc. 832.4 m.u.).

UV-VIS (CH$_2$Cl$_2$, 1.0 × 10^{-5} mol dm^{-3}): λ$_{abs}$/nm 226 (ε/dm^3 mol^{-1} cm^{-1} 92100), 307 (87600), 343 (73800).

Found: C, 77.25; H, 5.95; N, 6.66; C$_{110}$H$_{102}$N$_8$O$_8$·2H$_2$O requires C, 77.71; H, 6.28; N, 6.59.

6.7.3 N^1,N$^{1'}$-((6,6'-Di-isobutyl-[2,2'-bipyridine]-4,4'-diyl)bis(4,1-phenylene))bis(N^1-(4-(bis(4-methoxyphenyl)amino)phenyl)-N^4,N^4-bis(4-methoxyphenyl)benzene-1,4-diamine): L3.3

SB303, SB332
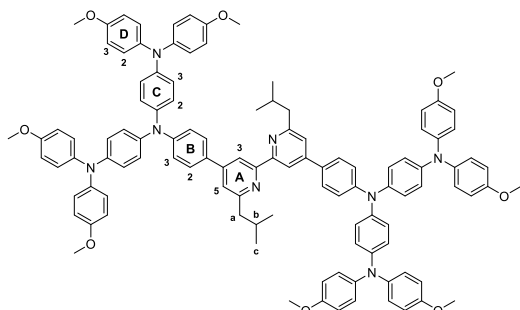
Ligand **L3.3** was prepared and purified in the same manner as **L3.1** starting with 4,4'-bis(4-bromophenyl)-6,6'-di-isobutyl-2,2'-bipyridine (196 mg, 0.34 mmol, 1.0 eq.), **amine2** (466 mg, 0.75 mmol, 2.2 eq.) and NaO^{t}Bu (185 mg, 1.87 mmol, 5.5 eq.) in dry toluene (60 mL). For the preparation of the catalyst suspension Pd(bda)$_2$ (19.5 mg, 0.034 mmol, 10 mol%), dry toluene (20 mL) and 1M toluene solution of P^{t}Bu$_3$ (34.0 μL, 0.034 mmol, 10 mol%) were used. Reaction time at 100°C was 16 h. Ligand **L3.3** was isolated as yellow-green solid (382 mg, 0.23 mmol, 68 %).

^{1}H NMR (500 MHz, CDCl$_3$, 25°C, TMS) δ/ppm: 8.46 (d, J = 1.6 Hz, 2H, H^{A3}), 7.62 (d, J = 8.7 Hz, 4H, H^{B2}), 7.28 (d, J = 1.6 Hz, 2H, H^{A5}), 7.11 (d, J = 8.4 Hz, 4H, H^{B3}), 7.07 (d, J = 9.0 Hz, 16H, H^{D2}), 7.00 (d, J = 8.7 Hz, 8H, H^{C2}), 6.89 (d, J = 8.9 Hz, 8H, H^{C3}), 6.83 (d, J = 9.0 Hz, 16H, H^{D3}), 3.80 (s, 24H, H^{OMe}), 2.76 (d, J = 7.2 Hz, 4H, H^a), 2.30 – 2.22 (m, 2H, H^b), 0.99 (d, J = 6.6 Hz, 12H, H^c).

^{13}C NMR (126 MHz, CDCl$_3$, 25°C, TMS) δ/ppm: 161.3 (C^{A6}), 156.8 (C^{A2}), 155.7 (C^{D4}), 148.6 (C$^{B1, B4}$), 144.8 (C^{C4}), 141.4 (C^{D1}), 140.5 (C^{C1}), 130.5 (C^{A4}), 127.8 (C^{B2}), 126.2 (C$^{D2, C2}$), 122.3 (C^{C3}), 120.9 (C^{B3}), 120.4 (C^{A5}), 116.0 (C^{A3}), 114.8 (C^{D3}), 55.6 (C^{OMe}), 47.9 (C^a), 29.2 (C^b), 22.7 (C^c).

IR (ṽ/cm^{-1}): 3038 (w), 2997 (w), 2952 (w), 2924 (w), 2903 (w), 2866 (w), 2830 (w), 1590 (m), 1499 (s), 1238 (s), 1036 (m), 825 (s), 574 (m), 526 (m).

Mp. [°C]: > 340.

ESI MS (m/z): 1665.6 m.u. [L3.3+H]$^+$, (calc. 1664.8 m.u.), 832.8 m.u. [L3.3+2H]$^{2+}$ (calc. 832.9 m.u.).

UV-VIS (CH$_2$Cl$_2$, 1.0 × 10^{-5} mol dm^{-3}): λ$_{abs}$/nm: 227 (ε/dm^3 mol^{-1} cm^{-1} 96300), 307 (91200), 344 (77800).

Found: C, 78.97; H, 6.21; N, 6.79; C$_{110}$H$_{102}$N$_8$O$_8$·$^1/_2$H$_2$O requires C, 78.97; H, 6.21; N, 6.70.

6.7.4 N^1,N$^{1'}$-((6,6'-Di-*n*-hexyl-[2,2'-bipyridine]-4,4'-diyl)bis(4,1-phenylene))bis(N^1-(4-(bis(4-methoxyphenyl)amino)phenyl)-N^4,N^4-bis(4-methoxyphenyl)benzene-1,4-diamine): L3.4

SB308, SB333
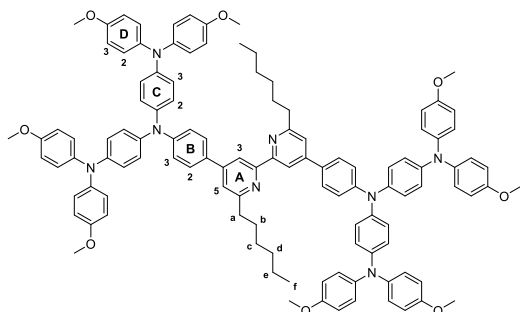
Ligand **L3.4** was prepared and purified in the same manner as **L3.1** starting with 4,4'-bis(4-bromophenyl)-6,6'-di-*n*-hexyl-2,2'-bipyridine (182 mg, 0.29 mmol, 1.0 eq.), **amine2** (394 mg, 0.63 mmol, 2.2 eq.) and NaO^{t}Bu (156 mg, 1.58 mmol, 5.5 eq.) in dry toluene (50 mL). For the preparation of the catalyst suspension Pd(bda)$_2$ (16.5 mg, 0.029 mmol, 10 mol%), dry toluene (10 mL) and 1M toluene solution of P^{t}Bu$_3$ (29.0 μL, 0.029 mmol, 10 mol%) were used. Reaction time at 100°C was 16 h. Ligand **L3.4** was isolated as yellow-green solid (399 mg, 0.23 mmol, 81 %).

^{1}H NMR (500 MHz, CDCl$_3$, 25°C, TMS) δ/ppm: 8.46 (d, J = 1.7 Hz, 2H, H^{A3}), 7.62 (d, J = 8.8 Hz, 4H, H^{B2}), 7.32 (d, J = 1.7 Hz, 2H, H^{A5}), 7.11 (d, J = 8.8 Hz, 4H, H^{B3}), 7.07 (d, J = 9.0 Hz, 16H, H^{D2}), 7.00 (d, J = 8.8 Hz, 8H, H^{C2}), 6.90 (d, J = 8.9 Hz, 8H, H^{C3}), 6.83 (d, J = 9.0 Hz, 16H, H^{D3}), 3.80 (s, 24H, H^{OMe}), 2.90 (t, J = 7.7 Hz, 4H, H^a), 1.90 – 1.78 (m, 4H, H^b), 1.46 – 1.41 (m, 4H, H^c), 1.39 – 1.30 (m, 8H, H^{d,e}), 0.89 (t, J = 7.1 Hz, 6H, H^f).

^{13}C NMR (126 MHz, CDCl$_3$, 25°C, TMS) δ/ppm: 162.3 (C^{A6}), 156.8 (C^{A2}), 155.7 (C^{D4}), 148.8 (C$^{B1, B4}$), 144.8 (C^{C4}), 141.3 (C^{D1}), 140.5 (C^{C1}), 130.4 (C^{A4}), 127.8 (C^{B2}), 126.2 (C$^{D2, C2}$), 122.3 (C^{C3}), 120.9 (C^{B3}), 119.6 (C^{A5}), 116.1 (C^{A3}), 114.8 (C^{D3}), 55.6 (C^{OMe}), 38.7 (C^a), 32.0 (C^b), 30.0 (C^c), 29.3 (C^d), 22.8 (C^e), 14.3 (C^f).

IR (ṽ/cm^{-1}): 3036 (w), 2999 (w), 2950 (w), 2928 (w), 2853 (w), 2833 (w), 1591 (m), 1497 (s), 1237 (s), 1036 (m), 824 (s), 572 (m), 523 (m).

Mp. [°C]: decomposition > 265.

ESI MS (*m/z*): 1720.5 m.u. [L3.4+H]$^+$, (calc. 1720.9 m.u.), 860.3 m.u. [L3.4+2H]$^{2+}$ (calc. 860.95m.u.).

UV-VIS (CH$_2$Cl$_2$, 1.0 × 10^{-5} mol dm^{-3}): λ$_{abs}$/nm 227 (ε/dm^3 mol^{-1} cm^{-1} 99300), 308 (96000), 343 (82600).

Found: C, 79.06; H, 6.58; N, 6.55; C$_{114}$H$_{110}$N$_8$O$_8$·$^1/_2$H$_2$O requires C, 79.18; H, 6.47; N, 6.48.

6.7.5 N^1,N$^{1'}$-((6,6'-Diphenyl-[2,2'-bipyridine]-4,4'-diyl)bis(4,1-phenylene))bis(N^1-(4-(bis(4-methoxyphenyl)amino)phenyl)-N^4,N^4-bis(4-methoxyphenyl)benzene-1,4-diamine): L3.5

SB306, SB334
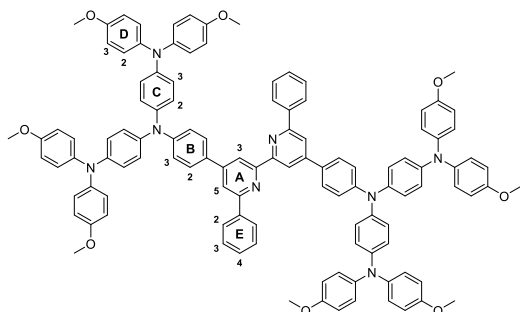
Ligand **L3.5** was prepared and purified in the same manner as **L3.1** starting with 4,4'-bis(4-bromophenyl)-6,6'-diphenyl-2,2'-bipyridine (49.1 mg, 79.4 µmol, 1.0 eq.), **amine2** (109 mg, 175 µmol, 2.2 eq.) and NaO^{t}Bu (41.9 mg, 436 µmol, 5.5 eq.) in dry toluene (50 mL). For the preparation of the

catalyst suspension Pd(bda)$_2$ (4.56 mg, 7.94 µmol, 10 mol%), dry toluene (10 mL) and 1M toluene solution of P^{t}Bu$_3$ (7.94 µL, 7.94 µmol, 10 mol%) were used. Reaction time at 100°C was 16 h. Ligand **L3.5** was isolated as yellow-green solid (88.0 mg, 51.6 µmol, 65%).

^{1}H NMR (400 MHz, CDCl$_3$, 25°C, TMS) δ/ppm: 8.83 (d, J = 1.7 Hz, 2H, H^{A3}), 8.23 (d, J = 7.2 Hz, 4H, H^{E3}), 7.96 (d, J = 1.7 Hz, 2H, H^{A3}), 7.71 (d, J = 8.8 Hz, 4H, H^{B2}), 7.54 (dd, J = 7.4 Hz, 4H, H^{E3}), 7.50 – 7.44 (m, 2H, H^{E4}), 7.16 (d, J = 8.6 Hz, 4H, H^{B3}), 7.08 (d, J = 8.9 Hz, 16H, H^{D2}), 7.03 (d, J = 8.9 Hz, 8H, H^{C2}), 6.92 (d, J = 8.8 Hz, 8H, H^{C3}), 6.84 (d, J = 9.0 Hz, 16H, H^{D3}), 3.80 (s, 24H, H^{OMe}).

^{13}C NMR (126 MHz, CDCl$_3$, 25°C, TMS) δ/ppm: 157.00 (C^{A6}), 156.8 (C^{A2}), 155.7 (C^{D4}), 149.7 (C^{B4}), 149.5 (C^{B1}), 145.0 (C^{C4}), 141.3 (C^{D1}), 140.3 (C^{C1}), 140.0 (C^{E1}), 130.4 (C^{A4}), 128.9 (C^{E4}), 128.8 (C^{E3}), 127.9 (C^{B2}), 127.3 (C^{E2}), 126.3 (C$^{C2, D2}$), 122.2 (C^{C3}), 120.7 (C^{B3}), 117.9 (C^{A5}), 117.3 (C^{A3}), 114.8 (C^{D3}), 55.7 (C^{OMe}).

IR (ṽ/cm^{-1}): 3037 (w), 2998 (w), 2949 (w), 2926 (w), 2900 (w), 2832 (w), 1591 (m), 1495 (s), 1235 (s), 1034 (m), 822 (s), 575 (m), 522 (m).

Mp. [°C]: decomposition > 321.

ESI MS (m/z): 852.4 m.u. [M+2H]$^{2+}$ (calc. 852.7 m.u.).

UV-VIS (CH$_2$Cl$_2$, 1.0×10^{-5} mol dm^{-3}): λ_{abs}/nm 227 (ε / dm^3 mol^{-1} cm^{-1} 133100), 310 (118800), 400 *sh.* (44100).

Found: C, 77.15; H, 5.46; N, 6.29; C$_{114}$H$_{94}$N$_8$O$_8$·4H$_2$O requires C, 77.09; H, 5.79; N, 6.31.

6.7.6 $N^1,N^{1''}$-((6,6'-Di(2-naphthyl)-[2,2'-bipyridine]-4,4'-diyl)bis(4,1-phenylene))bis(N^1-(4-(bis(4-methoxyphenyl)amino)phenyl)-N^4,N^4-bis(4-methoxyphenyl)benzene-1,4-diamine): L3.6

SB319, SB335
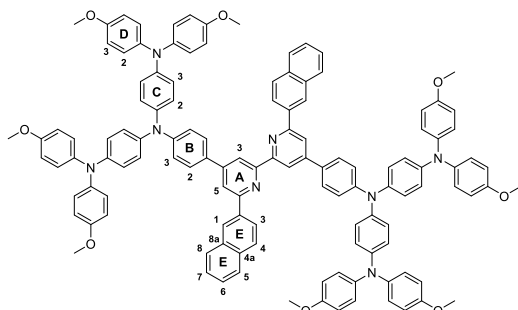
Ligand **L3.6** was prepared and purified in the same manner as **L3.1** starting with 4,4'-bis(4-bromophenyl)-6,6'-di-2-naphthyl-2,2'-bipyridine (240 mg, 0.34 mmol, 1.0 eq.), **amine2** (459 mg, 0.74 mmol, 2.2 eq.) and NaO^{t}Bu (182 mg, 1.84 mmol, 5.5 eq.) in dry toluene (100 mL). For the preparation of the catalyst suspension Pd(bda)$_2$ (19.2 mg, 33.5 µmol, 10 mol%), dry toluene (20 mL) and 1M toluene solution of P^{t}Bu$_3$ (33.5 µL, 33.5 µmol, 10 mol%) were used. Reaction time at 100°C was 16 h. Ligand **L3.6** was isolated as yellow solid (432 mg, 0.24 mmol, 72%).

^{1}H NMR (500 MHz, CDCl$_3$, 25°C, TMS) δ/ppm: 8.93 (d, J = 1.7 Hz, 2H, H^{A3}), 8.65 – 8.63 (m, 2H, H^{E1}), 8.43 (dd, J = 8.6, 1.8 Hz, 2H, H^{E3}), 8.12 (d, J = 1.6 Hz, 2H, H^{A5}), 8.05 – 7.99 (m, 4H, H^{E4}, H$^{E5/E8}$), 7.94 – 7.90 (m, 2H, H$^{E5/E8}$), 7.77 (d, J = 8.7 Hz, 4H, H^{B2}), 7.54 (ddd, J = 10.4, 6.6, 4.8 Hz, 4H, H^{E6}, H^{E7}), 7.18 (d, J = 8.8 Hz, 4H, H^{B3}), 7.08 (d, J = 9.0 Hz, 16H, H^{D2}), 7.04 (d, J = 9.0 Hz, 8H, H^{C2}), 6.92 (d, J = 9.0 Hz, 8H, H^{C3}), 6.84 (d, J = 8.9 Hz, 16H, H^{D3}), 3.80 (s, 24H, H^{OMe}).

^{13}C NMR (126 MHz, CDCl$_3$, 25°C, TMS) δ/ppm: 157.00 (C^{A2,6}), 155.7 (C^{D4}), 149.9 (C^{B1}), 149.5 (C^{B4}), 145.0 (C^{C4}), 141.3 (C^{D1}), 140.3 (C^{C1}), 137.4 (C^{E2}), 133.7 (C^{E4a,E8a}), 130.4 (C^{A4}), 128.9 (C$^{E4, E5/E8}$), 128.0 (C^{B2}), 127.6 (C$^{E5/E8}$), 126.4 (C$^{E1, E6/7}$), 125.2 (C^{E3}), 122.2 (C^{C3}), 120.8 (C^{B3}), 118.1 (C^{A5}), 117.3 (C^{A3}), 114.6 (C^{D3}), 55.7 (C^{OMe}).

IR (ṽ/cm^{-1}): 3038 (w), 2994 (w), 2947 (w), 2931 (w), 2900 (w), 2832 (w), 1599 (m), 1587 (m), 1495 (s), 1235 (s), 1034 (m), 822 (s), 575 (m), 523 (m), 471 (m).

Mp. [°C]: 333.

ESI MS (m/z): 1804.6 m.u. [M+H]$^+$, (calc. 1804.8 m.u.), 902.9 m.u. [M+2H]$^{2+}$ (calc. 902.4 m.u.).

UV-VIS (CH$_2$Cl$_2$, 1.0×10^{-5} mol dm^{-3}): λ_{abs}/nm 228 (ε/dm^3 mol^{-1} cm^{-1} 165000), 306 (140300), 400 sh. (49800).

Found: C, 80.26; H, 5.48; N, 6.18; C$_{122}$H$_{98}$N$_8$O$_8$·H$_2$O requires C, 80.42; H, 5.53; N, 6.15.

6.8 Coppper(I) complexes III: C3.1-3.6

General procedure III

In a typical reaction, the ligand (1.0 eq.) was dissolved in a 1:1 mixture of MeCN and CH$_2$Cl$_2$ (only CH$_2$Cl$_2$ for **L3.5** and **L3.6**) and [Cu(MeCN)$_4$][PF$_6$] (0.5 eq.) was added. The solution turned red immediately for **L3.1-L3.4** and green-black for **L3.5** and **L3.6** respectively. The solution was stirred over night at r.t. after which time, the volume of the solvent was reduced *in vacuo* and the product was precipitated by addition of Et$_2$O. The solid was removed by filtration and washed with Et$_2$O and dried in a stream of air.

6.8.1 [Cu(L3.1)$_2$][PF$_6$]: C3.1

SB242, SB247
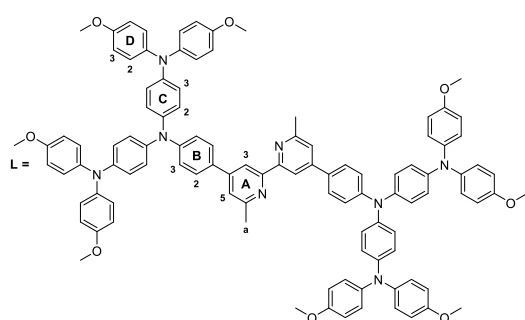
[Cu(MeCN)$_4$][PF$_6$] (69.1 mg, 0.185 mmol, 0.5 eq.) was reacted with **L3.1** (586 mg, 0.371 mmol, 1.0 eq.) in MeCN (15 mL) and CH$_2$Cl$_2$ (15 mL). Complex **C3.1** was isolated as a red solid (601 mg, 0.179 mmol, 96%).

^{1}H NMR (500 MHz, CDCl$_3$, 25°C, TMS) δ/ppm: 8.26 (s, 2H, H^{A3}), 7.62 (d, *J* = 8.6 Hz, 4H, H^{B2}), 7.57 (s, 2H, H^{A5}), 7.11 (d, *J* = 8.6 Hz, 4H, H^{B3}), 7.07 (d, *J* = 8.9 Hz, 16H, H^{D2}), 7.01 (d, *J* = 8.8 Hz, 8H, H^{C2}), 6.90 (d, *J* = 8.9 Hz, 8H, H^{C3}), 6.83 (d, *J* = 9.0 Hz, 16H, H^{D3}), 3.78 (s, 24H, H^{OMe}), 2.31 (s, 6H, H^a).

^{13}C NMR (126 MHz, CDCl$_3$, 25°C, TMS) δ/ppm: 157.1 (C^{A6}), 155.7 (C^{D4}), 152.3 (C^{A2}), 150.3 (C^{A4}), 150.0 (C^{B4}), 145.2 (C^{C4}), 141.0 (C^{D1}), 139.4 (C^{C1}), 127.7 (C^{B2}), 127.4 (C^{B1}), 126.3 (C^{D2}), 126.3 (C^{C2}), 121.6 (C^{C3}), 120.0 (C^{B3}), 122.3 (C^{A5}), 115.9 (C^{A3}), 114.6 (C^{D3}), 55.4 (C^{OMe}), 25.3 (C^a).

MALDI-TOF MS (*m/z*): 3223.9 m.u. [C3.1−PF$_6$]$^+$ (calc. 3222.3 m.u.), 1580.0 m.u. [L3.1+H]$^+$ (calc. 1580.7 m.u.).

UV-VIS (CH$_2$Cl$_2$, 1.0 × 10^{-5} mol dm^{-3}): λ$_{abs}$/nm 224 (ε/dm^3 mol^{-1} cm^{-1} 175400), 309 (162200), 340 *sh.* (138100), 480 *sh.* (41100).

IR (ṽ/cm^{-1}): 3036 (w), 2999 (w), 2951 (w), 2929 (w), 2908 (w), 2834 (w), 1597 (m), 1498 (s), 1313 (m), 1238 (s), 1034 (m), 824 (s), 577 (m), 537 (m).

Mp. [°C]: decomposition > 194.

6.8.2 [Cu(L3.2)₂][PF₆]: C3.2
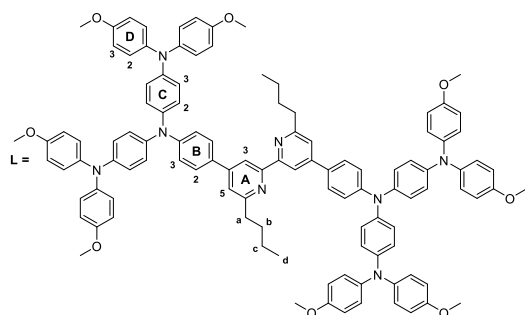
[Cu(MeCN)₄][PF₆] (27.6 mg, 73.9 μmol, 0.5 eq.) was reacted with **L3.2** (246 mg, 0.148 mmol, 1.0 eq.) in MeCN (18 mL) and CH₂Cl₂ (18 mL). Complex **C3.2** was isolated as a red solid (202 mg, 57.2 μmol, 77%).

^{1}H NMR (500 MHz, CD₂Cl₂, 25°C, TMS) δ/ppm: 8.34 (d, J = 1.0 Hz, 4H, H^{A3}), 7.65 (d, J = 8.8 Hz, 8H, H^{B2}), 7.60 (d, J = 1.0 Hz, 4H, H^{A5}), 7.11 (d, J = 8.8 Hz, 8H, H^{B3}), 7.07 (d, J = 9.0 Hz, 32H, H^{D2}), 7.02 (d, J = 8.9 Hz, 16H, H^{C2}), 6.90 (d, J = 8.9 Hz, 16H, H^{C3}), 6.84 (d, J = 9.0 Hz, 32H, H^{D3}), 3.77 (s, 48H, H^{OMe}), 2.64 (t, J = 8.1 Hz, 8H, H^a), 1.39 (tt, J = 15.7, 8.0 Hz, 8H, H^b), 0.90 (tq, J = 14.7, 7.3 Hz, 8H, H^c), 0.48 (t, J = 7.3 Hz, 12H, H^d).

^{13}C NMR (126 MHz, CD₂Cl₂, 25°C, TMS) δ/ppm: 162.0 (C^{A6}), 156.5 (C^{D4}), 153.1 (C^{A2}), 151.0 (C^{B4}), 150.5 (C^{A4}), 146.2 (C^{C4}), 141.4 (C^{D1}), 139.9 (C^{C1}), 128.2 (C^{B2}), 128.0 (C^{B1}), 127.2 (C^{C2}), 126.9 (C^{D2}), 122.1 (C^{A5,C3}), 120.1 (C^{B3}), 116.8 (C^{A3}), 115.2 (C^{D3}), 56.0 (C^{OMe}), 40.2 (C^a), 32.4 (C^b), 23.1 (C^c), 13.8 (C^d).

IR ($\tilde{v}$/cm^{-1}): 3036 (w), 2997 (w), 2954 (w), 2929 (w), 2905 (w), 2834 (w), 1595 (m), 1497 (s), 1313 (m), 1237 (s), 1033 (m), 824 (s), 576 (m), 539 (m).

MALDI-TOF MS (*m/z*): 1728.2 m.u. [L3.2+Cu]$^+$ (calc. 1726.7 m.u.), 1664.8 m.u.[L3.2+H]$^+$ (calc. 1664.8 m.u.).

UV-VIS (CH₂Cl₂, 1.0×10^{-5} mol dm^{-3}): λ_{abs}/nm 225 (ε/dm^3 mol^{-1} cm^{-1} 170200), 309 (159600), 340 *sh.* (134200), 480 *sh.* (39600).

Mp. [°C]: decomposition > 176.

Found: C, 73.53; H, 6.33; N, 6.03; C₂₂₀H₂₀₄CuF₆N₁₆O₁₆P·3H₂O requires C, 73.59; H, 5.89; N, 6.24.

6.8.3 [Cu(L3.3)₂][PF₆]: C3.3

SB324, SB337
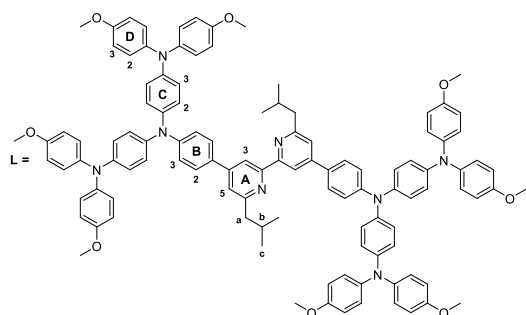
[Cu(MeCN)₄][PF₆] (31.9 mg, 85.7 μmol, 0.5 eq.) was reacted with **L3.3** (285 mg, 171 μmol, 1.0 eq.) in MeCN (10 mL) and CH_2Cl_2 (20 mL). Complex **C3.3** was isolated as a red solid (251 mg, 70.9 μmol, 83%).

^{1}H NMR (500 MHz, CD_2Cl_2, 25°C, TMS) δ/ppm: 8.35 (d, J = 1.3 Hz, 4H, H^{A3}), 7.66 (d, J = 8.9 Hz, 8H, H^{B2}), 7.56 (d, J = 1.3 Hz, 4H, H^{A5}), 7.11 (d, J = 8.8 Hz, 8H, H^{B3}), 7.07 (d, J = 9.0 Hz, 32H, H^{D2}), 7.02 (d, J = 9.0 Hz, 16H, H^{C2}), 6.89 (d, J = 9.0 Hz, 16H, H^{C3}), 6.84 (d, J = 9.0 Hz, 32H, H^{D3}), 3.77 (s, 48H, H^{OMe}), 2.49 (d, J = 7.2 Hz, 8H, H^a), 1.72 (ts, J = 13.7, 6.7 Hz, 4H, H^b), 0.54 (d, J = 6.6 Hz, 24H, H^c).

^{13}C NMR (126 MHz, CD_2Cl_2, 25°C, TMS) δ/ppm: 160.9 (C^{A6}), 156.5 (C^{D4}), 153.6 (C^{A2}), 151.1 (C^{B4}), 150.2 (C^{A4}), 146.2 (C^{C4}), 141.5 (C^{D1}), 139.9 (C^{C1}), 128.2 (C^{B2}), 127.8 (C^{B1}), 127.2 (C^{C2}), 126.9 (C^{D2}), 123.2 (C^{A5}), 122.1 (C^{C3}), 120.2 (C^{B3}), 117.0 (C^{A3}), 115.2 (C^{D3}), 56.0 (C^{OMe}), 49.2 (C^a), 28.8 (C^b), 22.4 (C^c).

IR (ṽ/cm^{-1}): 3030 (w), 2997 (w), 2970 (w), 2952 (w), 2926 (w), 2903 (w), 2866 (w), 2834 (w), 1595 (m), 1497 (s), 1312 (m), 1236 (s), 1034 (m), 824 (s), 576 (m), 528 (m).

MALDI-TOF MS (*m/z*): 3397.1 m.u. [C3.3-PF₆]$^+$ (calc. 3391.5 m.u.), 1729.1 m.u. [L3.3+Cu]$^+$ (calc. 1726.7 m.u.), 1666.0 m.u. [L3.3+H]$^+$ (calc. 1664.8 m.u.).

UV-VIS (CH_2Cl_2, 1.0×10^{-5} mol dm^{-3}): λ_{abs}/nm 225 (ε/dm^3 mol^{-1} cm^{-1} 164000), 309 (159900), 340 *sh*. (134000), 480 *sh*. (41400).

Mp. [°C]: decomposition > 185.

Found: C, 74.30; H, 6.03; N, 6.49; $C_{220}H_{204}N_{16}O_{16}CuPF_6$ requires C, 74.71; H, 5.81; N, 6.34.

6.8.4 [Cu(L3.4)₂][PF₆]: C3.4
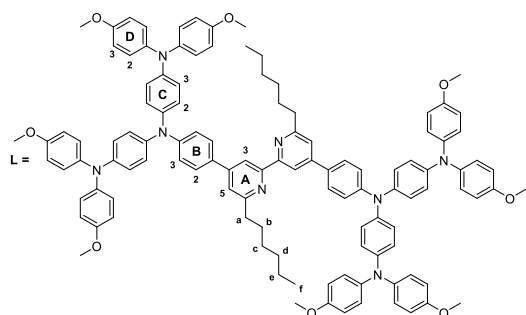
[Cu(MeCN)₄][PF₆] (29.5 mg, 79.1 μmol, 0.5 eq.) was reacted with **L3.4** (272 mg, 158 μmol, 1.0 eq.) in MeCN (20 mL) and CH₂Cl₂ (20 mL). Complex **C3.4** was isolated as a red solid (242 mg, 66.2 μmol, 84%).

^{1}H NMR (500 MHz, CD₂Cl₂, 25°C, TMS) δ/ppm: 8.34 (d, J = 1.2 Hz, 4H, H^{A3}), 7.65 (d, J = 8.9 Hz, 8H, H^{B2}), 7.61 (d, J = 1.2 Hz, 4H, H^{A5}), 7.11 (d, J = 8.8 Hz, 8H, H^{B3}), 7.07 (d, J = 9.0 Hz, 32H, H^{D2}), 7.02 (d, J = 9.0 Hz, 16H, H^{C2}), 6.90 (d, J = 9.0 Hz, 16H, H^{C3}), 6.84 (d, J = 9.0 Hz, 32H, H^{D3}), 3.77 (s, 48H, H^{OMe}), 2.63 (t, J = 8.2 Hz, 8H, H^a), 1.40 (tt, J = 16.0, 7.8 Hz, 4H, H^b), 1.01 – 0.89 (m, 8H, H^c), 0.91 – 0.83 (m, 8H, H^d), 0.83 – 0.75 (m, 8H, H^e), 0.61 (t, J = 7.3 Hz, 12H, H^f).

^{13}C NMR (126 MHz, CD₂Cl₂, 25°C, TMS) δ/ppm: 162.1 (C^{A6}), 156.5 (C^{D4}), 153.1 (C^{A2}), 151.0 (C^{B4}), 150.5 (C^{A4}), 146.2 (C^{C4}), 141.4 (C^{D1}), 139.9 (C^{C1}), 128.2 (C^{B2}), 127.9 (C^{B1}), 127.1 (C^{C2}), 126.9 (C^{D2}), 122.2 (C^{A5}), 122.1 (C^{C3}), 120.2 (C^{B3}), 116.6 (C^{A3}), 115.2 (C^{D3}), 56.0 (C^{OMe}), 40.6 (C^a), 32.0 (C^b), 30.5 (C^c), 29.9 (C^d), 23.0 (C^e), 14.3 (C^f).

IR (ṽ/cm^{-1}): 3037 (w), 2997 (w), 2950 (w), 2928 (w), 2853 (w), 2834 (w), 1594 (m), 1495 (s), 1312 (m), 1235 (s), 1032 (m), 822 (s), 575 (m), 536 (m).

MALDI-TOF MS (*m/z*): 1784.7 m.u. [L3.4+Cu]$^+$ (calc. 1782.8 m.u.), 1720.9 m.u. [L3.4+H]$^+$ (calc. 1720.9 m.u.).

UV-VIS (CH₂Cl₂, 1.0 × 10^{-5} mol dm^{-3}): λ$_{abs}$/nm 225 (ε/dm^3 mol^{-1} cm^{-1} 164100), 309 (155400), 340 *sh.* (131200), 480 *sh.* (42200).

Mp. [°C]: 168.

Found: C, 73.54; H, 6.25; N, 6.14; C₂₂₈H₂₂₀N₁₆O₁₆CuPF₆·4H₂O requires C, 73.60; H, 6.18; N, 6.02.

6.8.5 [Cu(L3.5)₂][PF₆]: C3.5
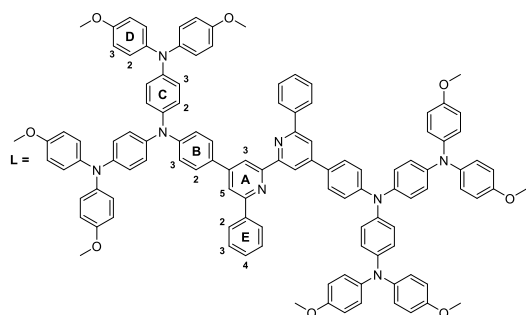
[Cu(MeCN)₄][PF₆] (27.8 mg, 74.5 μmol, 0.5 eq.) was reacted with **L3.5** (254 mg, 149 μmol, 1.0 eq.) in CH₂Cl₂ (40 mL). Complex **C3.5** was isolated as a green-black solid (233 mg, 64.3 μmol, 86%).

^{1}H NMR (500 MHz, CD₂Cl₂, 25°C, TMS) δ/ppm: 8.02 (d, J = 1.7 Hz, 4H, H^{A3}), 7.66 (d, J = 1.7 Hz, 4H, H^{A5}), 7.65 – 7.61 (m, 16H, H^{B2,E2}), 7.14 (d, J = 8.5 Hz, 8H, H^{B3}), 7.09 (d, J = 9.0 Hz, 32H, H^{D2}), 7.07 – 7.03 (m, 20H, H^{C2,E4}), 6.96 – 6.89 (m, 24H, H^{C3,E3}), 6.86 (d, J = 9.0 Hz, 32H, H^{D3}), 3.78 (s, 48H, H^{OMe}).

^{13}C NMR (126 MHz, CD₂Cl₂, 25°C, TMS) δ/ppm: 157.4 (C^{A6}), 156.5 (C^{D4}), 154.2 (C^{A2}), 151.1 (C^{B4}), 150.2 (C^{A4}), 146.6 (C^{C4}), 141.5 (C^{D1}), 139.8 (C^{C1}), 139.2 (C^{E1}), 129.5 (C^{E4}), 128.2 (C^{E2}), 128.0 (C^{E3}), 127.9 (C^{B1}), 127.2 (C^{C1}), 126.9 (C^{D2}), 122.1 (C^{C3}), 121.9 (C^{A5}), 120.1 (C^{B3}), 118.4 (C^{A3}), 115.2 (C^{D3}), 55.9 (C^{OMe}).

IR (ṽ/cm^{-1}): 3033 (w), 3004 (w), 2989 (w), 2952 (w), 2929 (w), 2903 (w), 2834 (w), 1593 (m), 1497 (s), 1314 (m), 1238 (s), 1032 (m), 824 (s), 765 (m), 750 (m), 576 (m), 538 (m).

MALDI-TOF MS (*m/z*): 3478.9 m.u. [C3.5-PF₆]$^+$ (calc. 3471.4 m.u.), 1769.1 m.u. [L3.5+Cu]$^+$ (calc. 1766.7 m.u.), 1705.7 m.u. [L3.5+H]$^+$ (calc. 1704.7 m.u.).

UV-VIS (CH₂Cl₂, 1.0×10^{-5} mol dm^{-3}): λ$_{abs}$/nm 226 (ε/dm³ mol^{-1} cm^{-1} 225900), 308 (190100), 340 *sh*. (166000), 435 *sh.* (57000), 580 *sh.* (11500).

Mp. [°C]: decomposition > 195.

Found: C, 73.04; H, 5.16; N, 6.16; C₂₂₈H₁₈₈N₁₆O₁₆CuPF₆·2CH₂Cl₂ requires C, 72.96; H, 5.11; N, 5.92.

6.8.6 [Cu(L3.6)₂][PF₆]: C3.6
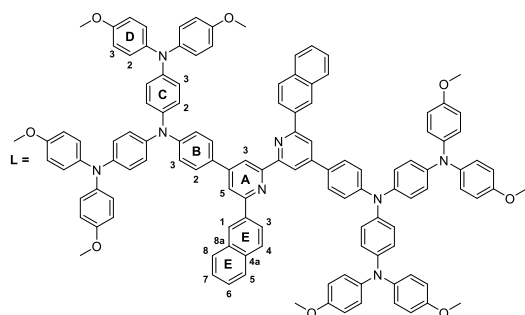
[Cu(MeCN)$_4$][PF$_6$] (25.3 mg, 67.8 μmol, 0.5 eq.) was reacted with **L3.6** (245 mg, 136 μmol, 1.0 eq.) in CH$_2$Cl$_2$ (100 mL). Complex **C3.6** was isolated as a green-black solid (231 mg, 60.6 μmol, 89%).

^{1}H NMR (500 MHz, CD$_2$Cl$_2$, 25°C, TMS) δ/ppm: 8.29 (d, J = 1.4 Hz, 4H, H^{E1}), 7.69 (dd, J = 8.5, 1.6 Hz, 4H, H^{E3}), 7.60 (d, J = 1.3 Hz, 4H, H^{A5}), 7.58 (d, J = 8.2 Hz, 4H, H^{E5}), 7.45 (d, J = 8.5 Hz, 4H, H^{E4}), 7.43 (d, J = 1.3 Hz, 4H, H^{A3}), 7.36 (d, J = 8.7 Hz, 8H, H^{B2}), 7.35 - 7.32 (m, 4H, H^{E7}), 7.24 – 7.19 (m, 8H, H^{E6,E8}), 7.14 – 7.05 (m, 56H, H$^{B3,C2,\,D2}$), 6.95 (d$_{AB}$, J = 8.9 Hz, 16H, H^{C3}), 6.87 (d$_{AB}$, J = 9.0 Hz, 32H, H^{D3}), 3.79 (s, 48H, H^{OMe}).

^{13}C NMR (126 MHz, CD$_2$Cl$_2$, 25°C, TMS) δ/ppm: 156.8 (C^{A6}), 156.6 (C^{D4}), 154.1 (C^{A2}), 151.0 (C^{B4}), 150.1 (C^{A4}), 146.2 (C^{C4}), 141.5 (C^{D1}), 139.9 (C^{C1}), 136.4 (C^{E4a}), 133.7 (C^{E2}), 132.6 (C^{E8a}), 128.5 (C^{E8}), 128.2 (C^{B2}), 128.0 (C^{E1}), 127.8 (C^{E5}), 127.7 (C^{E4,E7}), 127.5 (C^{B1}), 127.2 (C^{C2}), 127.0 (C^{D2,E6}), 125.6 (C^{E3}), 122.1 (C^{C3}), 121.5 (C^{A5}) 120.0 (C^{B3}), 118.0 (C^{A3}), 115.2 (C^{D3}), 56.0 (C^{OMe}).

IR ($\tilde{v}$/cm^{-1}): 3036 (w), 3002 (w), 2991 (w), 2950 (w), 2926 (w), 2903 (w), 2833 (w), 1592 (m), 1496 (s), 1314 (m), 1275 (m), 1261 (m), 1237 (s), 1033 (m), 823 (s), 765 (s), 751 (s), 575 (m), 525 (m), 477 (m).

MALDI-TOF MS (*m/z*): 3676.2 m.u. [C3.6-PF$_6$]$^+$ (calc. 3671.4 m.u.), 1869.9 m.u. [L3.6+Cu]$^+$ (calc. 1867.7 m.u.), 1805.9 m.u. [L3.6+H]$^+$ (calc. 1804.8 m.u.).

UV-VIS (CH$_2$Cl$_2$, 1.0 × 10^{-5} mol dm^{-3}): λ_{abs}/nm: 226 (ε/dm^3 mol^{-1} cm^{-1} 276400), 240 *sh.* (237300), 306 (194300), 340 *sh.* (170200), 448 (56000), 580 *sh.* (10700).

Mp. [°C]: decomposition > 195.

Found: C, 75.83; H, 5.42; N, 5.81; C$_{244}$H$_{196}$N$_{16}$O$_{16}$CuPF$_6$·2H$_2$O requires C, 76.06; H, 5.23; N, 5.82.

References

[1]   *APEX2, Version 2 User Manual, M86-E01078, Bruker Anal. X-Ray Syst. Inc., Madison, WI*, **2006**.

[2]   G. M. Sheldrick, *Acta Crystallogr. A.* **2008**, *64*, 112–122.

[3]   I. J. Bruno, J. C. Cole, P. R. Edgington, M. Kessler, C. F. Macrae, P. McCabe, J. Pearson, R. Taylor, *Acta Crystallogr. Sect. B Struct. Sci.* **2002**, *58*, 389–397.

[4]   C. F. Macrae, I. J. Bruno, J. A. Chisholm, P. R. Edgington, P. McCabe, E. Pidcock, L. Rodriguez-Monge, R. Taylor, J. van de Streek, P. A. Wood, *J. Appl. Crystallogr.* **2008**, *41*, 466–470.

[5]   "World Population Prospects The 2012 Revision Volume I : Comprehensive Tables" can be found under, http://esa.un.org/unpd/wpp/Documentation/pdf/WPP2012_Volume-I_Comprehensive-Tables.pdf, last time accessed 04.06.2014.

[6]   "World population projected to reach 9.6 billion by 2050" can be found under, http://esa.un.org/unpd/wpp/Documentation/pdf/WPP2012_Press_Release.pdf, last time accessed 04.06.2014.

[7]   "International Energy Outlook 2013" can be found under, http://www.eia.gov/forecasts/ieo/pdf/0484%25282013%2529.pdf, last time accessed 22.05.2014.

[8]   O. Hahn, L. Meitner, F. Straßmann, *Berichte der Dtsch. Chem. Gesellschaft (A B Ser.* **1936**, *69*, 905–919.

[9]   O. Hahn, F. Strassmann, E. Walling, *Naturwissenschaften* **1937**, *25*, 189.

[10]   O. Hahn, F. Strassmann, *Naturwissenschaften* **1938**, *26*, 755–756.

[11]   O. Hahn, F. Strassmann, *Naturwissenschaften* **1938**, *27*, 89–95.

[12]   O. Hahn, F. Strassmann, *Naturwissenschaften* **1939**, *27*, 11–15.

[13]   L. Meitner, O. R. Frisch, *Nature* **1939**, 239–240.

[14]   L. Meitner, O. R. Frisch, *Nature* **1939**, *143*, 471–472.

[15]   *Pop. Mech.* **1952**, 105.

[16]   "From Obninsk Beyond: Nuclear Power Conference Looks to Future," can be found under http://www.iaea.org/newscenter/news/2004/obninsk.html, last time accessed 04.06.2014.

[17]   "Nuclear power plants, world-wide," can be found under http://www.euronuclear.org/info/encyclopedia/n/nuclear-power-plant-world-wide.htm, last time accessed 04.06.2014.

[18]   H. Kragh, *Quantum Generations: A History of Physics in the Twentieth Century*, Princeton University Press, Princeton NJ, **1999**.

[19]   "IAEA/PRIS Power Reactor Information System", can be found under http://www.iaea.org/pris/home.aspx, last time accessed 04.06.2014.

[20]   "Electricity generation" can be found under http://www.oecd-ilibrary.org/sites/factbook-2013-en/06/01/03/index.html?itemId=/content/chapter/factbook-2013-43-en, last time accessed 04.06.2014.

[21]   "Emissions of Carbon Dioxide", can be found under http://www.oecd-ilibrary.org/sites/factbook-2013-en/09/02/01/airqty_g1.html?itemId=/content/chapter/factbook-2013-70-en, last time accessed 04.06.2014.

[22]   J. K. Bates, J. P. Bradley, A. Teetsov, C. R. Bradley, M. B. Ten Brink, *Science* **1992**, *256*, 649–651.

[23]   *Site Characterization Plan: Yucca Mountain Site, Nevada Research and Development Area, Nevada*, Washington, DC, **1988**.

[24] E. S. Patera, D. E. Hobart, A. Meijer, R. S. Rundberg, *J. Radioanal. Nucl. Chem. Artic.* **1990**, *142*, 331–347.

[25] H. Nitsche, *Radiochim. Acta* **1991**, *52-53*, 3–8.

[26] J. Hansen, M. Sato, R. Ruedy, K. Lo, D. W. Lea, M. Medina-Elizade, *Proc. Natl. Acad. Sci. U. S. A.* **2006**, *103*, 14288–14293.

[27] "International Energy Statistics", can be found under http://www.eia.gov/cfapps/ipdbproject/iedindex3.cfm?tid=6&pid=29&aid=12&cid=ww,r1,r2,r3,r4,r5,r6,r7,&syid=1980&eyid=2012&unit=BKWH, last time accessed 04.06.2014.

[28] "International Energy Statistics" can be found under http://www.eia.gov/cfapps/ipdbproject/IeDIndex3.cfm?tid=6&eyid=2010&syid=2010&reverseAxes=0&cid=&cid=ww&pid=alltypes&aid=12&unit=BKWH&updateB=UPDATE, last time accessed 04.06.2014.

[29] Solar Fuels and Artificial Photosynthesis: Science and innovation to change our future energy options, *R. Soc. Chem.* **2012**, 5–20.

[30] OECD/IEA, "Solar Energy Perspectives: Executive Summary," **2011**.

[31] David Archer, *Global Warming: Understanding the Forecast*, Wiley, **2011**.

[32] Q. Schiermeier, J. Tollefson, T. Scully, A. Witze, O. Morton, *Nature* **2008**, *454*, 816–823.

[33] A. Hagfeldt, G. Boschloo, L. Sun, L. Kloo, H. Pettersson, *Chem. Rev.* **2010**, *110*, 6595–6663.

[34] R. F. Service, *Science* **2005**, *309*, 548–551.

[35] J. Potocnik, *Science* **2007**, *315*, 810–811.

[36] "Reference Solar Spectral Irradiance: Air Mass 1.5", can be found under http://rredc.nrel.gov/solar/spectra/am1.5/ASTMG173/ASTMG173.html, last time accessed 04.06.2014.

[37] K. G. Reddy, T. G. Deepak, G. S. Anjusree, S. Thomas, S. Vadukumpully, K. R. V Subramanian, S. V Nair, a S. Nair, *Phys. Chem. Chem. Phys.* **2014**, *16*, 6838–6858.

[38] P. V. Kamat, *J. Phys. Chem. C* **2007**, *111*, 2834–2860.

[39] "Application of Nanotechnologies in the Energy Sector", can be found under http://www.hessen-nanotech.de/mm/NanoEnergy_web.pdf, last time accessed 04.06.2014.

[40] J. N. M. Fischedick, O. Langniß, *Nach Dem Ausstieg - Zukunftskurs Erneuerbare Energien*, S. Hirzel Verlag, **2000**.

[41] J. R. Bolton, D. O. Hall, *Annu. Rev. Energy* **1979**, *4*, 353–401.

[42] A. J. Bard, M. A. Fox, *Acc. Chem. Res.* **1995**, *28*, 141–145.

[43] A. E. Becquerel, *Comptes Rendues Acad. Sci.* **1839**, 145.

[44] J. Moser, *Monatshefte für Chemie* **1887**, *8*, 373–373.

[45] G. Ciamician, *Science* **1912**, *36*, 385–394.

[46] B. O'Regan, M. Grätzel, *Nature* **1991**, *353*, 737–740.

[47] J. Burschka, N. Pellet, S.-J. Moon, R. Humphry-Baker, P. Gao, M. K. Nazeeruddin, M. Grätzel, *Nature* **2013**, *499*, 316–319.

[48] "Evonik: Products & Applications", can be found under http://corporate.evonik.de/en/products/industry-teams/solar-power/products-applications/Pages/aeroxide.aspx, last time accessed 04.06.2014.

[49] K. Kalyanasundaram, *Dye-Sensitized Solar Cells*, EPFL Press, Lausanne, Switzerland, **2010**.

[50] J. N. Clifford, E. Martínez-Ferrero, E. Palomares, *J. Mater. Chem.* **2012**, *22*, 12415–12422.

[51] J. B. Asbury, R. J. Ellingson, H. N. Ghosh, S. Ferrere, A. J. Nozik, T. Lian, *J. Phys. Chem. B* **1999**, *103*, 3110–3119.

[52] G. Benkö, J. Kallioinen, J. E. I. Korppi-Tommola, A. P. Yartsev, V. Sundström, *J. Am. Chem. Soc.* **2002**, *124*, 489–493.

[53] G. Ramakrishna, D. A. Jose, D. K. Kumar, A. Das, D. K. Palit, H. N. Ghosh, *J. Phys. Chem. B* **2005**, *109*, 15445–15453.

[54] D. Kuang, S. Ito, B. Wenger, C. Klein, J.-E. Moser, R. Humphry-Baker, S. M. Zakeeruddin, M. Grätzel, *J. Am. Chem. Soc.* **2006**, *128*, 4146–4154.

[55] S. E. Koops, B. C. O'Regan, P. R. F. Barnes, J. R. Durrant, *J. Am. Chem. Soc.* **2009**, *131*, 4808–4818.

[56] P. Wang, B. Wenger, R. Humphry-Baker, J.-E. Moser, J. Teuscher, W. Kantlehner, J. Mezger, E. V Stoyanov, S. M. Zakeeruddin, M. Grätzel, *J. Am. Chem. Soc.* **2005**, *127*, 6850–6856.

[57] A. Hagfeldt, G. Boschloo, H. Lindström, E. Figgemeier, A. Holmberg, V. Aranyos, E. Magnusson, L. Malmqvist, *Coord. Chem. Rev.* **2004**, *248*, 1501–1509.

[58] T. W. Hamann, R. a. Jensen, A. B. F. Martinson, H. Van Ryswyk, J. T. Hupp, *Energy Environ. Sci.* **2008**, *1*, 66–78.

[59] M. Pagliaro, G. Palmisano, R. Ciriminna, V. Loddo, *Energy Environ. Sci.* **2009**, *2*, 838–844.

[60] R. Jose, V. Thavasi, S. Ramakrishna, *J. Am. Ceram. Soc.* **2009**, *92*, 289–301.

[61] Q. Zhang, C. S. Dandeneau, X. Zhou, G. Cao, *Adv. Mater.* **2009**, *21*, 4087–4108.

[62] A. Hagfeldt, M. Graetzel, *Chem. Rev.* **1995**, *95*, 49–68.

[63] V. C. Fuertes, C. F. a Negre, M. B. Oviedo, F. P. Bonafé, F. Y. Oliva, C. G. Sánchez, *J. Phys. Condens. Matter* **2013**, *25*, 115304–115310.

[64] A. Di Paola, M. Bellardita, R. Ceccato, L. Palmisano, F. Parrino, *J. Phys. Chem. C* **2009**, *113*, 15166–15174.

[65] F. Pichot, J. R. Pitts, B. A. Gregg, *Langmuir* **2000**, *16*, 5626–5630.

[66] H. Lindström, E. Magnusson, A. Holmberg, S. Södergren, S. Lindquist, A. Hagfeldt, *Sol. Energy Mater. Sol. Cells* **2002**, *73*, 91–101.

[67] H. Lindström, A. Holmberg, E. Magnusson, S. Lindquist, L. Malmqvist, A. Hagfeldt, *Nano Lett.* **2001**, *1*, 97–100.

[68] T. Yamaguchi, N. Tobe, D. Matsumoto, H. Arakawa, *Chem. Commun. (Camb).* **2007**, 4767–4769.

[69] K. D. Benkstein, N. Kopidakis, J. van de Lagemaat, a. J. Frank, *J. Phys. Chem. B* **2003**, *107*, 7759–7767.

[70] H. Gerischer, H. Tributsch, *Berichte der Bunsen-Gesellschaft* **1968**, *72*, 437–445.

[71] H. Gerischer, M. E. Michel-Beyerle, F. Rebentrost, H. Tributsch, *Electrochim. Acta* **1968**, *13*, 1509–1515.

[72] G. M. Hasselman, D. F. Watson, J. R. Stromberg, D. F. Bocian, D. Holten, J. S. Lindsey, G. J. Meyer, *J. Phys. Chem. B* **2006**, *110*, 25430–25440.

[73] J. Desilvestro, M. Graetzel, L. Kavan, J. Moser, J. Augustynski, *J. Am. Chem. Soc.* **1985**, *107*, 2988–2990.

[74] G. K. Mor, O. K. Varghese, M. Paulose, K. Shankar, C. a. Grimes, *Sol. Energy Mater. Sol. Cells* **2006**, *90*, 2011–2075.

[75] E. Galoppini, *Coord. Chem. Rev.* **2004**, *248*, 1283–1297.

[76] P. Péchy, F. P. Rotzinger, M. K. Nazeeruddin, O. Kohle, S. M. Zakeeruddin, R. Humphry-Baker, M. Graetzel, *J. Chem. Soc. Chem. Commun.* **1995**, *369*, 65–66.

[77] H. Park, E. Bae, J.-J. Lee, J. Park, W. Choi, *J. Phys. Chem. B* **2006**, *110*, 8740–8749.

[78] K. Murakoshi, G. Kano, Y. Wada, S. Yanagida, H. Miyazaki, M. Matsumoto, S. Murasawa, *J. Electroanal. Chem.* **1995**, *396*, 27–34.

[79] Z.-S. Wang, K. Hara, Y. Dan-oh, C. Kasada, A. Shinpo, S. Suga, H. Arakawa, H. Sugihara, *J. Phys. Chem. B* **2005**, *109*, 3907–3914.

[80] M. K. Nazeeruddin, R. Humphry-Baker, P. Liska, M. Grätzel, *J. Phys. Chem. B* **2003**, *107*, 8981–8987.

[81] A. Hagfeldt, M. Grätzel, *Acc. Chem. Res.* **2000**, *33*, 269–277.

[82] C. Klein, M. K. Nazeeruddin, D. Di Censo, P. Liska, M. Grätzel, *Inorg. Chem.* **2004**, *43*, 4216–4226.

[83] I. Chung, B. Lee, J. He, R. P. H. Chang, M. G. Kanatzidis, *Nature* **2012**, *485*, 486–489.

[84] K.-L. Wu, S.-T. Ho, C.-C. Chou, Y.-C. Chang, H.-A. Pan, Y. Chi, P.-T. Chou, *Angew. Chem. Int. Ed. Engl.* **2012**, *51*, 5642–5646.

[85] A. Yella, H.-W. Lee, H. N. Tsao, C. Yi, A. K. Chandiran, M. K. Nazeeruddin, E. W.-G. Diau, C.-Y. Yeh, S. M. Zakeeruddin, M. Grätzel, *Science* **2011**, *334*, 629–634.

[86] L. Schmidt-Mende, W. M. Campbell, Q. Wang, K. W. Jolley, D. L. Officer, M. K. Nazeeruddin, M. Grätzel, *ChemPhysChem* **2005**, *6*, 1253–1258.

[87] S. Mathew, A. Yella, P. Gao, R. Humphry-Baker, B. F. E. Curchod, N. Ashari-Astani, I. Tavernelli, U. Rothlisberger, M. K. Nazeeruddin, M. Grätzel, *Nat. Chem.* **2014**, *6*, 242–247.

[88] A. Burke, L. Schmidt-Mende, S. Ito, M. Grätzel, *Chem. Commun. (Camb).* **2007**, 234–236.

[89] S. Ferrere, A. Zaban, B. A. Gregg, *J. Phys. Chem. B* **1997**, *101*, 4490–4493.

[90] Z. Wang, F. Li, C. Huang, *J. Phys. Chem. B* **2001**, *105*, 9210–9217.

[91] K. Sayama, S. Tsukagoshi, T. Mori, K. Hara, Y. Ohga, A. Shinpou, Y. Abe, S. Suga, H. Arakawa, *Sol. Energy Mater. Sol. Cells* **2003**, *80*, 47–71.

[92] K. Hara, K. Sayama, H. Arakawa, Y. Ohga, A. Shinpo, S. Suga, *Chem. Commun.* **2001**, 569–570.

[93] G. K. R. Senadeera, P. V. V. Jayaweera, V. P. S. Perera, K. Tennakone, *Sol. Energy Mater. Sol. Cells* **2002**, *73*, 103–108.

[94] S. Ardo, G. J. Meyer, *Chem. Soc. Rev.* **2009**, *38*, 115–164.

[95] D. Kuang, C. Klein, S. Ito, J.-E. Moser, R. Humphry-Baker, N. Evans, F. Duriaux, C. Grätzel, S. M. Zakeeruddin, M. Grätzel, *Adv. Mater.* **2007**, *19*, 1133–1137.

[96] S. A. Haque, E. Palomares, B. M. Cho, A. N. M. Green, N. Hirata, D. R. Klug, J. R. Durrant, *J. Am. Chem. Soc.* **2005**, *127*, 3456–3462.

[97] M. K. Nazeeruddin, A. Kay, I. Rodicio, R. Humphry-Baker, E. Mueller, P. Liska, N. Vlachopoulos, M. Graetzel, *J. Am. Chem. Soc.* **1993**, *115*, 6382–6390.

[98] M. K. Nazeeruddin, P. Péchy, M. Grätzel, *Chem. Commun.* **1997**, *1*, 1705–1706.

[99] M. K. Nazeeruddin, S. M. Zakeeruddin, R. Humphry-Baker, M. Jirousek, P. Liska, N. Vlachopoulos, V. Shklover, C.-H. Fischer, M. Grätzel, *Inorg. Chem.* **1999**, *38*, 6298–6305.

[100] N. Alonso-Vante, J.-F. Nierengarten, J. Sauvage, *J. Chem. Soc. Dalt. Trans.* **1994**, *11*, 1649–1654.

[101] S. Sakaki, T. Kuroki, T. Hamada, *J. Chem. Soc. Dalt. Trans.* **2002**, 840–842.

[102] J. Cong, X. Yang, L. Kloo, L. Sun, *Energy Environ. Sci.* **2012**, *5*, 9180–9194.

[103] T. Daeneke, T.-H. Kwon, A. B. Holmes, N. W. Duffy, U. Bach, L. Spiccia, *Nat. Chem.* **2011**, *3*, 211–215.

[104] A. Hauch, A. Georg, *Electrochim. Acta* **2001**, *46*, 3457–3466.

[105] N. Papageorgiou, *J. Electrochem. Soc.* **1997**, *144*, 876.

[106] S.-S. Kim, Y.-C. Nah, Y.-Y. Noh, J. Jo, D.-Y. Kim, *Electrochim. Acta* **2006**, *51*, 3814–3819.

[107] S. Kim, K. Park, J. Yum, Y. Sung, *Sol. Energy Mater. Sol. Cells* **2006**, *90*, 283–290.

[108] A. Kay, M. Grätzel, *Sol. Energy Mater. Sol. Cells* **1996**, *44*, 99–117.

[109] K. Imoto, K. Takahashi, T. Yamaguchi, T. Komura, J. Nakamura, K. Murata, *Sol. Energy Mater. Sol. Cells* **2003**, *79*, 459–469.

[110] T. N. Murakami, S. Ito, Q. Wang, M. K. Nazeeruddin, T. Bessho, I. Cesar, P. Liska, R. Humphry-Baker, P. Comte, P. Péchy, et al., *J. Electrochem. Soc.* **2006**, *153*, A2255.

[111] E. Ramasamy, W. J. Lee, D. Y. Lee, J. S. Song, *Appl. Phys. Lett.* **2007**, *90*, 173103.

[112] E. Olsen, G. Hagen, S. Eric Lindquist, *Sol. Energy Mater. Sol. Cells* **2000**, *63*, 267–273.

[113] D. R. McMillin, M. T. Buckner, B. T. Ahn, *Inorg. Chem.* **1977**, *16*, 943–945.

[114] C. a. Bignozzi, R. Argazzi, C. J. Kleverlaan, *Chem. Soc. Rev.* **2000**, *29*, 87–96.

[115] N. Armaroli, *Chem. Soc. Rev.* **2001**, *30*, 113–124.

[116] N. Armaroli, L. De Cola, V. Balzani, J.-P. Sauvage, C. O. Dietrich-Buchecker, J.-M. Kern, *J. Chem. Soc. Faraday Trans.* **1992**, *88*, 553–556.

[117] C. C. Phifer, D. R. McMillin, *Inorg. Chem.* **1986**, *25*, 1329–1333.

[118] A. K. Ichinaga, J. R. Kirchhoff, D. R. McMillin, C. O. Dietrich-Buchecker, P. A. Marnot, J. P. Sauvage, *Inorg. Chem.* **1987**, *26*, 4290–4292.

[119] M. T. Miller, T. B. Karpishin, *Inorg. Chem.* **1999**, *38*, 5246–5249.

[120] M. T. Miller, P. K. Gantzel, T. B. Karpishin, *Inorg. Chem.* **1998**, *37*, 2285–2290.

[121] W. Kylberg, Ph.D. Thesis, University of Basel, **2008**.

[122] R. M. Everly, D. R. McMillin, *Photochem. Photobiol.* **1989**, *50*, 711–716.

[123] M. Ruthkosky, C. A. Kelly, M. C. Zaros, G. J. Meyer, *J. Am. Chem. Soc.* **1997**, *119*, 12004–12005.

[124] M. Ruthkosky, C. A. Kelly, F. N. Castellano, G. J. Meyer, *Coord. Chem. Rev.* **1998**, *171*, 309–322.

[125] A. Kirsch-De Mesmaeker, L. Wilputte-Steinert, J. Nasielski, *Inorg. Chim. Acta* **1980**, *45*, L37–L39.

[126] P. A. Breddels, P. A. M. Berdowski, G. Blasse, *Recl. des Trav. Chim. des Pays-Bas* **1981**, *100*, 439–440.

[127] "What the Earth is Made Of", can be found under http://www.uwgb.edu/dutchs/PLANETS/Geochem.htm, last time accessed 04.06.2014.

[128] "Rare Earth Elements—Critical Resources for High Technology", can be found under http://pubs.usgs.gov/fs/2002/fs087-02/, last time accessed 04.06.2014.

[129] "RARE EARTH ELEMENTS", can be found under http://www.periodni.com/rare_earth_elements.html, last time accessed 04.06.2014.

[130] "Kupfer, Grad A Kathode monatlicher Preis", can be found under http://www.indexmundi.com/de/rohstoffpreise/?ware=kupfer&monate=360, 04.06.2014.

[131] "Copper and Ruthenium Prices", can be found under http://www.quandl.com/markets/, 04.06.2014.

[132] S. Anderson, E. C. Constable, M. P. Dare-Edwards, J. B. Goodenough, A. Hamnett, K. R. Seddon, R. D. Wright, *Nature* **1979**, *280*, 571–573.

[133] A. H. Rendondo, E. C. Constable, C. E. Housecroft, *Chimia.* **2009**, *63*, 205–207.

[134] B. Bozic-Weber, E. C. Constable, C. E. Housecroft, P. Kopecky, M. Neuburger, J. a Zampese, *Dalton Trans.* **2011**, *40*, 12584–12594.

[135] J. Nelson, *The Physics of Solar Cells*, Imperial College Press, London, **2003**.

[136] X. Yang, M. Yanagida, L. Han, *Energy Environ. Sci.* **2013**, *6*, 54–66.

[137] F. Kröhnke, *Synthesis (Stuttg).* **1976**, 1–24.

[138] F. Kröhnke, *Angew. Chem. Int. Ed.* **1963**, 225–238.

[139] L. C. King, *J. Am. Chem. Soc.* **1944**, *66*, 894–895.

[140] L. C. King, M. McWhirter, R. L. Rowland, *J. Am. Chem. Soc.* **1948**, *70*, 239–242.

[141] L. C. King, *J. Am. Chem. Soc.* **1948**, *70*, 242–244.

[142] W. Zecher, F. Kröhnke, *Chem. Ber.* **1961**, *94*, 690–697.

[143] W. Zecher, F. Kröhnke, *Chem. Ber.* **1961**, *94*, 698–706.

[144] A. Michael, *J. Prakt. Chem.* **1886**, *35*, 349–356.

[145] A. Michael, *J. Prakt. Chem.* **1894**, *49*, 20–25.

[146] C. Mannich, W. Koch, F. Borkowsky, *Berichte der Dtsch. Chem. Gesellschaft (A B Ser.* **1937**, *70*, 355–359.

[147] A. Hantzsch, *Berichte der Dtsch. Chem. Gesellschaft* **1881**, *14*, 1637–1638.

[148] A. E. Tschitschibabin, *J. Prakt. Chem.* **1924**, *107*, 122–128.

[149] M. Weiss, *J. Am. Chem. Soc.* **1952**, *74*, 200–202.

[150] J. J. Lie, *Name Reactions: A Collection of Detailed Reaction Mechanisms*, Springer-Verlag; Berlin, Heidelberg, **2006**.

[151] F. Paul, J. Patt, J. F. Hartwig, *J. Am. Chem. Soc.* **1994**, *116*, 5969–5970.

[152] A. S. Guram, S. L. Buchwald, *J. Am. Chem. Soc.* **1994**, *116*, 7901–7902.

[153] D. S. Surry, S. L. Buchwald, *Angew. Chem. Int. Ed.* **2008**, *47*, 6338–6361.

[154] J. F. Hartwig, *Acc. Chem. Res.* **2008**, *41*, 1534–1544.

[155] S. L. Buchwald, C. Mauger, G. Mignani, U. Scholz, *Adv. Synth. Catal.* **2006**, *348*, 23–39.

[156] M. S. Driver, J. F. Hartwig, *J. Am. Chem. Soc.* **1995**, *117*, 4708–4709.

[157] J. F. Hartwig, S. Richards, D. Barañano, F. Paul, *J. Am. Chem. Soc.* **1996**, *118*, 3626–3633.

[158] R. A. Widenhoefer, S. L. Buchwald, *Organometallics* **1996**, *15*, 2755–2763.

[159] M. S. Driver, J. F. Hartwig, *J. Am. Chem. Soc.* **1997**, *119*, 8232–8245.

[160] B. Bozic-Weber, V. Chaurin, E. C. Constable, C. E. Housecroft, M. Meuwly, M. Neuburger, J. A. Rudd, E. Schönhofer, L. Siegfried, *Dalton Trans.* **2012**, *41*, 14157–14169.

[161] T. Maruyama, T. Yamamoto, *Inorg. Chim. Acta* **1995**, *238*, 9–13.

[162] N. a Gothard, M. W. Mara, J. Huang, J. M. Szarko, B. Rolczynski, J. V Lockard, L. X. Chen, *J. Phys. Chem. A* **2012**, *116*, 1984–92.

[163] M. K. Eggleston, D. R. McMillin, K. S. Koenig, A. J. Pallenberg, *Inorg. Chem.* **1997**, *36*, 172–176.

[164] H. Mohan, J. P. Mittal, *J. Phys. Chem.* **1995**, *99*, 6519–6524.

[165] F. Fabrizi de Biani, E. Grigiotti, F. Laschi, P. Zanello, A. Juris, L. Prodi, K. S. Chichak, N. R. Branda, *Inorg. Chem.* **2008**, *47*, 5425–5440.

[166] B. Bozic-Weber, S. Y. Brauchli, E. C. Constable, S. O. Fürer, C. E. Housecroft, I. a Wright, *Phys. Chem. Chem. Phys.* **2013**, *15*, 4500–4504.

[167] R. J. Williams, *Eur. J. Biochem.* **1995**, *234*, 363–381.

[168] M. Nič, J. Jirát, B. Košata, A. Jenkins, A. McNaught, Eds., *IUPAC Compendium of Chemical Terminology*, IUPAC, Research Triangle Park, NC, **2009**.

[169] Y. Hirao, H. Ino, A. Ito, K. Tanaka, T. Kato, *J. Phys. Chem. A* **2006**, *110*, 4866–4872.

[170] P. J. Burke, D. R. McMillin, W. R. Robinson, *Inorg. Chem.* **1980**, *19*, 1211–1214.

[171] S. Itoh, N. Kishikawa, T. Suzuki, H. D. Takagi, *Dalton Trans.* **2005**, *2*, 1066–1078.

[172] P. Yang, X.-J. Yang, B. Wu, *Eur. J. Inorg. Chem.* **2009**, *2009*, 2951–2958.

[173] S. Kume, M. Murata, T. Ozeki, H. Nishihara, *J. Am. Chem. Soc.* **2005**, *127*, 490–491.

[174] R. M. Williams, L. De Cola, F. Hartl, J. Lagref, J. Planeix, A. De Cian, M. W. Hosseini, *Coord. Chem. Rev.* **2002**, *230*, 253–261.

[175] H. Akdas-Kilig, J.-P. Malval, F. Morlet-Savary, A. Singh, L. Toupet, I. Ledoux-Rak, J. Zyss, H. Le Bozec, *Dye. Pigment.* **2012**, *92*, 681–688.

[176] D. A. Bardwell, J. C. Jeffery, C. A. Otter, M. D. Ward, *Polyhedron* **1996**, *15*, 191–194.

[177] M. Cesario, C. O. Dietrich-Buchecker, J. Guilhem, C. Pascard, J. P. Sauvage, *J. Chem. Soc. Chem. Commun.* **1985**, 244–247.

[178] C. O. Dietrich-Buchecker, J. Guilhem, A. K. Khemiss, J.-P. Kintzinger, C. Pascard, J.-P. Sauvage, *Angew. Chemie Int. Ed. English* **1987**, *26*, 661–663.

[179] C. Dietrich-Buchecker, N. Geum Hwang, J.-P. Sauvage, *New J. Chem.* **1999**, *23*, 911–914.

[180] C. Dietrich-Buchecker, G. Rapenne, J.-P. Sauvage, A. De Cian, J. Fischer, *Chem. - A Eur. J.* **1999**, *5*, 1432–1439.

[181] J. Chambron, J. Sauvage, K. Mislow, J. Fischer, *Chem.–Eur. J.* **2001**, *7*, 4085–4096.

[182] M. Geoffroy, M. Wermeille, C. O. Buchecker, J.-P. Sauvage, G. Bernardinelli, *Inorg. Chim. Acta* **1990**, *167*, 157–164.

[183] B. Wu, P. Yang, X. Huang, Y. Liu, X. Liu, C. Xia, *Z. Anorg. Allg. Chemie* **2006**, *632*, 684–688.

[184] C. T. Cunningham, J. J. Moore, K. L. H. Cunningham, P. E. Fanwick, D. R. McMillin, *Inorg. Chem.* **2000**, *39*, 3638–3644.

[185] A. Hernández Redondo, Ph.D. Thesis, University of Basel, **2009**.

[186] B. Bozic-Weber, S. Y. Brauchli, E. C. Constable, S. O. Fürer, C. E. Housecroft, F. J. Malzner, I. a Wright, J. a Zampese, *Dalton Trans.* **2013**, *42*, 12293–12308.

[187] V. Penicaud, F. Odobel, B. Bujoli, *Tetrahedron Lett.* **1998**, *39*, 3689–3692.

[188] T. Bessho, E. C. Constable, M. Graetzel, A. Hernandez Redondo, C. E. Housecroft, W. Kylberg, M. K. Nazeeruddin, M. Neuburger, S. Schaffner, *Chem. Commun.* **2008**, 3717–3719.

[189] B. Bozic-Weber, V. Chaurin, E. C. Constable, C. E. Housecroft, M. Meuwly, M. Neuburger, J. A Rudd, E. Schönhofer, L. Siegfried, *Dalton Trans.* **2012**, *41*, 14157–14169.

[190] P. Kopecky, Ph.D. Thesis, University of Basel, **2012**.

[191] B. Wenger, M. Grätzel, J.-E. Moser, *Chimia* **2005**, *59*, 123–125.

[192] B. Wenger, M. Grätzel, J.-E. Moser, *J. Am. Chem. Soc.* **2005**, *127*, 12150–12151.

[193] V. K. Thorsmølle, B. Wenger, J. Teuscher, C. Bauer, J.-E. Moser, *Chimia* **2007**, *61*, 631–634.

[194] S. Ito, M. K. Nazeeruddin, P. Liska, P. Comte, R. Charvet, P. Péchy, M. Jirousek, A. Kay, S. M. Zakeeruddin, M. Grätzel, *Prog. Photovoltaics Res. Appl.* **2006**, *14*, 589–601.

[195] H. J. Snaith, *Energy Environ. Sci.* **2012**, *5*, 6513–6520.

[196] S. Ito, T. N. Murakami, P. Comte, P. Liska, C. Grätzel, M. K. Nazeeruddin, M. Grätzel, *Thin Solid Films* **2008**, *516*, 4613–4619.

[197] S. Ito, P. Chen, P. Comte, M. K. Nazeeruddin, P. Liska, P. Péchy, M. Grätzel, *Prog. Photovoltaics Res. Appl.* **2007**, *15*, 603–612.

[198] B. Bozic-Weber, E. C. Constable, N. Hostettler, C. E. Housecroft, R. Schmitt, E. Schönhofer, *Chem. Commun.* **2012**, *48*, 5727–5729.

[199] S. Ito, H. Miura, S. Uchida, M. Takata, K. Sumioka, P. Liska, P. Comte, P. Péchy, M. Grätzel, *Chem. Commun.* **2008**, 5194–5196.

[200] N. Koumura, Z.-S. Wang, S. Mori, M. Miyashita, E. Suzuki, K. Hara, *J. Am. Chem. Soc.* **2006**, *128*, 14256–14257.

[201] A. K. Jena, P. Bhargava, *RSC Adv.* **2013**, *3*, 2655.

[202] A. C. Khazraji, S. Hotchandani, S. Das, P. V Kamat, *J. Phys. Chem. B* **1999**, *103*, 4693–4700.

[203] S. Jang, J. Yum, C. Klein, K. Kim, P. Wagner, D. Officer, M. Grätzel, M. K. Nazeeruddin, *J. Phys. Chem. C* **2009**, *113*, 1998–2003.

[204] S. M. Zakeeruddin, M. K. Nazeeruddin, R. Humphry-Baker, P. Péchy, P. Quagliotto, C. Barolo, G. Viscardi, M. Grätzel, *Langmuir* **2002**, *18*, 952–954.

[205] G. Schlichthörl, S. Y. Huang, J. Sprague, A. J. Frank, *J. Phys. Chem. B* **1997**, *101*, 8141–8155.

[206] J. E. Kroeze, N. Hirata, S. Koops, M. K. Nazeeruddin, L. Schmidt-Mende, M. Grätzel, J. R. Durrant, *J. Am. Chem. Soc.* **2006**, *128*, 16376–16383.

[207] Z. Ning, Q. Zhang, W. Wu, H. Pei, B. Liu, H. Tian, *J. Org. Chem.* **2008**, *73*, 3791–3797.

[208] Z. Ning, H. Tian, *Chem. Commun.* **2009**, 5483–5495.

[209] W. W. Brandt, F. P. Dwyer, E. D. Gyarfas, *Chem. Rev.* **1954**, *54*, 959–1017.

[210] Y. Jahng, J. Hazelrigg, D. Kimball, E. Riesgo, F. Wu, R. P. Thummel, *Inorg. Chem.* **1997**, *36*, 5390–5395.

[211] D. V. Scaltrito, D. W. Thompson, J. a. O'Callaghan, G. J. Meyer, *Coord. Chem. Rev.* **2000**, *208*, 243–266.

[212] L. Schmidt-Mende, J. E. Kroeze, J. R. Durrant, M. K. Nazeeruddin, M. Grätzel, *Nano Lett.* **2005**, *5*, 1315–1320.

[213] Z.-S. Wang, F. Li, C. Huang, L. Wang, M. Wei, L. Jin, N.-Q. Li, *J. Phys. Chem. B* **2000**, *104*, 9676–9682.

[214] D. P. Hagberg, T. Edvinsson, T. Marinado, G. Boschloo, A. Hagfeldt, L. Sun, *Chem. Commun. (Camb).* **2006**, 2245–2247.

[215] A. Mishra, M. K. R. Fischer, P. Bäuerle, *Angew. Chem. Int. Ed.* **2009**, *48*, 2474–2499.

[216] H. Tian, X. Yang, R. Chen, R. Zhang, A. Hagfeldt, L. Sun, *J. Phys. Chem. C* **2008**, *112*, 11023–11033.

[217] J.-H. Yum, D. P. Hagberg, S.-J. Moon, K. M. Karlsson, T. Marinado, L. Sun, A. Hagfeldt, M. K. Nazeeruddin, M. Grätzel, *Angew. Chem. Int. Ed.* **2009**, *48*, 1576–1580.

[218] H. Imahori, T. Umeyama, S. Ito, *Acc. Chem. Res.* **2009**, *42*, 1809–1818.

[219] M. Liang, W. Xu, F. Cai, P. Chen, B. Peng, J. Chen, Z. Li, *J. Phys. Chem. C* **2007**, *111*, 4465–4472.

[220] G. Li, K. Jiang, Y.-F. Li, S. Li, L. Yang, *J. Phys. Chem. C* **2008**, *112*, 11591–11599.

[221] D. Liu, R. W. Fessenden, G. L. Hug, P. V Kamat, *J. Phys. Chem. B* **1997**, *101*, 2583–2590.

[222] P. Wen, M. Xue, Y. Ishikawa, H. Itoh, Q. Feng, *ACS Appl. Mater. Interfaces* **2012**, *4*, 1928–1934.

[223] Q.-B. Meng, K. Takahashi, X.-T. Zhang, I. Sutanto, T. N. Rao, O. Sato, A. Fujishima, H. Watanabe, T. Nakamori, M. Uragami, *Langmuir* **2003**, *19*, 3572–3574.

[224] B. O. Regan, T. Ghaddar, *Energy Environ. Sci.* **2012**, 7203–7215.

[225] V. Gusak, L.-P. Heiniger, V. P. Zhdanov, M. Grätzel, B. Kasemo, C. Langhammer, *Energy Environ. Sci.* **2013**, *6*, 3627–3636.

[226] R. Chen, G. Zhao, X. Yang, X. Jiang, J. Liu, H. Tian, Y. Gao, X. Liu, K. Han, M. Sun, *J. Mol. Struct.* **2008**, *876*, 102–109.

[227] D. P. Wilson, D. Sporleder, M. G. White, *J. Phys. Chem. C* **2012**, *116*, 16541–16552.

[228] D. P. Hagberg, J.-H. Yum, H. Lee, F. De Angelis, T. Marinado, K. M. Karlsson, R. Humphry-Baker, L. Sun, A. Hagfeldt, M. Grätzel, et al., *J. Am. Chem. Soc.* **2008**, *130*, 6259–6266.

[229] S. Y. Huang, G. Schlichthörl, A. J. Nozik, M. Grätzel, A. J. Frank, *J. Phys. Chem. B* **1997**, *101*, 2576–2582.

[230] P. Péchy, T. Renouard, S. M. Zakeeruddin, R. Humphry-Baker, P. Comte, P. Liska, L. Cevey, E. Costa, V. Shklover, L. Spiccia, et al., *J. Am. Chem. Soc.* **2001**, *123*, 1613–1624.

[231] P. Salvatori, G. Marotta, A. Cinti, C. Anselmi, E. Mosconi, F. De Angelis, *J. Phys. Chem. C* **2013**, *117*, 3874–3887.

[232] A. Kay, M. Graetzel, *J. Phys. Chem.* **1993**, *97*, 6272–6277.

[233] T. Daeneke, T.-H. Kwon, A. B. Holmes, N. W. Duffy, U. Bach, L. Spiccia, *Nat. Chem.* **2011**, *3*, 211–215.

[234] P. Vijitjunya, S. Keawket, C. Thanachayanont, A. Heawchin, N. Pungwiwu, *J. Microsc. Soc. Thail.* **2010**, *24*, 140–144.

[235] A. Ehret, L. Stuhl, M. T. Spitler, *J. Phys. Chem. B* **2001**, *105*, 9960–9965.

[236] S. Tatay, S. A. Haque, B. O'Regan, J. R. Durrant, W. J. H. Verhees, J. M. Kroon, A. Vidal-Ferran, P. Gaviña, E. Palomares, *J. Mater. Chem.* **2007**, *17*, 3037–3044.

[237] Z.-S. Wang, Y. Cui, Y. Dan-oh, C. Kasada, A. Shinpo, K. Hara, *J. Phys. Chem. C* **2007**, *111*, 7224–7230.

[238] M. Pastore, F. De Angelis, *ACS Nano* **2010**, *4*, 556–562.

[239] C. Bauer, G. Boschloo, E. Mukhtar, A. Hagfeldt, *J. Phys. Chem. B* **2002**, *106*, 12693–12704.

[240] J. Jiu, S. Isoda, F. Wang, M. Adachi, *J. Phys. Chem. B* **2006**, *110*, 2087–2092.

[241] J.-H. Yum, S.-R. Jang, R. Humphry-Baker, M. Grätzel, J.-J. Cid, T. Torres, M. K. Nazeeruddin, *Langmuir* **2008**, *24*, 5636–5640.

[242] J. H. Yum, S. J. Moon, R. Humphry-Baker, P. Walter, T. Geiger, F. Nüesch, M. Grätzel, M. D. K. Nazeeruddin, *Nanotechnology* **2008**, *19*, 424005–424010.

[243] K.-M. Lee, V. Suryanarayanan, K.-C. Ho, K. R. Justin Thomas, J. T. Lin, *Sol. Energy Mater. Sol. Cells* **2007**, *91*, 1426–1431.

[244] X. Jiang, T. Marinado, E. Gabrielsson, D. P. Hagberg, L. Sun, A. Hagfeldt, *J. Phys. Chem. C* **2010**, *114*, 2799–2805.

[245] K. Hara, Y. Dan-oh, C. Kasada, Y. Ohga, A. Shinpo, S. Suga, K. Sayama, H. Arakawa, *Langmuir* **2004**, *20*, 4205–4210.

[246] H.-P. Lu, C.-Y. Tsai, W.-N. Yen, C.-P. Hsieh, C.-W. Lee, C.-Y. Yeh, E. W.-G. Diau, *J. Phys. Chem. C* **2009**, *113*, 20990–20997.

[247] J.-H. Yum, P. Walter, S. Huber, D. Rentsch, T. Geiger, F. Nüesch, F. De Angelis, M. Grätzel, M. K. Nazeeruddin, *J. Am. Chem. Soc.* **2007**, *129*, 10320–10321.

[248] A. Zaban, S. Ferrere, B. A. Gregg, *J. Phys. Chem. B* **1998**, *102*, 452–460.

[249] Y. Hirao, A. Ito, K. Tanaka, *J. Phys. Chem. A* **2007**, *111*, 2951–2956.

[250] D. Sakamaki, A. Ito, K. Tanaka, K. Furukawa, T. Kato, M. Shiro, *Angew. Chemie* **2012**, *124*, 8406–8410.

[251] C. Li, J. Schöneboom, Z. Liu, N. G. Pschirer, P. Erk, A. Herrmann, K. Müllen, *Chemistry* **2009**, *15*, 878–884.